Modélisation et simulation d'écoulements et transferts convectifs. Applications en thermoacoustique

Catherine Weisman

SORBONNE UNIVERSITÉ
Laboratoire d'Informatique pour la Mécanique et les Sciences de l'Ingénieur

Mémoire présenté pour obtenir
L'HABILITATION À DIRIGER DES RECHERCHES

par

Catherine WEISMAN

Modélisation et simulation d'écoulements et transferts convectifs. Applications en thermoacoustique

---

soutenue le **24 juin 2020**,

devant le jury composé de :

Président	**Pierre-Yves Lagrée**	Directeur de Recherche, CNRS, ∂'Alembert, Paris Paris
Rapporteurs	**Bénédicte Cuenot**	Chercheur Senior, CERFACS, Toulouse
	Pierrick Lotton	Directeur de Recherche, CNRS, LAUM, Le Mans
	Shihe Xin	Professeur des Universités, INSA Lyon & CETHIL
Examinateurs	**Marie-Catherine Charrier-Mojtabi**	Professeur Emérite, Université Paul Sabatier, IMFT, Toulouse
	Bérengère Podvin	Chargée de Recherche HDR, CNRS, LIMSI, Orsay

Préambule

La préparation d'une Habilitation à Diriger des Recherches est avant tout un travail personnel, mais dans le cas présent elle s'inscrit également dans une démarche collective. Cela fait près de 20 ans que je travaille avec ma collègue et amie Diana Baltean-Carlès, et plus de 10 ans que Virginie Daru s'est jointe à nous. Nous formons une équipe féminine, enthousiaste et solidaire. Il y a un an, nous avons pris la décision d'entreprendre côte à côte la rédaction du document, d'organiser nos soutenances au LIMSI au même moment, et de terminer par une belle fête collective. Alors que je n'envisageais plus une HDR à ce stade de ma carrière, j'ai été séduite par la convivialité et l'originalité de cette démarche. Nous avons fixé une date vers la fin de l'année universitaire afin d'organiser les 3 soutenances.

Nous étions loin d'imaginer que nous rédigerions une grande partie du document chacune chez soi, en échangeant et se soutenant par visioconférence pendant la crise sanitaire du Coronavirus. Isolées de nos collègues du laboratoire, de l'Université et de nos collaborateurs habituels, avec très peu de documents papiers à notre disposition, nous avons donc préparé cette HDR dans des conditions particulières.

De plus, j'avais envisagé ce premier semestre 2020 comme une période de rédaction calme, avec peu ou presque plus d'enseignement. Au lieu de cela, nous avons dû mettre en place des enseignements à distance, organiser l'étalement des plannings, coordonner les équipes enseignantes pour garantir la meilleure équité possible entre les étudiants, mettre en place de nouvelles évaluations, répondre à des centaines de mails. Cette période est devenue extrêmement chargée.

La rédaction du mémoire, je le reconnais, est un travail de réflexion utile pour un enseignant-chercheur. Lorsqu'elle survient après presque 30 ans de carrière comme pour moi, elle permet de revenir sur les travaux passés, de prendre un véritable recul et de faire le lien entre mes diverses activités. Je réalise à quel point les rencontres ont compté pour moi et m'ont guidée à travers ces années d'enseignement et de recherche.

Mes professeurs et directeurs de thèse aux Etats-Unis m'ont fait découvrir les attraits et défis de la recherche interdisciplinaire. A l'UPMC (devenue Sorbonne Université), j'ai beaucoup appris à travers de longs échanges avec mes collègues enseignants, en particulier ceux du plateau d'Orsay. Les chercheurs du LIMSI ont marqué mes activités de recherche et m'ont insufflé l'envie de progresser. J'ai profité de l'ambiance chaleureuse et conviviale de notre laboratoire, un atout si précieux. Les collaborations avec des chercheurs hors LIMSI m'ont fait découvrir des approches et méthodes différentes. Enfin tous mes jeunes stagiaires, thésards et post-doctorants m'ont donné l'énergie de travailler et progresser avec eux.

J'adresse tous mes remerciements aux membres de mon jury : rapporteurs, examinateurs et président, pour leur participation enrichissante et bienveillante à cette aventure. J'espère sincèrement que nous pourrons organiser une belle fête au LIMSI à l'automne.

Je remercie aussi toute ma famille qui m'a si grandement aidée pendant toute cette période.

Cette rédaction permet enfin d'envisager de multiples pistes sur les études à venir. Nous avons encore beaucoup de travail devant nous, et surtout la perspective de continuer ensemble, Diana, Virginie et moi.

Table des matières

Curriculum Vitae

Catherine WEISMAN, née FUNK
Maître de Conférences Hors Classe 60ème section
U.F.R. 919 Ingénierie
Faculté des Sciences et Ingénierie, Sorbonne Université, 4 Place Jussieu, 75005 Paris
Laboratoire d'Informatique pour la Mécanique et les Sciences de l'Ingénieur LIMSI, CNRS UPR 3251
Campus Universitaire bât 507, rue du Belvédère, 91405 Orsay Cedex

Renseignements personnels

Date et lieu de naissance	le 24 décembre 1963 à Paris 14ème
Nationalité	Française
Situation de famille	Mariée, 3 enfants
Courrier électronique	catherine.weisman@upmc.fr

Diplômes

1990	Ph.D. Univ. of Rochester, Mechanical Engineering Dpt, New York, U.S.A.
1990	Doctorat, Institut National Polytechnique de Lorraine, Génie Biomédical Titre de la thèse : « Modélisation mathématique du système des phosphates à haute énergie au cours des échanges énergétiques de la cellule musculaire. »
1986	Master of Science, Mechanical Engineering, University of Rochester, U.S.A.
1985	Diplôme d'ingénieur de l'Ecole Nationale Supérieure d'Electricité et de Mécanique de Nancy option Mécanique

Déroulement de carrière

1991 -présent	Maître de Conférences à l'Université Pierre et Marie Curie UFR 923 (Mécanique, Energétique, Robotique), puis UFR 919 (Ingénierie) intégrée depuis janvier 2016 dans la Faculté des Sciences et Ingénierie Sorbonne Université. Titularisée en 1993 Promotion Première Classe en 1998 (avant passage à la Classe Normale MC en 2001) Travail à temps partiel (80%) pour raisons familiales de 1998 à 2009 Promotion Hors Classe en 2010 Promotion échelon exceptionnel en 2018
1990-1991	Stage post-doctoral et vacations d'enseignement, Mechanical Engineering Dpt University of Rochester, NY, USA
1987-1990	Assistante de Recherche (doctorante) et chargée de TD et d'un cours Mechanical Engineering Dpt, University of Rochester, NY, USA

Recherche

1987-1991 : thèse et stage post-doctoral à l'Université de Rochester, Etats-Unis
Thèmes : transport couplé par réaction/diffusion dans les cellules musculaires.

1991-1995 : recherche au Laboratoire de Modélisation, Matériaux et Structures LM2S de l'UPMC
Thèmes : ondes électromagnétiques dans les milieux composites à structure périodique

Depuis 1995 : recherche au Laboratoire d'Informatique pour la Mécanique et les Sciences de l'Ingénieur, LIMSI
Thèmes : convection naturelle en milieu fluide et poreux, instabilités, convection hors Boussinesq, modélisation faible Mach, modélisation et simulation numérique des phénomènes d'excitation et de pompage de chaleur thermoacoustiques. Etude de l'instabilité thermoacoustique. Modélisation et simulation numérique du streaming acoustique linéaire et non linéaire en guide d'ondes.

Publications

18 articles de revue internationale (dont 5 dans des revues « special issue »)
2 articles de revue nationale
1 conférence invitée, 12 actes de congrès internationaux
11 actes de congrès nationaux
16 participations à des congrès sans actes et 14 colloques ou séminaires

Co-encadrement de travail post-doctoral

Omar Hireche (12 mois 2018-2019), contrat de recherche dans le cadre de l'ANR TACOT, Thermo-Acoustic Cooler for On road Transportation, Défi « Energie Propre, Sûre et Efficace », 2017-2020 (porteur H. Bailliet Institut P', LIMSI partenaire).
Sujets de recherche : Convection naturelle dans les machines thermoacoustiques (étude numérique avec comparaison avec les mesures réalisées à P') ; Comparaison de l'approximation faible Mach et de l'approche compressible pour la simulation du pompage de chaleur thermoacoustique dans une machine compacte.
Participation à l'encadrement : 60% (co-encadrement avec D. Baltean-Carlès et V. Daru)
1 conférence CFM 2019 avec actes et prise en compte pour publication dans Mechanics&Industry,
1 publication soumise à IJHMT.

Ida Reyt (2 ans 2012-2014) pendant ses contrats ATER UPsud + ENSAM
Sujet de recherche : comparaison simulations numériques/expérience du streaming acoustique non linéaire dans un résonateur cylindrique.
Participation à l'encadrement : 30% (co-encadrement avec D. Baltean-Carlès et V. Daru)
3 publications, 3 conférences nationales avec actes, 2 conférence sans actes.

Jean-François Mercier (12 mois, 2001-2002 pendant son contrat ATER Univ. Paris VI)
Sujet de recherche : simulation numérique des écoulements de convection naturelle en cavité différentiellement chauffée partiellement remplie d'un milieu poreux.
Participation à l'encadrement : 80% (co-encadrement avec M. Firdaouss)
1 publication, 1 conférence avec actes, 1 conférence sans acte

Co-directions de thèse

Lin Ma (2011-14), ED SMAER, Thèse de Doctorat de l'UPMC
« Modélisation et simulation des effets non linéaires et multidimensionnels d'un moteur thermoacoustique : influence d'une charge résistive »
Directeur de thèse : I. Delbende
Participation à l'encadrement : 50% (autre co-encadrante : D. Baltean-Carlès)
Publications : 1 article de revue int., 1 article de revue int. « special issue », 3 congrès int. avec actes, 1 congrès/acte à diffusion restreinte
Lin Ma est enseignant-chercheur en Chine

Omar Hireche (2007-10), thèse Algérienne de l'USTO Oran
« Analyse faible Mach et étude numérique d'un système thermoacoustique »
Directeurs de thèse : M.-X. François et M. Abidat –USTO
Participation à l'encadrement : 60% (autre co-encadrante : D. Baltean-Carlès)
Publications : 2 articles de revues int., 1 congrès int. avec actes, 1 congrès/acte à diffusion restreinte, 1 congrès sans acte, 1 colloque
Omar Hireche est Maître de Conférences classe A au Département de Mécanique de l'Ecole Nationale Polytechnique d'Oran, Algérie

Patxi Duthil (2001-03), thèse Université Pierre et Marie Curie, en co-tutelle Hong Kong University of Science and Technology
« Etude du pompage de chaleur Thermoacoustique : approches numérique et expérimentale »,
Directeur de thèse : M.-X. François et P. Cheng- HKUST,
Participation à l'encadrement : 60%
Publications : 1 article de revue int. « special issue », 2 congrès int. avec actes, 1 congrès/acte à diffusion restreinte, 1 colloque.
Patxi Duthil est ingénieur de recherche à l'Institut de Physique Nucléaire d'Orsay

Alain Oster (1991-94), thèse Université Pierre et Marie Curie,
« Electromagnétisme dans les composites, homogénéisation et propagation d'ondes »
Directeur de thèse : N. Turbé
Participation à l'encadrement : 10%
Pas de publication

Encadrement de stages niveau M2 en laboratoire

2011	L. Ma, M2 Master Sciences de l'ingénieur UPMC spécialité Mécanique des Fluides Fondements et Applications MF2A co-encadrement 50% avec D. Baltean-Carlès, Thermoacoustique
2009	K. Sodjavi, M2 Master Sciences de l'ingénieur UPMC spécialité Mécanique des Fluides et Energétique MFE co-encadrement 50% avec D. Baltean-Carlès, Thermoacoustique
2006	A. Guet (M2 Professionnel SFDT, Univ Paris XI) co-encadrement 50% avec B. Goyeau, Couplage fluides-poreux
2002	L. Vodinh (M2 – DEA Propulsion), Thermoacoustique
1994	A. Delnevo (DEA UPMC), Propagation d'ondes dans les milieux composites

Encadrement de stages niveau M1 en laboratoire

2017	S. Benyahia, M1 MF2A, co-encadrement 50% avec D. Baltean-Carlès, Thermoacoustique
2016	V.D.R. Dalli, M1 ENSAM, co-encadrement 50% avec D. Baltean-Carlès, Thermoacoustique
2015	D. H. Truong, M1 MF2A, co-encadrement 50% avec D. Baltean-Carlès, Thermoacoustique
2014	W. Gault, projet de synthèse ECP, co-encadrement 50% avec D. Baltean-Carlès Thermoacoustique
2010	B. Belhassein, Master Sciences de l'ingénieur UPMC, spécialité Energie et Environnement, co-encadrement 50% avec D. Baltean-Carlès, Thermoacoustique
2001	R. Beraun, Master Sciences de l'Ingénieur UPMC, spécialité Mécanique des Fluides et Energétique MFE), Thermoacoustique
1996	D. Agenhen, FIUPSO, Sciences et Génie des Matériaux co-encadrement 50% avec B. Goyeau, Couplage fluides-poreux

Encadrement de stage d'été niveau L en laboratoire

2019	A. Krishnakumar (L3 Sorbonne-Université), Thermoacoustique
2012	M. Elkoby (L2 UPMC), Thermoacoustique
2000	L. Calsyn et C. Dubois (L3 UPMC), Convection hors-Boussinesq
1999	B. Maheraut et B. Vaillant (L3 UPMC), Convection hors-Boussinesq

Ecole d'été
Cours (avec D. Baltean-Carlès) à l'école "Space Trips Summer School", "Mathematical modeling and numerical simulation in Thermoacoustics", Riga, Latvia, 2014.

Membre de jurys de thèse
A. Boufermel (juillet 2010), A. Genot (juin 2019)

Participation à des projets de recherche & partenariats industriels

ANR TACOT 2017-2020	Thermo-Acoustic Cooler for On road Transportation, Défi « Energie Propre, Sûre et Efficace » (Porteur Hélène Bailliet P', partenaire LIMSI)
Projet Arts&Science 2015-2016	La Diagonale, Paris Saclay, « Thermophones », (porteurs D. Baltean-Carlès et J. Rémus).
Action Incitative LIMSI 2015-16	« Thermoacoustique et audio» (porteur D. Baltean-Carlès).
Action Incitative LIMSI 2012-13	« Thac3G, thermoacoustique» (porteur C. Weisman).
Projet CMEP 2010-2014, 10MDU809	« Étude numérique et expérimentale de systèmes thermoacoustiques (porteur P. Le Quéré). Financement des stages de S.A. Litim (2010, 2011) et K. Nehar Belaïd (2012, 2013), et de plusieurs séjours de M. Abidat et O. Hireche au LIMSI.
Action Incitative LIMSI 1997-98	« convection naturelle en milieu poreux».

Activités administratives liées à la recherche

Expert désignée par l'HCERES pour participer à l'évaluation du LAUM (février 2016).
Membre du comité d'organisation de la première école de Thermoacoustique (labellisée CNRS), organisée à Roscoff du 30 mai au 4 juin 2010, 42 participants
Organisation des journées 2008 du GDR Thermoacoustique au LIMSI, 15/16 déc. 2008, 40 participants
Co-organisation de 2 journées de rencontres au LIMSI sur les effets non linéaires en thermoacoustique, les 3/4 juillet 2006.
Participation au GDR Thermoacoustique (créé en 2007 et clos en 2014).
Participation à la Fédération « Transferts de masse et de chaleur» dans l'axe 3 « instabilités thermo-convectives » sur le thème de la convection hors Boussinesq. Participation aux premières réunions de la Fédération, aux réunions de bilan, et à une journée organisée sur le thème « convection hors Boussinesq ».
Membre de : AUM, Euromech, SFT, SFA.
Expertises d'articles : J. Heat Transfer, Int. J. Heat Mass Transfer, J. Comp. Physics, Mechanics & Industry, Physics of Fluids, Comptes-rendus de Mécanique
Depuis 2004, Membre du Conseil de Département de Mécanique du LIMSI.
1997-2004, Membre du Conseil de Laboratoire du LIMSI
1997-2004, Membre de la Commission doctorants du LIMSI

Enseignement

Enseignement à l'U.F.R. 919 Ingénierie, Faculté des Sciences et Ingénierie, Sorbonne Université (anciennement Univ. Paris VI, Université Pierre et Marie Curie).

Thèmes et niveaux des enseignements

Licence de mécanique : Introduction à la mécanique (énergétique, acoustique), thermodynamique et thermique, méthodes et pratiques numériques en mécanique, mathématiques, mécanique des fluides, insertion professionnelle, (+ avant 2010 : Mécanique des milieux continus, Mécanique des solides)
Master (Sciences pour l'Ingénieur, spécialité MF2A, Mécanique des Fluides, Fondements et Applications) : Méthodes numériques et simulation en mécanique des fluides, Écoulements et transferts en milieux fluides et poreux

Responsabilités et activités pédagogiques remarquables

Direction des études du L2 d'Ingénierie Mécanique depuis 2010, environ 250-300 étudiants chaque année, avec une décharge associée de 40h TD par an. Organisation des enseignements, mise au point des emplois du temps, orientation des étudiants, amphis de présentation, inscriptions pédagogiques, suivi individualisé des étudiants, organisation des examens, préparation et tenue des jurys mono- et bi-disciplinaires, coordination avec les autres départements de formation de l'Université, participation annuelle aux journées portes ouvertes aux lycéens, aux journées d'information aux étudiants (JOR)
Responsabilité de l'UE « Bases de Thermodynamique » depuis 2014 (L2, env. 200 étudiants/an)
Responsabilité de l'UE « Méthodes numériques pour la Mécanique » depuis 2017 (L3, env. 200 étudiants/an)

Participation à la mise en place en 2004 de l'UE « Introduction à la Mécanique » et co-responsabilité du thème « Energétique » en L1 de 2004 à 2016.
Réalisation d'un SPOC (1h30 min de vidéos-support de cours en ligne pour l'enseignement à distance de l'Introduction à la Mécanique – thème Énergétique)
Co-responsabilité des UE de Master « Méthodes numériques et simulation en mécanique des fluides » (2008-2019), Écoulements et transferts en milieux fluides et poreux (2008-2015)
Organisation en 2008 et 2009 des 2 premières éditions de l'Atrium des Métiers (Forum Industriels)

Fonctions d'intérêt collectif liées à l'enseignement

2019	Vice-présidente et membre du comité d'experts pour un concours MCF 60ème section, Sorbonne-Université
2017 - 2019	Membre du jury de Concours ATER 60-62è sections, 2018 et 2019, Sorbonne-Université
2016	Membre du jury de Concours ATER 2016, UFR 919, UPMC
2015 - 2016	Participation au groupe d'experts de la faculté d'Ingénierie pour la préparation des Commissions de Spécialistes.
Depuis 2008	Membre désignée (Représentante EC domaine Mécanique) du Conseil des Enseignements de l'UFR 919.
Depuis 2010	Membre élue du Conseil du Département de Licence de Mécanique (2010-2014) puis membre invitée.
2005	Membre du jury de concours de recrutement IRTF, pour le recrutement d'un ingénieur informatique pour l'UFR 923 .
1997-2004	Membre du Conseil de l'UFR 923 de l'UPMC
1994-2003	Membre de la Commission de Spécialistes, section 60, de l'UPMC.
1996-1998	Membre de la Commission de Spécialistes, section 60, de l'Université de Reims (Champagne-Ardennes).

Liste de publications

(Le nom des étudiants ou post-doctorants encadrés est souligné)

Articles dans des revues internationales à comité de lecture reconnues

0. V. Daru, **C. Weisman**, D. Baltean-Carlès, H. Bailliet, « Thermal effects on fast acoustic streaming inside a resonator », soumis à J. Fluid Mech.
1. O. Hireche, I. Ramadan, **C. Weisman**, D. Baltean-Carlès, V. Daru, H. Bailliet, Y. Fraigneau, « Experimental and numerical investigation of natural convection flows in two horizontal thermoacoustic cavities », Int. J. Heat Mass Transfer 149, 119195, 2020.
2. D. Baltean-Carlès, V. Daru, **C. Weisman**, S. Tabakova, H. Bailliet, « An unexpected balance between outer Rayleigh streaming sources », J. Fluid Mech. 867, 985-1011, 2019.
3. V. Daru, **C. Weisman**, D. Baltean-Carlès, I. Reyt, H. Bailliet, « Inertial effects on acoustic Rayleigh streaming flow : Transient and established regimes », Wave Motion 74, 1-17, 2017.
4. V. Daru, I. Reyt, H. Bailliet, **C. Weisman**, D. Baltean-Carlès, Acoustic and streaming velocity components in a resonant wave guide at high acoustic levels, J. Acoust. Soc. Am. 141(1), 563-574, 2017.
5. L. Ma, **C. Weisman**, D. Baltean-Carlès, I. Delbende, L. Bauwens, Effect of a resistive load on the starting performance of a standing wave thermoacoustic engine : A numerical study, J. Acoust. Soc. Am. 138 (2), 847–857, 2015.
6. I. Reyt, V. Daru, H. Bailliet, S. Moreau, J.-C. Valière, D. Baltean-Carlès, **C. Weisman**, "Fast acoustic streaming in standing waves : Generation of an additional outer streaming cell", J. Acoust. Soc. Am. 134 (3), 1791-1801, 2013.
7. V. Daru, D. Baltean-Carlès, **C. Weisman**, P. Debesse, G. Gandikota, "Two-dimensional numerical simulations of nonlinear acoustic streaming in standing waves", Wave Motion 50, 955-963, 2013.
8. O. Hireche, **C. Weisman**, D. Baltean-Carlès, P. Le Quéré, L. Bauwens, "Low Mach number analysis of idealized thermoacoustic engines with numerical solution", J. Acoust. Soc. Am. 128 (6), 3438-3448, 2010.
9. O. Hireche, **C. Weisman**, D. Baltean-Carlès, P. Le Quéré, M.-X. François and L. Bauwens, "Numerical model of a thermoacoustic engine", Comptes Rendus Mécanique 338, 18-23, 2010.
10. P. Le Quéré, **C. Weisman**, H. Paillère, J. Vierendeels, E. Dick, R. Becker, M. Braack, J. Locke, "Modelling of natural convection flows with large temperature differences : A Benchmark problem for low Mach number solves. Part 1. Reference solutions", ESAIM : Mathematical Modelling and Numerical Analysis, vol. 39 (3), 609-616, 2005.
11. H. Paillère, P. Le Quéré, **C. Weisman**, J. Vierendeels, E. Dick, M. Braack, F. Dabbene, A. Beccantini, E. Studer, T. Kloczko, C. Corre, V. Heuveline, M. Darbandi, S. F. Hosseinizadeh, "Modelling of natural convection flows with large temperature differences : A Benchmark problem for low Mach number solves. Part 2. Contributions to the June 2004 conference", ESAIM : Mathematical Modelling and Numerical Analysis, vol. 39 (3), 617-621, 2005.
12. J.-F. Mercier, **C. Weisman**, M. Firdaouss and P. Le Quéré, "Heat transfer associated to

natural convection flow in a partly porous cavity", Journal of Heat Transfer, V. 124, 1, 130-143, 2002.
13. **C. I. Funk**, A. Clark Jr., R. J. Connett, "A simple model of aerobic metabolism. Applications to work transitions in muscle", Am. J. Physiol. 258 (Cell Physiol. 27), C995-C1005, 1990.

Articles dans des revues internationales à comité de lecture « special issues »

14. O. Hireche, **C. Weisman**, D. Baltean-Carlès, V. Daru, Y. Fraigneau, Numerical study of the effects of natural convection in a thermoacoustic configuration, Mechanics & Industry 20, 807, 2019.
15. L. Ma, **C. Weisman**, D. Baltean-Carlès, I. Delbende, L. Bauwens, Numerical simulation of flow dynamics in the periodic regime in an idealized thermoacoustic engine, Magnetohydrodynamics, vol. 51, 3, 601-608, 2015.
16. P. Duthil, **C. Weisman**, E. Bretagne, M-X. Francois, "Experimental and numerical investigation of heat transfer and flow within a thermoacoustic cell", International Journal of Transport Phenomena, vol. 6 (4), 265-272, 2004.
17. **C. I. Funk**, A. Clark Jr., R. J. Connett. "Temporal buffering of adenine nucleotide concentrations by phosphocreatine during sub-maximal work of skeletal muscle", FASEB Journal, vol 4(4), 1990.
18. **C. I. Funk**, A. Clark Jr., R. J. Connett, "How phosphocreatine buffers cyclic ATP demand in working muscle", Oxygen Transport to Tissue XI, Plenum Press, New York, p.687-693, 1989.

Articles dans des revues nationales à comité de lecture

19. **C. Weisman**, L. Calsyn, C. Dubois, P. Le Quéré, « Sur la nature de la transition à l'instationnaire d'un écoulement de convection naturelle en cavité différentiellement chauffée à grands écarts de température », C.R. Acad. Sci., T. 329, Série IIb, 343-350, 2001
20. **C. Weisman**, P. Le Quéré, M. Firdaouss, « Sur une solution exacte de la convection naturelle en cavité partiellement remplie d'un milieu poreux », C.R. Acad. Sci., T. 327, Série IIb, N○2/3, 235-240, 1999

Conférence invitée

1. D. Baltean-Carlès et **C. Weisman**, Invited lecture, « Modelling and numerical simulations of thermoacoustics », as part of the 'Space trips' Summer School on thermoacoustic and space Technologies, Riga, 2014.

Communications dans des congrès internationaux à comité de lecture et actes publiés

1. V. Daru, D. Baltean-Carlès, **C. Weisman**, « Inertial Effects on Non Linear Acoustic Streaming », 20th International Symposium on Nonlinear Acoustics, Lyon, France, 2015.
2. L. Ma, **C. Weisman**, D. Baltean-Carlès, I. Delbende, L. Bauwens, « Numerical simulation of flow dynamics in the periodic regime inside an idealized thermoacoustic engine », PAMIR International Conference on Fundamental and Applied MHD, Riga, Latvia, 2014.
3. V. Daru, D. Baltean-Carlès, **C. Weisman**, « Numerical Simulation of nonlinear acoustic streaming in a standing wave resonator », 19th International Symposium on Nonlinear Acoustics, Tokyo, Japon, 2012.
4. L. Ma, **C. Weisman**, D. Baltean-Carlès, L. Bauwens, « Multiple scale model and numerical simulation of thermoacoustic devices », Int. Stirling Engine Conf., Dubrovnik, Croatie, 2012.

5. L. Ma, **C. Weisman**, D. Baltean-Carlès, P. Le Quéré, L. Bauwens, « Low Mach number simulation of a loaded standing-wave thermoacoustic engine », Congrès Français d'Acoustique & Annual IOA Meeting, Nantes, France, 2012.
6. **C. Weisman**, D. Baltean-Carlès, P. Le Quéré, L. Bauwens, « Comparison of different heat exchanger models in a thermoacoustic engine simulation », US-European Fluids Engineering Summer Meeting, FEDSM-ICNMM2010-31166, Montreal, Canada, 2010.
7. **C. Weisman**, D. Baltean-Carlès, P. Le Quéré, L. Bauwens, « Numerical study of thermoacoustic wave amplification », V European Conference on Computational Fluid Dynamics, ECCOMAS CFD, Lisbon, Portugal, 2010.
8. O. Hireche, **C. Weisman**, D. Baltean-Carlès, L. Bauwens, M.-X. François and P. Le Quéré, "Numerical model of a thermoacoustic engine", proceedings of the acoustic week in Canada 2008, Vancouver, 6-8 oct. 2008, Canadian acoustics - acoustique canadienne, vol. 36 (3), 164-165, 2008.
9. **C. Weisman**, D. Baltean-Carlès, P. Duthil, P. Le Quéré, " Natural convection in a stack of horizontal plates in a differentially heated cavity", International Symposium on Transport Phenomena, Reykjavik, Island, 2008.
10. **C. Weisman**, D. Barkley, P. Le Quéré, "Transition to unsteadiness of non-Boussinesq natural convection solutions", Proc. I.C.C.H.M.T, Cachan, 2005.
11. P. Duthil, **C. Weisman**, E. Bretagne, M.-X. Francois, "Experimental and numerical investigation of heat transfer and flow within a thermoacoustic cell", Eurotherm seminar 74, Eindhoven, 2003.
12. **C. I. Funk**, A. Clark Jr., R. J. Connett, "How phosphocreatine buffers cyclic ATP demand in working muscle", Proc. of 16th annual meeting of I.S.O.T.T., Ottawa (Canada), 1988.

Communications dans des congrès nationaux à comité de lecture et actes publiés

1. O. Hireche, **C. Weisman**, D. Baltean-Carlès, V. Daru, Y. Fraigneau, « Numerical study of the effects of natural convection in a thermoacoustic device », Congrès Français de Mécanique, Brest, 2019.
2. D.H. Truong, **C. Weisman**, D. Baltean-Carlès, F. Jebali Jerbi et J. Rémus, « Etude du démarrage du son produit par un instrument de musique thermoacoustique : le thermophone. », Congrès Français d'Acoustique, Le Mans, 2016.
3. V. Daru, H. Bailliet, D. Baltean-Carlès, I. Reyt et **C. Weisman**, « Transitoire et changement de régime des écoulements redressés de Rayleigh à forts niveaux : Etudes numérique et expérimentale », Congrès Français d'Acoustique, Le Mans, 2016.
4. V. Daru, D. Baltean-Carlès, I. Reyt et **C. Weisman**, « Streaming non linéaire : rôle de la composante radiale acoustique », Congrès Français d'Acoustique, Le Mans, 2016.
5. I. Reyt, H. Bailliet, D. Baltean-Carlès, V. Daru, J-C. Valière, **C. Weisman**, « Influence de la propagation non-linéaire et de l'inertie sur le vent acoustique », Congrès Français de Mécanique, Bordeaux, 2013.
6. **C. Weisman**, D. Baltean-Carlès, P. Le Quéré, L. Bauwens, « Modélisation nonlinéaire des écoulements et transferts de la cellule active d'un moteur thermoacoustique », Congrès Français de Mécanique, Besançon, 2011.
7. V. Daru, D. Baltean-Carlès, G. Gandikota, **C. Weisman**, « Etude numérique du vent acoustique non linéaire dans un résonateur à ondes stationnaires », Congrès Français de Mécanique, Besançon, 2011.
8. **C. Weisman**, D. Baltean-Carlès, P. Le Quéré, L. Bauwens, « Modèle faible Mach et simulations numériques 2D de l'amplification d'onde thermoacoustique », Congrès Français d'Acoustique, Lyon, 2010.

9. **C. Weisman**, L. Tuckerman, P. Le Quéré, « Transition a l'instationnaire en convection naturelle non-Boussinesq », 15ème Congrès Français de Mécanique, Nancy, 2001.
10. J.-F. Mercier, **C. Weisman**, M. Firdaouss, P. Le Quéré, « Structuration d'un écoulement de convection naturelle dans un milieu partiellement poreux », Congrès Français de Mécanique, Toulouse, 1999.
11. **C. Weisman**, M. Firdaouss, P. Le Quéré, «Transition à l'instationnaire dans une cavité différentiellement chauffée partiellement remplie d'un milieu poreux », Congrès Français de Thermique, Valenciennes, 1996.

Communications dans des congrès avec actes à diffusion restreinte

1. **C. Weisman**, D. Baltean-Carlès, I. Delbende, L. Ma, L. Bauwens, « Effect of a resistive load on the starting performance of a standing wave thermoacoustic engine », Eurotherm Symposium 107, 3rd International Workshop on Thermoacoustics, University of Twente, Enschede, The Netherlands, 2015.
2. O. Hireche, **C. Weisman**, D. Baltean-Carlès, L. Bauwens, M.-X. François and P. Le Quéré, "Numerical simulation of a thermoacoustic engine", 17th Annual Conference of the CFD Society of Canada, Ottawa, Canada, 2009.
3. P. Duthil, **C. Weisman**, E. Bretagne, "Numerical simulation of heat transfer and flow in a thermoacoustic refrigerator cell using low Mach number equations", 3rd International Symposium on Finite Volumes for Complex Applications, Porquerolles, 2002.
4. J.-F. Mercier, **C. Weisman**, M. Firdaouss, P. Le Quéré, « Structuration d'un écoulement de convection naturelle en cavité fluide- poreux », 4èmes Journées d'Etude sur les Milieux Poreux, ENSIC, Nancy, 1999.
5. **C. I. Funk**, A. Clark Jr., R. J. Connett. "Temporal buffering of adenine nucleotide concentrations by phosphocreatine during sub-maximal work of skeletal muscle", Proc. of 74th meeting of the Federation of American Societies for Experimental Biology, Washington, D.C., U.S.A., 1990.

Communications dans des congrès sans actes diffusés

6. V. Daru, D. Baltean-Carlès, **C. Weisman**, « A numerical study of Rayleigh streaming at high acoustic level », Acoustofluidics, Lille, France, 2018.
7. V. Daru, I. Reyt, D. Baltean-Carlès, **C. Weisman**, H. Bailliet, « Evolution of Rayleigh streaming flow velocity components in a resonant wave guide at high acoustic levels », Acoustics'17, Boston, USA, 2017.
8. D. Baltean-Carlès, V. Daru, **C. Weisman**, H. Bailliet, I. Reyt, « Numerical and experimental investigation of the role of inertia on acoustic Rayleigh streaming in a standing waveguide », Acoustics'17, Boston, USA, 2017.
9. J. Rémus, D. Baltean, **C. Weisman**, Thermophones, Ateliers du Forum IRCAM, Paris, 2015.
10. O. Hireche, **C. Weisman**, D. Baltean-Carlès, M.-X. François, P. Le Quéré, L. Bauwens, "Numerical simulation of a thermoacoustic wave amplification", Acoustics'08, Paris, 2008.
11. **C. Weisman**, P. Le Quéré, D. Barkley, « Transition vers l'instationnaire en convection naturelle non-Boussinesq. », 17ème séminaire "Mécanique des fluides numérique" du CEA, Institut Henri Poincaré, 2005.
12. **C. Weisman**, D. Barkley, P. Le Quéré, "Linear stability of Bursting Solutions in non-Boussinesq natural convection", Conference on Mathematical and Numerical aspects of Low Mach number flows, Porquerolles, 2004.

13. **C. Weisman**, D. Barkley, P. Le Quéré, "Bursting near transition in non-Boussinesq natural convection ", 55th Annual Meeting of Division of Fluid Dynamics, American Physical Society, Dallas, Texas, USA, 2002.
14. **C. Weisman**, M. Firdaouss, P. Le Quéré, “Heat transfer associated to natural convection flows in a partially porous cavity”. 2nd International Conference on Computer Methods for Engineering in Porous Media, Besançon, 2000.
15. P. Le Quéré, **C. Weisman**, B. Vaillant, B. Maherault, « Description of finite-volume algorithm for integrating the low Mach number equations » 12th Seminar « Computational Fluid Dynamics » Benchmark « Modelling and simulation of natural convection flows with large temperature differences », CEA, INSTN, Saclay, 2000.
16. **C. I. Funk** and R. J. Connett, "Reevaluation of phosphofructokinase kinetics -Application to in vivo conditions in skeletal muscle", 75th meeting of FASEB, Atlanta, U.S.A, 1991.

Autres : Colloques et séminaires sans actes diffusés

1. V. Daru, D. Baltean, **C. Weisman**, H. Bailliet, I. Reyt, Numerical investigation of acoustic streaming in standing waves, Thermoacoustic Hub Date Workshop, Le Mans, 2018
2. **C. Weisman**, D. Baltean-Carlès, F. Jebali Jerbi, D.H. Truong et J. Rémus, « Le Thermophone : un moteur thermoacoustique particulier », Journée Dynamique des Fluides, Orsay, 2016.
3. L. Ma, **C. Weisman**, D. Baltean, I. Delbende, L. Bauwens, « Etude numérique de la stabilité d’un moteur thermoacoustique chargé », colloque du GDR thermoacoustique, 2013.
4. **C. Weisman**, L. Ma, D. Baltean, P. Le Quéré, L. Bauwens, « Simulations numériques d’un moteur thermoacoustique à ondes stationnaires chargé », Journée Dynamique des Fluides, Orsay, 2012.
5. V. Daru, D. Baltean, **C. Weisman**, « Etude numérique du vent acoustique non linéaire dans un résonateur à ondes stationnaires, colloque du GDR thermoacoustique, 2011.
6. **C. Weisman**, D. Baltean, P. Le Quéré, L. Bauwens, « Analyse faible Mach et simulation d’un moteur thermoacoustique », Journée scientifique de la fédération francilienne des Transferts de Masse et de Chaleur (TMC), Evry, 2010
7. D. Baltean, **C. Weisman**, P. Le Quéré, L. Bauwens, « Modélisation faible Mach d’un moteur thermoacoustique à ondes stationnaires », Journée Dynamique des Fluides, Orsay, 2010.
8. **C. Weisman**, D. Baltean-Carlès, O. Hireche, K. Sodjavi, P. Le Quéré, « Modèle Faible Mach et simulations numériques 2D de l’amplification d’onde thermoacoustique », Journée Dynamique des Fluides, Orsay, 2009.
9. **C. Weisman**, « Modèle Faible Mach et simulations numériques 2D de l’amplification d’onde thermoacoustique », 3ème colloque du GDR 3058 « Thermoacoustique », Ecole Nationale Supérieure d’ingénieurs du Mans (ENSIM), 2009.
10. **C. Weisman**, D. Baltean-Carlès, P. Le Quéré, P. Duthil, « Convection naturelle en cavité contenant un empilement de plaques horizontales », 1er colloque du GDR 3058 « Thermoacoustique », Orsay, 2008.
11. **C. Weisman**, O. Hireche, D. Baltean-Carlès, P. Le Quéré, « Simulation de l’amplification d’onde thermoacoustique à l’aide d’un code Faible Mach », Journée de la Fédération Transfert de Masse et de Chaleur, Orsay, 2008.
12. **C. Weisman**, M. Firdaouss, P. Le Quéré, « Transferts de chaleur en cavité fluide-poreux », Journée Dynamique des Fluides, Orsay, 2000.
13. **C. Weisman**, P. Le Quéré, « Transition à l’instationnaire en convection non-Boussinesq », Journée de Dynamique des Fluides, Orsay, 2000.

14. **C. Weisman**, M. Firdaouss, P. Le Quéré, « Etude des instabilités hydrodynamiques d'écoulements de convection naturelle en cavités partiellement remplies d'un milieu poreux », Journée d'Etude de la Société Française des Thermiciens Thermique et Physique non-linéaire. Paris, 1996

Thèse

Catherine Funk, "An Integrated Model of High-Energy Phosphates in Muscle Metabolism", Ph.D. thesis, University of Rochester, April 1990
Catherine Funk, « Modélisation mathématique du système des phosphates à haute énergie au cours des échanges énergétiques de la cellule musculaire», thèse I.N.P.L., septembre 1990

Chapitre 1

Activités liées à l'enseignement

1.1 Introduction

La mission d'enseignement de l'enseignant-chercheur est primordiale pour moi, d'abord parce que j'ai toujours souhaité devenir enseignante, et également parce que je n'ai l'impression de maîtriser complètement un sujet que lorsque je suis capable de le présenter clairement à quelqu'un d'autre. C'est cette vocation d'enseigner qui m'a conduite, après l'obtention de mon diplôme d'ingénieur, à vouloir poursuivre en thèse et devenir enseignant-chercheur.

Aux Etats-Unis, pendant ma thèse, j'ai eu l'opportunité d'assurer des travaux dirigés en thermodynamique et en mathématiques appliquées (niveaux L3 et M1). C'était l'équivalent d'un monitorat, et ma première expérience face à une classe. J'ai pris beaucoup de plaisir à enseigner en anglais, et à part certaines difficultés liées aux ordres de grandeurs en thermodynamique dans des unités improbables (pression en psi - pound per square inch, énergie en btu - British thermal unit, température en F - Farenheit) l'expérience a été concluante. J'ai été sélectionnée par les étudiants pour un prix récompensant la qualité des travaux dirigés, ce qui m'a permis ensuite d'être chargée de deux cours de mathématiques appliquées (niveaux M1 et M2) sur les EDP (en particulier sur les formules de Green et les développements asymptotiques raccordés). Cette expérience américaine a été extrêmement enrichissante, motivante et déterminante.

Lorsque j'ai été recrutée en 1991, j'ai découvert les méthodes d'enseignement à l'Université Française, puisque je n'y avais moi-même jamais étudié. J'ai tout de suite apprécié les contacts avec les étudiants et avec mes collègues au sein d'équipes pédagogiques enthousiastes. Par la suite, j'ai découvert les spécificités de l'enseignement en amphi. En enseignement, j'apprécie particulièrement l'impression de dominer le sujet, d'avoir accompli mon travail et de pouvoir passer à la tâche suivante. C'est très complémentaire de la recherche pour laquelle on est en perpétuelle remise en question et évolution. J'ai commencé par des TD en Mécanique des Milieux Continus (avec Georges Duvaut, Hélène Dumontet, Abdelwahed Ben Hamida) et en méthodes numériques (avec Daniel Euvrard, Mouaouia Firdaouss, Jean-Paul Duruisseau, Joël Chaskalovic). Mon investissement en MMC m'a permis de bien connaître cette discipline au cœur de la Mécanique à l'UPMC, et en lien direct avec les méthodes numériques.

Lors de ces 29 années à l'UPMC devenue Sorbonne-Université, j'ai enseigné du L1 au M1, dans les domaines de la mécanique générale, la mécanique des milieux continus, la mécanique des fluides, les méthodes et pratiques numériques pour la mécanique, les mathématiques appliquées, la thermodynamique et les transferts thermiques. J'ai assuré des cours, des travaux dirigés et des travaux pratiques, des ateliers de Méthodologie en L1, des ateliers d'insertion professionnelle, ainsi que l'encadrement de projets et de stages au niveau Licence et Master. En Master 2, j'ai participé pendant 15 ans à un enseignement sur les transferts convectifs en

milieux Fluides et Poreux.
Mes enseignements actuels sont centrés sur les méthodes et pratiques numériques pour la mécanique, les mathématiques appliquées, la thermodynamique et les transferts thermiques.

Je détaille ci-dessous mes contributions essentielles à l'enseignement de la mécanique au sein de Sorbonne-Université.

1.2 Mathématiques et méthodes numériques

A mon recrutement en 1991, j'ai été sollicitée pour participer aux enseignements de méthodes numériques (en L3 et M1). Au cours de ma carrière, j'ai maintenu une activité d'enseignement dans ce domaine que j'apprécie particulièrement, avec mes collègues Mouaouia Firdaouss pendant une quinzaine d'années, Daniel Euvrard à mes débuts, puis Ivan Delbende, Anne Sergent, Laurent Martin-Witkowski avec qui nous avons formé une équipe du LIMSI dédiée à l'enseignement des méthodes numériques, et plus récemment avec Han Zhao, Fatiha Bouchelaghem, Anca Belme.

J'ai participé, pendant 15 ans puis à nouveau depuis 2015, à un enseignement de méthodes numériques en L3, afin d'initier les étudiants à la résolution de systèmes linéaires par des méthodes directes par points et par blocs (LU, Cholesky), et itératives (Jacobi, Gauss-Seidel, SOR, Gradient, Gradients conjugués préconditionnés ou non), l'interpolation polynômiale, l'intégration et la dérivation numérique, la résolution d'équations différentielles, et la résolution par différences finies d'équations aux dérivées partielles. C'est avec cet enseignement que j'ai véritablement assimilé les fondements des méthodes numériques que j'ai utilisées en recherche au LIMSI.

Outre les compétences numériques acquises par la pratique, les étudiants sont sensibilisés à la validation des codes de calcul qu'ils écrivent ou utilisent, et à l'interprétation des résultats. Cet enseignement où j'ai assuré des cours, TD, TP et projets qui sont vraiment complémentaires, est très valorisant pour l'étudiant (qui en ressort en maîtrisant la démarche de modélisation et de simulation numérique) et pour l'enseignant qui fait un peu le lien entre plusieurs UE de Mécanique. J'ai pris la responsabilité de cette UE depuis 2017 (environ 250 étudiants/an).

Je suis très attachée à la cohérence de l'enseignement des méthodes des méthodes numériques sous forme de cours, travaux dirigés et travaux pratiques sur machine, projets. Il me semble en effet essentiel de maintenir cet équilibre entre théorie et pratique pour l'appropriation des méthodes. Au sein de l'équipe pédagogique, nous avons longuement débattu sur les langages appropriés pour cet enseignement. Je suis toujours partisane du Fortran car il utilise une syntaxe très pédagogique et rigoureuse. Cependant, les étudiants sont de plus en plus gênés par la compréhension des erreurs indiquées (en anglais) par les compilateurs. Je me suis également formée à l'usage de codes industriels (Fluent par exemple), et de Matlab que j'ai enseignés pendant une quinzaine d'année dans des UEs de pratiques numériques pour la Mécanique en L3 puis en L2.

J'ai participé pendant de nombreuses années à un enseignement général des méthodes numériques en M1 (introduction aux méthodes de résolution des EDP par différences finies, volumes finis, éléments finis, et utilisation de méthodes avancées de résolution des systèmes linéaires telles ADI, GMRES, Multigrille). J'ai également participé pendant de nombreuses années (avec mes collègues Alain Rigolot, Hélène Dumontet, Diana Baltean-Carlès) à un enseignement d'analyse fonctionnelle (espaces de Hilbert, formulations variationnelles, théorème de Lax-Milgram, distributions) très en lien avec cet enseignement de méthodes numériques, et également avec le cours de Mécanique des Milieux Continus.

J'ai participé pendant plus de 15 ans (co-responsable pendant 10 ans avec Thomas Gomez puis Anne Sergent) à une UE de méthodes numériques en M1. Depuis 10 ans, cette UE de méthodes numériques, simulation et projet en mécanique des fluides (entre 30 et 50 étudiants) est centrée autour de la méthode des volumes finis. J'assurais des cours, TD, TP et l'encadrement de projets numériques (écriture de code et utilisation de logiciels commerciaux).

Depuis cette année, les enseignements de mathématiques et méthodes numériques sont associées en L2 et en L3 au sein d'UEs communes. Nous avons souhaité montrer le lien étroit entre les deux disciplines, et l'aspect appliqué des mathématiques. Nos étudiants ont une attitude méfiante envers les mathématiques, et le fait d'associer cette discipline aux méthodes numériques devrait la rendre plus attractive. Cela nous permet également de maintenir une activité de programmation chez les étudiants dans la durée, à chaque semestre de la licence.

1.3 Energétique et thermodynamique

La thermodynamique est une matière que j'ai trouvée très difficile à aborder en tant qu'étudiante en classes préparatoires. Cela reste une discipline ardue pour nos étudiants, car elle requiert de bonnes connaissances en mathématiques (fonctions de plusieurs variables, formes différentielles, intégration) qui sont souvent acquises tardivement. Depuis 2004, j'ai participé à la mise en place d'un programme d'apprentissage progressif de cette matière (avec mes collègues Pierre Carlès, Diana Baltean-Carlès, Laurent Martin-Witkowski, Sophie Mergui, Frédéric Doumenc, Régis Wunenburger, Jean-François Krawczynski entre autres).

J'ai participé à la mise en place en 2004 d'un enseignement d'introduction à la Mécanique en L1 (environ 400 étudiants), qui abordait quatre aspects de la mécanique : mécanique du solide, mécanique du vol, acoustique et énergétique. Jusqu'en 2016, je suis intervenue dans le thème « Energétique », en assurant le cours (200 étudiants), plusieurs groupes de TD, et la co-responsabilité du thème : organisation pédagogique, rédaction de polycopié, de sujets de TD, examens, corrections. Nous avons décidé de suivre un fil conducteur (l'exemple du turbopropulseur) pour présenter les lois d'état, les notions de travail, chaleur, énergie interne et le premier principe. Nous avons fait appel à peu de notions mathématiques (intégrales de fonctions simples), et avons surtout insisté sur les représentations graphiques des transformations, l'homogénéité dimensionnelle, les unités, ordres de grandeur. En 2015, L. Martin Witkowski et moi-même avons préparé et enregistré 1h30 de vidéos-support en ligne pour l'enseignement à distance du thème « énergétique » de ce cours. J'ai également adapté certaines vidéos pour l'enseignement présentiel, ce qui permet de rendre plus vivant l'apprentissage. Cette UE a permis d'intéresser beaucoup d'étudiants à la Mécanique, et a certainement contribué à l'augmentation du nombre d'étudiants en L2-L3 de Mécanique au cours des 10 dernières années. Depuis cette année, les équipes pédagogiques de physique et de mécanique se sont regroupées pour organiser ensemble les enseignements en L1. J'ai participé aux réunions préparatoires, et je pense m'investir dans ces UEs à partir de l'année prochaine. La thermodynamique est enseignée au premier semestre. Nos vidéos sont encore utilisées, et notre cours a servi de base à l'élaboration du programme.

Après avoir participé pendant plusieurs années à l'enseignement de thermodynamique et thermique, j'ai participé à la mise en place en 2014 d'une petite UE de Bases de Thermodynamique en L2. J'en ai assuré la responsabilité et l'animation pédagogique, le cours (environ 200 étudiants) et plusieurs groupes de TD. Dans cette UE on reprend les notions de lois d'état, premier et second principes de la thermodynamique en systèmes fermés, mais en s'appuyant sur les notions de fonctions de plusieurs variables et de formes différentielles. Nous avons repris les sujets de TD pour les rendre plus progressifs. J'illustre le cours en résolvant au tableau de

nombreux exemples. Les étudiants font aussi un TP d'application, en se rendant une fois dans le semestre sur la plateforme expérimentale de Saint-Cyr L'Ecole. Cette année, nous avons modifié à nouveau cet enseignement, en le déplaçant au second semestre de L2, de façon à pouvoir s'appuyer sur l'enseignement de mathématiques ayant lieu au premier semestre (qui porte sur l'analyse vectorielle, les fonctions de plusieurs variables et les intégrales multiples). La thermodynamique est à nouveau associée à la thermique dans une UE à 6 ECTS. Cette UE est proposée à 450 étudiants de tous parcours.

J'ai participé pendant environ 15 ans (co-responsable pendant 10 ans avec Benoît Goyeau, puis Maurice Rossi et Pierre-Yves Lagrée) à un cours en M2 sur les écoulements et transferts de chaleur en milieux fluides et poreux (modélisation, mise en équations, analyse dimensionnelle, solutions analytiques et numériques, dans des configurations de convection naturelle et forcée en milieu fluide et poreux). J'ai particulièrement apprécié le fait de pouvoir partager avec les étudiants de M2 certains résultats obtenus en recherche.

1.4 Encadrement de stages et de projets

J'ai régulièrement encadré (ou co-encadré) au LIMSI des stagiaires pendant l'été, que ce soit pour des stages volontaires (6 stages L2/L3) ou bien faisant partie de la formation (7 stages M1, 5 stages M2). Ces sujets portaient en général sur des sujets de recherche accessibles aux étudiants. Ils m'ont permis de mener une petite étude que je n'avais pas le temps ou pas le courage de démarrer, et souvent cette responsabilité envers le stagiaire m'a insufflé l'énergie nécessaire pour mener l'étude à son terme. Les résultats des stages sont mentionnés dans la partie recherche.

1.5 Orientation et Insertion professionnelle

Je me suis intéressée depuis longtemps au devenir des étudiants, en étant d'abord référent universitaire pour une vingtaine de stages en entreprise ou en centre de Recherche, entre 1991 et 2009, au sein de Metravib, S.N.E.C.M.A., Williams F1, EDF Chatou, Bouygues, Wärtsilä, CERAM, IRCN , IFP, ONERA, Ecole des Mines Fontainebleau, Northwestern University, ENSAM Paris. Ce travail consistait à suivre l'étudiant pendant son stage et pendant la rédaction du rapport ainsi que pendant la préparation de la soutenance, et à intervenir en cas de problème. J'ai également participé aux jurys de soutenance. J'ai ainsi pu nouer des contacts avec des ingénieurs intéressés par nos formations.

Une partie de mes enseignements s'est effectuée entre 2004 et 2018 sous la forme d'ateliers d'insertion professionnelle en Licence et en Master. Après avoir suivi plusieurs formations à l'APEC et à l'UPMC auprès de D. Piccinini (responsable de l'AFIP : Accompagnement et Formation à l'Insertion Professionnelle), j'ai assuré chaque année un atelier (U.E. obligatoire de L3). Les étudiants y découvrent et étudient les métiers de la mécanique auxquels conduit leur formation, sont formés à l'élaboration d'un Projet Personnel et Professionnel et à la rédaction de CV et lettres de motivation. J'ai beaucoup apprécié cet enseignement qui m'a permis de connaître les étudiants différemment, et de les aider dans leur parcours universitaire. J'ai également assuré pendant 3 ans un atelier d'insertion professionnelle en M2 (Master Sciences de l'Ingénieur, U.E. obligatoire), centré autour de la finalisation et la concrétisation du Projet Personnel et Professionnel. Les séances comprennent la rédaction de CV, lettres de motivation, la préparation aux entretiens d'embauche (individuel et collectif), une découverte des diverses fonctions et missions des ingénieurs dans les entreprises.

J'ai co-organisé en 2008 et 2009 (avec Dominique Piccinini et Fabienne Fellah) les deux premières éditions de l'Atrium des Métiers (Forum Université-Entreprises) :
Le 1er atrium des métiers à l'U.P.M.C. s'est tenu les 28 et 29 janvier 2008. Ce forum pluridisciplinaire Université/Entreprises a permis de réunir, sous forme de stands, de conférences et de tables rondes, une cinquantaine d'entreprises et organismes extérieurs (dont une vingtaine de grands groupes industriels) et environ 1000 étudiants présents (L3, M1 et M2). Nous avons pris en charge l'élaboration du projet, les contacts avec les entreprises et la gestion de leur inscription, la présentation du projet aux responsables de formation, la préparation des documents de communication, programmes, affiches, badges (en liaison avec le service communication de l'Université), l'organisation et la logistique complète. Nous avons également recruté et encadré une équipe de 30 étudiants pilotes. La préparation a duré environ 6 mois. Nous avons organisé la tenue de deux conférences sur les sujets suivants : "Les grandes lignes de l'entreprise (vocation, implantations, effectifs, stratégies de développement, politique de recherche et innovation....)" et "Les principaux métiers et compétences associées, en rapport aux recrutements de jeunes diplômés en Sciences, Bac+3, Bac +5, Bac+8." Deux tables rondes ont été organisées sur les thèmes : « Université – Entreprises, quels liens construire ? » et « Quelles compétences pour aujourd'hui et demain ». Les débats ont été enregistrés.

Le deuxième Atrium des métiers a réuni, les 22 et 23 octobre 2009, sur le même format que le premier, une cinquantaine d'entreprises dont une vingtaine de grands groupes industriels, malgré le contexte économique difficile. Il était ouvert à l'ensemble des étudiants (public étudiant essentiellement concerné : L3, M1, M2). Nous avons assuré, de la même façon que pour la première édition, l'élaboration et la réalisation du projet, les prises de contacts avec les entreprises et la gestion de leur inscription (sur le site UPMC Pro, en liaison avec le service UPMC-Pro), la présentation du projet aux responsables de formation, la préparation des documents de communication, programmes, affiches, badges, (en liaison avec le service communication) et la prise en charge entière de l'organisation et de la logistique. Nous avons également recruté et encadré une équipe de 25 étudiants pilotes. Enfin, nous avons préparé, recueilli et analysé 30 questionnaires de satisfaction. Pour cette édition, nous avons également organisé des conférences par les responsables des formations sur les diverses filières d'enseignement, ainsi que des rendez-vous individuels entre les représentants des entreprises et les responsables de formations. Le thème de la table ronde était : « Le profil de l'étudiant recherché : par l'entreprise, le laboratoire de recherche, l'université » La participation des responsables de formation a été remarquable. Les entreprises ont souligné la qualité de l'accueil et de l'organisation, et la richesse des échanges avec les étudiants et les enseignants.

Dans le cadre de l'orientation, j'ai également participé à la réalisation, en 2016, d'un film de présentation de la formation en Mécanique à destination des étudiants de L1.

1.6 Gestion et administration

En Licence, les effectifs étudiants sont généralement de l'ordre de 200 par unité d'enseignement (UE). Nous fonctionnons donc en équipes pédagogiques, constituées en majorité par des moniteurs ou ATER qu'il faut former à leur arrivée. Mon investissement dans une UE, même lorsque je n'en suis pas responsable, comprend donc toujours une part importante de réunions pédagogiques, préparation de documents, réalisation et maintenance d'un site internet dédié, organisation des examens, rédaction de sujets et de corrigés, aide à la collecte des notes et participation aux jurys.

Depuis 2010, je suis directrice des études du L2 Mécanique (250-350 étudiants chaque

année), avec une décharge associée de 32 à 40h TD par an. En 2015, l'Université a mis en place une nouvelle maquette de la forme majeure/mineure pour les niveaux L2 et L3. Les étudiants ont donc la possibilité de s'inscrire en L2 dans un parcours mono-disciplinaire ou bi-disciplinaire. La mécanique est ainsi associée dans des parcours bi-disciplinaires (en tant que discipline majeure ou mineure) avec la physique, les mathématiques, l'informatique, l'électronique, les géosciences, la biologie, la chimie, les sciences humaines et sociales. Il existe aussi des parcours sélectifs, mono-disciplinaire et bi-disciplinaires. La mécanique est associée dans quatre parcours bi-disciplinaires intensifs (avec la physique, les mathématiques, l'électronique et plus récemment les géosciences).

L'attractivité de cette maquette, et la multiplicité des parcours possibles entraîne aussi un grand nombre d'interrogations de la part des étudiants concernant notamment les choix de parcours. Dans ce contexte, un suivi individualisé des étudiants est essentiel. L'organisation générale est complexifiée par la maquette, et doit s'effectuer en coordination avec les autres départements de l'Université.

Ainsi, je participe à l'organisation des enseignements, à la mise au point des emplois du temps, aux inscriptions pédagogiques, à la réorientation de certains étudiants, au suivi individualisé des étudiants (1/2 journée de permanence au moins par semaine, rendez-vous individuels), à l'organisation des examens, à la préparation et tenue des jurys mono- et bi-disciplinaires, aux amphis de présentation, aux journées portes ouvertes aux lycéens et journées d'information à nos étudiants (JOR).

J'ai participé également aux réflexions concernant les évolutions de la maquette à chaque changement de quinquennal.

Je mentionne ici les conditions exceptionnelles de cette année : en raison de la pandémie de Covid19, nous avons dû mettre en place des enseignements à distance, organiser l'étalement des plannings, coordonner des équipes d'une dizaine d'enseignants pour garantir la meilleure équité possible entre les étudiants, mettre en place de nouvelles évaluations, répondre à des centaines de mails chaque semaine. Cette période a été difficile, mais étudiants et collègues ont été exemplaires.

Chapitre 2

Travaux de recherche - Introduction générale

2.1 Présentation chronologique

Ce mémoire d'HDR est l'occasion de revoir les différents sujets de recherche que j'ai abordés au cours de ma carrière. Bien qu'il n'y ait pas de réel fil conducteur entre ces divers sujets, ils ont en commun l'approche de modélisation et de simulation numérique et l'interdisciplinarité.

Mes travaux de thèse à l'Université de Rochester, aux Etats-Unis, ont porté sur la modélisation du système énergétique dans une cellule musculaire, à partir de l'analyse mathématique et la simulation numérique des mécanismes de transport couplés de diffusion moléculaire et de réaction chimique. L'étude est centrée sur les molécules contenant des liaisons phosphates riches en énergie. Les voies métaboliques de production et de consommation d'Adénosine TriPhosphate (ATP) sont incorporées dans un modèle du système cytosolique des composés phosphates riches en énergie (ou *système énergie phosphate*, comprenant les adénylates, la phosphocréatine, la créatine et le phosphate inorganique). Le modèle est un système d'équations différentielles ordinaires qui permet de calculer les variations en temps du système énergie phosphate au cours de transitions entre différents taux de travail musculaire. Le modèle est validé par l'expérience en utilisant des mesures de la vitesse de consommation d'oxygène et de la concentration en phosphocréatine au cours de transitions repos-travail : ceci pour deux muscles différents. On utilise ensuite le modèle pour étudier la régulation in vivo de la consommation d'oxygène. Enfin, on étudie l'effet tampon de la phoscréatine sur les concentrations en adénylates au cours d'un protocole expérimental de stimulation par secousses. Un calcul en ordre de grandeur permet de montrer que dans tous les cas envisagés, la diffusion moléculaire est si rapide que les gradients associés sont négligeables [22].

Mon directeur de thèse principal était spécialisé en mathématiques appliquées à la mécanique (au sein du Département "Mechanical Engineering") et mon deuxième directeur était chercheur en physiologie (au sein de l'hôpital Universitaire de Rochester). J'ai donc eu la chance de cotoyer deux milieux de recherche aux fonctionnements très différents du point de vue à la fois de l'approche et du langage utilisés. J'ai aussi effectué un travail post-doctoral de un an au sein de l'hôpital Universitaire de Rochester sur la cinétique des enzymes caractéristiques de l'activité musculaire (acquisition in vivo et analyse des données).

Au moment de ma prise de poste à l'Université Paris VI, on m'a proposé de choisir un laboratoire d'accueil. J'ai choisi le laboratoire LM2S dirigé par Georges Duvaut, pour y travailler sur la modélisation et la simulation par éléments finis de la propagation des ondes électromagnétiques dans les matériaux composites. Cela représentait un changement thématique drastique

par rapport à mon travail de thèse. Grâce à l'enseignement, j'ai complété ma formation en analyse fonctionnelle (formulations variationnelles) et en méthodes numériques (éléments finis, résolution de systèmes linéaires). J'ai travaillé avec Alain Oster qui terminait sa thèse encadrée par Nicole Turbé sur les solutions de Bloch des équations de Maxwell. L'étude était basée sur la méthode de l'homogénéisation périodique, et la mise en œuvre numérique par éléments finis 3-D. J'ai ensuite étudié la diffraction d'une onde par un obstacle diélectrique de forme quelconque entouré d'une couche conductrice mince, en utilisant la technique des développements asymptotiques. L'étude théorique et la mise en œuvre numérique par éléments finis de la diffraction d'une onde électromagnétique par un obstacle cylindrique a ensuite été ébauchée (stage de DEA de A. Delnevo). Mais ces débuts en recherche ont été difficiles et je n'ai pas publié sur ces travaux. Je suis restée pendant 4 ans dans ce laboratoire.

Par la suite, Mouaouia Firdaouss (avec qui je partageais un enseignement de méthodes numériques en licence) m'a proposé de travailler avec lui sur des problèmes de convection naturelle en cavité composée d'un milieu fluide et d'un milieu poreux. J'ai rencontré Patrick Le Quéré, alors directeur du département de Mécanique Energétique du Laboratoire d'Informatique pour la Mécanique et les Sciences de l'Ingénieur (LIMSI) qui a accepté que je rejoigne son département. Ce nouveau changement de laboratoire a donc aussi été accompagné d'une conversion thématique. J'ai apprécié le travail en équipe, l'atmosphère du laboratoire, le cadre scientifique et matériel et même la séparation géographique de mes lieux de recherche et d'enseignement, malgré les difficultés de gestion d'emploi du temps associées. Malgré cela, il m'a fallu plusieurs années pour me remettre véritablement à la recherche.

J'ai commencé (1995-2002) par étudier la convection naturelle en cavité fluide partiellement remplie d'un milieu poreux par résolution numérique des équations de Navier-Stokes modifiées de façon à décrire de manière unifiée l'écoulement dans la partie fluide et dans le milieu poreux (collab. M. Firdaouss et P. Le Quéré). Pour cela j'ai utilisé le code volumes finis développé par Patrick Le Quéré. Nous avons étudié les solutions stationnaires en cavité différentiellement chauffée et refroidie à flux homogène et montré l'existence d'une solution analytique 1D dans une fente d'extension verticale infinie (collab. J.F. Mercier pendant son travail post-doctoral, détails en section 3.1).

Entre 1999 et 2005, j'ai étudié (collab. P. Le Quéré) les écoulements de convection naturelle en cavité différentiellement chauffée à grands écarts de température (convection hors Boussinesq, hypothèse faible Mach). Nous avons ainsi participé en 2000 et 2002 à un Benchmark numérique sur les solutions stationnaires de ces équations et obtenu des valeurs de référence (détails en section 4.1). J'ai également travaillé sur la transition vers l'instationnaire des solutions, par simulation directe utilisant le code instationnaire non linéaire, et par une méthode de pseudo-linéarisation (collab. D. Barkley, détails en section 4.2).

A partir de 2001, après avoir réalisé l'applicabilité des modèles bas Mach en thermoacoustique, j'ai travaillé sur l'adaptation du code faible Mach pour l'étude du pompage de chaleur thermoacoustique. C'est ainsi que je me suis intéressée à ce domaine de recherche qui faisait l'objet d'une action transversale dans le laboratoire depuis une dizaine d'années (action dirigée par Maurice-Xavier François). J'ai co-encadré la thèse de Patxi Duthil sur le pompage de chaleur thermoacoustique, avec une approche conjointe expérimentale et numérique. Les simulations ont été validées avec des mesures expérimentales réalisées au laboratoire (détails en section 5.1).

Depuis 2004, J'ai développé une collaboration étroite et très bénéfique avec ma collègue Diana Baltean-Carlès, spécialiste des développements asymptotiques et de la modélisation mathématique des écoulements. Nous travaillons ensemble à la fois en recherche et en enseignement. Nous avons étudié la modélisation théorique du phénomène de conversion d'énergie dans les moteurs thermoacoustiques. Nous avons mené une analyse asymptotique (collaboration avec

Luc Bauwens de l'Université de Calgary) qui a permis de dégager les conditions de couplage entre l'écoulement dans le stack et le champ acoustique dans le résonateur. Le code faible Mach utilisé dans la thèse de P. Duthil a été adapté (thèse Omar Hireche) pour une étude des écoulements et transferts au sein de la cellule active thermoacoustique (stack+échangeurs de chaleur) lors du fonctionnement « moteur » de la cellule. Le couplage a été réalisé par l'intermédiaire des conditions aux limites en vitesse, qui sont écrites en tenant compte de l'insertion du stack en un point précis du tube résonant. Nous avons ainsi simulé la phase de démarrage et de saturation d'un moteur thermoacoustique (détails en section 5.2) Nous avons ensuite déterminé numériquement le seuil de l'instabilité thermoacoustique et étudié l'influence de la charge sur le déclenchement d'un moteur thermoacoustique (thèse Lin Ma, collab. Ivan Delbende, détails en section 5.3).

Grâce à cette activité, nous nous sommes rapprochées d'autres chercheurs français travaillant dans le petit monde de la thermoacoustique. Nous avons participé à la création et à la vie du GDR Thermoacoustique (2007-2014), et avons notamment organisé une école thématique de Thermoacoustique à Roscoff en 2010.

Dans le cadre des activités en thermoacoustique, nous avons repris en 2007 les études de convection naturelle en milieu poreux pour la description des écoulements de convection dans le stack d'un moteur thermoacoustique, modélisé comme un empilement de plaques parallèles horizontales, encadré par deux échangeurs de chaleur (collab. P. Duthil, D. Baltean-Carlès, P. Le Quéré). En effet, les écoulements de convection naturelle peuvent modifier le champ de température au sein du stack, et par conséquence modifier ou même empêcher le démarrage du moteur thermoacoustique (détails en section 3.2.1).

Depuis 2009, nous avons entamé et établi une collaboration durable, Diana Baltean-Carlès, Virginie Daru et moi-même, sur la modélisation théorique et la simulation numérique du streaming acoustique en guide d'ondes. Cet écoulement stationnaire du second ordre peut être notamment très pénalisant dans les machines thermoacoustiques. A faible niveau acoustique cet écoulement est bien connu (section 6.1). Les simulations numériques et les expériences réalisées à l'Institut P' (Poitiers) ont notamment mis en évidence la déformation à fort niveau acoustique des cellules de streaming avec apparition de nouvelles cellules au centre du guide (section 6.2). Cela a permis d'établir une collaboration avec H. Bailliet (Institut P'), et I. Reyt, qui a effectué un stage post-doctoral au LIMSI en 2012. C'est ainsi que l'équipe des "filles du vent" s'est agrandie. Nous collaborons depuis très régulièrement, et bien que nous n'ayons pas encadré de thèse sur ce sujet, nous avons écrit 5 articles de revue ensemble (dont un soumis). Les résultats des études numériques et notamment l'analogie avec un écoulement en cavité entraînée ont montré que, à fort niveau acoustique, les effets d'inertie sur le streaming restent faibles et ne sont pas responsables du changement de régime dans l'évolution du streaming (section 6.3). Nous avons mis en évidence l'interaction non linéaire entre l'acoustique et l'écoulement de streaming. Nous avons obtenu une solution analytique pour l'écoulement lent de streaming, en régime linéaire, qui a permis d'analyser l'influence de chaque terme source acoustique (section 6.1). Nous avons trouvé qu'un des termes sources, en général négligé dans la littérature, peut générer des nouvelles cellules de streaming contra-rotatives, pour certaines valeurs du rapport de forme du guide d'onde. Nos travaux actuels concernent l'influence des inhomogénéités de température sur le streaming acoustique dans un résonateur (section 6.4).

Nous avons aussi modélisé et étudié l'instabilité thermoacoustique à l'origine du démarrage d'un moteur thermoacoustique « musical », dans le cadre d'un projet Art&Sciences « Thermophonia » (collab. J. Rémus - Ipotam Mécamusique). Cela nous a permis de travailler sur une application originale de la thermoacoustique (section 5.4).

Enfin, les collaborations renforcées avec les équipes travaillant sur la thermoacoustique de l'institut P', du LAUM, du LMFA et l'entreprise PSA, ont permis d'obtenir en 2017 un finan-

cement pour le développement et l'étude d'une pompe à chaleur thermo-acoustique pour le transport terrestre (ANR TACOT, porteur H. Bailliet). Je suis responsable scientifique pour le LIMSI, et notre équipe (V. Daru, D. Baltean-Carlès et moi-même) réalise les simulations numériques des écoulements dans le prototype en construction. Nous nous intéressons notamment aux effets liés à la compacité de la machine et au fort niveau acoustique généré : phénomènes de convection naturelle dans le stack régénérateur considéré comme un milieu poreux, effets multi-dimensionnels liés à la complexité de la géométrie, acoustique nonlinéaire en milieu poreux. Nous avons effectué des simulations numériques des écoulements de convection naturelle dans des machines thermoacoustiques (pour ce travail nous avons fait appel à Omar Hireche) et obtenu d'excellentes comparaisons avec des mesures réalisées à Pprime (collab. O. Hireche, D. Baltean-Carlès, V. Daru, Y. Fraigneau, I. Ramadan, H. Bailliet). Nous avons montré que ces écoulements peuvent affecter de manière significative le fonctionnement des machines thermoacoustiques (section 3.2.2). Nous étudions actuellement la faisabilité de simulations sous l'approximation faible Mach du prototype construit à l'institut P'. Ce projet permet donc de faire le lien entre tous les thèmes de recherche que j'ai abordés au LIMSI.

2.2 Généralités sur les machines thermoacoustiques

2.2.1 Réfrigérateurs et moteurs thermoacoustiques

La thermoacoustique concerne l'interaction entre les oscillations acoustiques et thermiques d'un gaz confiné à proximité d'une paroi solide, ayant comme effet une conversion d'énergie thermique en énergie acoustique (moteur thermoacoustique) ou vice-versa (pompe à chaleur ou réfrigérateur thermoacoustique).

L'intérêt principal des dispositifs thermoacoustiques réside dans leur simplicité, leur fiabilité (absence de composants mécaniques mobiles) et l'utilisation de fluides non polluants. Le champ d'applications en réfrigération est très large : cryogénie [14], climatisation [75], froid domestique, refroidissement des micro-composants électroniques. Les moteurs thermoacoustiques peuvent utiliser des énergies non fossiles, comme l'énergie solaire [1]. Couplés à des réfrigérateurs thermoacoustiques, ils peuvent être utilisés pour le refroidissement des composants électroniques sur des systèmes embarqués dans l'espace : satellites, station spatiale, ou pour la climatisation des avions. Les systèmes thermoacoustiques peuvent aussi être utilisés dans les procédés industriels pour récupérer la chaleur perdue à basse température [63], puis la réintroduire dans le procédé, ou encore pour la cogénération : utilisation de la puissance acoustique produite par un moteur thermoacoustique pour une production d'électricité [7].

Un système thermoacoustique de réfrigération se compose, d'une manière générale, d'un tube résonant, rempli d'un gaz compressible, au sein duquel est inséré un milieu poreux (par exemple un ensemble de grilles ou un empilement de plaques planes) placé entre deux échangeurs de chaleur. L'application d'une onde acoustique au sein du fluide induit une interaction fluide-solide qui va provoquer un pompage de chaleur le long des plaques dans la direction de propagation de l'onde et qui se caractérise par la génération d'un gradient longitudinal de température le long du milieu poreux. L'introduction des échangeurs permet de récupérer la chaleur pompée.

Un moteur thermoacoustique est un système constitué d'un tube résonant à l'intérieur duquel est placée la cellule active thermoacoustique. Cette dernière est composée de deux échangeurs, l'un chaud, l'autre froid, séparés par une structure poreuse ou par un empilement de plaques (stack), qui est le siège des échanges surfaciques de chaleur. Par l'intermédiaire des échangeurs, on impose une différence de température donnée entre l'entrée et la sortie de la cellule active. Lorsque cette différence de température est suffisamment importante, une instabilité

thermoacoustique se déclenche, et toute perturbation initiale de pression est amplifiée.

Les études et les dimensionnements des systèmes thermoacoustiques complets s'effectuent actuellement en utilisant des codes 1D [68] basés sur l'approximation acoustique linéaire de Rott [56, 58]. Les travaux de référence sur les machines thermoacoustique sont issus du groupe de recherche de Gregory Swift (Los Alamos, USA) [65]. Les équations fondamentales (équation des ondes vue sous la forme de deux équations différentielles du premier ordre couplées, et équation de l'énergie) sont intégrées sur la section d'un canal. On obtient ainsi des équations 1D pour les amplitudes complexes de pression, vitesse volumique et température, l'influence de la géométrie étant prise en compte par des facteurs de forme. Dans les codes classiques ces équations sont intégrées numériquement, en fonction de la coordonnée de position axiale, la géométrie étant définie comme une succession de segments, avec des conditions de raccord à la jonction entre deux segments. Ces codes permettent de dimensionner les machines avec une bonne précision (80-90% dans certains cas), mais sont d'une applicabilité limitée lorsqu'il s'agit de concevoir et d'optimiser des machines thermoacoustiques de puissance, car ils ne prennent pas en compte des phénomènes complexes tels que le streaming acoustique, les couplages non linéaires acoustique-thermique, les effets aérodynamiques et thermiques de bord et, en général, les effets non linéaires et multidimensionnels, qui limitent les performances des systèmes thermoacoustiques.

(a) (b) (c)

FIGURE 2.1 – *Prototypes de systèmes thermoacoustiques construits au LIMSI : (a) générateur d'ondes stationnaires (b) générateur d'ondes progressives (c) réfrigérateur.*

De nombreux laboratoires, en France et à l'étranger (USA, Japon, Chine), s'intéressent à cette thématique de recherche qui connaît un essor important depuis les années 80. En France, le laboratoire LAUM (Le Mans) est le plus reconnu, avec une équipe dont les travaux sont dédiés à la thermoacoustique. L'activité de recherche développée au LIMSI s'est d'abord concentrée sur le développement et l'étude de démonstrateurs (réfrigérateurs, moteurs ou systèmes couplés, à ondes stationnaires ou progressives) fonctionnant sous haute pression (figure 2.1). Les systèmes les plus efficaces fonctionnent avec des ondes progressives (architectures en boucle). Depuis plus de 15 ans, nous nous intéressons également à la modélisation et à la simulation numérique des machines thermoacoustiques.

2.2.2 Principe de conversion d'énergie thermoacoustique

Les moteurs et réfrigérateurs thermoacoustiques reposent sur l'existence d'un effet thermoacoustique. Les acousticiens en présentent généralement une vision lagrangienne en suivant une particule de fluide qui oscille sous l'effet d'une onde acoustique. Lorsque cette particule est loin de toute paroi solide, les oscillations sont adiabatiques. Lorsque la particule est proche d'une paroi solide, les oscillations sont accompagnées d'échanges thermiques avec celle-ci.

Pour décrire l'effet d'amplification de l'onde, Lord Rayleigh [52] a expliqué qualitativement que : si un gaz qui oscille absorbe de la chaleur pendant la phase de compression et cède de la chaleur pendant la phase de détente, alors l'oscillation est amplifiée. Au contraire, si le gaz qui oscille absorbe de la chaleur pendant la phase de détente, et cède de la chaleur pendant la phase de compression, alors l'oscillation est amortie. Le critère de Rayleigh conditionne donc l'apparition de l'instabilité thermoacoustique à la présence d'un déphasage entre les fluctuations de pression et celles de température.

Pour décrire de manière très simplifiée l'effet moteur (dans un système à ondes stationnaires), on suit, au cours de son cycle acoustique, une particule qui se trouve à une distance de l'ordre de l'épaisseur de couche limite thermique de la paroi (ni plus près, ni plus loin). On suppose que la paroi est soumise à un gradient de température donné, et que la direction de propagation de l'onde est parallèle à la paroi. On peut de manière très simplifiée, décomposer ce cycle en 4 étapes :

— 1 : La particule se déplace rapidement d'une zone basse pression vers une zone de pression plus élevée sans échange de chaleur avec la paroi (compression adiabatique).
— 2 : En bout de course, la particule est presque immobile mais plus froide que la plaque, et reçoit une quantité de chaleur Q_1 de la plaque, à pression constante (dilatation isobare).
— 3 : La particule retourne rapidement vers une zone basse pression (détente adiabatique).
— 4 : En bout de course, la particule est presque immobile mais plus chaude que la paroi, et cède une quantité de chaleur Q_2 à la plaque, à pression constante (contraction isobare).

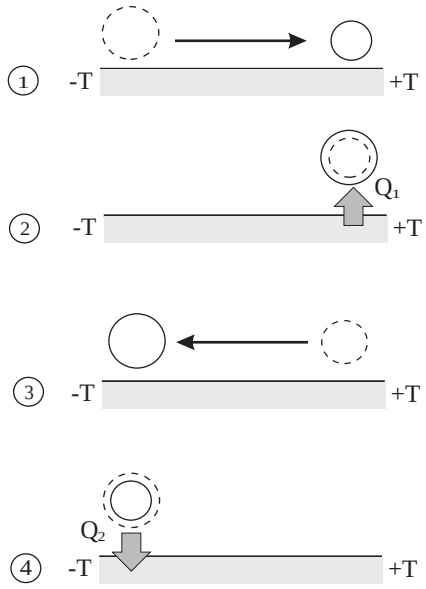

FIGURE 2.2 – *Schématisation du déplacement de la particule suivant le cycle de Brayton (configuration moteur), d'après [64].*

Le cycle de la particule s'apparente du point de vue énergétique à un cycle de Joule-Brayton. L'effet thermoacoustique étant localisé près des parois, on utilise des empilements d'un grand nombre de plaques (stack) pour amplifier l'effet global. La vision lagrangienne du pompage de chaleur est similaire, mais la paroi est initialement à température homogène. Lorsque l'onde est progressive, le cycle thermodynamique décrit par la particule est différent et se rapproche d'un cycle de Stirling. Les phases de compression-détente s'effectuent en plus proche paroi de manière isotherme, et il est alors intéressant d'utiliser des empilements de grille à la place d'un stack.

On peut aussi illustrer le phénomène de pompage de chaleur thermoacoustique avec une

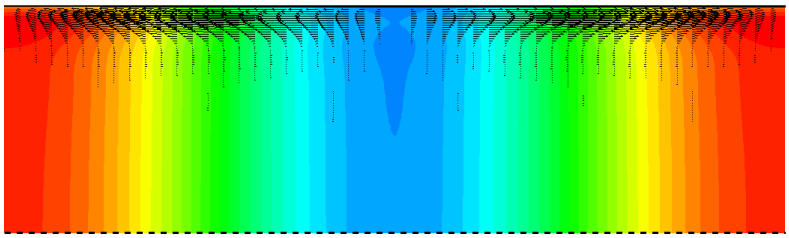

FIGURE 2.3 – *Illustration de l'effet de pompage de chaleur thermoacoustique dans un résonateur secoué : isothermes du champ moyen de température, et flux d'entropie thermoacoustique (flèches).*

vision plus "mécanicienne" en considérant le résultat de la simulation de l'écoulement compressible d'un gaz obtenu dans un résonateur plan secoué à sa fréquence propre avec une faible amplitude (onde stationnaire). Les parois sont ici conductrices, avec l'extérieur de la paroi maintenu à température constante. Ces résultats ont été obtenus dans le cadre de l'étude du streaming acoustique non linéaire dans un résonateur (voir chapitre 6). La figure 2.3 montre une demi-section longitudinale du tube, limitée par la paroi en haut et l'axe de symétrie en bas, et dont l'extension est une demi-longueur d'onde. Les extrémités gauche et droite correspondent aux nœuds de vitesse acoustique, et le centre à un ventre. Les isothermes du champ de température moyen obtenu après stabilisation de l'écoulement sont presque parallèles et montrent que les extrémités de la cellule se réchauffent, tandis que le centre se refroidit. Les flèches indiquent le flux thermoacoustique (qui est concentré en proche paroi). Ces résultats confirment ceux de l'approche Lagrangienne.

2.3 Organisation de la présentation des travaux de recherche

La suite de ce mémoire est consacrée à la présentation détaillée de mes activités de recherche, regroupées par thématique. Le chapitre 3 concerne les couplages fluides-poreux, et le chapitre 4 traite des écoulements de convection hors Boussinesq. Les applications du modèle faible nombre de Mach en thermoacoustique sont détaillées dans le chapitre 5, et enfin le chapitre 6 rassemble les études autour du streaming acoustique.

Chapitre 3

Couplages fluides-poreux

Je me suis intéressée aux écoulements de convection naturelle dans des cavités renfermant à la fois un fluide et un milieu poreux pendant plusieurs périodes au cours de ma carrière. Tout d'abord à mon arrivée au LIMSI, j'ai étudié des configurations académiques de cavités différentiellement chauffées partiellement remplies d'un milieu poreux. Puis nous nous sommes intéressés à la modélisation des écoulements de convection naturelle dans le stack d'un moteur thermoacoustique. Enfin, nous avons repris ces études dans le cadre de l'ANR TACOT pour étudier de façon plus générale l'importance des écoulements de convection naturelle dans les systèmes thermoacoustiques qui sont des systèmes fermés avec certaines parties poreuses et d'autres uniquement fluides.

3.1 Convection naturelle en cavité différentiellement chauffée partiellement remplie d'un milieu poreux

A mon arrivée au LIMSI, et pendant de nombreuses années, la simulation numérique des écoulements de convection naturelle en cavité différentiellement chauffée avec des rapports de forme variés a constitué l'une des spécialités du laboratoire. La cavité est chauffée sur une paroi verticale et refroidie sur l'autre. Les parois haute et basse sont généralement adiabatiques. J'ai utilisé, en les modifiant, les codes volumes finis de P. Le Quéré, écrits pour la simulation numérique d'écoulements de convection naturelle en milieu fluide sous l'hypothèse de Boussinesq. Pour représenter les champs de température et de vitesse, j'ai utilisé le programme "rasiso" (P. Le Quéré), également un grand classique au LIMSI, qui manie une palette de couleurs originale pour représenter des isolignes.

Nous avons donc étudié l'écoulement de convection naturelle produit dans une cavité rectangulaire 2D différentiellement chauffée de largeur L et de hauteur H, divisée en une couche verticale poreuse de largeur d adjacente à la paroi chaude, et une seconde purement fluide.

On applique l'hypothèse de Boussinesq en supposant que la masse volumique du fluide ρ varie linéairement en fonction de la température $\tilde{T}$,

$$\rho = \rho_c[1 - \beta(\tilde{T} - T_c)].$$

où β est le coefficient de dilatation isobare, T_c et ρ_c sont les température et masse volumique de référence respectivement. Les équations de la convection naturelle sont écrites de façon unifiée dans le fluide et dans le milieu poreux en introduisant une variable de phase ϵ (égale à 0 dans le fluide et à 1 dans le poreux). On appelle k la conductivité thermique et c_p la chaleur massique à pression constante du milieu (on utilise l'indice m pour indiquer la valeur moyenne dans le poreux). On note κ la diffusivité thermique, $\kappa = k/(\rho_c c_p)$, et ν la viscosité cinématique du

fluide. Dans le domaine fluide, on retrouve les équations classiques de la convection naturelle dans l'approximation de Boussinesq. Dans la couche poreuse définie par sa porosité ϕ et sa perméabilité K (supposée isotrope) on adopte une formulation de Darcy-Brinkman, présentée dans de nombreux ouvrages [31, 41] et articles de référence [24]. Les équations s'écrivent donc :

$$(1-\epsilon+\frac{\epsilon}{\phi})\frac{\partial\vec{U}}{\partial t}+(1-\epsilon)(\vec{U}.\vec{\nabla})\vec{U} = -\frac{1}{\rho_c}\vec{\nabla}P+\frac{\rho}{\rho_c}\vec{g}+\nu\Delta\vec{U}-\epsilon\frac{\nu}{K}\vec{U} \quad (3.1)$$

$$((1-\epsilon)(\rho_c c_p)+\epsilon(\rho c_p)_m)\ \frac{\partial T}{\partial t}+(\rho_c c_p)\vec{U}.\vec{\nabla}\tilde{T} = ((1-\epsilon)k+\epsilon k_m)\,\Delta\tilde{T} \quad (3.2)$$

$$\vec{\nabla}.\vec{U} = 0 \quad (3.3)$$

Dans ces équations, P est la pression et $\vec{U}$ est le vecteur vitesse, qui représente la vitesse de filtration dans la couche poreuse [41]. Le terme de Darcy $-\frac{\nu}{K}\vec{U}$ traduit le ralentissement de l'écoulement dans le milieu poreux. Dans le milieu poreux, la viscosité qui intervient dans le terme de Brinkman $\nu\Delta\vec{U}$ est égale à ν_{eff} donnée par la relation $\nu_{eff}=\frac{\nu}{\phi}$. Cette formulation unifiée des équations impose implicitement la continuité des température, flux de chaleur, vitesse et contrainte à l'interface fluide-poreux, ce qui représente une simplification importante du modèle [3].

Dans le milieu poreux, on a exclu les terme d'advection $\frac{1}{\phi^2}\vec{U}.\vec{\nabla}\vec{U}$ [10] et de Forchheimer $\frac{c_f}{K^{\frac{1}{2}}}|\vec{U}|\vec{U}$ [2]. Ces deux termes peuvent être négligés lorsque le Reynolds de pore (défini à partir du rayon hydraulique) est petit, typiquement $Re_p \leq 1$.

Nous avons adopté une approche couplée numérique et analytique. Les simulations ont été réalisées en adaptant le code volumes finis (P. Le Quéré). La variable de phase ϵ permet de fixer les valeurs des paramètres en chaque point de maillage. L'algorithme numérique d'intégration des équations instationnaires, est basé sur la méthode de prédiction-projection [25, 26]. On traite implicitement, avec une discrétisation spatiale et temporelle précise au second ordre, les termes visqueux et de Darcy. Les termes convectifs et le gradient de pression sont discrétisés par un schéma explicite du second ordre. La résolution des problèmes de Helmholtz s'effectue soit par une méthode ADI [46], soit par une relaxation ponctuelle (SOR). Pour assurer l'incompressibilité, l'équation de Poisson est résolue par une méthode multigrille [60].

Nous avons étudié en particulier les solutions stationnaires en cavité différentiellement chauffée et refroidie à flux homogène (voir l'article [40] en annexe, étude menée en collaboration avec Jean-François Mercier lors de son post-doctorat au LIMSI). On note φ la densité de flux de chaleur imposée sur les parois verticales. Pour l'exemple de cette étude académique, on se restreint au cas où la viscosité effective ν et la conductivité thermique k sont les mêmes pour le milieu poreux équivalent et pour le fluide ($\nu_{eff}=\nu$ et $k_m=k$). La valeur de $(\rho c_p)_m$ n'influe pas sur la solution stationnaire.

Les simulations numériques ont montré que dans une large plage autour de la mi-hauteur de la cavité, l'écoulement pouvait être approché par un écoulement unidimensionnel purement vertical (figure 1 de [40] en annexe). Avec L la longueur de référence, on peut définir plusieurs nombres adimensionnels caractéristiques de l'écoulement : le nombre de Rayleigh fluide $Ra=g\beta\varphi L^4/(k\nu\kappa)$, le nombre de Darcy défini par K/L^2, et le nombre de Prandtl $Pr=\nu/\kappa$. Après introduction des grandeurs de référence $U^\star=\kappa Ra^{\frac{2}{5}}/L$, $\Delta T^\star=\varphi L Ra^{-\frac{1}{5}}/k$, $P^\star=\rho_c\nu\kappa Ra^{\frac{2}{5}}/L^2$ et $t^\star=L^2/\kappa Ra^{\frac{2}{5}}$, le système d'équations 3.1 à 3.3 est mis sous forme adimensionnelle. Les variables sans dimension sont notées $\vec{u}$, T et p. On note $ep=d/L$, l'épaisseur sans dimension de la couche poreuse.

L'écoulement stationnaire 1D présent dans le centre de la cavité (figure 3.1a) correspond à une vitesse purement verticale $\vec{u}_0=w_0(x)\,\vec{z}$ et à une température de la forme $T-T_c=\delta z+\theta_0(x)$, c'est-à-dire comprenant une distribution verticale linéaire de température (on note

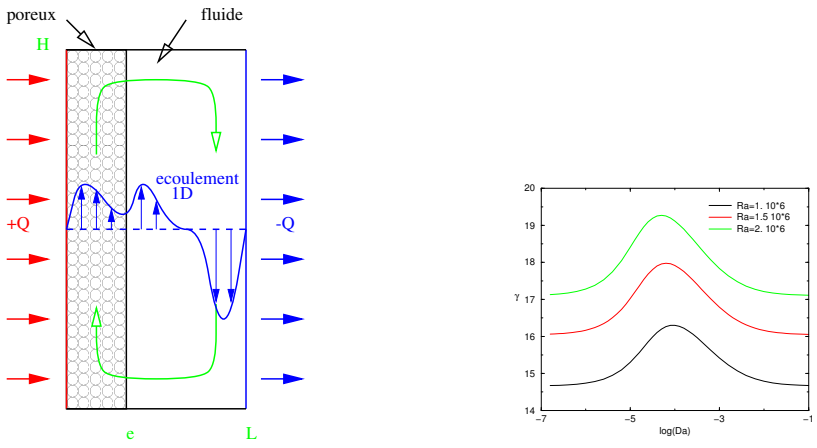

(a) (b)

FIGURE 3.1 – *(a) Ecoulement 1D dans une cavité rectangulaire partiellement remplie d'une couche poreuse. (b) stratification verticale en température γ en fonction du nombre de Darcy pour $Ra = 10^6$, $1.5\,10^6$, $2.\,10^6$.*

δ la stratification verticale) et une distribution horizontale à déterminer. La solution semi-analytique se présente comme la somme de huit exponentielles complexes de la variable x, dont les amplitudes sont déterminées numériquement.

On introduit un paramètre de stratification verticale de température noté γ par $4\gamma^4 = Ra^{\frac{4}{5}}\,\delta$. La résolution des équations de Navier-Stokes ne permet pas de déterminer la valeur de γ, mais celle-ci peut être obtenue à partir d'un bilan énergétique. Les parois horizontales de la cavité sont adiabatiques. Comme le flux de chaleur horizontal injecté au niveau de la paroi en $x = 0$ est égal à celui extrait au niveau de la paroi $x = L$, le flux vertical de chaleur à travers toute section horizontale de la cavité doit être nul. Ce dernier est constitué des contributions du flux conductif et convectif. En écrivant de plus la conservation de la masse sur toute coupe horizontale, on obtient la relation sans dimension :

$$\int_0^1 w_0\theta_0 dx = \frac{4\gamma^4}{Ra^{\frac{6}{5}}}.$$

Cette équation, dans laquelle le produit $w_0\theta_0$ est fonction de γ et Da, est résolue par une méthode de Newton-Raphson.

Les valeurs de γ en fonction de Da pour différentes valeurs du nombre de Rayleigh et pour une couche poreuse d'épaisseur $d = L/4$ (qui correspond à un régime d'écoulement à couches limites séparées) sont représentées sur la figure 3.1b. Pour les grandes valeurs du nombre de Darcy ($Da = 10^{-1}$) la couche poreuse étant très perméable, la cavité se comporte comme une cavité fluide. Pour de très faibles valeurs de Da, ($Da = 10^{-7}$), on est dans le cas d'une cavité fluide bordée par un milieu imperméable en conduction thermique. Ainsi, dans ces deux cas de cavité purement fluide, on retrouve les mêmes valeurs de stratification verticale en température.

3.2 Applications en thermoacoustique

3.2.1 Convection naturelle dans un empilement de plaques planes

Des essais sur un moteur thermoacoustique de grande dimension construit à l'Institut de Physique Nucléaire d'Orsay (IPNO) ont révélé la présence potentielle de courants convectifs

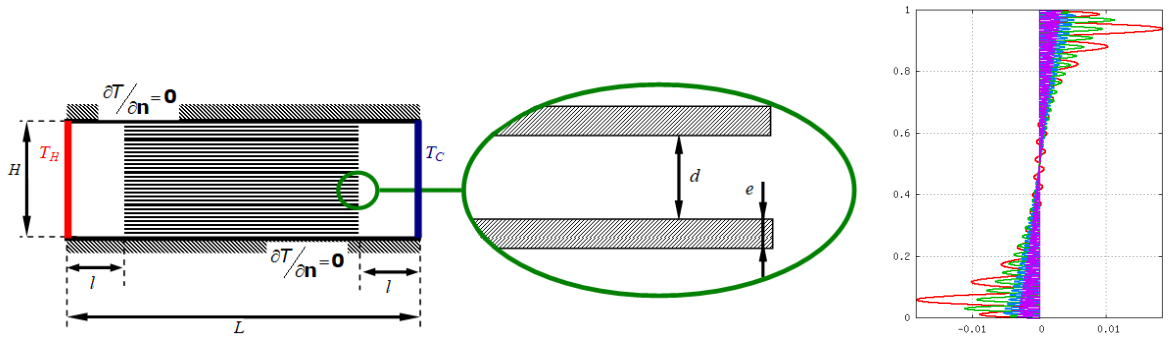

(a) (b)

FIGURE 3.2 – *(a) Géométrie de cavité rectangulaire partiellement remplie d'un empilement de plaques planes horizontales. (b) Profil vertical de vitesse horizontale pour* $Ra = 10^7$ *et un nombre de plaques variables* $(17, 34, 68, 100)$.

dans l'empilement de plaques (stack) de la cellule motrice. Ces courants sont néfastes au démarrage du moteur puisqu'ils empêchent l'établissement du gradient thermique longitudinal qui conditionne l'instabilité thermoacoustique. Ces essais ont motivé en 2007 une étude spécifique des écoulements de convection naturelle dans le stack modélisé comme un empilement de plaques parallèles horizontales conductrices (collab. P. Duthil, D. Baltean-Carlès, P. Le Quéré, présenté au 19ème International Symposium on Transport Phenomena [70]). Pour cette étude, on ne prend pas en compte l'acoustique. Le stack placé entre deux échangeurs de chaleur, mais le contact imparfait crée une petite zone fluide entre les extrémités des plaques et les échangeurs. L'analyse est menée en 2D dans une cavité de longueur L et hauteur H différentiellement chauffée (les parois verticales à température fixée modélisent les échangeurs, avec T_H la température chaude, et T_C la température froide) contenant un empilement de plaques planes horizontales conductrices. Le rapport de forme de la cavité est $L/H = 2.5$ et il existe un espacement entre les extrémités des plaques et les parois (figure 3.2a).

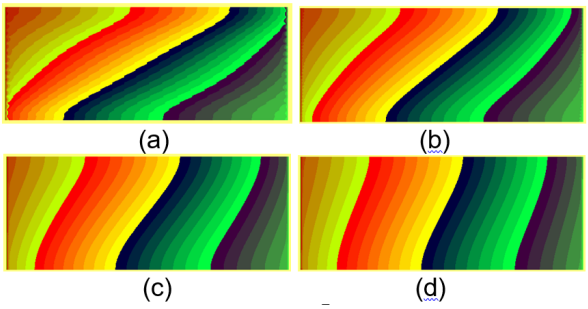

FIGURE 3.3 – *Champ de température pour* $Ra = 10^7$ *et un nombre de plaques variables (a) 17, (b) 34, (c) 68, (d) 100.*

Les stacks utilisés comportent plusieurs centaines de plaques et le calcul complet nécessite un maillage très fin. L'étude que nous avons menée consiste à effectuer des calculs (avec un code instationnaire résolvant les équations de Boussinesq en milieu fluide) pour un nombre restreint de plaques conductrices (l'équation de la chaleur seule est résolue dans les plaques) afin d'évaluer la pertinence d'un calcul utilisant un modèle de milieu poreux représentant l'empilement. Nous avons effectué les calculs pour plusieurs valeurs du nombre de Rayleigh (basé sur la hauteur de la cavité) entre 10^5 et 10^8, ainsi que l'étude de convergence en maillage (maillages

1024×1024 et 2048×2048). Nous avons fait varier le nombre de plaques (17, 34, 68, 100). Les calculs ont montré qu'en fonction de la distance entre les plaques, le phénomène global de convection s'accompagne éventuellement de transferts convectifs de plus petite échelle localisés entre deux plaques (figure 3.2b). Plus le nombre de plaques est grand, plus l'écoulement est ralenti dans le stack et plus le champ de température est stratifié horizontalement (voir un exemple sur la figure 3.3).

Plusieurs modèles de milieu poreux ont été testés pour proposer une formulation analytique approchée de l'écoulement au cœur de la cavité, montrant la nécessité d'utiliser une description anisotrope. Les équations générales de la convection naturelle stationnaire en milieu poreux darcéen 2D sont écrites sous l'hypothèse de Boussinesq (masse volumique de référence ρ_c à la température de référence $T_c = (T_H + T_C)/2$). En notant $\vec{V}$ le vecteur vitesse de composantes u et w, p la pression et T la température exprimées en quantités moyennées sur la cellule de base, les équations sont [41] :

$$\nabla.\vec{V} = 0 \tag{3.4}$$

$$\mu\vec{V} = -\overline{\overline{K}}(\nabla p - \rho_c g\beta(T - T_c)\vec{e}_z) \tag{3.5}$$

$$\vec{V}.\nabla T = \nabla.(\overline{\overline{\kappa}}_m \nabla T) \tag{3.6}$$

où $\overline{\overline{K}}$ est le tenseur de perméabilité et $\overline{\overline{\kappa}}_m$ est le tenseur de diffusivité thermique effective du milieu poreux. Pour représenter en 2D le milieu poreux homogène et anisotrope que constitue l'empilement de plaques, on pose :

$$\overline{\overline{K}} = \begin{bmatrix} K_{xx} & 0 \\ 0 & K_{zz} \end{bmatrix} \qquad \overline{\overline{\kappa}}_m = \begin{bmatrix} \kappa_{xx} & 0 \\ 0 & \kappa_{zz} \end{bmatrix} \tag{3.7}$$

avec, en notant d l'espace interplaque, e l'épaisseur d'une plaque (figure 3.2a), et $\phi = d/(d+e)$ la porosité

$$K_{xx} = \frac{d^3}{12(d+e)}, \quad K_{zz} = 0$$

$$\kappa_{xx} = \frac{k_{xx}}{\rho_c c_p}, \quad \kappa_{zz} = \frac{k_{zz}}{\rho_c c_p}, \quad \text{avec} \quad k_{xx} = \phi k + (1-\phi)k_s \quad \text{et} \quad \frac{1}{k_{zz}} = \frac{\phi}{k} + \frac{(1-\phi)}{k_s}$$

où c_p est la chaleur spécifique du fluide, k est la conductivité thermique du fluide et k_s celle du solide.

On introduit un nombre de Rayleigh modifié $Ra_K = g\beta\Delta T H K_{xx}/\nu\kappa_{zz}$ et une vitesse de référence $U_{refK} = \frac{\kappa_{zz}}{L} Ra_K$. Dans le cœur de la cavité il existe une solution approchée 1D adimensionnée qui approche très bien la solution numérique lorsque le rapport de forme de la cavité est suffisamment grand.

3.2.2 Convection naturelle dans une configuration thermoacoustique

Nous avons repris récemment une étude similaire dans le cadre du contrat ANR TACOT, par lequel nous avons pu bénéficier de 12 mois de travail post-doctoral (Omar Hireche). Nous avons effectué des simulations numériques 3D des écoulements de convection naturelle dans deux configurations de machines thermoacoustiques et obtenu d'excellentes comparaisons avec des mesures réalisées à Pprime (collab. O. Hireche, D. Baltean-Carlès, V. Daru, Y. Fraigneau, I. Ramadan, H. Bailliet). Nous avons montré que ces écoulements peuvent affecter de manière significative le fonctionnement des machines thermoacoustiques. Les deux configurations expérimentales étudiées sont décrites dans un article publié à IJHMT (2020) figurant en annexe [30].

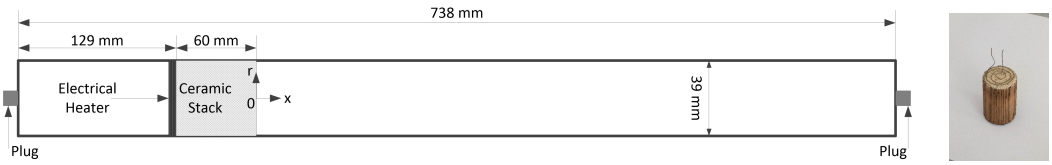

FIGURE 3.4 – *Schéma de petit moteur thermoacoustique à ondes stationnaires, d'après [30].*

La première configuration est celle d'un petit moteur thermoacoustique à ondes stationnaires, constitué d'un tube cylindrique fermé rempli d'air à l'intérieur duquel est positionné un stack en céramique chauffé à l'une de ses extrémités par l'intermédiaire d'une résistance électrique (figure 3.4). Les simulations et mesures comparées ici sont réalisées dans des conditions ne permettant pas le démarrage de l'onde acoustique (bouchons aux extrémités du tube retirés). Pour les simulations, nous avons simplifié la géométrie en considérant un simple tube fermé, contenant un milieu poreux homogène anisotrope, l'échangeur chaud étant modélisé par 3 anneaux solides à température fixée. On a imposé la température le long des parois du tube en se basant sur les mesures disponibles (figure 3.5).

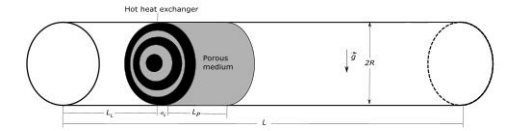

(a)

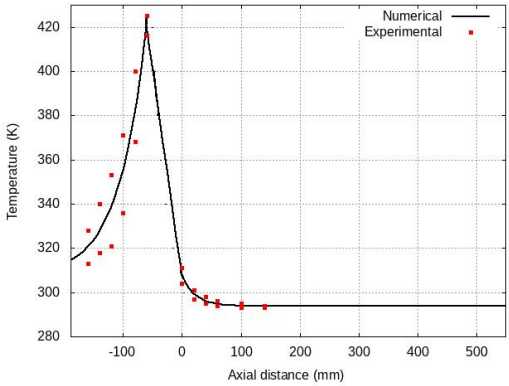

(b)

FIGURE 3.5 – *(a) Configuration utilisée pour les simulations du moteur à ondes stationnaires et (b) conditions limites en température imposées le long des parois du tube [30].*

Le stack est constitué d'un assemblage de capillaires de section carrée, de côté a et porosité ϕ. La perméabilité dans la direction axiale a été fixée par $K_{xx} = a^2\phi/8$, et sa perméabilité dans les deux autres directions (radiale et azimutale) est proche de zéro. La conductivité thermique équivalente est choisie isotrope and homogène, $k_m = \phi k_{fluid} + (1-\phi)k_{solid}$. On a pris $\nu_{eff} \simeq \nu$. On peut évaluer les nombres caractéristiques de l'écoulement de convection naturelle dans le milieu poreux. Avec les données expérimentales, on calcule le nombre de Rayleigh modifié dans le milieu poreux, (avec R la longueur de référence) $Ra_K = \rho_c g \beta \Delta T R K_{xx}/(\mu\kappa_m) = 1.1$. L'ordre de grandeur de la vitesse est $V_{ref} = \kappa_m Ra_K/R = 0.02$ m/s. Le nombre de Reynolds de pore est estimé à $Re_p \simeq 0.3$. Il est inférieur à 1, et donc l'utilisation du modèle de Darcy-Brinkman se justifie. On peut cependant se demander si l'hypothèse de Boussinesq est valide, puisque $\Delta T/(2T_{moy}) = 0.28$ (voir chapitre suivant). Nous avons dans cette première approche

utilisé cette hypothèse.

On a repris la modélisation unifiée en milieu fluide-poreux présentée dans les équations 3.1 à 3.3, étendue en trois directions, pour effectuer le calcul sur l'ensemble du domaine. On a également introduit une nouvelle fonction de phase pour tenir compte des solides immergés modélisant l'échangeur chaud. Les simulations ont été réalisées avec Sunfluidh (code LIMSI de Yann Fraigneau qui a été adapté pour le calcul en milieu poreux).

L'interprétation des courbes obtenues montre l'existence de 3 zones distinctes le long de l'axe : à gauche de l'échangeur, l'écoulement correspond à une cavité fluide différentiellement chauffée, avec la paroi chaude à droite et la paroi froide à gauche. A droite du stack, l'écoulement correspond à une cavité fluide différentiellement chauffée, avec la paroi chaude à gauche et la paroi froide à droite. A l'intérieur du stack, l'écoulement est très ralenti, avec globalement un mouvement vers la droite sur la partie haute du cylindre, et un mouvement vers la gauche sur la partie basse, et une structure qui retient l'empreinte des parties solides (voir les figures 3-4-8 et 9 de [30] en annexe). La correspondance entre les résultats de simulations et les mesures relevées sur deux plans situés à droite du stack est excellente compte-tenu du caractère simplifié de la modélisation (voir les figures 3 à 8 de [30] en annexe). L'amplitude des écoulements de convection est du même ordre de grandeur (voire supérieure) à celle de l'écoulement de streaming qui pourrait être mesuré en présence de l'onde acoustique [50]. La prise en compte de ces écoulements dans le dimensionnement des machines pourrait donc jouer un rôle non négligeable.

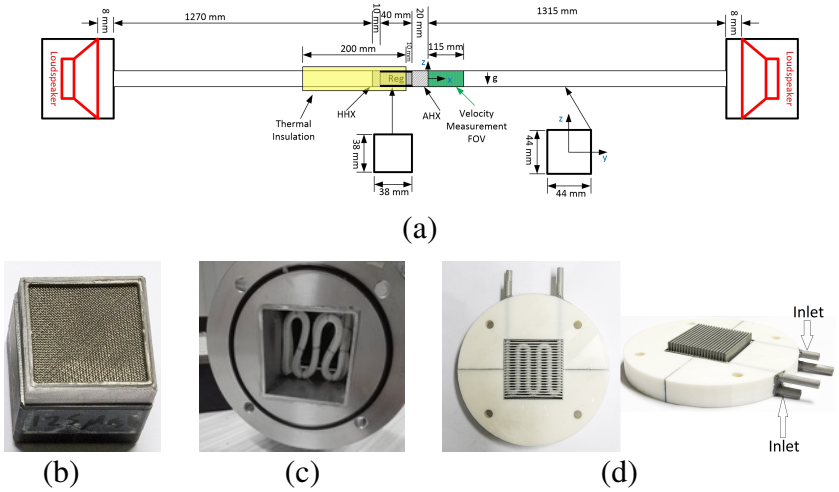

FIGURE 3.6 – *(a) Expérience réalisée à l'institut P' dans le cadre de l'ANR TACOT avec (b) régénérateur, (c) échangeur chaud, (d) échangeur froid [30].*

La deuxième configuration a été construite à l'institut P' pour analyser les effets de bord dans le prototype construit pour l'ANR TACOT. Il s'agit d'un cylindre de section carrée de côté H à l'intérieur duquel est placé un milieu poreux régénérateur (empilement de grilles) encadré de deux échangeurs de chaleur (figure 3.6). Ici aussi, les simulations et mesures comparées sont réalisées sans acoustique. Pour les simulations, la géométrie simplifiée est un cylindre fermé de section carrée. L'échangeur chaud est modélisé par 6 parallélépipèdes rectangles solides verticaux à température chaude fixée. L'échangeur froid est modélisé par 6 parallélépipèdes rectangles solides horizontaux à température froide donnée. Entre ces derniers est positionné un milieu poreux homogène anisotrope, pour modéliser des ailettes verticales (voir la figure 3.7).

Ici aussi, on utilise les données expérimentales pour estimer le nombre de Rayleigh dans le milieu poreux. Avec H la longueur de référence, on a $Ra_K = \rho_c g \beta \Delta T H K / (\mu \kappa_m) = 0.13$.

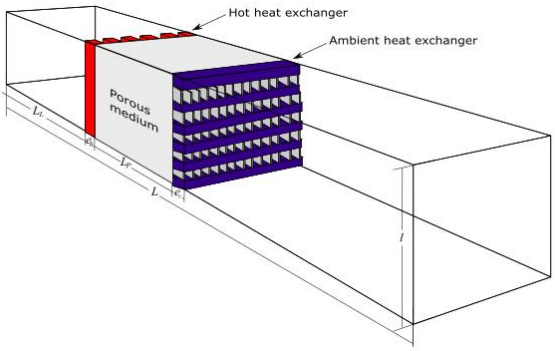

FIGURE 3.7 – *Configuration utilisée pour les simulations du dispositif expérimental avec échangeur ambient dans le cadre de l'ANR TACOT [30].*

L'ordre de grandeur de la vitesse est $V_{ref} = \kappa_m Ra_p/H = 2.2$ mm/s. Le nombre de Reynolds de pore est estimé à $Re_p \simeq 0.04$. Il est très inférieur à 1 ce qui justifie l'utilisation du modèle de Darcy-Brinkman. Ici aussi on a $\Delta T/(2T_{moy}) \simeq 0.2$ et donc en toute rigueur on ne devrait pas utiliser l'approximation de Boussinesq (voir chapitre suivant). Dans une première approche, nous avons utilisé cette hypothèse. Les équations résolues sont les mêmes que précédemment. Les parois du tube sont adiabatiques à gauche de l'échangeur chaud (de façon à modéliser la couche isolante mise en place dans l'expérience) et les parois sont maintenues à température ambiante à droite de l'échangeur froid (assez bonne approximation de la réalité). Entre les échangeurs, la température des bords est imposée avec une variation linéaire du chaud au froid.

Ici aussi les comparaisons entre les mesures réalisées à droite de l'échangeur froid et les simulations sont excellentes (voir les figures 12 à 14 de [30]). La présence de l'échangeur froid modifie de façon importante l'écoulement obtenu à sa droite, puisque le mouvement de convection est dans le sens inverse (la température de l'échangeur froid est plus froide que la température ambiante). Globalement, l'écoulement de convection est d'amplitude bien moins importante.

3.3 Conclusions

Nous avons étudié les écoulements de convection naturelle dans des configurations comportant des parties poreuses à partir d'un modèle de Darcy-Brinkman qui s'applique lorsque le Reynolds de pore est petit. Une analyse dimensionnelle avec résolution analytique simplifiée en cavité allongée a été appliquée au cas de stacks utilisés en thermoacoustique. Enfin, la simulation numérique a récemment permis de mieux comprendre les écoulements dans des configurations applicables en thermoacoustique. Nous avons obtenu un excellent accord avec les mesures, et nous pouvons donc espérer utiliser ce code pour prédire les écoulements dans des zones où les mesures sont moins accessibles. Ces résultats sont néanmoins limités dans la mesure où l'acoustique n'est pas du tout prise en compte. Il serait intéressant d'étendre cette étude pour permettre la prise en compte de la gravité dans l'analyse des écoulements en thermoacoustique.

Chapitre 4

Convection hors Boussinesq

La majorité des études de convection naturelle utilisent l'approximation de Boussinesq, où toutes les propriétés physiques du fluide sont supposées uniformes et constantes, mise à part une dépendance linéaire de la densité en température dans le terme moteur de la poussée d'Archimède. En conséquence, le fluide peut être considéré comme effectivement incompressible. Cette approximation n'est valable que lorsque les variations de température sont petites. Lorsque les écarts de température deviennent plus grands, on peut utiliser les équations établies par Paolucci [43], correspondant à l'hypothèse de faible nombre de Mach, intermédiaires en complexité entre l'approximation de Boussinesq et les équations compressibles complètes. On filtre ainsi les ondes sonores, qui pénaliseraient la résolution numérique du système d'équations initial en imposant un critère de stabilité très contraignant.

4.1 Benchmark numérique

Nous avons étudié (collab. P. Le Quéré) les écoulements de convection naturelle en cavité 2D différentiellement chauffée à grands écarts de température (convection hors Boussinesq, hypothèse faible Mach). Nous avons ainsi participé en 2000 et 2002 à un Benchmark numérique sur les solutions stationnaires de ces équations en cavité carrée. L'étude a débuté dans le cadre d'un stage de Licence en 1999 effectué par un binôme d'étudiants [36], à partir de deux codes écrits par Patrick le Quéré. Nous avons obtenu des solutions de référence, présentées en 2000 lors du 12^{eme} séminaire "Mécanique des fluides numérique" du CEA (voir l'article [33], figurant en annexe).

La cavité est bidimensionnelle, de largeur L_0 et de hauteur H_0, remplie d'air à la température moyenne T_0. On note A le rapport de forme $A = H_0/L_0$ (dans le Benchmark $A = 1$). On maintient la température des parois verticales constante de façon à imposer une différence de température $\varepsilon = \Delta T/(2T_0)$. La température de la paroi gauche est alors $T_h = T_0(1+\varepsilon)$ et celle de la paroi droite $T_c = T_0(1-\varepsilon)$. Les faibles valeurs de ε correspondent au cas de l'approximation de Boussinesq. On étudie ici la gamme $\varepsilon \in [0.01, 0.6]$ qui, pour l'air, est en dehors de la gamme d'utilisation de l'approximation de Boussinesq. Les parois horizontales sont adiabatiques. On note ρ la masse volumique de l'air, μ sa viscosité dynamique, ν sa viscosité cinématique, k sa conductivité thermique, c_v sa chaleur massique à volume constant, γ le rapport des chaleurs massiques, κ sa diffusivité thermique. La viscosité dynamique μ est prise soit constante, soit donnée par la loi de Sutherland :

$$\frac{\mu(T)}{\mu^*} = \left(\frac{T}{T^*}\right)^{3/2} \frac{T^* + S}{T + S}$$

avec $T^* = 273K, S = 110.5K, \mu^* = 1.68 * 10^{-5} kg/m/s, c_p = \frac{\gamma R}{\gamma - 1}, \gamma = 1.4$ et $R =$

$287.0 J/kg/K$. La conductivité thermique k est donnée à partir du nombre de Prandtl $Pr = 0.71$ (maintenu constant) par $k(T) = \frac{\mu(T)c_p}{Pr}$. Les valeurs de référence de ρ, ν et k, indiquées par l'indice "0", sont celles correspondant à la température de référence T_0. On choisit L_0 comme longueur de référence.
Le nombre de Rayleigh caractéristique de l'écoulement est défini par

$$Ra = Pr\frac{g\rho_0^2(T_h - T_c)L_0^3}{T_0\mu_0^2}.$$

Les équations de continuité, de conservation de la quantité de mouvement et de l'énergie, associées à l'équation d'état, sont celles décrites par Chenoweth et Paolucci [13]. Dans l'approximation faible Mach, la pression est partagée en deux composantes, une composante moyenne thermodynamique et la déviation par rapport à la pression moyenne et à la composante hydrostatique dans la cavité isotherme. En introduisant la vitesse de référence $V_0 = (\frac{\kappa}{L_0})Ra^{1/2}$, on obtient la forme adimensionnée de la déviation de pression

$$\pi = \frac{(P - \overline{P} + \rho_0 gz)}{\rho_0 V_0^2}$$

La pression thermodynamique, sous forme adimensionnée par $\overline{P_0} = c_v(\gamma - 1)T_0\rho_0$ est notée $\overline{P}$. Avec $t_0 = L_0/V_0$ le temps de référence, on obtient les équations suivantes sous forme adimensionnée :

$$\rho[\frac{\partial T}{\partial t} + (V.\nabla)T] = \frac{1}{Ra^{1/2}}\nabla.(k\nabla T) + \frac{\gamma - 1}{\gamma}\frac{d\overline{P}}{dt} \quad (4.1)$$

$$\rho[\frac{\partial V}{\partial t} + (V.\nabla)V] = -\nabla\pi + \frac{Pr}{Ra^{1/2}}\nabla.\tau - Pr\frac{\rho - 1}{2\varepsilon}\vec{z} \quad (4.2)$$

$$\frac{\partial \rho}{\partial t} + \nabla.\rho V = 0 \quad (4.3)$$

$$\overline{P} = \rho T \quad (4.4)$$

$$\frac{d\overline{P}}{dt} = \frac{\gamma}{A\,Ra^{1/2}}\int_0^1 \left(k\left(\frac{1}{A}, z\right)\frac{\partial T}{\partial x}\left(\frac{1}{A}, z\right) - k(0, z)\frac{\partial T}{\partial x}(0, z)\right) dz \quad (4.5)$$

où τ est le tenseur des contraintes visqueuses. La dernière équation, nécessaire à cause de la séparation de la pression en deux variables, est une équation intégrale qui exprime que les variations de la pression moyenne sont liées, en l'absence de flux de masse aux parois, aux flux de chaleur pariétaux ($\vec{n}$ est la normale extérieure à la paroi, et $\partial\omega$ la frontière de la cavité). On aurait pu alternativement écrire une équation intégrale traduisant la conservation de la masse globale [33].

Les conditions limites aux parois sont des conditions limites d'adhérence pour la vitesse, de flux nul sur les parois horizontales et de température constante sur les parois verticales pour la température. On impose des conditions initiales spatialement uniformes $T = 1$, $\rho = 1$, $U = V = \pi = 0$ (en variables adimensionnées).

Les maillages utilisés sont uniformes dans la direction verticale et non uniformes (Chebyshev) dans la direction horizontale. Les équations sont intégrées sous forme instationnaire en utilisant une méthode à pas fractionnaire, dérivée des méthodes classiques de projection en incompressible afin d'obtenir à chaque pas de temps des champs de vitesse à la divergence voulue. La discrétisation en temps allie un traitement implicite des termes visqueux ou diffusifs et un traitement explicite des termes convectifs. L'équation de l'énergie est discrétisée sous forme convective, et les équations de conservation de la quantité de mouvement sous forme conservative. Dans le code volumes finis, les systèmes linéaires sont résolus par une méthode ADI, et

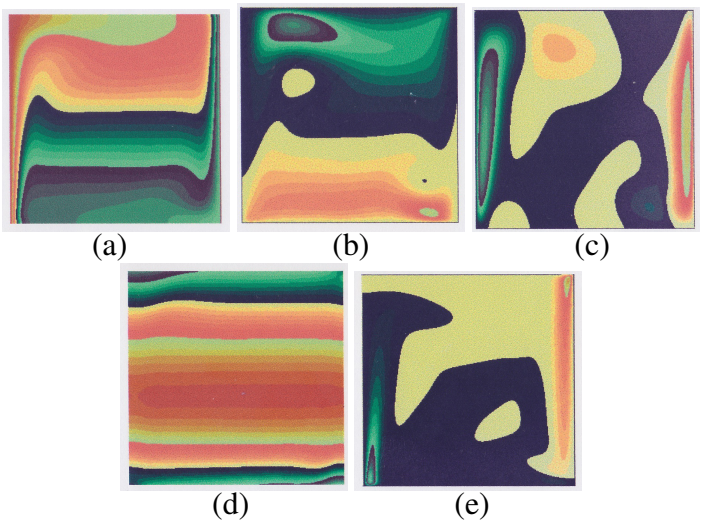

FIGURE 4.1 – *Solutions en cavité carrée pour $\varepsilon = 0.6$ et $Ra = 10^6$, propriétés physiques constantes. (a) Température, échelle de couleurs 1.6,0.4 (b) Vitesse horizontale, échelle -0.2,0.2 (c) Vitesse verticale, échelle -0.3,0.3 (d) Pression dynamique π, échelle 0 ,0.12 (d) Divergence, échelle -0.7,0.7. D'après [36].*

l'équation elliptique donnant la correction de pression est résolue par une méthode multi-grille. L'algorithme est le suivant (écrit pour la cavité carrée, avec $A = 1$)

- début du pas de temps
- calcul du nouveau champ de température T^{n+1} à partir de k^n.
- correction de $\overline{P}^{n+1}$ et ρ^{n+1} par conservation de la masse
- calcul des nouvelles propriétés physiques k^{n+1} et μ^{n+1}
- calcul de $\dfrac{d\overline{P}}{dt}^{n+1} = \dfrac{\gamma}{Ra^{1/2}} \displaystyle\int_0^1 \left(k(1,z)\frac{\partial T}{\partial x}(1,z) - k(0,z)\frac{\partial T}{\partial x}(0,z) \right) dz$
- calcul des vitesses intermédiaires $\mathbf{V}^*$.
- calcul du terme source dans l'équation de la divergence, $(\nabla.\mathbf{V})^{n+1} = \dfrac{\nabla.(k\nabla T)}{Ra^{1/2}\overline{P}} - \dfrac{1}{\gamma}\dfrac{1}{\overline{P}}\dfrac{d\overline{P}}{dt}$.
- solution pour la "correction de pression" ϕ (multigrille)
- mise à jour des vitesses et de la pression : $\pi^{n+1} = \pi^n + \frac{3}{2}\phi$
  $\mathbf{V}^{n+1} = \mathbf{V}^* - \frac{\Delta t}{\rho^{n+1}}\nabla\phi$
- fin du pas de temps

Le code spectral utilisé est décrit dans [32].

Le nombre de Rayleigh est fixé égal à 10^6 et 10^7 dans les cas-tests considérés dans le Benchmark. L'écoulement est alors laminaire et il existe une solution stationnaire. Les équations sont intégrées jusqu'à stationnarité (voir sur la figure 4.1 un exemple de champs obtenus pour $\varepsilon = 0.6$, $Ra = 10^6$, avec les propriétés physiques du gaz maintenues constantes).

L'obtention de solutions de référence dans le cadre d'un benchmark est conditionnée par le soin apporté pour satisfaire les convergences en temps et en maillage. Pour cela, on a utilisé le principe d'extrapolation de Richardson qui utilise des solutions obtenues sur des maillages de finesse différente, supposés dans la zone de convergence asymptotique.

Si $N + 1$ est le nombre de points de maillage suivant une direction, on pose $h = 1/N$. On note f_h, $f_{h'}$, $f_{h/2}$, $f_{h'/2}$ les approximations numériques obtenues pour une quantité scalaire f sur quatre maillages dans la zone de convergence (dont deux sont 2 fois plus fins que les deux premiers) telle que $f_h = f + Ch^\alpha$. On trouve les valeurs suivantes de α, C et f (valeur

extrapolée)

$$\alpha = \ln\left(\frac{f_h - f_{h/2}}{f_{h'} - f_{h'/2}}\right)/\ln\left(\frac{h}{h'}\right), \qquad C = \frac{f_h - f_{h/2}}{h^\alpha(1-2^{-\alpha})}, \qquad \text{et} \qquad f = f_h - Ch^\alpha.$$

Ceci nous a permis de montrer (fig. 4.2) que la loi de convergence est en $1/N^2$. Nous avons ensuite extrapolé au maillage $N \to \infty$ les valeurs locales et globales demandées. Pour $Ra = 10^7$, il est nécessaire d'utiliser un maillage 1024×1024 pour obtenir la convergence spatiale. Avec l'algorithme spectral un maillage de 80×80 est suffisant à $Ra = 10^6$.

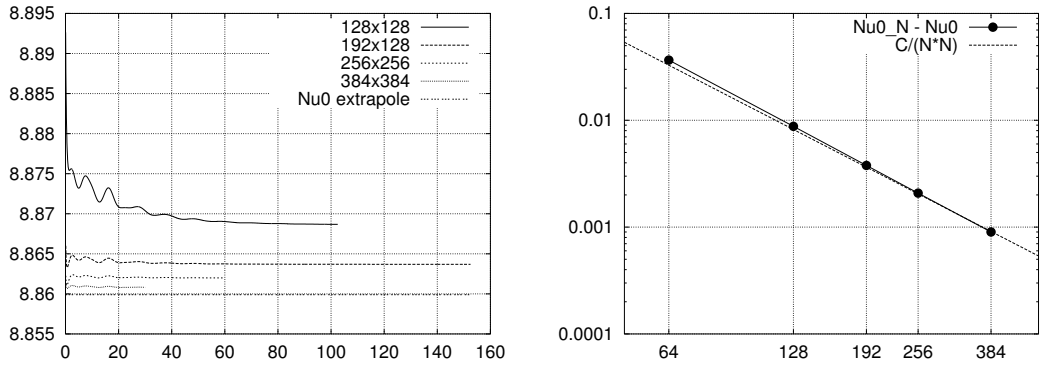

(a) (b)

FIGURE 4.2 – *Cavité carrée avec $\varepsilon = 0.6$, $Ra = 10^6$, propriétés physiques constantes. Convergence en maillage du nombre de Nusselt à la paroi chaude Nu_0. (a) variation temporelle de Nu_{0N} pour plusieurs maillages, (b) $Nu_{0N} - Nu_{0extrapole}$ en fonction de N.*

4.2 Transition à l'instationnaire

J'ai ensuite étudié la transition vers l'instationnaire des solutions, par simulation directe utilisant le code instationnaire non linéaire, et par une méthode de pseudo-linéarisation (collab. D. Barkley). Ces résultats ont été présentés au congrès I.C.C.H.M.T [69] ainsi qu'à un séminaire au CEA en 2005. La nature de la transition vers des états instationnaires dépend de la valeur du rapport de forme vertical, que nous avons fait varier entre $A = 1$ et $A = 10$. Les simulations directes sont effectuées sur un maillage 128x256 (pour certains cas 256x512).

Dans le cas où les propriétés physiques du fluide sont supposées indépendantes de la température, la transition vers l'instationnaire est une transition de Hopf, analogue au cas Boussinesq. Les fluctuations de température sont surtout importantes dans la couche limite montante, avec un nombre de Rayleigh critique inférieur à la situation en Boussinesq [74].

Dans le cas où les propriétés physiques du fluide sont données suivant la loi de Sutherland, La nature de la transition vers des états instationnaires dépend de la valeur du rapport de forme vertical.

Pour un rapport de forme supérieur à 5, la transition vers l'instationnaire est une transition de Hopf, analogue au cas Boussinesq. L'écoulement stationnaire est asymétrique et les solutions instationnaires le sont également (voir sur la figure 4.3a le champ de fluctuations de température pour $A = 6$, $Ra = 3.7\,10^5$), les fluctuations étant amplifiées dans la couche limite montante, et amorties dans la couche limite descendante. Il s'agit d'une instabilité de type «couche limite». On a retrouvé les résultats obtenus pour le rapport de forme 8 à partir d'un code spectral [32].

Pour des petites valeurs du rapport de forme, les solutions se déstabilisent également par une bifurcation de Hopf, mais la solution monopériodique finale est différente. Les fluctuations

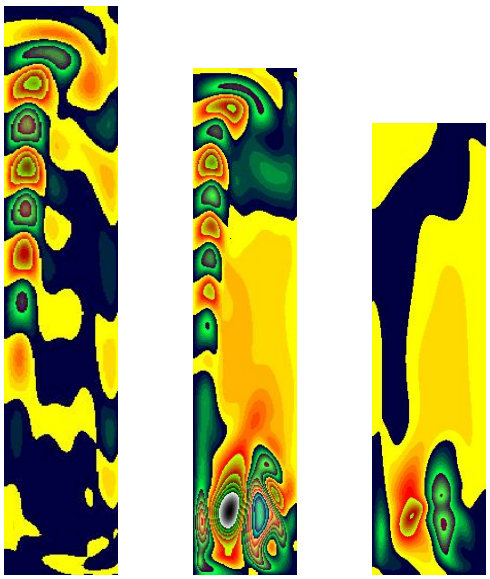

(a) (b) (c)

FIGURE 4.3 – $\varepsilon = 0.6$, *propriétés physiques suivant la loi de Sutherland, champ de fluctuation de température, pour différents rapports de forme (a)* $A = 6$, *(b)* $A = 5$, *(c)* $A = 4$.

ne sont plus concentrées dans les couches limites, mais remplissent plutôt le tiers inférieur de la cavité (voir sur la figure 4.3c le champ de fluctuations de température pour $A = 4$, $Ra = 4.3\,10^5$). Il s'agit d'une instabilité de type «ressaut hydraulique».

Pour une valeur intermédiaire du rapport de forme, la transition est sous-critique vers une solution doublement périodique. La composante haute fréquence correspond à l'instabilité de couche limite, la composante basse fréquence correspond à la solution fluctuante des cas à faible rapport de forme (voir sur la figure 4.3b le champ de fluctuations de température pour $A = 5$, $Ra = 5.5\,10^5$). Lorsque l'on diminue ensuite le nombre de Rayleigh, la solution redevient monopériodique avec la période longue, puis stationnaire.

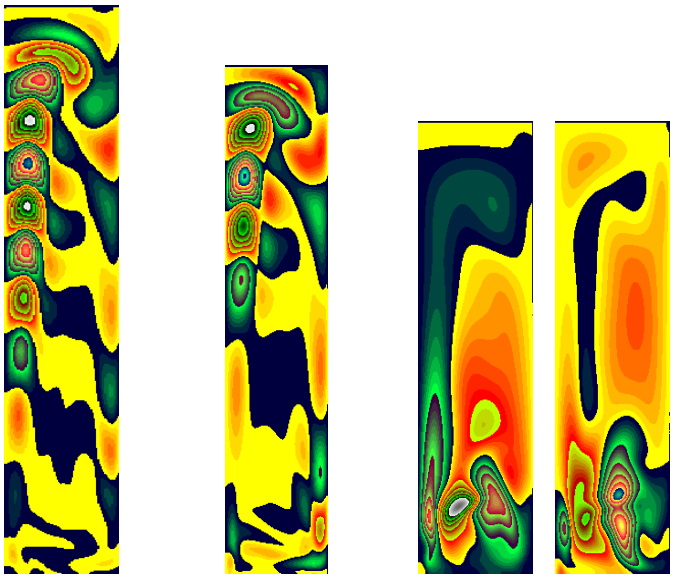

(a) (b) (c-a) (c-b)

FIGURE 4.4 – $\varepsilon = 0.6$, *Analyse de stabilité quasi-linéaire, solutions stables (température) - mode dominant, propriétés physiques Sutherland, Rapports de forme (a)* $A = 6$, *partie réelle (b)* $A = 5$, *partie réelle (c)* $A = 4$, *parties réelle (c-a) et imaginaire (c-b).*

Afin de compléter cette étude directe, nous avons développé une méthode de pseudo - linéarisation, qui nous permet de calculer les solutions linéarisées en utilisant uniquement le code initial non linéaire instationnaire. Une solution instationnaire notée U sert d'état de base (constituée des 2 composantes de vitesse, température, pression et masse volumique). La solution obtenue après N pas de temps du code instationnaire est notée U_1. On introduit une perturbation u de la solution U et, à partir de la solution $U + u$, on obtient une nouvelle solution instationnaire notée U_1' après le même nombre N de pas de temps. On calcule alors $u_1 = U_1' - U_1$ que l'on normalise pour que sa norme soit ϵ petit donné ($\epsilon = 10^{-3}$ par exemple pour s'approcher d'une analyse de stabilité linéaire). En pratique, pour construire la perturbation, on modifie le champ de température en un ou plusieurs points choisis au hasard. L'algorithme résumant la méthode est le suivant

$$
\begin{array}{ll}
(1) & U \rightarrow U_1 \text{ en } N \text{ pas de temps } \delta t \\
(2) & U + u \rightarrow U_1' \text{ en } N \text{ pas de temps } \delta t \\
\rightarrow & u_1 = U_1' - U_1 \\
(3) & u = \epsilon \dfrac{u_1}{\|u_1\|} \\
(4) & \text{retour à } (2)
\end{array}
$$

On associe ensuite cette pseudo-linéarisation avec une méthode de Arnoldi pour pouvoir calculer les modes propres dominants et les valeurs propres associées des états stationnaires ou instationnaires étudiés. Sur la figure 4.4 sont représentés les modes dominants des solutions stationnaires proches du seuil, obtenus avec 400 itérations de la méthode de Arnoldi, avec pour chaque itération $N = 50$, $\delta t = 0.01$ et $\epsilon = 10^{-3}$. On retrouve les caractéristiques des modes dominants obtenus par la simulation directe.

4.3 Conclusions

Cette étude purement numérique des écoulements de convection naturelle hors Boussinesq a permis d'établir des solutions de référence à travers un Benchmark numérique regroupant des numériciens des fluides issus de communautés diverses : codes compressibles, incompressibles, approche spectrale, codes industriels. Nous avons ensuite étudié la transition à l'instationnaire par une méthode paramétrique de suivi des solutions instationnaires, puis par une étude de pseudo-linéarisation. J'ai par la suite cessé de travailler sur ce problème, mais le savoir faire a été précieux pour la simulation numérique des machines thermoacoustiques.

Chapitre 5

Thermoacoustique : modélisation et simulation des phénomènes de pompage de chaleur et d'excitation

Après avoir pris connaissance des travaux de Worlikar et Knio [72, 73], je me suis intéressée aux applications des modèles faibles Mach pour la description du pompage de chaleur thermoacoustique. Après avoir adapté le code volumes finis bas Mach utilisé en convection Non-Boussinesq dans le cadre d'un stage de Master 1 en 2001 (R. Beraun), j'ai encadré un stage de Master 2 (L. Vodinh) et co-encadré la thèse de P. Duthil pour la partie numérique (thèse en cotutelle avec l'Université de Hong-Kong).

Nous avons ensuite (collab. D. Baltean-Carlès et L. Bauwens, Univ. Calgary) étudié l'effet moteur en thermoacoustique pour des configurations simplifiées d'un moteur à ondes stationnaires. Nous avons ainsi co-encadré deux thèses (O. Hireche et L. Ma).

5.1 Pompage de chaleur thermoacoustique

Dans cette étude, on s'intéresse au pompage de chaleur thermoacoustique le long d'un stack réfrigérant, sans échangeur de chaleur, inséré dans un tube résonant qui est le siège d'une onde acoustique stationnaire. Nous réalisons une simulation 2D de l'écoulement et de l'échange de chaleur à proximité et aux alentours de l'empilement en utilisant une approche similaire à celle de Worlikar et al. [72, 73]. L'amplitude des oscillations de pression dynamique reste très inférieure à la pression moyenne et la longueur du stack est petite devant la longueur d'onde, ce qui implique un nombre de Mach petit (de l'ordre de 10^{-3}). Nous utilisons alors une approximation faible Mach des équations de Navier-Stokes, selon le modèle développé par Paolucci en 1982 par filtrage des ondes sonores [43]. La propagation acoustique est ainsi ignorée alors que les effets de compressibilité sont préservés en termes de variations thermodynamiques en temps mais spatialement uniformes.

Le domaine de calcul est restreint à une tranche de stack comprenant deux demi-plaques en opposition. Sur les frontières supérieure et inférieure, on applique des conditions de symétrie. Sur les plaques on écrit l'adhérence du fluide. Des profils de vitesse oscillante $U_{left}(t)$ (resp. $U_{right}(t)$) sont appliqués à proximité de l'entrée (resp. de la sortie) du stack, les débit entrant et sortant étant différents (figure 5.1).

Pour l'entrée et la sortie, quand la vitesse imposée est entrante ($U_{left} \geq 0$ ou $U_{right} \leq 0$) on impose des températures données par la température du fluide oscillant (onde acoustique), et sinon, on impose des conditions adiabatiques.

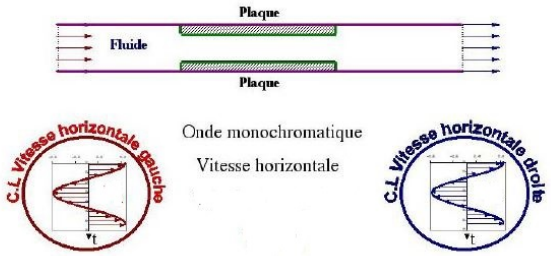

FIGURE 5.1 – *Domaine de calcul et profils de vitesses imposés en entrée/sortie.*

On note H la hauteur et L la longueur du domaine (avec $R_f = L/H$ le rapport de forme), ω la pulsation acoustique. La vitesse de référence est $U_{ref} = \omega H$, l'échelle de temps est $t_{ref} = \omega^{-1}$, la température $T_{ref} = T_{t=0}$, et la pression moyenne P_0. La masse volumique de référence est $\rho_0 = \rho(T_{ref})$. Les autres paramètres thermophysiques du gaz sont constants et égaux à leur valeur à la température T_{ref} : la vitesse du son c_0, la viscosité dynamique μ_0, la conductivité thermique k_0, les chaleurs massiques c_{p_0} et c_{v_0} (avec $\gamma = c_{p_0}/c_{v_0}$). On néglige l'effet de la gravité. On peut en déduire les paramètres sans dimension caractérisant le problème, nombre de Mach M, de Reynolds R_e, de Péclet P_e :

$$M = \frac{\omega H}{c_0}, R_e = \frac{\rho_0 \omega H^2}{\mu_0}, P_e = \frac{\rho_0 c_{p_0} \omega H^2}{k_0}, \tag{5.1}$$

Le développement de l'approximation faible Mach impose le partage de la pression totale en une pression moyenne $\overline{P}$, et une déviation notée π, avec $p = \overline{P} + M^2\pi + o(M^2)$. Les équations sans dimension dans l'approximation faible Mach s'écrivent alors

$$\frac{\partial \rho}{\partial t} + \nabla.\rho\mathbf{V} = 0, \tag{5.2}$$

$$\frac{\partial(\rho\mathbf{V})}{\partial t} + \nabla.(\rho\mathbf{V} \otimes \mathbf{V}) = -\nabla\pi + \frac{1}{R_e}\nabla.\tau, \tag{5.3}$$

$$[\frac{\partial T}{\partial t} + (\mathbf{V}.\nabla)T] = \frac{1}{P_e}\nabla.(k\nabla T) + \frac{\gamma - 1}{\gamma}\frac{d\overline{P}}{dt}, \tag{5.4}$$

$$\overline{P} = \rho T, \tag{5.5}$$

où $\tau = \mu[\nabla\mathbf{V} + (\nabla\mathbf{V})^t - \frac{2}{3}(\nabla.\mathbf{V})\mathbf{I}]$, $\overline{P}(t) = \frac{P_m(t)}{P_0}$ et $\pi = \frac{P(t) - P_m(t)}{\rho_0 U_{ref}^2}$. L'introduction de deux inconnues pour la pression nécessite une équation de fermeture, qui, en fonction des conditions limites du problème considéré, s'écrit :

$$\frac{d\overline{P}}{dt} = \frac{\gamma}{Rf}\overline{P}\left[U_{left}(t) - U_{right}(t) + \frac{1}{Pe}\int_S k\nabla T(t) \cdot \mathbf{n} dS\right] \tag{5.6}$$

où S est la frontière du domaine fluide, $\mathbf{n}$ la normale extérieure. Sur les plaques solides on résout l'équation de la chaleur :

$$\frac{\partial T}{\partial t} = \frac{1}{P_{es}}\nabla^2 T, \tag{5.7}$$

où $P_{es} = \rho_s c_{p_s} \omega H^2/k_s$ est le nombre de Péclet solide, l'indice "s" désignant le solide constituant les plaques. La continuité de la température et du flux de chaleur sont imposées de manière implicite aux interfaces solide-fluide.

Le code volumes finis de résolution des équations dans l'hypothèse faible nombre de Mach décrit dans le chapitre précédent a été adapté pour ce type de configuration. Les discrétisations spatiale et temporelle sont d'ordre 2.

Le code a été validé par confrontation aux expériences de Atchley [4] ainsi qu'aux résultats numériques de Worlikar et al [72, 73]. La figure 5.3 montre la superposition de ces résultats ainsi que les prédictions de la théorie linéaire pour différentes valeurs du Drive ratio Dr (rapport entre l'amplitude de pression acoustique et la pression moyenne). Les résultats (expérimentaux et numériques) divergent de la théorie linéaire pour $Dr = 2\%$

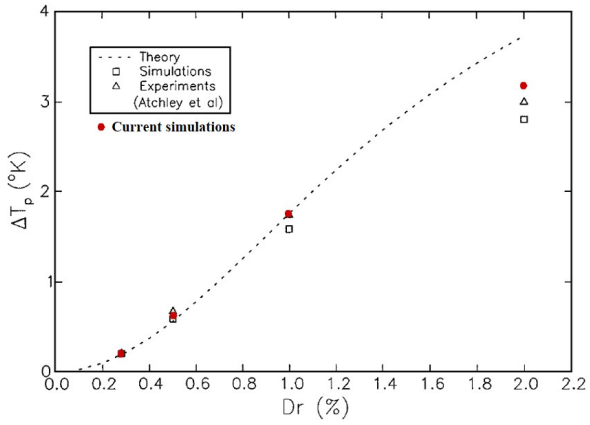

FIGURE 5.2 – *Superposition des résultats des simulations avec ceux de la théorie linéaire, des résultats publiés expérimentaux [4] et numériques [73] sur la figure extraite de [73].*

Le code a ensuite été testé [20] sur le dispositif expérimental du LIMSI qui couple deux systèmes thermoacoustiques dont l'un fonctionne en mode moteur et l'autre en mode pompage de chaleur (HDTAR, voir la figure 5.3). Ce système fonctionne sous une forte pression moyenne (11 bar). La particularité du système est un confinement important et une très grande constante de temps de diffusion thermique solide.

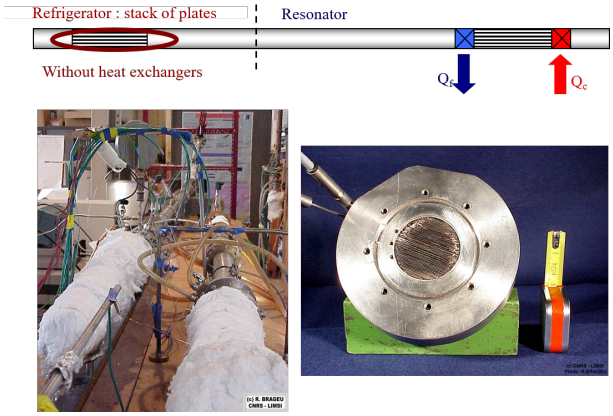

FIGURE 5.3 – *Dispositif HDTAR (LIMSI). En haut : schéma simplifié. Bas : dispositif expérimental (gauche) et détail du stack côté pompage de chaleur (droite).*

Les calculs ont montré une bonne concordance avec les mesures sur la différence de température $\Delta T_{num} = 11$ K et $\Delta T_{exp} = 9.4$ K, pour $Dr = 0.77\%$. Par contre le temps physique d'établissement de cette différence de température est complètement différent entre la simulation (36 s) et la mesure (700 s), ce qui peut s'expliquer par plusieurs considérations : dans la simulation l'onde est instantanément stabilisée (elle est imposée en conditions limites), alors que dans l'expérience, elle est générée par l'instabilité thermoacoustique et donc elle s'établit bien plus progressivement [20]. Il y a également beaucoup d'incertitudes au niveau de la mesure elle-même.

Sur les figures 5.4 et 5.5 sont représentées les évolutions temporelles sur une période acoustique en fin de simulation du champ de vitesse horizontale et de température sur le domaine de calcul. Le pompage de chaleur est établi et le gradient de température visible le long des plaques.

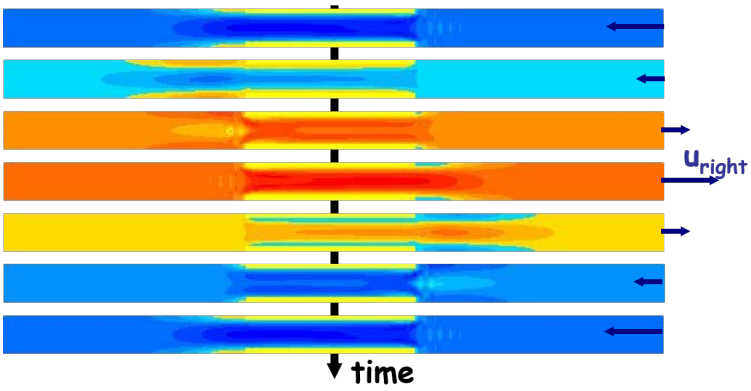

FIGURE 5.4 – *Evolution temporelle du champ de vitesse horizontale instantanée pendant une période acoustique.*

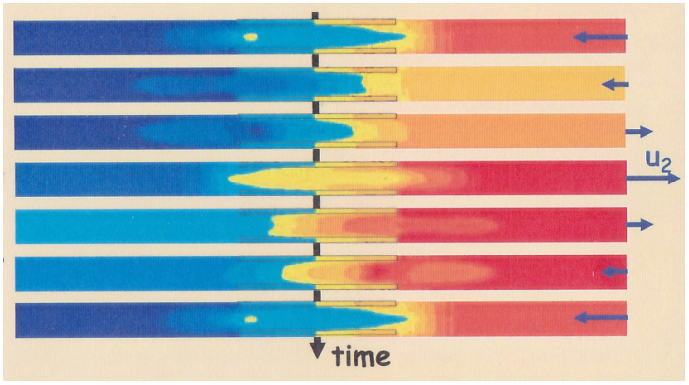

FIGURE 5.5 – *Evolution temporelle du champ de température instantané pendant une période acoustique.*

Malgré l'utilisation de l'approximation faible Mach plusieurs difficultés demeurent lors des simulations. La grande disparité des échelles temporelles (acoustique-thermique) mais aussi spatiales (espace inter-plaques, longueur du stack) implique l'utilisation d'un pas de temps petit ainsi qu'un maillage suffisamment fin pour décrire convenablement les plaques et les couches limites au sein desquelles s'effectue le processus de conversion thermoacoustique d'énergie.

5.2 Moteur thermoacoustique : couplage entre la cellule active et l'acoustique résonante

A partir de 2004, j'ai travaillé sur l'application d'un modèle faible nombre de Mach pour la description des écoulements et des transferts de chaleur dans un moteur thermoacoustique à onde stationnaire. C'est ainsi que j'ai commencé à travailler avec ma collègue D. Balteau-Carlès, collaboration qui s'est renforcée au cours des années, et qui perdure aujourd'hui. Un moteur thermoacoustique à onde stationnaire est constitué d'un résonateur droit au sein du duquel est inséré, en une position choisie proche d'une extrémité fermée, un milieu poreux (empilement de plaques ou assemblage de capillaires de sections variées) placé entre deux échangeurs

de chaleur. A l'autre extrémité est placée la charge du moteur, par exemple un réfrigérateur thermoacoustique (voir les figures 5.6 et 5.7).

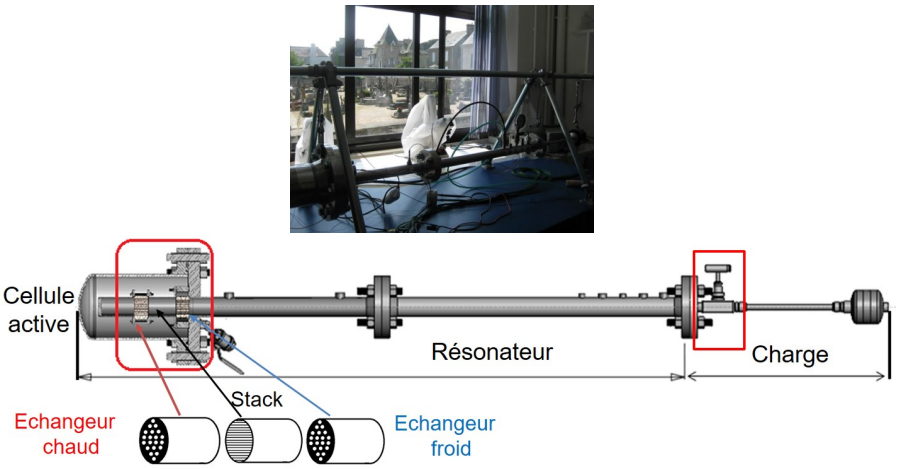

FIGURE 5.6 – *Photographie du démonstrateur de l'IPNO à l'école de Thermoacoustique, Roscoff 2007 et représentation schématique.*

Le fonctionnement typique d'un tel moteur est le suivant : par l'intermédiaire des échangeurs, on établit un gradient de température longitudinal le long du milieu poreux. Si ce gradient est suffisamment fort, toute perturbation sera amplifiée par effet thermoacoustique. Une onde acoustique s'établit alors dans le moteur, dont l'amplitude et la fréquence dépendent de la géométrie du système et des propriétés physiques des constituants. L'ensemble formé de l'empilement et des échangeurs de chaleur constitue ce qu'on appelle la cellule active. Un des problèmes

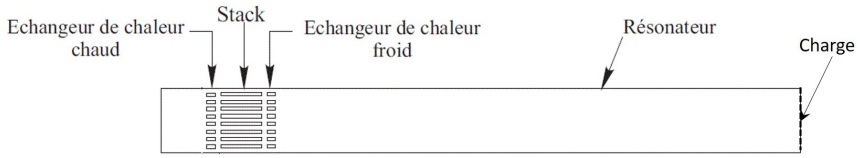

FIGURE 5.7 – *Schéma simplifié d'un moteur thermoacoustique.*

principaux liés à l'étude de ces systèmes est la grande disparité des échelles de temps (période acoustique de l'ordre de la milliseconde, temps de diffusion thermique en heure) et d'espace (longueur d'onde en mètre, longueur du stack en centimètres, épaisseur de couche limite inférieure au millimètre). Par exemple, sur un dispositif construit au LIMSI (décrit dans [29]), la période acoustique est de 7.5 ms, le temps caractéristique de diffusion thermique de 20 mn, la longueur du résonateur est de 7.57 m, celle du stack de 15 cm, l'espace inter-plaques de 0.97 mm.

Si la cellule active est courte devant la longueur d'onde, l'hypothèse faible nombre de Mach peut s'appliquer. Le phénomène de transfert de chaleur est initié au niveau du gaz situé dans les couches limites proches des parois solides du stack. Cependant, l'amplification de l'onde est un résultat global qui provient du couplage entre la cellule active et le résonateur.

Nous avons donc mené une analyse asymptotique (collab. L. Bauwens Univ. Calgary, P. Le Quéré) qui a permis de dégager les conditions de couplage entre l'écoulement dans le stack et le champ acoustique dans le résonateur. Cette étude et ses résultats ont fait l'objet de la thèse Algérienne de Omar Hireche que nous avons co-encadrée, et sont reportés pour grande partie dans [27] et dans l'article publié au JASA en 2010 figurant en annexe [29].

La pression de référence notée $\tilde{P}_{ref}$ est la pression moyenne du gaz au repos, la température est celle imposée à l'échangeur froid (souvent égale à la température ambiante) et notée $\tilde{T}_{ref}$ et la masse volumique par la valeur donnée par l'équation d'état au repos, $\tilde{\rho}_{ref} = \tilde{P}_{ref}/(R\tilde{T}_{ref})$.

Les longueurs de référence sont d'une part celle du stack $\tilde{L}_{stack}$, et d'autre part celle du résonateur $\tilde{L}_{res}$, qui est de l'ordre de grandeur de la longueur d'onde λ (dans un simple résonateur droit fermé aux deux extrémités le mode fondamental est tel que $\tilde{L}_{res} = \lambda/2$, on parle de résonateur à demi-longueur d'onde). L'hypothèse de stack court se traduit alors par $\tilde{L}_{stack} \ll \tilde{L}_{res}$. Une échelle de temps est donnée par $\tilde{t}_{ref} = \tilde{L}_{res}/\tilde{c}_{ref}$, où $\tilde{c}_{ref}$ est la vitesse du son de référence.

L'hypothèse principale de notre étude est le postulat que lorsque l'onde est amplifiée et que le moteur fonctionne en régime permanent, la longueur du stack est du même ordre de grandeur que le déplacement acoustique, et donc les vitesses sont d'ordre $\tilde{U}_{ref} = \tilde{L}_{stack}/\tilde{t}_{ref}$, ce qui donne donc un nombre de Mach de référence : $M = \tilde{U}_{ref}/\tilde{c}_{ref} = \tilde{L}_{stack}/\tilde{L}_{res} \ll 1$. On introduit alors les développements en fonction du nombre de Mach de toutes les variables adimensionnées, par exemple pour la pression : $p = p^{(0)} + Mp^{(1)} + M^2p^{(2)} + \mathcal{O}(\mathcal{M}^\ni)$.

On considère alors un modèle hybride constitué de deux domaines raccordés, avec chacun son système de coordonnées adimensionnées.

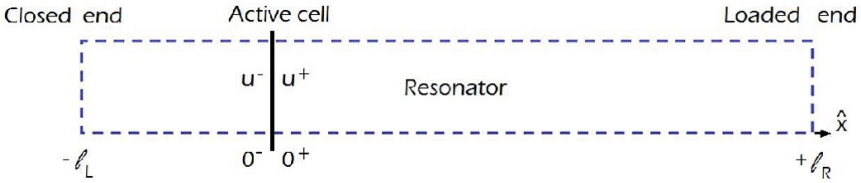

FIGURE 5.8 – *Géométrie du résonateur, coordonnée $\hat{x}$.*

Dans le résonateur pour laquelle la longueur de référence est $\tilde{L}_{res}$ et le problème unidimensionnel, la coordonnée est $\hat{x}$, centrée au centre du stack (figure 5.8). Elle varie entre $-l_L = -\tilde{l}_L/\tilde{L}_{res}$ et $l_R = \tilde{l}_R/\tilde{L}_{res}$ et le raccord avec la cellule active s'effectue en $\hat{x} \to 0$. Les équations développées à l'ordre dominant en nombre de Mach sont celles de l'acoustique linéaire, avec l'extrémité gauche fermée et une charge à droite notée f. Toutes les dissipations sont concentrées à l'extrémité chargée. Pour la partie gauche du résonateur, on suppose la température moyenne constante et homogène égale à la température chaude. Sur la partie droite, on suppose la température moyenne constante et homogène égale à la température froide. La vitesse du son adimensionnelle $\sqrt{T^{(0)}}$ est donc différente sur ces deux parties de résonateur. La solution s'exprime simplement par la méthode des caractéristiques (avec les variables de Riemann reliant u, $p^{(1)}$ et $T^{(0)}$ définies de façon classique). On peut alors relier les variables $(u, p^{(1)})$ au niveau de $\hat{x} = 0^+$ et $\hat{x} = 0^-$ à un instant t donné aux variables qui étaient relevées au même point en un instant antérieur correspondant à la propagation de l'onde jusqu'à l'extrémité et retour (voir un exemple sur la figure 5.9).

Dans la cellule active pour laquelle la longueur de référence est $\tilde{L}_{stack}$, les coordonnées sont (x, y), centrées au centre du stack, et le raccord avec le milieu extérieur s'effectue pour $x \to \pm\infty$ (figure 5.10). En prenant en compte la périodicité de l'empilement, et en supposant que les échangeurs sont eux aussi formés (chacun) d'un empilement de solides à température fixée, on se limite à un domaine constitué d'un seul espace interplaques (figure 5.10). Dans ce domaine, le développement à l'ordre dominant conduit à l'écriture des équations faible Mach comme dans les études précédentes, reliant la vitesse u, la pression moyenne $p^{(0)}$, la pression dynamique $p^{(2)}$, la masse volumique à l'ordre dominant $\rho^{(0)}$, la température $T^{(0)}$. La pression moyenne ne dépend que du temps $p^{(0)}(t)$. On modélise également chacun des échangeurs de chaleur par un empilement de plaques solides à température fixée, avec $T^{(0)} = T_h$ sur l'échangeur chaud et $T^{(0)} = T_c = 1$ en variables adimensionnées (en prenant pour référence la température froide).

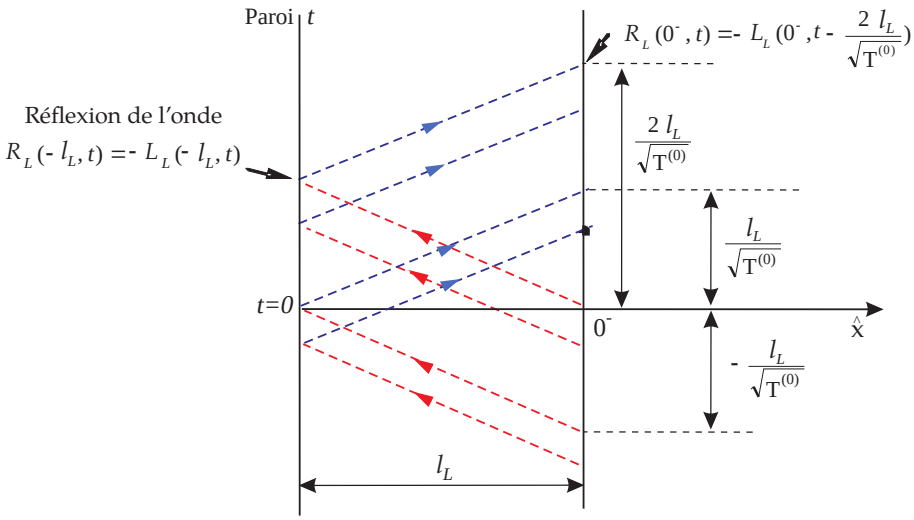

FIGURE 5.9 – *Evolution des variables de Riemann le long des caractéristiques en* $\hat{x} < 0$*, à gauche de la cellule active.*

Dans les plaques solides du stack, on résout l'équation de la chaleur. Aux interfaces solide-fluide, il y a adhérence du gaz et continuité de la température et du flux de chaleur.

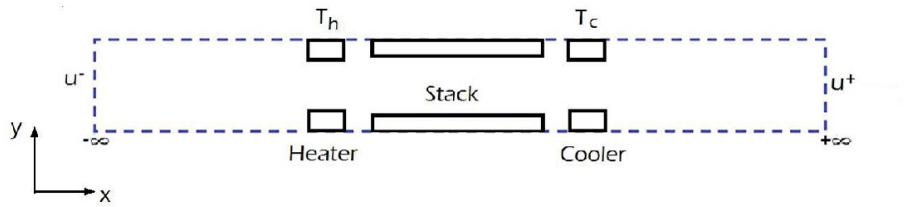

FIGURE 5.10 – *Géométrie d'une tranche de la cellule active, coordonnées* (x, y).

Le couplage est ensuite réalisé par raccord asymptotique entre les deux domaines. Le raccord sur la pression moyenne $p^{(0)}(t)$ implique que celle-ci est égale à la pression moyenne imposée dans le résonateur, et reste donc constante dans la cellule. Cela conduit à une simplification des équations faible Mach à l'intérieur de la cellule. Le raccord asymptotique permet d'égaler à chaque instant les vitesses en $x = \pm\infty$ et celles obtenues en $\hat{x} = 0^{\pm}$. On obtient donc à chaque instant une relation entre la différence des vitesses entre les deux extrémités de la cellule active et le transfert de chaleur dans la cellule active :

$$H[u(0^-) - u(0^+)] + \frac{1}{Pe}\int \nabla T^{(0)} \cdot \mathbf{n} ds = 0$$

La pression acoustique dans la cellule étant homogène pour tout x (elle ne dépend que du temps $p^{(1)}(t)$) est égale à celle écrite en $\hat{x} = 0$. Elle n'intervient pas explicitement dans les équations faible Mach écrites dans la cellule active. Cependant, elle intervient dans les variables de Riemann et donc dans le couplage. La cellule active est donc transparente à la pression acoustique, mais se comporte dans le résonateur comme une source ponctuelle de volume. La vitesse u est discontinue en $\hat{x} = 0$, ce qui engendre l'amplification de l'onde. Il ne s'agit donc pas d'analyser localement le phénomène thermoacoustique de conversion d'énergie, mais d'en simuler son effet global. On a également accès en chaque instant à tous les champs locaux au sein de la cellule active, et on peut donc analyser l'écoulement.

Nous avons ainsi simulé la phase de démarrage et de saturation d'un moteur thermoacoustique. Les simulations ont été effectuées sur deux configurations : tube fermé aux deux extré-

mités, et un tube fermé à une extrémité et muni d'une charge à l'autre. Cette charge, notée f est telle que $f = p^{(1)}/u$ en $\hat{x} = l_R$ (c'est une résistance, si on considère l'analogie électrique). Dans le premier cas, on montre qu'une ou plusieurs fréquences de résonance propre du tube peuvent être excitées. Dans la configuration avec charge, les résultats montrent à la fois la dynamique de l'instabilité thermoacoustique (démarrage du moteur) suivie de la saturation de l'onde, à une amplitude dépendant de la valeur de la charge f.

L'approche utilisée est un bon exemple d'utilisation des modèles à échelles multiples, qui permet de concentrer l'effort de calcul là où il est nécessaire. Toutefois, même avec ce type de traitement les calculs restent longs et coûteux.

5.3 Instabilité thermoacoustique, influence de la charge sur le fonctionnement d'un moteur thermoacoustique

Nous avons poursuivi l'exploitation du modèle hybride pour l'analyse des conditions de démarrage d'un moteur thermoacoustique chargé (stage M2 K. Sodjavi, stage M2 et thèse L. Ma). Une partie des résultats obtenus figure dans l'article [35] reporté en annexe.

On considère ici un moteur chargé (charge f réelle, comprise entre 0 et $+\infty$), et on introduit le coefficient réel $Z = \frac{\gamma - f}{\gamma + f}$ compris entre -1 et 1. Pour les valeurs limites $Z = -1$ (extrémité fermée) ou $+1$ (ouverte) l'onde est purement stationnaire, et pour $Z = 0$ elle est purement progressive de la cellule active vers l'extrémité droite du résonateur. Entre ces deux cas limites, l'onde n'est ni stationnaire ni progressive, mais une combinaison de deux ondes se déplaçant dans les directions opposées avec des amplitudes différentes. On peut aussi interpréter ce que représente la charge f à l'aide du standing wave ratio, qui ici correspond à $SWR = f/\gamma$ et varie entre 0 et 1.

Le démarrage d'un tel moteur résulte d'une instabilité thermoacoustique, qui se déclenche lorsque la différence de température imposée entre les échangeurs chaud et froid atteint une valeur critique.

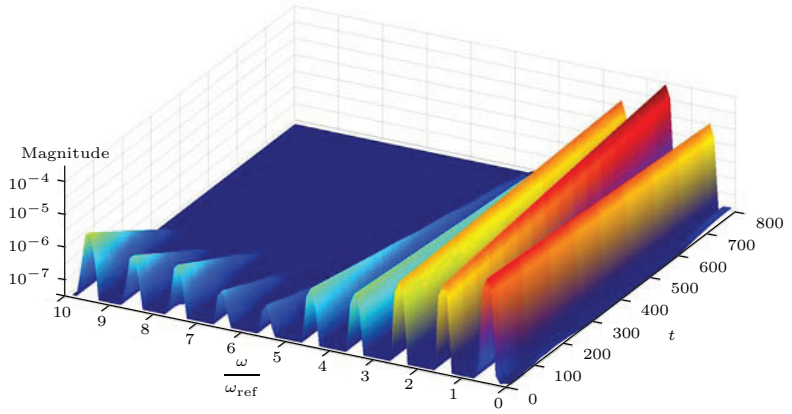

FIGURE 5.11 – *Spectrogramme d'un signal temporel de pression. l'amplitude représentée est la racine carrée de la densité spectrale de puissance.*

Pour déterminer ce seuil à partir des simulations numériques, on analyse le signal de pression acoustique au niveau de la cellule active pour en extraire les modes propres et les taux de croissance. Par exemple, la figure 5.11 montre le spectrogramme associé à une simulation, pour une configuration donnée et pour des valeurs choisies de la charge Z et de la température chaude adimensionnée T_h.

En représentant le taux de croissance du mode le plus instable en fonction du rapport des températures, on obtient la valeur critique pour la configuration étudiée. Ensuite, on peut tracer un diagramme de stabilité dans le plan (Z, T_h), qui montre la zone instable (fig.5.12a) et les fréquences angulaires du mode le plus instable en fonction de la charge (fig.5.12b). Les fréquences sont adimensionnées par une fréquence de référence correspondant au premier mode de résonance du tube fermé aux deux extrémités (sans cellule active) rempli de gaz aux conditions de référence (tube froid). Ces diagrammes permettent de prévoir les conditions de démarrage d'un moteur dans une configuration de la cellule active donnée (ici il s'agit du dispositif construit au LIMSI [29]). Noter que dès que les valeurs de Z s'éloignent des cas limites ± 1, il faut des rapports de température très importants pour déstabiliser le système et démarrer le moteur. Cela signifie que la configuration géométrique de cet exemple pratique n'est pas adaptée à un fonctionnement en onde progressive (en particulier en raison des dimensions du stack). On a également fait varier dans les simulations la position de la cellule active dans le tube.

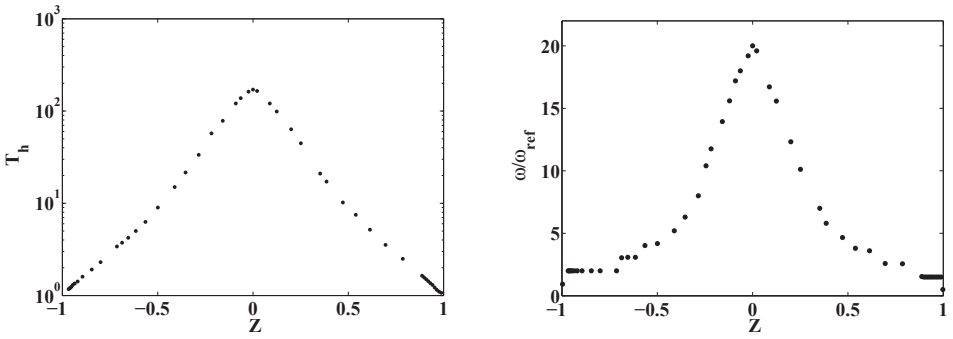

(a) (b)

FIGURE 5.12 – *Exemple sur configuration d'un prototype du LIMSI [29] (a) Diagramme de stabilité dans le plan (Z, T_h). La région au-dessus de la courbe est instable. (b) Fréquence angulaire du mode le plus instable adimensionnée par ω_{ref}, en fonction de Z.*

On a également comparé ces résultats avec ceux obtenus par la théorie linéaire que nous avons adaptée à la géométrie étudiée : on impose à gauche de la cellule active la solution des équations de l'acoustique 1D linéaire isentropique avec une température moyenne homogène chaude (ce qui fixe la vitesse du son). A droite de la cellule, on procède de même en imposant une température moyenne homogène froide. Les équations dans la zone du stack sont écrites en suivant l'approche de Rott (hypothèse de couche limite, intégration sur la hauteur de l'empilement du stack, hypothèse de stack acoustiquement compact [56, 58]), et on obtient une équation 1D (Eq. 5 de [35] figurant en annexe, rapportée également dans [65] p.90, Eq 4.70), faisant intervenir les facteurs de forme $\tilde{f}_\kappa$ et $\tilde{f}_\nu$. Après raccord avec l'acoustique, on obtient une équation de dispersion que l'on résout numériquement par une méthode de tir. Une comparaison entre les résultats obtenus à partir du modèle hybride et la théorie linéaire montre que les résultats sont très proches (voir figure 11 de [35] figurant en annexe), à la fois sur les températures critiques et la fréquence acoustique dominante.

Les résultats numériques sur le démarrage de l'onde ont également été comparés avec ceux d'expériences rapportés dans la littérature [5], réalisées dans un moteur simplifié fermé aux deux extrémités, sous différentes conditions de pression moyenne. Il n'y a donc pas de charge à proprement parler, mais une dissipation visqueuse et thermique tout le long des parois du résonateur. On a calculé avec le modèle hybride la valeur de la charge f à imposer en extrémité de résonateur pour obtenir les mêmes seuils critiques que dans l'expérience. On a ensuite comparé les valeurs de charge (dimensionnée) avec une estimation de la résistance du gaz, et conclu que les valeurs étaient du même ordre de grandeur [35].

On a mené avec le modèle hybride un certain nombre de calculs jusqu'à l'obtention du régime périodique de fonctionnement. La saturation est liée aux dissipations à l'intérieur de la cellule active. Cette approche a permis de mener une petite étude paramétrique, relativement limitée par la durée des calculs. Pour l'initiation du calcul on a imposé 200 pas de temps par période acoustique de référence. Avec l'augmentation de l'amplitude de la vitesse, ce nombre est augmenté jusqu'à 2000 pas de temps par période pour assurer la condition CFL (simulations avec un code vectoriel, machine INTEL XEON). Il faut environ 100 heures de calcul pour obtenir la saturation (maillage régulier 2048×32). Si l'on choisit le maillage régulier 4096×64, il faut environ 360 heures de calcul pour atteindre la saturation du moteur. Un exemple de résultat est représenté sur la figure 5.13 en variables physiques dans le cas de configuration d'un dispositif construit au LIMSI (décrit dans [29]), pour une charge fixée ($Z = -0.96$, $\tilde{T}_h = 352$ K, $\tilde{T}_c = 293$ K). Le Drive ratio obtenu est moyen ($Dr = 3.2\%$). La figure 5.13a montre la

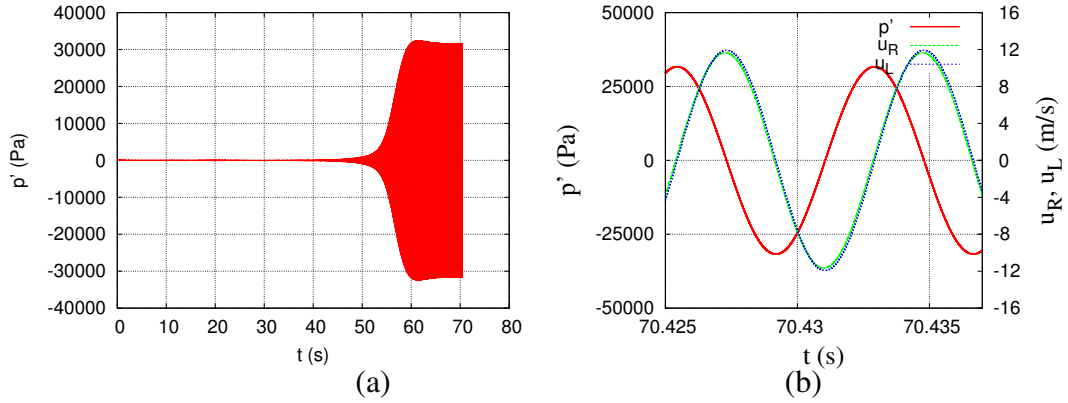

FIGURE 5.13 – *Exemple de résultat : (a) Variation temporelle de la pression acoustique $\tilde{p}'$ au niveau de la cellule active. (b) Zoom sur le signal temporel à la fin du calcul montrant $\tilde{p}'$ au niveau de la cellule active et les vitesses acoustiques à gauche et à droite de la cellule $\tilde{u}_L$, $\tilde{u}_R$.*

variation de pression acoustique au niveau de la cellule active sur la totalité de la simulation. La figure 5.13b montre un zoom sur la pression acoustique et les vitesses longitudinales à gauche et à droite de la cellule active à la fin du calcul (en grandeurs dimensionnées). Le déphasage entre $\tilde{p}'$ et $\tilde{u}_L$ (ou $\tilde{u}_R$) est très proche de $\pi/2$. Une FFT du signal donne la fréquence acoustique finale (133.3 Hz), qui correspond à peu près au 1er harmonique du tube fermé (la fréquence du mode fondamental est 66.7 Hz).

Le transitoire présente une bosse, ou "overshoot". Ce phénomène peut être rapproché des observations expérimentales lors du démarrage d'un moteur thermoacoustique (lorsque l'onde démarre, toutes les températures baissent, et un overshoot est observé dans le signal de pression). Il est généralement interprété comme étant lié au pompage de chaleur thermoacoustique. Ici, la bosse "overshoot" obtenue semble plutôt liée au décalage entre la fréquence de fonctionnement et la fondamentale (phénomène de battement). Les températures des échangeurs sont maintenues constantes tout au long du calcul. Cependant il aurait été intéressant d'enregistrer et de suivre des grandeurs moyennes (par exemple celle du champ de température) sur la période acoustique au cours du transitoire. Cela aurait permis d'analyser ce transitoire et d'interpréter aussi le mécanisme de saturation. Une des difficultés de ce suivi est l'évolution de la période acoustique au cours du calcul.

L'analyse du régime périodique est plus simple car la période est stabilisée. On peut utiliser les résultats numériques pour calculer la puissance acoustique disponible en sortie de cellule

active, et la puissance thermique $\tilde{Q}_h$ apportée à l'échangeur chaud :

$$\tilde{P}_{ac} = \frac{\tilde{S}}{\tilde{t}_{ac}} \int_{\tilde{t}_{ac}} \tilde{p}'(\tilde{t}) \tilde{u}_R(\tilde{t}) d\tilde{t} \qquad \tilde{Q}_h = -\frac{1}{\tilde{t}_{ac}} \int_{\tilde{t}_{ac}} \int_{\tilde{S}_h} \tilde{\lambda} \frac{\partial \tilde{T}}{\partial n} d\tilde{S} d\tilde{t} \tag{5.8}$$

avec $\tilde{S}$ la section totale du résonateur, $\tilde{S}_h$ la surface totale de l'échangeur chaud, $\vec{n}$ le vecteur normal extérieur au solide, $\tilde{t}_{ac}$ la période acoustique, $\tilde{u}_R$ la vitesse longitudinale et $\tilde{p}'$ la pression acoustique au niveau de la cellule active. Le rendement $\eta = \frac{\tilde{P}_{ac}}{\tilde{Q}_h}$ peut être calculé et comparé avec le rendement de Carnot. Le bilan énergétique pour l'exemple choisi est présenté dans le tableau ci dessous.

Dr	$\tilde{P}_{ac}$	$\tilde{Q}_h$	η	η/η_C
%	(W)	(W)	(%)	(%)
3.2	66.5	3910	1.70	10.1

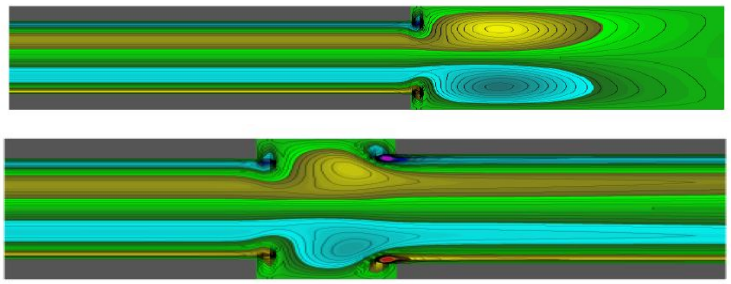

FIGURE 5.14 – *Exemple de champ de vorticité instantanée à la sortie de l'échangeur froid (haut) et entre le stack et l'échangeur chaud (bas).*

On a également analysé la dynamique tourbillonnaire en sortie d'échangeur et dans les espaces échangeur/stack (voir un exemple fig. 5.14). A petit Dr, ces dynamiques sont très régulières, alors qu'à grand Dr, des instabilités sont susceptibles de se déclencher : dans la couche limite et à la sortie des échangeurs où l'on s'attend à des tourbillons alternés de von Kármán. Ces tourbillons n'ont pas été observés dans les simulations à cause des conditions de symétrie imposées numériquement. Il aurait fallu positionner la plaque au milieu du domaine de simulation.

Nous aurions souhaité mener plus d'études à partir du modèle. En particulier la modélisation des échangeurs est délicate. Il serait plus approprié de fixer une quantité de chaleur apportée à l'échangeur chaud et retirée sur l'échangeur froid plutôt que de fixer les températures. Le problème des études paramétriques vient du fait que les calculs, même s'ils sont moins coûteux qu'en écoulement compressible, restent longs. Nous disposons actuellement d'une version parallélisée du code, que nous n'avions pas en 2014, et il serait intéressant de mener d'autres simulations avec notamment un suivi des grandeurs moyennées sur la période acoustique.

5.4 Etude de thermophones

Notre rencontre avec Jacques Rémus ([53] Société Ipotam Mécamusique) date de 2010 à l'école de Thermoacoustique. Nous avons renoué le contact par la suite, et obtenu le financement d'un projet Art&Sciences. Le projet intitulé « Thermophonia », consistait à étudier les thermophones créés par J. Rémus, instruments de musique particuliers où le son est produit par

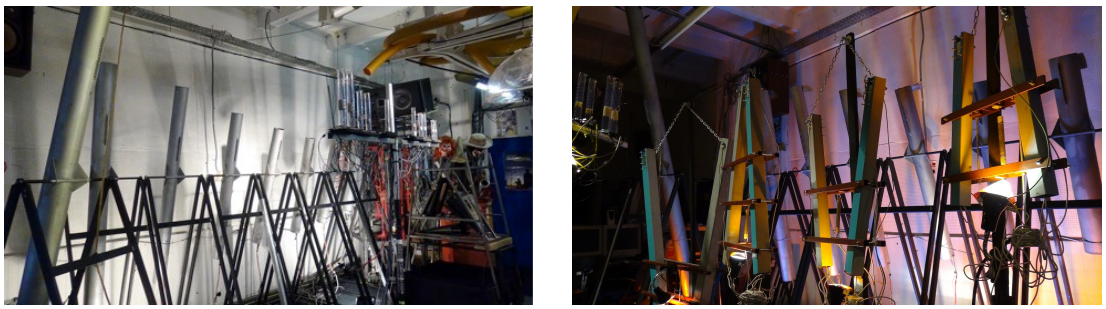

FIGURE 5.15 – *Thermophones illuminés dans l'atelier de J. Rémus (Les Frigos, Paris).*

effet thermoacoustique. Cette étude a fait l'objet d'un stage de Master 1, d'une présentation au CFA en 2016 [67], et de plusieurs représentations artistiques (figure 5.15).

Un thermophone est constitué d'un tube en acier doux, verre ou aluminium, de section circulaire ou rectangulaire, à l'intérieur duquel est positionné judicieusement un « stack » formant un milieu poreux, dont l'une des extrémités est chauffée à l'aide d'une résistance électrique. Lorsque la température de l'extrémité chauffée devient suffisamment élevée, le thermophone se met à chanter. Un thermophone s'apparente donc à un moteur thermoacoustique de type ondes stationnaires, où le gaz utilisé est de l'air atmosphérique. Le résonateur, ouvert au moins à l'une de ses extrémités pour rendre le son audible, est dépourvu d'échangeur froid permettant de maintenir un gradient de température constant dans le stack. Le démarrage du son est le résultat d'une instabilité thermoacoustique. La théorie linéaire de Rott [56, 58] a été adaptée pour prendre en compte les particularités du thermophone. L'équation de dispersion a été résolue numériquement pour une variété de thermophones existants. Les températures de déclenchement de l'instabilité ont été déterminées ainsi que la fréquence du son produit par le thermophone, en assez bon accord avec les mesures.

5.5 Conclusions

Une simulation fine complète des machines thermoacoustiques, prenant en compte les effets multi-dimensionnels et nonlinéaires est actuellement irréalisable et l'utilisation de modèles simplifiés est donc incontournable. L'approximation faible Mach permet de s'affranchir localement de la propagation acoustique en considérant la cellule active d'un système thermoacoustique comme acoustiquement compacte. Une analyse dimensionnelle a permis de dégager les conditions d'application de cette approximation (cellule active courte par rapport à la longueur d'onde). En tout cas, ce type de modèle ne permet de capturer qu'une partie des phénomènes.

Nous avons montré que ce modèle permet de simuler le pompage de chaleur le long d'un empilement de plaques. Nous avons également développé un modèle hybride où la cellule compacte est couplée au résonateur, ce qui permet de simuler l'effet moteur. Nous avons ainsi étudié les écoulements et transferts de chaleur à l'intérieur de la cellule active pendant l'établissement de l'onde. Nous avons simulé le démarrage du moteur et sa saturation dans plusieurs situations. Cependant, malgré l'utilisation de l'approximation faible Mach, les simulations restent longues et peu adaptées aux études paramétriques et prédictives. On envisage par contre d'utiliser l'approximation faible Mach dans des prototypes où les longueurs caractéristiques du système sont effectivement petites devant la longueur d'onde (en particulier sur le prototype compact construit dans le cadre de l'ANR TACOT).

Chapitre 6

Streaming acoustique en guide d'onde

Le vent acoustique (appelé aussi streaming ou écoulement redressé) est un écoulement stationnaire du second ordre en nombre de Mach qui s'établit suite à l'interaction entre une onde acoustique et des parois solides. Cet écoulement peut être notamment très pénalisant dans les machines thermoacoustiques, car il peut transporter de la chaleur et modifier ainsi la distribution de température, aussi bien dans un générateur d'onde que dans un réfrigérateur. Il s'agit d'un effet non linéaire qui n'est pas pris en compte dans la théorie linéaire de Rott (et donc pas dans les codes 1D de type DeltaEC).

Trois types d'écoulements de streaming sont distingués dans la littérature : streaming de Rayleigh [51] dans les résonateurs à ondes stationnaires, streaming de Gedeon dans les résonateurs annulaires à ondes progressives [6], streaming d'Eckart [21] (dû à l'absorption par un volume fluide d'un faisceau acoustique ultrasons, encore appelé Quartz wind dans l'air). Notre étude concerne uniquement l'écoulement de streaming de type Rayleigh, lié au frottement visqueux sur les parois d'un résonateur.

Nous avons commencé à travailler sur le streaming acoustique, Virginie Daru, Diana Balteau-Carlès et moi-même en 2009, à partir de simulations numériques des équations de Navier-Stokes compressibles. Lors d'une présentation des résultats numériques aux membres du GDR Thermoacoustique en 2011, nous avons assisté à la présentation de Ida Reyt qui effectuait une thèse expérimentale sur le même sujet, sous la direction de Hélène Bailliet (institut P'). Les résultats sur le streaming à fort niveau coïncidant de façon étonnante, nous avons alors décidé de poursuivre cette étude de façon conjointe. Nous avons lié avec Hélène Bailliet une amitié durable et cette collaboration perdure. Nous avons publié 4 articles ensemble sur ce sujet (et un soumis). Sur ce problème difficile à simuler, à mesurer et à modéliser, notre approche a été à la fois numérique, expérimentale et théorique, avec de multiples allers-retours stratégiques.

Les simulations numériques directes étant irréalisables sur les configurations (même simplifiées) calées sur les expériences, on a travaillé sur des résonateurs de longueur et fréquence très différentes : dans les expériences réalisées à l'institut P', la demi-longueur d'onde est d'environ 0.7 m, soit une fréquence de 240 Hz. Dans les simulations numériques, la demi-longueur d'onde est d'environ 8 mm, soit une fréquence de 20000 Hz. Nous avons donc été très vite questionné les critères de similitude entre nos configurations. Par ailleurs, pour étudier l'écoulement de streaming généré à fort niveau acoustique, nous avons été amenées à reconsidérer l'écoulement généré à faible niveau.

Dans la présentation qui suit, j'ai regroupé les différents résultats que nous avons obtenus sur le streaming à faible et à fort niveau acoustique dans un ordre non-chronologique.

6.1 Streaming de Rayleigh à faible niveau acoustique

On s'intéresse à l'écoulement de streaming se produisant soit dans un canal plan entre deux plaques parallèles (de hauteur $2R$ et longueur L), soit dans un résonateur cylindrique de section circulaire (de rayon R et longueur L), lorsque le résonateur est le siège d'une onde acoustique plane dans la direction axiale, avec $R \ll L$. On se place dans des conditions de résonance telles que $L = \lambda/2$. La gravité est négligée et on suppose donc la symétrie axiale des écoulements.

A bas niveau acoustique, l'écoulement de streaming qui s'établit est bien connu et décrit par la théorie classique dite de Rayleigh-Nyborg-Westervelt, résumée dans [34]. Une schématisation de cet écoulement est présentée sur la figure 6.1. Lord Rayleigh [51] a établi les équations de l'écoulement généré dans la partie centrale du résonateur, loin des parois (streaming extérieur) pour des tubes larges : on parle de tube large lorsque le rayon R est grand devant l'épaisseur de couche limite visqueuse définie par $\delta_\nu = \sqrt{2\nu/\omega}$, où ν est la viscosité cinématique du gaz et ω la pulsation. Les équations sont obtenues par approximations successives en termes de puissances du nombre de Mach acoustique (défini par $M = U_{ac}/c_0$, avec U_{ac} l'amplitude de vitesse acoustique au ventre de vitesse acoustique et c_0 la vitesse du son), et correspondent au cas où le streaming est lent. Ce sont des équations linéaires, où les termes sources proviennent de la solution du problème d'ordre 1 (acoustique linéaire) supposée incompressible dans la couche limite.

En géométrie plane, les composantes axiale $\bar{u}_{Rayleigh}$ et transverse $\bar{v}_{Rayleigh}$ de la vitesse de streaming sont alors données par :

$$\bar{u}_{Rayleigh} = -\frac{3U_{ac}^2}{16c_0} \sin(2\mathbf{k}x) \left[1 - 3\left(\frac{y}{R}\right)^2\right], \tag{6.1}$$

$$\bar{v}_{Rayleigh} = +\frac{3U_{ac}^2}{8c_0} \mathbf{k}R \cos(2\mathbf{k}x) \left[\frac{y}{R} - \left(\frac{y}{R}\right)^3\right] \tag{6.2}$$

où $\mathbf{k}$ est le nombre d'onde, x la coordonnée axiale, y la distance à l'axe. Les tourbillons associés s'étendent sur un quart de longueur d'onde.

En géométrie cylindrique, en notant r la coordonnée radiale, les composantes axiale et radiale de la vitesse de streaming sont données par [62] :

$$\bar{u}_{Rayleigh} = -\frac{3U_{ac}^2}{8c_0} \sin(2\mathbf{k}x) \left[1 - 2\left(\frac{r}{R}\right)^2\right], \tag{6.3}$$

$$\bar{v}_{Rayleigh} = +\frac{3U_{ac}^2}{8c_0} \mathbf{k}R \cos(2\mathbf{k}x) \left[\frac{r}{R} - \left(\frac{r}{R}\right)^3\right], \tag{6.4}$$

Les termes en $e^{-(R-y)/\delta_\nu}$ ont été négligés dans les expressions ci-dessus. Les vitesses obtenues sont d'ordre M^2. Westervelt [71] et Nyborg [39] ont amélioré cette solution analytique pour s'affranchir de l'hypothèse de divergence nulle de la vitesse acoustique.

Schlichting [61] a été le premier à décrire les tourbillons proches de la paroi (streaming intérieur ou streaming de Schlichting), qui tournent dans le sens opposé (figure 6.1), sous l'hypothèse d'écoulement incompressible. Par la suite, Qi [49] a amélioré cette description en incluant la compressibilité du fluide et les effets thermiques. C'est ensuite Rott [57] qui a intégré la prise en compte des effets thermiques. Enfin, des modèles semi-analytiques adaptés pour les applications thermoacoustiques ont été développés [8, 28]. Nous avons utilisé le calcul formel (Mathematica) pour analyser plus en détail le streaming de Rayleigh à faible niveau acoustique (écoulement isentropique dans [9], et avec prise en compte des effets thermiques dans [19]). La démarche se décompose en deux étapes :

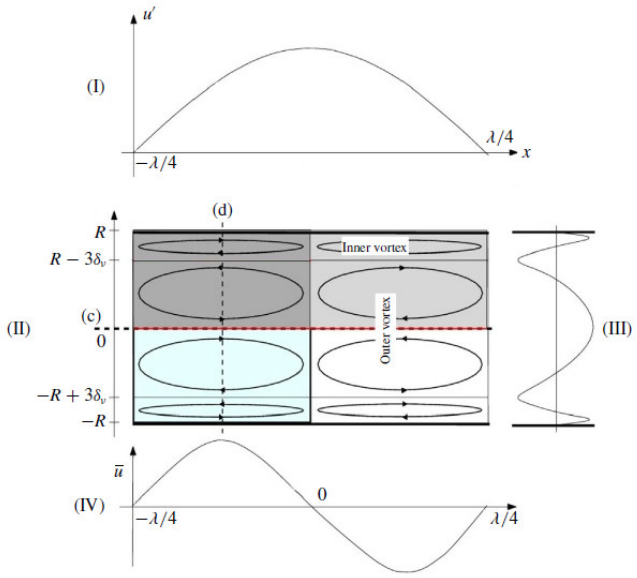

FIGURE 6.1 – *Représentation schématique à bas niveau (théorie RNW), montrant (II) les cellules de streaming (intérieur et extérieur). Les profils de vitesse axiale indiqués sont : (I) vitesse acoustique, (IV) vitesse de streaming le long de l'axe (c), (III) vitesse de streaming le long de (d), d'après [9].*

- On résout d'abord les équations de l'acoustique linéarisée, ce qui donne les composantes de la vitesse acoustique (u', v', p', ρ').
- Ensuite, on décompose chaque variable f en une composante f' fluctuante, périodique en temps, et une moyenne $\overline{f}$ sur la période acoustique (correspondant à l'écoulement de streaming) avec $f = \overline{f} + f'$. Pour calculer la moyenne du produit de deux variables f et g, on applique la relation $\overline{fg} = \overline{f}\,\overline{g} + \overline{f'g'}$.
A partir des équations de Navier-Stokes compressibles moyennées sur une période acoustique, on obtient celles de l'écoulement de streaming en fonction des contraintes de Reynolds (moyennes des produits des grandeurs acoustiques).

En tenant compte de la linéarité du problème à faible niveau acoustique, on peut alors analyser séparément l'effet des différents termes sources [9], puis superposer les solutions. On a ainsi montré, avec la contribution des deux termes sources habituellement dominants, que l'écoulement de streaming est bien initié par les effets visqueux dans la couche limite. Le streaming extérieur est généré par la diffusion de quantité de mouvement vers le centre du guide, et n'est pas dû à des effets de gradient de pression. Cet écoulement peut être considéré comme un écoulement en cavité entraînée (l'analogie a été développée dans [17]). On a quantifié la relation entre la composante axiale de la vitesse de streaming sur l'axe (normalisée par la solution de Rayleigh) et le rapport R/δ_ν. L'effet d'un terme source habituellement négligé a été analysé. On a montré qu'il pouvait devenir important pour des valeurs intermédiaires du rapport R/L (tout en gardant $R/L < 1$), et pouvait générer un écoulement de streaming extérieur en sens inverse de celui de la théorie RNW.

Nous avons suivi une démarche similaire pour étudier l'influence des effets thermiques sur l'écoulement de streaming dans un article soumis [19]. On a ainsi mis en évidence que la présence d'un gradient de température transverse par rapport à la direction de l'onde génère des modifications très importantes de l'écoulement de streaming, pouvant également conduire à une inversion de sens de l'écoulement extérieur.

6.2 Streaming à fort niveau acoustique : simulations numériques directes et comparaisons avec l'expérience

Pour des niveaux acoustiques supérieurs, les travaux théoriques de [37] ont montré que les effets inertiels sur l'écoulement de streaming peuvent être différenciés selon la valeur du nombre de Reynolds non-linéaire défini par $Re_{NL} = (M \times R/\delta_\nu)^2$. Ils ont mis en évidence une distorsion des tourbillons extérieurs due à l'inertie pour $Re_{NL} > 1$, alors que les tourbillons intérieurs ne sont pas modifiés. Cependant cette étude est limitée aux valeurs modérées de Re_{NL} (jusqu'à $Re_{NL} = 6$), et suppose l'écoulement isentropique.

6.2.1 Simulations numériques

Les simulations numériques directes ont été réalisées grâce aux codes de résolution des équations de Navier-Stokes compressibles écrits par Virginie Daru. Les calculs sont réalisés sur un domaine rectangulaire plan de longueur L et de hauteur R, représentant soit la demi-section haute d'un canal vertical, soit la section d'un résonateur cylindrique axisymétrique [15, 54]. Le domaine renferme de l'air initialement au repos. Dans les deux cas, la frontière basse représente l'axe de symétrie, et la haute est une paroi solide. Aux frontières gauche et droite on impose soit une adhérence aux parois [15], soit des conditions de symétrie (composante axiale de vitesse nulle et dérivée normale de la composante transverse nulle) [54]. Dans ces deux articles, la paroi et les frontières gauche et droites sont isothermes.

On impose une onde dans la direction longitudinale en secouant l'ensemble du domaine à la fréquence de résonance du tube fermé. On se place dans le repère lié au tube, et dans les équations de Navier-Stokes compressibles on introduit un terme source pour rendre compte du secouage : $\mathbf{V}(t) = (V(t), 0)^T$, où $V(t) = x_p\omega\cos(\omega t)$. Pour varier le niveau acoustique il suffit donc de modifier l'amplitude x_p. Les équations à résoudre sont :

$$\left\{\begin{array}{lcl} \dfrac{\partial \rho}{\partial t} + \nabla\cdot(\rho\mathbf{v}) & = & 0 \\ \dfrac{\partial \rho\mathbf{v}}{\partial t} + \nabla\cdot(\rho\mathbf{v}\otimes\mathbf{v}) + \nabla p & = & \nabla\cdot(\bar{\bar{\tau}}) - \rho\dfrac{d\mathbf{V}}{dt} \\ \dfrac{\partial \rho E}{\partial t} + \nabla\cdot(\rho E\mathbf{v} + p\mathbf{v}) & = & \nabla\cdot(k\nabla T) + \nabla\cdot(\bar{\bar{\tau}}\mathbf{v}) - \rho\mathbf{v}\cdot\dfrac{d\mathbf{V}}{dt} \end{array}\right. \tag{6.5}$$

avec $\mathbf{v}$ le champ de vitesse, p la pression, ρ la masse volumique, $E = e + \frac{1}{2}\mathbf{v}\cdot\mathbf{v}$ l'énergie totale, $e = \frac{p}{(\gamma-1)\rho}$ l'énergie interne, γ le rapport des chaleurs massiques, $\bar{\bar{\tau}} = -\frac{2}{3}\mu(\nabla\cdot\mathbf{v})\bar{\bar{I}} + 2\mu\bar{\bar{D}}$ le tenseur des contraintes visqueuses du fluide supposé Newtonien, $\bar{\bar{D}}$ le tenseur de taux de déformations, μ la viscosité dynamique, k la conductivité thermique. Les propriétés thermophysiques μ et k sont supposées constantes. L'air est considéré comme un gaz parfait vérifiant l'équation d'état $p = r\rho T$, avec T la température et r la constante du gaz.

Ces équations sont résolues par différences finies avec des schémas d'ordre élevé (upwind ordre 3 en temps et en espace pour les termes convectifs, et centré d'ordre 2 pour les termes diffusifs). L'algorithme est décrit dans [15]. Les maillages utilisés sont cartésiens, réguliers, avec 5 points de discrétisation dans la couche limite, et 500 points dans la direction axiale. Les critères de stabilité du schéma permettent de fixer le pas de temps. L'établissement de l'écoulement de streaming pouvant prendre plusieurs centaines de périodes, on a souhaité conserver un nombre "raisonnable" de pas de temps par période acoustique. C'est pourquoi on a fixé une longueur de domaine très petite ($L = 8.59$ mm), correspondant à une fréquence de 20000 Hz, nécessitant 6250 pas de temps par période acoustique.

Pour calculer l'écoulement de streaming on effectue la moyenne de chaque grandeur physique sur une période acoustique. On reproduit ceci après chaque période, de façon à pouvoir suivre l'établissement de l'écoulement stationnaire. Les résultats ont été présentés pour un canal plan [15] et pour un guide d'onde axisymétrique [54]. Ils sont qualitativement similaires pour ces deux configurations. Pour de faibles niveaux acoustiques, on a retrouvé la solution de Rayleigh décrite précédemment (voir par exemple les lignes de courant de l'écoulement de streaming, fig. 6.2b). On remarque sur la figure 6.2a un overshoot dans l'établissement de la vitesse acoustique au centre du canal, que l'on peut attribuer peut-être à la légère différence entre la fréquence de résonance et la fréquence imposée par le secouage (phénomène de battement). Les simulations montrent également une inhomogénéité du champ de température moyenne (figure 6.2c), liée à l'effet thermoacoustique de transport de chaleur qui crée d'abord un gradient longitudinal en proche paroi, puis la chaleur diffuse vers l'axe du tube.

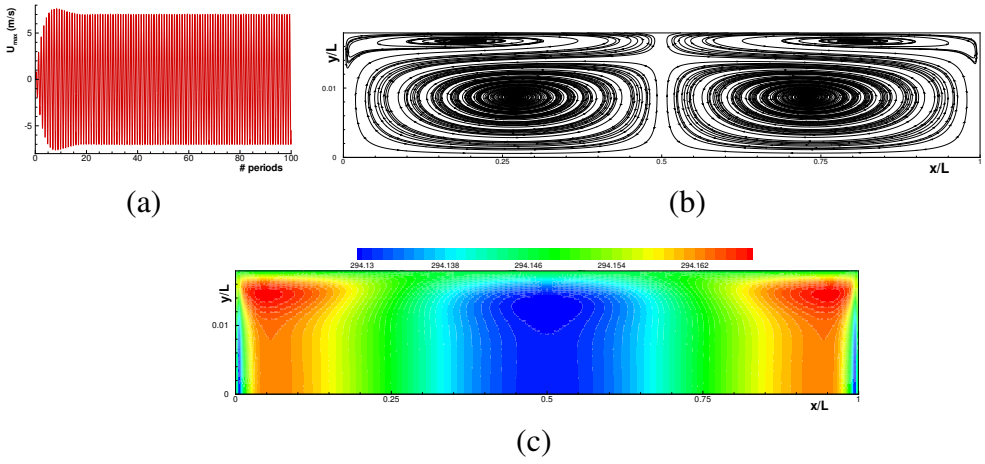

(a) (b)

(c)

FIGURE 6.2 – *Exemple en canal plan, faible niveau acoustique, (a) Evolution de la vitesse acoustique au centre du canal au cours de la simulation, (b) Lignes de courant de l'écoulement de streaming, (c) Isothermes du champ de température moyen, extrait de [15].*

Lorsque l'amplitude du forçage augmente, on note la présence d'ondes de chocs, d'où un fort taux d'harmoniques dans le signal acoustique final (voir par exemple la figure 11 de [54], en annexe). Les cellules de streaming se déforment. La valeur maximale de la vitesse axiale de streaming le long de l'axe (normalisée par l'amplitude de la vitesse de Rayleigh) diminue, et la position du maximum se déplace vers les nœuds de vitesse (figure 6.3). Au centre du guide, la pente du profil axial de vitesse axiale de streaming diminue jusqu'à s'annuler puis changer de signe. Cela correspond à l'émergence d'une nouvelle cellule de streaming contrarotative au centre du guide. Du fait des ondes de chocs, la température moyenne augmente considérablement et le champ de température devient très inhomogène.

6.2.2 Comparaison des résultats numériques et expérimentaux

L'article [54] figurant en annexe montre les résultats des simulations, ainsi que des comparaisons avec les mesures LDV et PIV réalisées à l'Institut P', menées sur le dispositif décrit sur la figure 1 de [54]. Grâce à la présence de deux haut-parleurs et deux convergents placés aux extrémités, l'onde qui s'établit est presque mono-fréquentielle (le taux d'harmonique est très faible). Les mesures présentées ont été prises en maintenant une température des parois presque constante au moyen de ventilateurs (pour approcher des conditions isothermes).

Les configurations physiques étant très différentes, on a présenté dans cet article une analyse dimensionnelle des équations 6.5. Dans toutes les configurations considérées, le gaz est le même

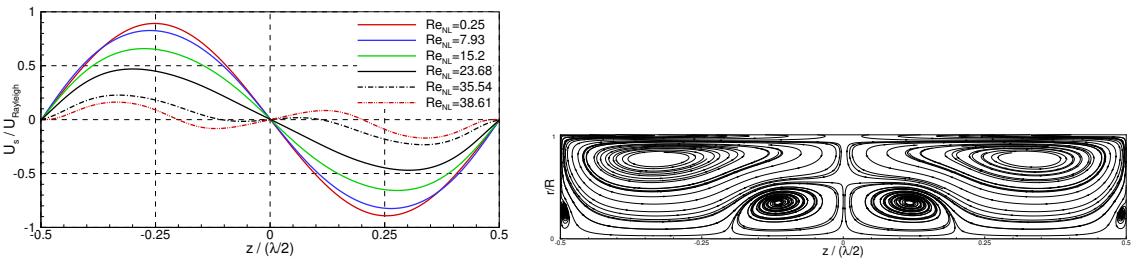

(a) (b)

FIGURE 6.3 – *Exemple en guide axisymétrique, évolution de faible à fort niveau acoustique, (a) Variation de la vitesse axiale de streaming normalisée le long de l'axe central du guide pour diverses valeurs de Re_{NL} et (b) Lignes de courant de l'écoulement de streaming pour le plus fort niveau de (a), extrait de [54].*

(air), et donc le nombre de Prandtl $Pr = \frac{\mu c_p}{k} \simeq 1$. On a isolé quatre nombres sans dimension caractérisant l'écoulement de streaming : le nombre de Mach acoustique M, le nombre de Reynolds acoustique $Re = \frac{\rho_0 c_0^2}{\mu\omega}$ (avec ρ_0 la masse volumique de référence), le nombre de Shear $Sh = \frac{\delta_\nu}{R}$, et le nombre de Reynolds non-linéaire Re_{NL}. L'analyse montre que les configurations seront en similitude si le nombre de Reynolds non-linéaire Re_{NL} est le même et que, pour la même valeur du nombre de Prandtl Pr, on a $M \ll 1$, $Sh \ll 1$ et $Re \gg 1$. On vérifie que ces conditions sont satisfaites pour les configurations comparées ici (voir Table 1 de [54], en annexe).

On observe que lorsque le nombre de Re_{NL} augmente, la déformation des cellules de streaming est similaire. La compréhension de cette déformation de l'écoulement a fait l'objet des études qui ont suivi cette confrontation initiale entre simulations et mesures. Les résultats étant similaires malgré les conditions différentes en termes de contenu harmonique et de champ de température, on a supposé que la propagation non linéaire et les effets thermiques n'étaient sans doute pas prédominants (ce point de vue a évolué depuis nos dernières études [19]). Pour essayer de comprendre le ou les mécanismes responsables de la déformation des cellules de streaming à fort niveau acoustique, on a exploré plusieurs pistes, détaillées dans les sections suivantes.

6.3 Simulations isentropiques : effet de l'inertie sur l'écoulement de streaming

Pour s'affranchir complètement des effets thermiques, on a effectué des simulations en considérant l'écoulement comme isentropique. Les études associées ont fait l'objet de deux articles en 2017 [17, 18] dont le premier figure en annexe.

Dans les simulations numériques directes, on ne résout donc plus que les deux premières équations du système 6.5. L'équation d'état isentropique est : $(p - p_0) = c_0^2(\rho - \rho_0)$, avec p_0 et ρ_0 les pression et masse volumique initiales. Les conditions aux limites, comme dans les simulations précédentes, sont l'adhérence à la paroi, avec des conditions de symétrie sur les frontières gauche, droite et sur l'axe.

Des ondes de choc sont générées dans le résonateur, mais elles sont de faible intensité. Lorsque le niveau acoustique augmente, les profils de vitesse axiale de streaming le long de l'axe sont déformés suivant la même évolution que dans la section précédente et des cellules supplémentaires de streaming sont générées au centre du guide.

Parmi les mécanismes responsables de la déformation des cellules de streaming à fort ni-

veau acoustique, le plus naturel semblait être l'inertie. Nous avons utilisé les simulations isentropiques pour étudier les effets de l'inertie sur la déformation de l'écoulement de streaming à fort niveau acoustique. Cette étude est présentée dans la section suivante.

6.3.1 Analyse des effets de l'inertie

Pour étudier les effets de l'inertie [17], nous avons commencé par analyser les transitoires de l'écoulement de streaming. Afin d'isoler ce transitoire de celui de l'acoustique, on a utilisé le code instationnaire en soustrayant à la fin de chaque période acoustique, le champ moyen au champ instationnaire avant de poursuivre le calcul (cela pendant tout l'établissement de l'acoustique). On a ainsi examiné, à faible et fort niveaux acoustiques, les transitoires de la composante axiale de la vitesse de streaming en plusieurs points (dans la couche limite, sur l'axe à $\lambda/8$ du bord, et en un point de vitesse maximale de la cellule supplémentaire, voir figures 4 et 6 de [17]). On a montré que le tourbillon intérieur s'établit d'abord, puis le tourbillon extérieur se stabilise suivant une courbe à une seule constante de temps (faible niveau acoustique) ou bien à deux (fort niveau acoustique). Le tourbillon supplémentaire s'établit dans un troisième temps.

On a interprété ces résultats à partir d'une analyse dimensionnelle des équations instantanées moyennées sur une période acoustique, écrites en décomposant chaque variable en sa composante moyenne et sa composante acoustique :

$$\left\{ \begin{array}{lcl} \dfrac{\partial \overline{\rho}}{\partial t} + \nabla \cdot (\overline{\rho}\, \overline{\mathbf{v}}) & = & -\nabla \cdot (\overline{\rho' \mathbf{v}'}) \\ \dfrac{\partial \overline{\rho}\, \overline{\mathbf{v}}}{\partial t} + \nabla \cdot (\overline{\rho}\, \overline{\mathbf{v}} \otimes \overline{\mathbf{v}}) + \nabla \overline{p} & = & \nabla \cdot (\overline{\overline{\tau}}) + \bar{F}, \end{array} \right. \tag{6.6}$$

où $\overline{p} - p_0 = c_0^2(\overline{\rho} - \rho_0)$, $\overline{\overline{\tau}}$ est le tenseur des contraintes visqueuses moyenné, et la force $\bar{F}$ est donnée par :

$$\bar{F} = -\nabla \cdot (\overline{\rho' \mathbf{v}'} \otimes \overline{\mathbf{v}} + \overline{\mathbf{v}} \otimes \overline{\rho' \mathbf{v}'} + \overline{\rho} \overline{\mathbf{v}' \otimes \mathbf{v}'} + \overline{\rho' \mathbf{v}' \otimes \mathbf{v}'}). \tag{6.7}$$

On note U_S la vitesse de streaming de référence. On peut alors identifier deux échelles de temps caractéristiques : $t_d = R^2/\nu$ le temps caractéristique de diffusion visqueuse dans la direction radiale, et $t_c = \lambda/(4U_S)$ le temps caractéristique de transport convectif par le streaming suivant l'axe. Le nombre de Reynolds caractérisant l'écoulement de streaming est donné par $Re_S = t_d/t_c = \frac{4U_S R^2}{\lambda \nu}$. A bas niveau acoustique, comme U_S est d'ordre M^2, on a $U_S = MU_{ac}$ et donc le nombre de Reynolds du streaming est du même ordre de grandeur que le nombre de Reynolds non-linéaire ($Re_S = \frac{4}{\pi} Re_{NL}$). A fort niveau acoustique cependant, les simulations montrent que U_S diminue, et donc $Re_S \leq Re_{NL}$.

Pour affiner la compréhension du rôle combiné de la diffusion visqueuse et de la convection dans l'établissement du tourbillon extérieur à partir du tourbillon intérieur, nous avons utilisé l'analogie avec un écoulement dans une cavité entraînée. On réduit le domaine d'étude au cylindre de rayon $r = R - 3\delta_\nu$ (position radiale pour laquelle la vitesse de streaming du tourbillon intérieur est maximale). Sur l'enveloppe du tube, on impose la vitesse de streaming U_w (axiale uniquement) extraite des calculs numériques (cette vitesse dépend de la coordonnée axiale). A l'intérieur de ce tube, on résout les équations de Navier-Stokes compressibles sans forçage acoustique (l'écoulement est pratiquement incompressible), en supposant qu'initialement le fluide est au repos. Les transitoires de la vitesse de streaming en différents points font apparaître les deux constantes de temps (diffusion, advection), comme dans la simulation numérique directe. Par contre, les amplitudes de vitesse axiales obtenues sont bien supérieures à celles de la simulation numérique directe, et aucune nouvelle cellule de streaming ne se forme (figures 9 à 11 de [17] en annexe).

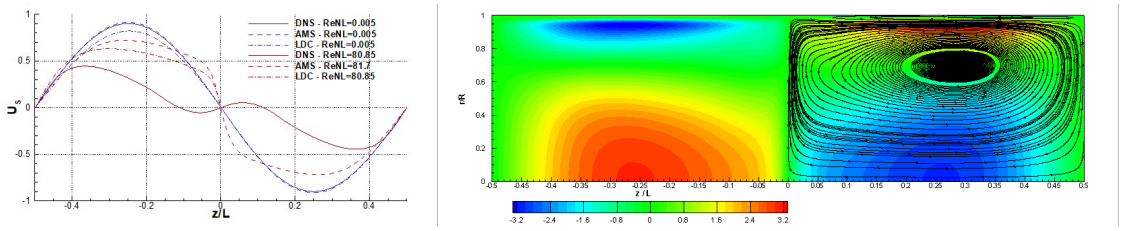

(a) (b)

FIGURE 6.4 – *Résultats de l'approche avec le code moyenné et avec l'analogie de cavité entraînée : (a) Evolution de faible à fort niveau acoustique du profil axial de la vitesse axiale de streaming normalisée le long de l'axe central du guide pour 2 valeurs de Re_{NL} (code moyenné, cavité entraînée, DNS) (b) Lignes de courant de l'écoulement de streaming à fort niveau acoustique (code moyenné) extrait de [17] et isolignes de la vitesse de streaming (code couleur).*

Enfin, ces résultats ont été confirmés en utilisant un code moyenné pour résoudre des équations approchées du système 6.6. L'approximation vient du fait que les termes sources sont calculés à partir des solutions de l'acoustique à faible niveau que l'on multiplie par un coefficient α pour simuler le fort niveau. Cette approche comme l'analogie de la cavité entraînée conduit à fort niveau acoustique à la déformation de l'écoulement de streaming extérieur similaire à celui décrit par l'analyse théorique de [37], mais contraire aux observations de la simulation numérique directe et des expériences conduites à l'institut P', comme le montre la figure 6.4a : la pente du profil axial de vitesse axiale de streaming augmente lorsque le niveau acoustique augmente. Aucune nouvelle cellule n'est générée au centre du guide (comparer les figures 6.4b et 6.3b).

Cette étude permet de conclure que les effets de l'inertie ne permettent pas à eux seuls d'expliquer les déformations de l'écoulement de streaming à fort niveau acoustique observées dans les simulations numériques directes. On s'est donc demandé si le nombre de Reynolds non-linéaire était vraiment le paramètre sans dimension le plus approprié pour caractériser les différents "régimes" de l'écoulement de streaming.

6.3.2 Analyse comparée des composantes axiale et radiale des vitesses acoustique et de streaming

Les résultats des simulations numériques directes ont été comparées à ceux des expériences [18]. On obtient des champs montrant l'écoulement de streaming similaires entre expériences et simulations, mais pour des nombres de Reynolds non-linéaires bien plus élevés dans la simulation (figure 6.5). Les expériences utilisées pour les comparaisons sont celles qui ont été réalisées avec des conditions thermiques "non-contrôlées". On a réalisé une analyse comparée des composantes de vitesse acoustique et de streaming [18], à faible et fort niveau acoustique, à partir des résultats expérimentaux et numériques. Les simulations sont notées N_1 à $N4$ et les expériences E_1 et E_2, avec pour chaque expérience une plage spécifique des paramètres Sh, Re_{NL}, R/L [18]. Une première constatation indique que les variations axiale et radiale de la composante axiale de la vitesse acoustique demeurent les mêmes lorsque le niveau acoustique augmente.

En ce qui concerne les isolignes de la composante axiale de la vitesse de streaming, elles évoluent en fonction du niveau acoustique. L'amplitude maximale relevée (notée U_S) est différente dans la couche limite et dans le tourbillon extérieur. Au centre du guide, à faible niveau acoustique, U_S est proportionnelle à U_{ac}^2 (on a précisé le coefficient en fonction de R/δ_ν grâce à un fit). Par contre, à fort niveau acoustique, toujours au centre du guide, U_S est proportionnelle

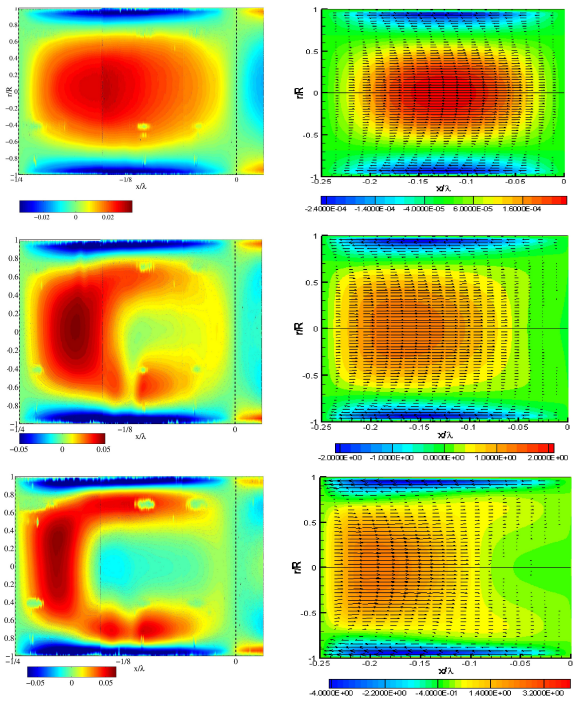

FIGURE 6.5 – *Isolignes de la vitesse axiale de streaming (avec l'échelle de couleur en m/s) et vecteurs vitesse. (a) résultats PIV, $Re_{NL} = 6, 14, 30$ de haut en bas, (b) résultats numériques complétés par symétrie axiale, $Re_{NL} = 0.006, 51, 111$ de haut en bas (extrait de [18]).*

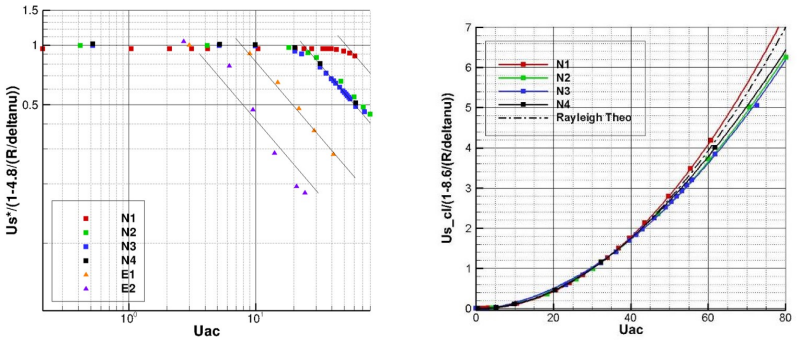

(a) (b)

FIGURE 6.6 – *(a) Au centre du guide (tourbillon extérieur) : amplitude de la composante axiale de la vitesse de streaming normalisée $\frac{U_S}{U_R}\frac{1}{\left(1-4.8\frac{\delta_\nu}{R}\right)}$ en fonction de U_{ac}, (b) Tourbillon intérieur U_S en fonction de U_{ac} (extrait de [18]).*

à U_{ac}. La figure 6.6a met en évidence ces deux régimes pour toutes les données expérimentales et numériques, sur un même tracé log-log. La quantité représentée est $\frac{U_S}{U_R}\frac{1}{\left(1-4.8\frac{\delta_\nu}{R}\right)}$, avec U_R l'amplitude de la vitesse de Rayleigh. Lorsque U_{ac} est petit, les points s'alignent sur la valeur 1 (solution de Rayleigh), et lorsque U_{ac} augmente les points s'alignent sur des droites de pentes -1.

En proche paroi, à tous niveaux acoustiques, U_S est proportionnelle à U_{ac}^2, comme le montre la figure 6.6b.

On a ensuite étudié les isolignes des composantes radiales de la vitesse acoustique et de streaming. Ces composantes radiales sont bien plus petites que les composantes axiales. On a montré que ces isolignes évoluent en fonction du niveau acoustique mesuré par U_{ac}. On note

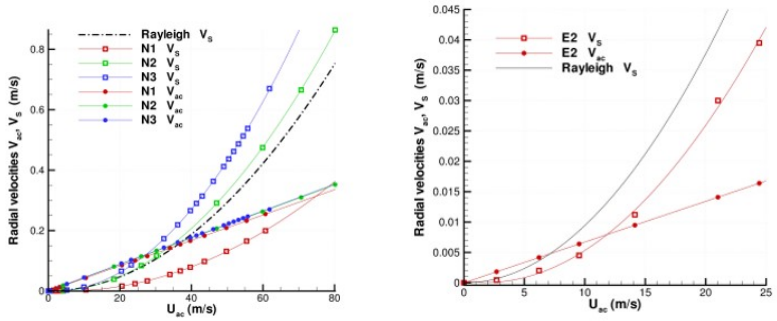

(a) (b)

FIGURE 6.7 – *(a) Amplitude maximale de la composante radiale de la vitesse acoustique V_{ac} et de streaming V_S en fonction du niveau acoustique U_{ac} pour l'ensemble des (a) simulations numériques, (b) résultats expérimentaux (extrait de [18]).*

V_{ac} (resp. V_S) l'amplitude maximale de la composante radiale de la vitesse acoustique (resp. de streaming). A tous niveaux acoustiques, on montre que V_{ac} est proportionnelle à U_{ac} (fig. 6.7a et 6.7b), avec un coefficient de proportionnalité indépendant de R/δ_ν. On montre aussi sur ces figures que V_S est proportionnelle à U_{ac}^2, avec un coefficient de proportionnalité qui augmente avec R/δ_ν. On trouve donc des situations où V_S est supérieure à V_{ac}, ce qui est incompatible avec la théorie consistant à appliquer des approximations successives. Une interaction non linéaire entre les vitesses existe donc qui pourrait justifier la modification des cellules de streaming à fort niveau acoustique : la vitesse de acoustique modifie la vitesse de streaming qui modifie la vitesse acoustique. On note que le changement du régime 1 au régime 2 se produit lorsque la vitesse radiale de streaming devient supérieure à la vitesse radiale acoustique. On observe l'apparition des cellules de streaming supplémentaires uniquement dans le régime 2.

6.4 Effets thermiques

Nos travaux actuels concernent l'influence des hétérogénéités de température sur le streaming acoustique dans un résonateur. Nous avons soumis récemment un article au Journal od Fluid Mechanics [19]. Des travaux récemment publiés dans la littérature ont montré que l'existence d'une hétérogénéité de température suivant la direction transverse du guide pouvaient entrainer des déformations sensibles de l'écoulement de streaming [66, 12, 38]. Comme indiqué à la fin de la partie 6.1 sur le streaming à faible niveau, on a montré par résolution formelle des équations en canal plan, que la présence d'un gradient vertical de température, même de petite amplitude, peut générer des modifications importantes de l'écoulement de streaming. En particulier, on montre que si l'axe est plus chaud que les parois, une cellule additionnelle de streaming contrarotative peut être générée, accompagnée d'une baisse globale de la vitesse de streaming extérieur.

Nous avons ensuite examiné si une telle hétérogénéité de température suivant la direction transverse du guide pouvait exister dans le problème que nous étudions. Sur la figure 6.8a, on voit une schématisation du champ de température qui s'établit à bas niveau acoustique dû au pompage de chaleur thermoacoustique dans la couche limite puis à la diffusion thermique vers le centre du guide. A fort niveau, l'écoulement de streaming transportant la chaleur vers le ventre de vitesse acoustique (près de l'axe) et vers le nœud de vitesse acoustique (en proche paroi), une large zone de stratification transverse en température s'établit (figure 6.8b). Le champ de température s'apparente à celui obtenu en cavité différentiellement chauffée, mais il n'est pas lié

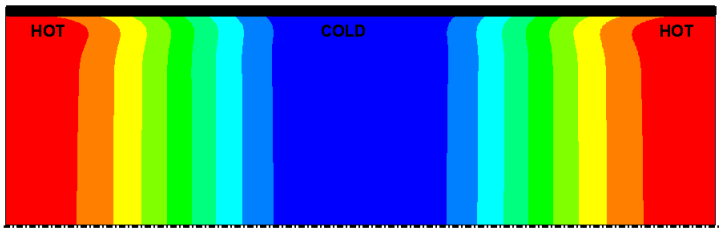

(a)

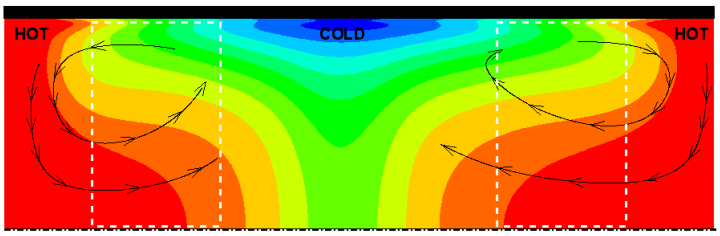

(b)

FIGURE 6.8 – *Schématisation des isothermes dans le guide d'ondes à (a) bas niveau acoustique et (b) fort niveau acoustique. Le rectangle indiqué par une ligne blanche indique une région de stratification transverse de température.*

à la gravité. On s'attend à obtenir une différence de température transverse proportionnelle à la différence de température longitudinale initiale. L'écoulement de streaming est ensuite modifié consécutivement à l'établissement de cette stratification en température et dans une moindre mesure à l'inertie de l'écoulement. On peut donc espérer étudier l'écoulement de streaming à fort niveau acoustique (malgré l'appellation streaming non linéaire) à partir de la résolution des équations linéaires de l'acoustique et du streaming en présence d'une inhomogénéité transverse de température.

Pour exprimer plus précisément la répartition longitudinale de température à la paroi, on suppose que la paroi a une épaisseur donnée $\hat{w}$ et que le matériau qui la constitue est caractérisé par sa masse volumique ρ_S, sa conductivité thermique k_S et sa chaleur massique c_S. Si l'on considère une configuration de température "non contrôlée", il y aura un échange convectif à la paroi avec l'air environnant supposé à température constante ambiante, pour lequel on peut estimer d'après la géométrie du guide d'ondes le coefficient d'échange h. On utilise la démarche de Swift [65] pour lier le gradient de température transverse à la paroi à l'intégrale du flux de chaleur thermoacoustique que l'on exprime en fonction de des grandeurs acoustiques. En écrivant la continuité du flux de chaleur aux interfaces, on obtient une expression pour la température intérieure à la paroi en fonction de la coordonnée axiale, U_{ac}, Pr, T_0 (la température moyenne), $\hat{w}$, δ_{nu}, h et les propriétés thermophysiques de la paroi et du gaz. On en déduit une expression de la différence de température longitudinale. En supposant la différence de température transverse égale à la moitié de la différence longitudinale existant le long de la paroi interne du résonateur. Il y a émergence d'une nouvelle cellule si la vitesse axiale de streaming s'annule sur l'axe entre un nœud et un ventre de vitesse acoustique. On en déduit un critère de la forme $Re_{NL} \geq K_C$, où K_C est donné par

$$K_C = 30 \frac{k_s/k}{\hat{w} + k_s/(h\delta_\nu)} \left(1 + \frac{3}{2} \frac{1+Pr}{(\gamma-1)\sqrt{Pr}}\right) \frac{1}{(1-Pr^{3/2})}. \tag{6.8}$$

On a testé le critère obtenu avec les résultats expérimentaux de [55, 66]. Pour cela on a estimé la valeur du coefficient d'échange h à partir des données expérimentales. Nous avons trouvé une

valeur de K_C légèrement inférieure aux valeurs expérimentales de Re_{NL} pour lesquelles une nouvelle cellule de streaming est observée dans [55]. Ceci peut s'expliquer en partie par le fait que la théorie a été menée en géométrie plane et non axisymétrique. Dans l'expérience de [66], les mesures LDV n'ont pas permis de mettre en évidence l'émergence d'une nouvelle cellule, mais ont montré un écrasement de la composante axiale de la vitesse de streaming sur l'axe, compatible avec une forte déformation du streaming à un nombre de Re_{NL} là aussi légèrement supérieur à l'estimation de K_C.

Avec des conditions isothermes, les valeurs de K_C que nous obtenons sont très supérieures. Ce résultat est cohérent avec les résultats de [66] qui ne montrent aucune déformation de l'écoulement de streaming à fort niveau acoustique si les parois sont isothermes.

6.5 Conclusions

Nous avons analysé en détail les écoulements de streaming de type Rayleigh à faible niveau acoustique, puis à des niveaux croissants jusqu'à atteindre de forts niveaux acoustiques, au moyen d'une approche combinée numérique, théorique et expérimentale (grâce à la collaboration avec Hélène Bailliet). Nous avons beaucoup progressé sur la compréhension des mécanismes responsables de la déformation de l'écoulement de streaming extérieur, et notamment l'apparition de nouvelles cellules au centre du guide. Les effets de l'inertie seuls ont été analysés, grâce en partie aux simulations en situation isentropique. On a montré qu'ils ne peuvent pas, à eux seuls, justifier l'émergence d'une nouvelle cellule. L'analyse dimensionnelle et le calcul symbolique ont permis de comprendre les effets des divers termes sources à faible niveau acoustique en profitant de la linéarité du système d'équations moyennées régissant l'écoulement de streaming. Enfin, l'étude récente des effets thermiques permet d'éclairer beaucoup de points et ouvre de multiples perspectives. L'effet combiné de l'inertie et du transport conductif et convectif de chaleur pourrait tout à fait expliquer l'émergence de nouvelles cellules.

Chapitre 7

Perspectives

Pour la suite de ma carrière, je souhaite poursuivre des activités de recherche sur la modélisation et la simulation numérique en mécanique des fluides, avec dans la mesure du possible une confrontation avec des résultats expérimentaux. Je souhaite aussi et surtout poursuivre la collaboration établie depuis une vingtaine d'années avec Diana Baltean-Carlès, et depuis une dizaine d'années avec Virginie Daru et Hélène Bailliet (P'). Grâce à ce travail d'équipe, nous progressons sur la compréhension des écoulements et des transferts de chaleur dans les systèmes thermoacoustiques.

Le projet ANR TACOT (2017-2020, prolongé jusqu'en juillet 2021) concerne le développement et l'étude d'une pompe à chaleur thermoacoustique compacte pour le transport automobile. Le prototype instrumenté compact qui a été construit à l'Institut Pprime comprend deux sources acoustiques et un régénérateur placé entre deux échangeurs de chaleur (figure 7.1). Il est également envisagé de construire un système avec deux cœurs thermoacoustiques face à face connectés par une même source acoustique. Le prototype à un cœur thermoacoustique a

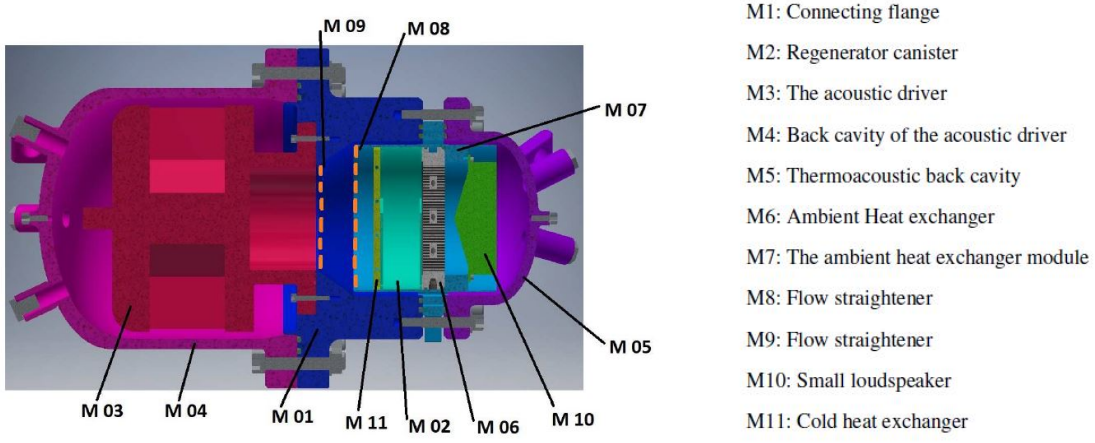

FIGURE 7.1 – *Projet ANR TACOT, schéma du prototype construit à l'institut Pprime.*

été conçu en utilisant le logiciel DeltaEC (Los Alamos, [68]). Il comprend une source acoustique principale (notée M3 sur la figure 7.1) qui fournit la puissance acoustique et une source acoustique secondaire (notée M10) qui permet d'ajuster le déphasage entre pression et vitesse acoustique, de façon à ce que l'onde dans le système soit progressive [47, 48]. On trouve aussi une fine enveloppe entourant le cœur thermoacoustique qui permet le passage du gaz pour réaliser une boucle de retour. Le cœur thermoacoustique est constitué d'un régénérateur entre deux échangeurs (un échangeur froid et un échangeur à température ambiante). Le prototype a été

fabriqué et instrumenté largement pour permettre le suivi de ses caractéristiques. Les premiers tests ont eu lieu cette année, et les performances sont proches des prédictions de DeltaEC. Le gaz utilisé est un mélange d'Helium et d'Argon à pression moyenne 40 bar (valeur maximale testée). Pour 210 Watt de puissance électrique fournie, 200 W sont pompés à la source froide avec une différence de température de 36 K entre les échangeurs. Le COP global de la machine est 0.95, et celui de la conversion d'énergie thermoacoustique seule est de 2.37. Ces résultats montrent l'intérêt du projet et des applications possibles pour le secteur automobile. Cependant l'instrumentation du prototype est délicate et les grandeurs mesurées disponibles sont insuffisantes pour suivre le mouvement du gaz et les échanges de chaleur à l'intérieur de la machine. La simulation numérique doit donc pouvoir apporter des informations précieuses.

Notre équipe du LIMSI, composée de Diana Baltean-Carlès, Virginie Daru, Yann Fraigneau et moi-même, est chargée de mener des études numériques. Nous avons pu bénéficier grâce à ce projet de 12 mois de chercheur associé, pour lesquels nous avons recruté Omar Hireche que nous connaissons bien et qui était intéressé par l'étude. Avec lui, nous avons étudié les possibles effets de la convection naturelle dans les dispositifs élaborés à l'institut P' pour étudier finement le cœur thermoacoustique [30]. Nous projetons de poursuivre cette étude en travaillant sur une géométrie simplifiée du prototype qui a été construit.

Par ailleurs, nous allons maintenant tenter de simuler les écoulements et transferts de chaleur dans le prototype pour analyser les effets multidimensionnels et nonlinéaires qui s'y produisent, liés à la compacité de la machine et au fort niveau acoustique généré. La taille de la machine étant très petite devant la longueur d'onde, l'usage d'un modèle de machine acoustiquement compacte, de type faible Mach, semble tout indiqué. Un point clé est la description du phénomène de pompage de chaleur thermoacoustique en milieu poreux.

Par ailleurs il serait intéressant d'étudier si l'on retrouve des écoulements de streaming dans la machine.

Ce projet permet de faire un lien entre les divers thèmes de recherche que j'ai abordés au LIMSI, et d'offrir plusieurs perspectives d'études à venir, que je détaille dans la suite de ce chapitre.

7.1 Convection naturelle et acoustique

Comme nous l'avons montré récemment, les écoulements de convection naturelle peuvent devenir importants dans une cavité thermoacoustique [30]. Les codes de dimensionnement des machines et l'ensemble des études numériques posant habituellement l'hypothèse que les effets de gravité sont négligeables, il nous semble important d'adresser ce point. Même si l'on peut s'affranchir des effets néfastes de la convection naturelle en inclinant une machine pour qu'elle soit verticale, cette méthode sera inefficace si l'on envisage de construire une machine à deux cœurs thermoacoustiques face-à-face partageant la même source acoustique principale.

Pour évaluer l'impact potentiel de la convection naturelle dans les prototypes de pompage de chaleur du TACOT, il nous faut considérer la modification de l'écoulement de convection naturelle en présence d'un champ acoustique.

Dans une première étape, nous allons poursuivre l'analyse des deux dispositifs expérimentaux présentés dans [30]. Dans ces deux dispositifs, nous avons montré qu'en absence d'acoustique, l'écoulement de convection naturelle est un écoulement stationnaire, et que les simulations sont en excellent accord avec les mesures [30]. Des expériences sur ces deux dispositifs ont été également effectuées en présence d'acoustique, et des mesures du champ de vitesse moyen ont été obtenues récemment ainsi que le suivi temporel de la température en plusieurs points des parois du tube. En présence d'acoustique, on peut se demander si les écoulements de convection naturelle et l'écoulement de streaming sont découplés et peuvent se superposer

simplement l'un à l'autre. Les dernières études que nous avons menées sur la modification de l'écoulement de streaming en présence d'un champ de température inhomogène semble montrer que ce n'est pas le cas. Il faudrait cependant étudier les temps caractéristiques d'établissement de ces écoulements pour évaluer la possibilité d'un découplage dans le temps. Une première comparaison semble indiquer que les vitesses de convection naturelle peuvent être du même ordre de grandeur que l'écoulement de streaming de Rayleigh.

La modification des écoulements de convection naturelle en présence d'acoustique a fait l'objet des travaux expérimentaux de [44, 45] qui ont étudié une portion de résonateur (guide d'onde en $\lambda/4$, fermé-ouvert) placée entre deux échangeurs de chaleur (qu'ils ont appelée cœur thermoacoustique mais qui s'apparente plus à un tube à gaz pulsé car il n'y a pas de milieu poreux). Ils ont conclu qu'en présence d'acoustique l'écoulement s'apparente à un écoulement de convection forcée.

Afin d'examiner si l'écoulement de convection naturelle est réellement modifié en présence d'acoustique sur les expériences précédentes, on souhaite réaliser des simulations. Comme la longueur du tube et la longueur d'onde sont du même ordre de grandeur, une simulation numérique complète exigerait l'utilisation d'un code compressible, avec prise en compte de la gravité, ce qui pose le problème de sa faisabilité en terme de coût numérique. Cette perspective est envisageable à plus long terme.

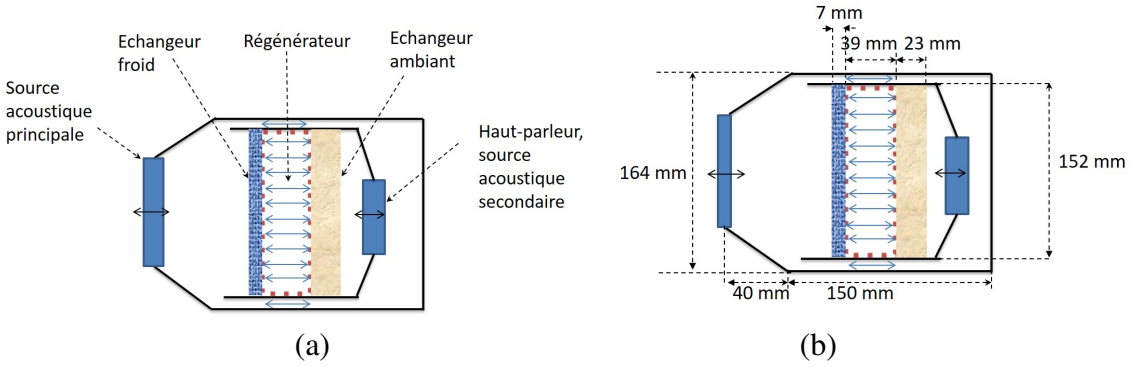

FIGURE 7.2 – *Projet ANR TACOT, (a) Géométrie simplifiée du prototype, (b) Dimensions approximatives du prototype.*

A court terme, nous allons estimer l'impact possible des écoulements de convection naturelle dans le prototype construit dans le cadre du projet TACOT. La figure 7.2 présente une schématisation de la géométrie du prototype. Dans ce dispositif le pompage de chaleur étant provoqué par l'acoustique, il n'y a pas de différence de température entre les échangeurs et donc pas de convection naturelle en absence d'acoustique. On peut cependant faire des estimations des différences de températures obtenues en régime établi final, et dans une première approche, étudier la convection naturelle qui en résulterait, en ne prenant pas en compte l'acoustique. En se basant sur les estimations de DeltaEC, et sur les premières mesures effectuées sur le prototype, la différence de température entre l'échangeur à température ambiante et l'échangeur froid peut atteindre 40 K. On peut noter que l'échangeur à température ambiante n'est pas complètement efficace, puisque la température moyenne mesurée au niveau de cet échangeur peut augmenter jusqu'à 340 K. Des mesures de température relevées en trois points situés sur une ligne verticale centrale du régénérateur montrent que la partie basse du régénérateur est bien plus froide que la partie haute, ce qui semble indiquer qu'il existe un écoulement de convection naturelle dans le cœur thermoacoustique. Pour estimer a priori l'ordre de grandeur des paramètres sans dimension, on choisit une expérience où la différence de température obtenue est 40 K pour une température moyenne dans le régénérateur

ρ	μ	k	c_p	ϵ	K	k_p
$kg.m^{-3}$	$kg.m^{-1}s^{-1}$	$W.m^{-1}.K^{-1}$	$J.kg^{-1}.K^{-1}$		m^2	$W.m^{-1}.K^{-1}$
23	$2.3 \cdot 10^{-5}$	0.08	1406	0.74	10^{-8}	3.7

TABLE 7.1 – *Exemple de paramètres thermophysiques pour le gaz et le milieu poreux, prototype ANR TACOT.*

de 310 K. Compte tenu des estimations des propriétés géométriques (figure 7.2b) et thermophysiques du gaz calculées à $T_{ref} = 310$ K et du milieu poreux (Table 7.1), le nombre de Rayleigh modifié, construit sur le rayon est $Ra_p = \rho g \beta \Delta T R K/(\mu \kappa_p) \simeq 9.1$, avec K la perméabilité du régénérateur, k_p la conductivité thermique équivalente et $\kappa_p = k_p/(\rho c_p)$ la diffusivité thermique du régénérateur [41]. L'ordre de grandeur de la vitesse de convection est $V_{ref} = \kappa_p Ra_p/H = 1.3$ cm/s [11]. Le nombre de Reynolds de pore, tenant compte du rayon hydraulique $a = 6 \times 10^{-5}$ m est $Re_p = \rho V_{ref} a/\mu \simeq 0.8 < 1$. L'hypothèse de Boussinesq semble justifiée car $\Delta T/(2T_{ref}) = 0.07 \ll 1$. Les zones où l'on s'attend à de forts écoulements de convection naturelle sont le régénérateur, ainsi que la fine enveloppe où le gaz circule, autour du cœur thermoacoustique. Nous prévoyons à court terme de mener une simulation de convection naturelle en milieu fluide et poreux. Le nombre de Reynolds de pore étant inférieur à 1, on peut raisonnablement utiliser le modèle de milieu poreux de Darcy Brinkman pour les simulations.

Pour évaluer l'impact réel de la convection naturelle dans la machine, il nous faut prendre en compte le forçage acoustique. La prise en compte de la gravité dans les calculs avec acoustique pourrait s'effectuer, en tenant compte de la compacité de la machine, avec un modèle faible Mach. Dans une première approche, on pourrait simplement imposer un forçage oscillant, en considérant la géométrie simplifiée de la machine et un seul piston se déplaçant à la fréquence imposée.

7.2 Couplage streaming non linéaire et thermique

A court terme, nous allons poursuivre les études du streaming acoustique nonlinéaire en guide d'ondes. Nos travaux actuels concernent l'influence des inhomogénéités de température sur le streaming acoustique. Nous souhaitons à présent effectuer des simulations numériques avec calcul du champ de température. Pour s'approcher des conditions expérimentales présentées dans [54, 17, 18] et s'affranchir des ondes de choc qui conduisent à un échauffement au centre du guide bien trop important, on envisage de modifier la géométrie de la simulation, en introduisant deux tubes convergents aux extrémités du guide. De plus, comme on l'a montré (article [19] soumis), les nouvelles cellules de streaming sont susceptibles d'apparaître pour des Re_{NL} plus petits lorsque l'on tient compte de la conductivité de la paroi et de l'échange convectif avec l'air extérieur supposé à température constante (conditions s'approchant des conditions appelées "incontrôlées" par notre équipe d'expérimentateurs). On modifiera la mise en place de la simulation pour imposer ces conditions aux limites.

A plus long terme, nous aimerions calculer les écoulements de streaming dans un résonateur (ou plutôt une portion de résonateur) pour laquelle un fort gradient de température est imposé sur la paroi. Cette configuration est celle des tubes à gaz pulsés (petit tube positionné en général entre 2 échangeurs de chaleur pour ramener la température à la température ambiante). L'écoulement de streaming qui s'établit dans ces tubes à gaz pulsés est souvent néfaste pour le fonctionnement de la machine, et donc présente un intérêt particulier pour les thermoacousticiens. Les couplages forts entre le champ de température et l'écoulement de streaming que

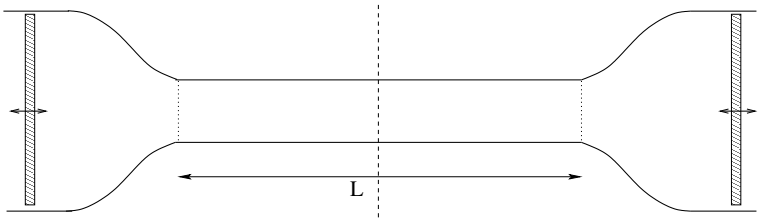

FIGURE 7.3 – *Schéma du domaine de simulation, calcul de l'écoulement de streaming.*

nous avons mis en évidence récemment pourront peut-être donner des pistes quant à la façon de diminuer ou annuler l'écoulement de streaming.

Nous aimerions également évaluer le niveau de l'écoulement de streaming pouvant s'établir entre les plaques d'un stack thermoacoustique.

Enfin, les études du streaming nonlinéaire peuvent être appliquées à d'autres problèmes intéressants, notamment en microfluidique.

7.3 Effet thermoacoustique en cavité compacte

Le code DeltaEC (Los Alamos) utilisé pour la conception du prototype, et couramment utilisé depuis plus de 20 ans pour la conception des machines thermoacoustiques est un code fréquentiel 1D, basé sur une intégration des équations sur la section du guide, qui permet de tenir compte seulement partiellement du caractère multidimensionnel et instationnaire des écoulements. Notre approche se différencie car elle se base sur les équations 3D instationnaires de la mécanique des fluides. L'usage d'hypothèses simplificatrices s'impose en raison de la présence de multiples échelles temporelles (acoustique, thermique) et spatiales (longueur d'onde, taille de la machine, épaisseur des couches limites) : l'approximation faible Mach peut être particulièrement intéressante pour limiter les temps de calcul, et son utilisation se justifie par la compacité des prototypes du projet TACOT par rapport à la longueur d'onde. En effet, la longueur caractéristique du prototype à un cœur thermoacoustique est de $\simeq 20$cm et la longueur d'onde $\simeq 10m$ pour un mélange Helium-Argon de vitesse du son $\simeq 500$m/s oscillant à 50Hz. Le rapport est de 2%. Ce rapport est appelé nombre d'Helmholtz He par les acousticiens, qui parlent également de compacité de la machine lorsque $He \ll 1$. Nous souhaitons appliquer cette approximation à la modélisation du pompage de chaleur thermoacoustique dans le propotype, en géométrie axisymétrique tout d'abord.

Nous comparerons d'abord les simulations faible Mach avec celles du code compressible sur des géométries planes simplifiées. Nous avons encadré un stagiaire de licence l'été dernier qui a effectué des simulations avec le code SunfluidH (LIMSI) sur une cavité rectangulaire fermée par un piston en mouvement oscillant à la période γ donnée. La solution numérique des équations d'Euler 1D est présentée sur la figure 7.4 [16]. Lorsque la période d'oscillation γ est petite l'écoulement est supersonique comme le montre la solution numérique (Fig 7.4a). Lorsque la période d'oscillation est suffisamment grande, le champ de vitesse devient très reproductible à chaque période, et la masse volumique devient homogène en espace, et ne dépend plus que du temps (Fig 7.4b). Il existe dans ce cas une solution analytique où la vitesse varie linéairement entre le piston et le fond de la cavité. Nous avons obtenu une parfaite coïncidence entre cette solution analytique et la simulation faible Mach de SunfluidH le long de l'axe central de la cavité.

Pour la suite de cette étude, nous souhaitons travailler sur la géométrie simplifiée du prototype, en imposant les déplacements des deux pistons modélisant les sources acoustiques (ampli-

(a)

(b)

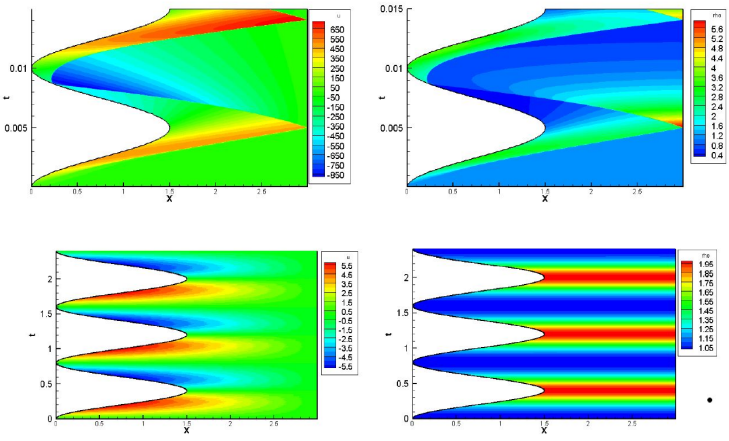

FIGURE 7.4 – *Résultat de simulations faible Mach des équations d'Euler 1D, gauche : vitesse* $u(x,t)$ *et droite : masse volumique* $\rho(x,t)$ *pour la période d'oscillation du piston (a)* $\gamma = 0.01s$ *et (b)* $\gamma = 0.8s$.

tude, fréquence et déphasage basés sur les expériences). Au départ, on travaillera dans une cavité plane, puis on traitera le cas axisymétrique. Pour simuler le pompage de chaleur thermoacoustique, on pourra insérer un empilement de plaques à la place du régénérateur. On pourra ainsi obtenir un pompage de chaleur le long des plaques. Le code de calcul SunfluidH est parallélisé MPI et devrait permettre d'effectuer les calculs. Une étude en maillage et une mise en place réfléchie des simulations est nécessaire pour limiter les temps de calcul, malgré l'utilisation du modèle Faible Mach.

Un point clé sera ensuite la modélisation des transferts de chaleur dans le régénérateur (considéré comme un milieu poreux homogène équivalent isotrope ou anisotrope) en présence d'un écoulement oscillant. Nous aimerions pouvoir obtenir un effet thermoacoustique de pompage de chaleur le long du milieu poreux, sans avoir à considérer l'échange entre le fluide et le solide au niveau de chaque pore.

La modélisation des échangeurs de chaleur est, elle aussi, délicate en raison des grandes disparités d'échelle de temps entre les phénomènes de pompage thermoacoustique et de conduction de la chaleur dans les échangeurs. Les idées d'études liées à cette machine sont donc nombreuses.

A plus long terme, nous souhaitons réaliser des simulations du prototype construit pour l'ANR TACOT, rendant compte à la fois des phénomènes de pompage de chaleur thermoacoustique, des écoulements de convection naturelle et des écoulements de streaming acoustique. Nous en sommes encore loin, mais la perspective est séduisante.

Une question ouverte reste celle de l'intégration de ces effets instationnaires, multidimensionnels et nonlinéaires dans les codes 1D comme DeltaEC, pour améliorer les outils de dimensionnement.

Bibliographie

[1] J.A. Adeff, T.J. Hofler, Design and construction of a solar-powered, thermoacoustically driven, thermoacoustic refrigerator, J. Acoust. Soc. Am. 107 (6), L37–L42, 2005.

[2] B. Alazmi and K. Vafai, Analysis of variance within the porous media transport models, J. Heat Transfer 122, 303–326, 2000.

[3] B. Alazmi and K. Vafai, Analysis of fluid flow and heat tranfer interfacial conditions between a porous medium and a fluid layer, Int. J. Heat Mass Transfer 44 , 1735–1740, 2001.

[4] A. Atchley, T. Hofler, M. Muzzerall, D. Kite and C. Ao, Acoustically generated temperature gradients in short plates, J. Acoust. Soc. Am. 88, 251-263, 1990.

[5] A.A Atchley and F.M. Kuo, Stability curves for a thermoacoustic prime mover, J. Acoust. Soc. Am. 95, 1401 – 1404, 1994

[6] S. Backhaus and G. Swift, A thermoacoustic-Stirling heat engine : Detailed study, J. Acoust. Soc. Am. 107 (6), 3148–3166, 2000.

[7] S. Backhaus, E. Tward, M. Petach, Traveling wave thermoacoustic electric generator, Appl. Phys. Lett. 85, 1085, 2004.

[8] H. Bailliet, V. Gusev, R. Raspet, and R. A. Hiller, Acoustic streaming in closed thermoacoustic devices, J. Acoust. Soc. Am. 110, 1808–1821, 2001.

[9] D. Baltean-Carlès, V. Daru, C. Weisman, S. Tabakova, H. Bailliet, « An unexpected balance between outer Rayleigh streaming sources », J. Fluid Mech. 867, 985-1011, 2019.

[10] J.L. Beck, 1972, Convection in a box of porous material saturated with fluid, Phys. Fluids 15, N° 8, 1377–1383, 1972

[11] A. Bejan, Convection Heat Transfer, Mac Graw Hill, 1985.

[12] M. Cervenka and M. Bednarrik, Effect of inhomogeneous temperature fields on acoustic streaming structures in resonators, J. Acoust. Soc. Am. 141, 4418–4426, 2017.

[13] D.R. Chenoweth and S. Paolucci, Natural convection in an enclosed vertical air layer with large horizontal temperature differences, J. Fluid Mech. 169, 173, 1986.

[14] W. Dai, E. Luo, J. Hu, H. Ling, A heat driven thermoacoustic cooler capable of reaching liquid nitrogen temperature, Appl. Phys. Lett. 86, 224103, 2005.

[15] V. Daru, D. Baltean-Carlès, C. Weisman, P. Debesse, G. Gandikota, Two-dimensional numerical simulations of nonlinear acoustic streaming in standing waves, Wave Motion 50, 955-963, 2013.

[16] V. Daru, Des écoulements compressibles aux écoulements faiblement dilatables, polycopié de cours de l'école Mécanique des Fluides Numérique, Porquerolles, mai 2015.

[17] V. Daru, C. Weisman, D. Baltean-Carlès, I. Reyt, H. Bailliet, Inertial effects on acoustic Rayleigh streaming flow : Transient and established regimes, Wave Motion 74, 1-17, 2017.

[18] V. Daru, I. Reyt, H. Bailliet, C. Weisman, D. Baltean-Carlès, Acoustic and streaming velocity components in a resonant wave guide at high acoustic levels, J. Acoust. Soc. Am. 141(1), 563-574, 2017.

[19] V. Daru, C. Weisman, D. Baltean-Carlès, H. Bailliet, Thermal effects on fast acoustic streaming inside a resonator, soumis à J. Fluid Mech.

[20] P. Duthil, C. Weisman, E. Bretagne, M-X. Francois, Experimental and numerical investigation of heat transfer and flow within a thermoacoustic cell, International Journal of Transport Phenomena, vol. 6 (4), 265-272, 2004.

[21] C. Eckart, Vortices and Streams Caused by Sound Waves, Phys. Rev, vol. 73, 68–76, 1948.

[22] C. I. Funk, A. Clark Jr., R. J. Connett, Am. J. Physiol. 258 (Cell Physiol. 27), C995-C1005, 1990.

[23] D. L. Gardner and G. W. Swift, A cascade thermoacoustic engine, J. Acoust. Soc. Am. 114(4), 1905–1919, 2003.

[24] D. Gobin and B. Goyeau, Natural convection in partially porous media : a brief overview, Int. J. Num. Meth. Heat Fluid Flow, Emerald 18 (3-4), 465–490, 2008.

[25] K. Goda, A multistep technique with implicit difference schemes for calculating two or three-dimensional cavity flows, J. Comput. Phys., 30, 76–95, 1979.

[26] J. L. Guermond, P. D. Minev, J. Shen, An overview of projection methods for incompressible flows., Comp. Meth. Appl. Mech. Eng., 195, 6011–6045, 2006.

[27] O. Hireche, C. Weisman, D. Baltean-Carlès, P. Le Quéré, M.X. François, L. Bauwens, numerical model of a thermoacoustic engines, C. R. Mécanique 338, 18–23, 2010.

[28] M.F. Hamilton, Y.A. Ilinskii, E.A. Zabolotskaya, Acoustic streaming generated by standing waves in two-dimensional channels of arbitrary width, J. Acoust. Soc. Am. 113(1), 153-160, 2003.

[29] O. Hireche, C. Weisman, D. Baltean-Carlès, P. Le Quéré, L. Bauwens, Low Mach number analysis of idealized thermoacoustic engines with numerical solution, J. Acoust. Soc. Am. 128 (6), 3438–3448, 2010.

[30] O. Hireche, I. Ramadan, C. Weisman, D. Baltean-Carlès, V. Daru, H. Bailliet, Y. Fraigneau, « Experimental and numerical investigation of natural convection flows in two horizontal thermoacoustic cavities », Int. J. Heat Mass Transfer 149, 119195, 2020.

[31] M. Kaviani, Principles of Heat Transfer in Porous Media, second ed., Springer, New York, 1999.

[32] P. Le Quéré, R. Masson, and P. Perrot, A Chebyshev collocation algorithm for 2D Non-Boussinesq Convection *J. Comp. Physics*, vol.103, No2, 1992.

[33] P. Le Quéré, C. Weisman, H. Paillère, J. Vierendeels, E. Dick, R. Becker, M. Braack, J. Locke, ESAIM : Mathematical Modelling and Numerical Analysis, vol. 39 (3), 609-616, 2005.

[34] J. Lighthill, Acoustic streaming., J. Sound Vib. 61, 391–418, 1978.

[35] L. Ma, C. Weisman, D. Baltean-Carlès, I. Delbende, L. Bauwens, Effect of a resistive load on the starting performance of a standing wave thermoacoustic engine : A numerical study, J. Acoust. Soc. Am. 138 (2), 847–857, 2015.

[36] B. Maherault, B. Vaillant, C. Weisman, P. Le Quéré, Ecoulement de convection naturelle en cavité carrée avec de grands écarts de température, *Notes et Doc. LIMSI* No 99-14, 1999.

[37] L. Menguy and J. Gilbert, Non-linear Acoustic Streaming Accompanying a Plane Stationary Wave in a Guide, Acta Acustica united with Acustica 86, 249–259, 2000.

[38] G. Michel and G.P. Chini, Strong wave-mean-flow coupling in baroclinic acoustic streaming, J. Fluid Mech. 858, 536–564, 2019.

[39] W.L. Nyborg, Acoustic streaming due to attenuated plane waves, J. Acoust. Soc. Am. 25, 68–75, 1953.

[40] J.-F. Mercier, C. Weisman, M. Firdaouss and P. Le Quéré, Heat transfer associated to natural convection flow in a partly porous cavity, Journal of Heat Transfer 124(1), 130–143, 2002.

[41] D.A. Nield, A. Bejan, Convection in Porous Media, third ed., Springer, New York, 2006.

[42] H. Paillère, P. Le Quéré, C. Weisman, J. Vierendeels, E. Dick, M. Braack, F. Dabbene, A. Beccantini, E. Studer, T. Kloczko, C. Corre, V. Heuveline, M. Darbandi, S. F. Hosseinizadeh, ESAIM : Mathematical Modelling and Numerical Analysis, vol. 39 (3), 617-621, 2005.

[43] S. Paolucci, On filtering of sound from the Navier-Stokes equations, *Sandia National lab. Report SAND 82-8257*, 1982 (non publié).

[44] N. Pan, S. Wang, C. Shen, Visualization investigation of the flow and heat transfer in thermoacoustic engine driven by loudspeaker, Int. J. Heat and Mass Transf. 55, 7737–7746, 2012.

[45] N. Pan, S. Wang, C. Shen, A fundamental study on characteristic of thermoacoustic engine with different tilt angles, Int. J. Heat and Mass Transf. 74, 228–237, 2014.

[46] D. W. Peaceman, H. H. Rachford, The numerical solution of parabolic and elliptic differential equations, J. Soc. Indust. Appl. Math., 3(1), 28–41, 1955.

[47] G. Poignand, P. Lotton, G. Penelet and M. Bruneau, Thermoacoustic, Small Cavity Excitation to Achieve Optimal Performance, Acta Acust. United Ac. 97, 926–932, 2011.

[48] G. Poignand, A. Podkovskiy, G. Penelet, P. Lotton and M. Bruneau, Analysis of a Coaxial, Compact Thermoacoustic heat pump, Acta Acust. United Ac. 99, 898–904, 2013.

[49] Q. Qi, The effect of compressibility on acoustic streaming near a rigid boundary for a plane traveling wave, J. Acoust. Soc. Am. 94, 1090–1098, 1993.

[50] I. Ramadan, H. Bailliet and J.-C. Valière, Experimental investigation of the influence of natural convection and end-effects on Rayleigh streaming in a thermoacoustic engine, J. Acoust. Soc. Am., 143(1), 361–372, 2018.

[51] L. Rayleigh, On the Circulation of air observed in Kundt's Tubes, and on some allied acoustical problems, Philos. Trans. R. Soc. 175, 1-21, 1884.

[52] Lord Rayleigh, The Theory of Sound, Second Edition, Macmillan, 1894.

[53] J. Rémus. http ://jacques-remus.fr/

[54] I. Reyt, V. Daru, H. Bailliet, S. Moreau, J.-C. Valière, D. Baltean-Carlès, C. Weisman, Fast acoustic streaming in standing waves : Generation of an additional outer streaming cell, J. Acoust. Soc. Am. 134 (3), 1791–1801, 2013.

[55] I. Reyt, H. Bailliet and J.C. Valière, Experimental investigation of acoustic streaming in a cylindrical wave guide up to high streaming Reynolds numbers, J. Acoust. Soc. Am. 135 (1), 27–37, 2014.

[56] N. Rott, Damped and thermally driven acoustic oscillations in wide and narrow tubes, Z. Angew. Math. Phys. 20, 230—243, 1969.

[57] N. Rott, The influence of heat conduction on acoustic streaming, Zeitschrift für Angewandte Mathematik und Physik (ZAMP) 25, 417–421, 1974.

[58] N. Rott, Thermoacoustics, Adv. Appl. Mech. 20, 135–243, 1980.

[59] N. Rott, Thermoacoustics, Dover, New York, 2nd ed., vol.2, sec. 232, 1980.

[60] Y. Saad, Iterative Methods for Sparse Linear Systems, 2nd Edition, Society for Industrial and Applied Mathematics, 2003.

[61] H. Schlichting, Berechnung ebener periodischer grenzschichtströmungen (calculation of plane periodic boundary layer streaming), Physikalische Zeitschrift 33(8), 327–335, 1932.

[62] V.K. Schuster and W. Matz, Uber stationare Strömungen im Kundtschen Rohr (On Stationary Streaming in Kundt Tubes). Akust. Zeitschrift 5, 349–352, 1940.

[63] S. Spoelstra, M.E.H. Tijani, Thermoacoustic heat pumps for energy savings, in seminar "Boundary crossing acoustics", in : Proceedings of the Acoustical Society of the Netherlands, 2005.

[64] G. W. Swift, Thermoacoustics Engines, J. Acoust. Soc. Am. 84, 1145-1180, 1988.

[65] G. W. Swift, Thermoacoustics : A unifying perspective for some engines and refrigerators, Acoustical Society of America, Melville, NY, 2002.

[66] M.W. Thompson, A.A. Atchley and M.J. Maccarone, Influences of a temperature gradient and fluid inertia on acoustic streaming in a standing wave, J. Acoust. Soc. Am. 117(4), 1839–1849, 2005.

[67] D.H. Truong, C. Weisman, D. Baltean-Carlès, F. Jebali Jerbi et J. Rémus, Etude du démarrage du son produit par un instrument de musique thermoacoustique : le thermophone, Congrès Français d'Acoustique, Le Mans, 2016.

[68] B. Ward, J. Clark and G.W. Swift, Design Environment for Low-Amplitude Thermoacoustic Energy Conversion (DeltaEC) User's Guide (version 6.2), Los Alamos National Laboratory, 2008.

[69] C. Weisman, D. Barkley, P. Le Quéré, Transition to unsteadiness of non-Boussinesq natural convection solutions, Proc. I.C.C.H.M.T, Cachan, 2005.

[70] C. Weisman, D. Baltean-Carlès, P. Duthil, P. Le Quéré, Natural convection in a stack of horizontal plates in a differentially heated cavity, in : Proceedings of the 19th International Symposium on Transport Phenomena (ISTP-19), Reykjavik, Island, 2008.

[71] P.J. Westervelt, The Theory of Steady Rotational Flow Generated by a Sound Field, J. Acoust. Soc. Am. 25, 60–67, 1953.

[72] A.S. Worlikar, O.M. Knio, R. Klein, Numerical simulation of a thermoacoustic refirgerator ; unsteady adiabatic flow around the stack, J. Comp. Physics 127, 424-451, 1996.

[73] A.S. Worlikar, O.M. Knio, R. Klein, Numerical simulation of a thermoacoustic refirgerator ; stratified flow around the stack, J. Comp. Physics 144, 299-324, 1998.

[74] S. Xin and P. Le Quéré, Stability of two-dimensional (2D) natural convection flows in air-filled differentially heated cavities : 2D/3D disturbances, Fluid Dynamics Research, IOP Publishing 44 (3), pp.031419, 2012.

[75] L. Zoontjens, C. Howard, A. Zander and B. Cazzolato, Feasibility Study of an Automotive Thermo acoustics Refrigerator, in : Proceedings of Acoustics, Busselton, Australia, 2005.

.

J.-F. Mercier, **C. Weisman**, M. Firdaouss and P. Le Quéré, “Heat transfer associated to natural convection flow in a partly porous cavity”, Journal of Heat Transfer, V. 124, 1, 130-143, 2002.

Jean-François Mercier[1]

Catherine Weisman[2]
e-mail: weisman@limsi.fr

Mouaouia Firdaouss
e-mail: firdaous@limsi.fr

Patrick Le Quéré
e-mail: plq@limsi.fr

LIMSI-CNRS, BP 133,
F-91403 Orsay Cedex,
France

Heat Transfer Associated to Natural Convection Flow in a Partly Porous Cavity

The object of this study is the heat transfer associated to a buoyancy-induced flow developing in a rectangular cavity, partly filled with porous medium, with given heat flux from the sides. Numerical experiments show the existence of a quasi parallel solution away from the top and bottom end walls, characterized by a linear vertical temperature profile. Analytical expressions are derived for the velocity and temperature which, combined with an energy balance, enable us to relate the stratification to the other governing parameters. Influence of the porous layer's permeability and width, and of the Rayleigh number on the flow structure and heat transfer is thoroughly investigated, and summarized in simple relationships. [DOI: 10.1115/1.1418372]

Keywords: Analytical, Heat Transfer, Natural Convection, Porous Media, Stratified

1 Introduction

Studies of flows developing in a system containing simultaneously a fluid and a porous layer are of both mathematical and practical interest. Such systems are important for instance in cooling or ventilation problems, and juxtaposition of porous and fluid layers is also involved in thermal insulation of buildings. Many numerical approaches have been applied to the study of these systems. Simulations were performed on flows developing in a rectangular cavity, either exclusively porous (Lauriat and Prasad [1]) or separated into a fluid part and a porous part. These last studies were lead for isothermal flows (Vafai and Kim [2]), natural convection flows (Beckerman et al. [3], Le Breton et al. [4]) and for thermal and solutal convection flows (Gobin et al. [5]). There is a thorough and up to date review of such studies in Nield and Bejan [6].

In this paper we focus on the buoyancy-induced flows created in a rectangular cavity partly filled with a porous layer, when natural convection is induced by imposing a given horizontal heat flux from the sides. We have not found any account of an experimental setup to ensure cooling under constant heat flux. However, although there are experimental setups with either constant temperature or constant heat flux on the hot side and constant temperature on the cold side, other boundary conditions may be used for modeling: Nield and Bejan [6] specified that in the field of thermal insulation engineering, a model including constant heat flux boundary conditions is more appropriate to describe the side heating of a porous layer. Moreover, in this paper we will perform a numerical-analytical study and we use these boundary conditions because they clearly lead to a quasi-parallel solution.

It is difficult to characterize the flow developing in a composite porous-fluid layer using a numerical approach because of the large number of independent parameters: there are physical parameters like the porous layer permeability and the thermal conductivity and heat capacity of both the porous medium and the fluid, geometrical parameters like the width of the porous layer or the aspect ratio of the cavity, and last the heat power injected in the cavity. Because numerical simulations are time consuming, exploration of the flow characteristics when all these parameters vary within a physical range is very difficult. Our purpose here is to use alternate means to direct numerical integration of Navier-Stokes and energy equations. This study is motivated by recent results obtained with numerical simulations of the two-dimensional flow produced in a cavity where the heat flux is imposed on the vertical boundaries (Weisman et al. [7]). The horizontal boundaries are maintained thermally insulated. Isothermal contour lines and streamlines are shown on Fig. 1.

The porous medium is adjacent to the heated wall and extends through a quarter of the cavity's width. It clearly appears that the two-dimensional flow becomes one-dimensional away from the horizontal boundaries, and that this approximation is valid on a large vertical extent. Also the temperature is found to vary linearly in the vertical direction. These flow properties allow us to seek an analytical form for the solution in the central part of the cavity.

The analytical form was found by solving the problem in a cavity of infinite vertical extent and finite width, partly filled with a porous layer (also of infinite vertical extent) adjacent to the hot wall. This calculation was analogous to the work previously done for a solely fluid cavity (Bergholz [8], Kimura and Bejan [9]) or a completely porous cavity (Trevisan and Bejan [10]). In all these studies, the analytical solution that was exhibited involves a stratification parameter γ, which in the case of a cavity of infinite vertical extent is a free parameter. But for a vertically bounded cavity, γ is a function of the characteristic parameters of the porous medium and of the Ra number. The value of γ appearing in the analytical solution can then be calculated by using an energy balance between conductive and convective heat transfer in the cavity. A similar method was first applied in the case of cavities with differentially heated walls, for a fluid cavity (Gill [11]) or a porous cavity (Weber [12]). Later the same method was used when the vertical walls are submitted to a heat flux, in the cases of fluid (Kimura and Bejan [9]) or porous (Trevisan and Bejan [10]) cavities.

After having presented the studied geometry, governing equations will be detailed and then the stationary analytical flow will be calculated. A full parameter study will be presented: the vertical velocity and temperature profiles will be shown and analyzed for a large range of the four independent parameters, the Rayleigh number, the Darcy number, the width of the porous medium *ep* and the vertical temperature stratification γ. Then, using the energy balance in the closed cavity to relate γ and *ep*, Ra and Da, thorough analysis of the hydrodynamic and thermal characteristics (and specifically Nusselt numbers) will be presented.

---

[1]Present address: Laboratoire de Simulation et de Modélisation des phénomènes de Propagation, Ensta, URA 853 du CNRS, Paris, France. E-mail: jmercier@ensta.fr

[2]Corresponding author.

Contributed by the Heat Transfer Division for publication in the JOURNAL OF HEAT TRANSFER. Manuscript received by the Heat Transfer Division September 26, 2000; revision received June 25, 2001. Associate Editor: H. H. Bau.

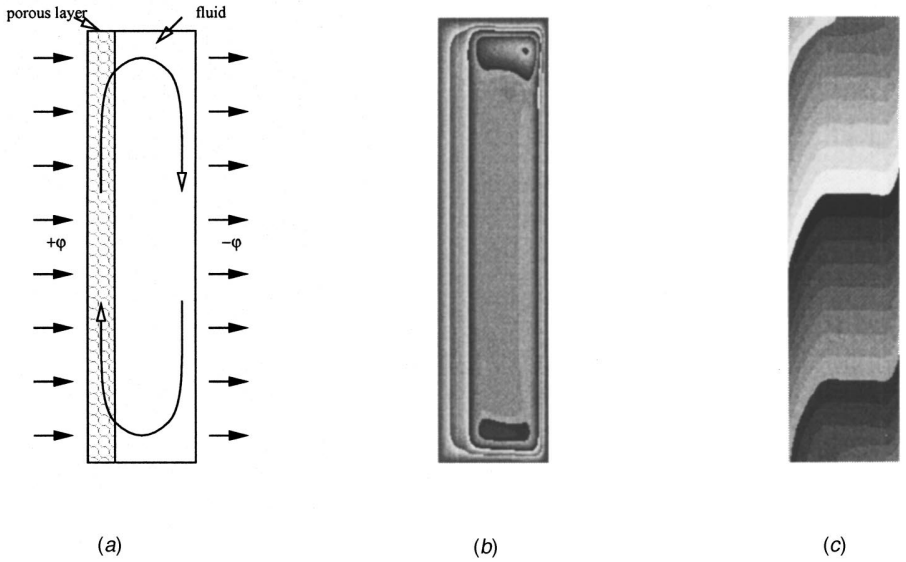

Fig. 1 Problem geometry (*a*) and steady flow in a cavity of aspect ratio 4, with heat flux imposed on the sides. A porous layer covers the heated wall and fills one quarter of the cavity. Ra=10^6, Da=10^{-4}: (*b*) streamlines, (*c*) isothermal lines.

2 Problem Geometry

We study the two-dimensional flow developing in a vertical rectangular cavity, as represented on Fig. 2. The cavity is of height H and of width L. The horizontal axis is noted x while the vertical axis is called z. The vertical wall located at $x=0$ is submitted to a horizontal heat flux density φ, constant and uniform. On the other vertical wall at $x=L$ is extracted the same heat flux density. The cavity is partly filled with a vertical porous layer of width d placed in contact of the heated vertical boundary. Before studying the heat transfer in the cavity, the first step consists in modelling the flow in the fluid and in the porous medium, which will be presented in the next paragraph.

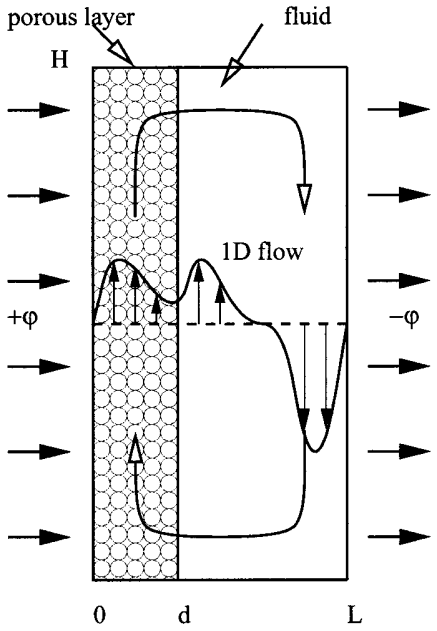

Fig. 2 Problem geometry and vertical flow $w_0(x)$ in the central part of the cavity

3 Generalized Navier-Stokes Equations in Partly Porous Cavities

3.1 Description of the Natural Convection Flow in a Partly Porous Medium. The flow in the cavity is induced by natural convection, and the fluid density ρ is assumed to vary linearly with respect to the temperature $\tilde{T}$, according to the law $\rho=\rho_c[1-\beta(\tilde{T}-T_c)]$. β is the thermal expansion coefficient, T_c and ρ_c are respectively the reference temperature and density. Outside the porous area the fluid is supposed to obey Navier-Stokes equations in the Boussinesq approximation.

In the porous medium the Navier-Stokes equations are modified using a Darcy-Brinkman formulation. The equations can be written in a unified form by using a parameter ϵ, equal to 1 in the porous medium, and equal to 0 in the fluid part.

$$\left(1-\epsilon+\frac{\epsilon}{\phi}\right)\frac{\partial\vec{U}}{\partial t}+(1-\epsilon)(\vec{U}.\vec{\nabla})\vec{U}$$
$$=-\frac{1}{\rho_c}\vec{\nabla}P+\frac{\rho}{\rho_c}\vec{g}+\nu_{\text{eff}}\Delta\vec{U}-\epsilon\frac{\nu}{K}\vec{U} \quad (1)$$

$$\rho_c c_p\left(\frac{\partial}{\partial t}+\vec{U}.\vec{\nabla}\right)\tilde{T}=\lambda\Delta\tilde{T}, \quad (2)$$

$$\vec{\nabla}.\vec{U}=0. \quad (3)$$

In these equations, $\vec{U}$ is the fluid velocity and P is the pressure, K is the porous medium permeability, ϕ the porosity and ν is the fluid viscosity. The effective viscosity ν_{eff} takes into account the influence of the porous medium on the fluid flow and is assumed to be related to the fluid viscosity through the relation $\nu_{\text{eff}}=\nu/\phi$. The momentum Eq. (1), which makes use of ϕ, implicitly takes into account the distinction between Darcy velocity and intrinsic velocity (see Nield and Bejan [6] and Amiri and Vafai [13,14]). However, since the porosity only appears in the time-dependent term, the value of ϕ will have no influence on the steady-state solution. The Darcy term included in Eq. 1 induces a decrease of the fluid velocity due to the presence of the porous medium. In the

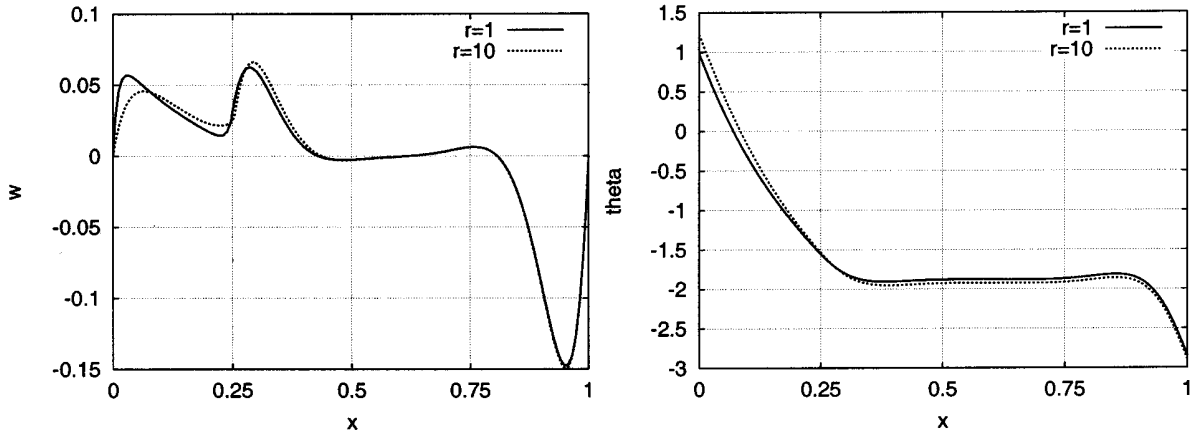

Fig. 3 Comparison of dimensionless vertical velocity profiles (left) and temperature profiles (right) at mid-height of the cavity for $r=1$ and $r=10$ for one given numerical setup, $A=4$, $\mathrm{Ra}=10^6$, $\mathrm{Da}=10^{-4}$, $ep=0.25$

porous medium only, the advective term $1/\phi^2 \vec{U}.\vec{\nabla}\vec{U}$ is excluded, which is consistent with the work of Beck [15]. Also in this equation, the Forchheimer term $c_f/K^{1/2}|\vec{U}|\vec{U}$, where c_f is a geometric function (Alazmi and Vafai [16]), is neglected, since all simulations are carried out for low values of the Reynolds number, typically $R_e \leqslant 1$. The Reynolds number can be calculated using the relation of the permeability (Cozeni-Karman formula) and of the geometric function c_f versus the porosity (Alazmi and Vafai [16]). This Darcy-Brinkman formulation is also used in Amahmid et al. [17] where low Reynolds number values are also found. Large values of the Reynolds number may be obtained for $\phi \to 1$. However, the Cozeni-Karman formula is not valid in this porosity limit. Moreover, there is some uncertainty about the validity of the Forchheimer law at large porosity (Nield and Bejan [6]). Therefore, this term will be omitted in the rest of this paper.

Givler and Altobelli [18] have estimated the ratio r of the effective viscosity to the fluid viscosity to be approximately 7.5 ± 3, for values of the Reynolds number comparable to ours. We have performed several numerical simulations with values of r ranging from 1 to 12. For a rather high ratio $r=10$, we observed small changes (see Fig. 3) in the flow in the porous part compared to the case of a ratio equal to 1, the maximum value of the stream function changing by 5.6 percent. The associated decrease of the vertical temperature stratification is small, of 0.4 percent. Also, for a given numerical setup, the vertical temperature stratification is found to vary almost linearly with r. The steady-state solutions obtained for $r=10$ are close to those obtained for $r=1$, i.e., $\nu_{\mathrm{eff}}=\nu$.

This ratio r should be varied in order to correctly describe several kinds of porous media, but based on these results, we will assume in the rest of this paper that $\nu_{\mathrm{eff}}=\nu$. Moreover since we cannot assess that our simulations would fit well with experimental data and because we do not pretend to cover all the experimental setups, we have chosen in our article to focus on the case of $r=1$. This assumption is commonly used when studying natural convection in a composite fluid-porous layer (Beckerman et al. [3], Lauriat and Prasad [1], Le Breton et al. [4]), and also when adding solutal convection (Gobin et al. [5]). It is also used in isothermal flows (Vafai and Kim [2]). Moreover the assumption $\nu_{\mathrm{eff}}=\nu$ has been found to be in good agreement with some experimental observations (Beckerman et al. [3]).

One main modeling issue is the choice of appropriate boundary conditions at the fluid-porous medium interface. In the numerical code, the viscosity coefficients are calculated in order to ensure the continuity of velocity and stress at the interface, which is in agreement with model number 2 in a recent study of Alazmi and Vafai [19]. The widest used condition is that of Beavers and Joseph (1967) relating the stress discontinuity to the difference between the fluid velocity at the interface and the velocity in the porous medium slightly away from the interface. This condition involves an empirical parameter, therefore requiring to be fitted with experimental data. Ochoa-Tapia and Whitaker [20,21] also provide an interface condition, introducing a stress discontinuity. Again their condition involves a parameter that needs to be fitted with experimental data. Such data are hard to find: in the experimental work of Le Breton [22], it is specified that they were able to measure the vertical velocity in a horizontally differentially heated cavity, but unable to access the velocity in the porous layer. Ochoa-Tapia and Whitaker also used a variable porosity model to continuously link the Darcy and Stokes equations, and then showed the complexity of the interface region. However, they still did not succeed in giving a representation model compatible with experimental observation. Therefore we have chosen to solve the motion equations without modifying the existing interface conditions in the numerical code. We will develop the appropriate conditions for the analytical solution in Section 4.

In the energy equation, we have considered the case of a porous medium of the same thermal conductivity λ_{eff} than the fluid conductivity λ. In this paper we also consider the special case where the porous medium heat capacity $(\rho c_p)_p$ is the same as the fluid's. Different models linking λ and λ_{eff} are available (Beckerman et al. [3]), but the previous assumptions are justified in the case of a porous medium porosity close to one (Le Breton et al. [4]). Although these assumptions may seem restrictive, they allow us to obtain a plan-parallel flow satisfying the generalized Navier-Stokes equations. Indeed these assumptions allow for the continuity of the temperature and of the heat flux through the fluid-porous interface, which is in agreement with model number I of Alazmi and Vafai [19]. Without these assumptions, the temperature would still be continuous, but no longer analytic.

3.2 Dimensionless Form of the Generalized Navier-Stokes Equations. Classical scaling analysis for the pure fluid buoyancy flow induced in a vertical plate heated with a given flux density leads to the following typical scales L, $\kappa \mathrm{Ra}^{2/5}/L$, $\Delta T^\star = \varphi L \mathrm{Ra}^{-1/5}/\lambda$, $L^2/\kappa \mathrm{Ra}^{2/5}$ and $\rho_c \nu \kappa \mathrm{Ra}^{2/5}/L^2$, respectively for length, velocities, temperature, time and pressure (Bejan [23]). One can note that the Rayleigh number appears with a power of 2/5 in this scaling analysis, which is directly related to the given heat flux boundary condition, as developed in Bejan [23] (see p. 131). Also, the non-dimensional parameters governing the problem are different when solely porous flow is considered (see for example Straughan [24]), as opposed to the fluid-porous flow considered here.

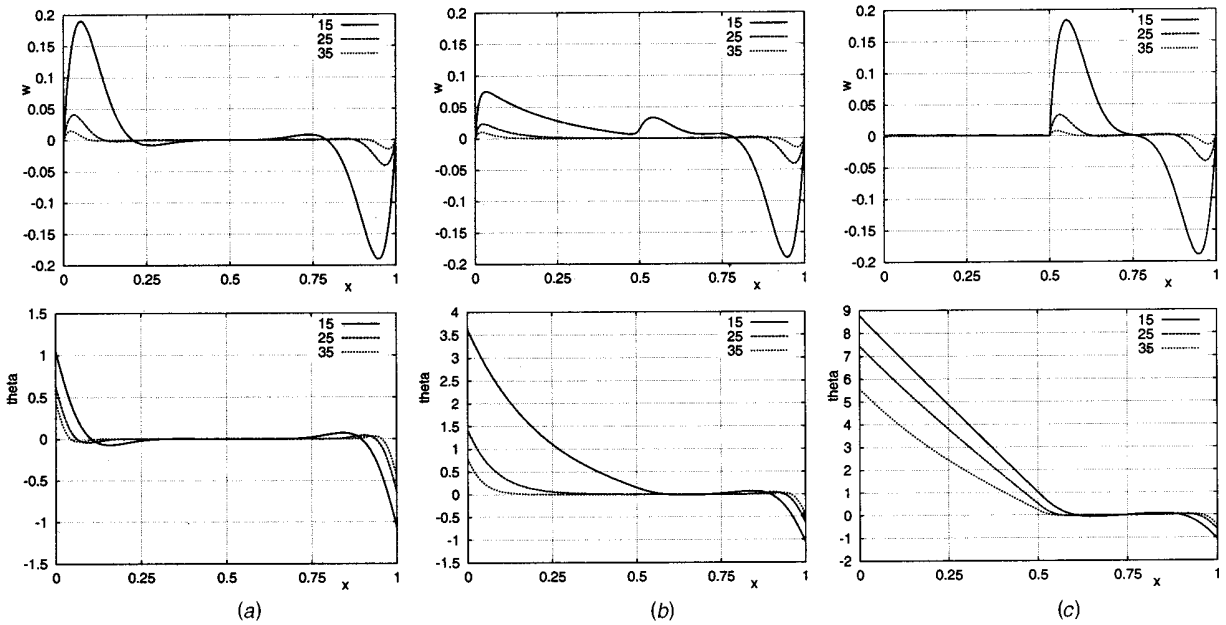

Fig. 4 Steady state profiles $w_0(x)$ and $\theta_0(x)$ for Ra$=10^6$, $ep=0.5$, and γ varying in the range [15,35]: (*a*) Da$=1$, (*b*) Da $=10^{-4}$, and (*c*) Da$=10^{-6}$

The Rayleigh number is defined as $\mathrm{Ra}=g\beta\varphi L^4/\lambda\nu\kappa$ where the thermal diffusivity is equal to $\kappa=\lambda/\rho_c c_p$. In a non-dimensional form, the governing Eqs. 1, 2, and 3 in the porous medium read:

$$\frac{\mathrm{Ra}^{2/5}}{\mathrm{Pr}}\left[\left(1-\epsilon+\frac{\epsilon}{\phi}\right)\frac{\partial}{\partial t}+(1-\epsilon)\vec{u}.\vec{\nabla}\right]\vec{u}$$

$$=-\vec{\nabla}p+\mathrm{Ra}^{2/5}(T-T_c)\vec{z}+\Delta\vec{u}-\frac{\epsilon}{\mathrm{Da}}\vec{u}, \qquad (4)$$

$$\mathrm{Ra}^{2/5}\left(\frac{\partial}{\partial t}+\vec{u}.\vec{\nabla}\right)T=\Delta T, \qquad (5)$$

$$\vec{\nabla}.\vec{u}=0, \qquad (6)$$

where the Prandtl number is defined as $\mathrm{Pr}=\nu/\kappa$ and the Darcy number as $\mathrm{Da}=K/L^2$.

4 Stationary Solution

In this paragraph we will determine analytically the one-dimensional flow created in a cavity of infinite vertical extent and finite width L, submitted to a given heat flux from the sides and partly filled with a porous layer of width d such that $ep=d/L$, adjacent to the heated wall. The stationary solution is a vertical velocity field depending only upon the horizontal coordinate $\vec{u}_0=w_0(x)\vec{z}$. The associated temperature field is made of two contributions $T-T_c=\delta z+\theta_0(x)$: a constant vertical temperature gradient δ, and a horizontal temperature distribution $\theta_0(x)$. δ is dimensionless and is deduced from the dimensional vertical temperature gradient α through the relation $\delta=\alpha L/\Delta T^\star=\alpha\lambda\mathrm{Ra}^{1/5}/\varphi$. The horizontal temperature distribution is due to the convective heat transport associated to the vertical temperature gradient δ through the vertical flow $w_0(x)\vec{z}$. Eq. 4 and Eq. 5 become for the stationary solution

$$\vec{0}=-\vec{\nabla}p_0+\mathrm{Ra}^{2/5}(\delta z+\theta_0)\vec{z}+D^2w_0\vec{z}-\frac{\epsilon}{\mathrm{Da}}w_0\vec{z}, \qquad (7)$$

$$\mathrm{Ra}^{2/5}\delta w_0=D^2\theta_0. \qquad (8)$$

Equation 8 can be integrated between $x=0$ and $x=1$, showing that $\int_0^1 w_0(x)dx=0$, and, therefore, this solution satisfies mass conservation. Projection on the x axis of Eq. 7 shows that p_0 is only a function of z. Equation 7 can then be projected onto the z axis, and variables can be separated. The stationary pressure field $p_0(z)$ is found to be a second order polynomial in z, and Eq. 8 can be used to eliminate the temperature, leading to a fourth order differential equation for $w_0(x)$. The new system is

$$D^4w_0-\frac{\epsilon}{\mathrm{Da}}D^2w_0+4\gamma^4w_0=0, \qquad (9)$$

$$\mathrm{Ra}^{2/5}(\theta_0-\theta_c)=\frac{\epsilon}{\mathrm{Da}}w_0-D^2w_0, \qquad (10)$$

where $D=d/dx$, θ_c is a free constant, and the parameter γ is given by

$$4\gamma^4=\mathrm{Ra}^{4/5}\delta=\alpha\lambda\mathrm{Ra}/\varphi. \qquad (11)$$

In the following the parameter δ will never appear again, and γ will be called the stratification parameter.

The boundary conditions on the left and right walls are zero velocity (no slip) and given dimensionless heat flux:

$$w_0=0 \text{ and } D\theta_0=-\mathrm{Ra}^{1/5}, \text{ at } x=0 \text{ and } 1. \qquad (12)$$

The boundary conditions at the interface between the fluid and the porous medium are the continuity of the velocity field, of the temperature and of their first derivative with respect to the x coordinate (Beckerman et al. [3]). These conditions are necessary to find a solution (w_0,θ_0) in the correct functional framework ($w_0 \in H^2(]0,1[)$, $\theta_0\in H^1(]0,1[)$).

A one-dimensional solution is found, taking the form of the sum of four complex exponential terms in each domain, the do-

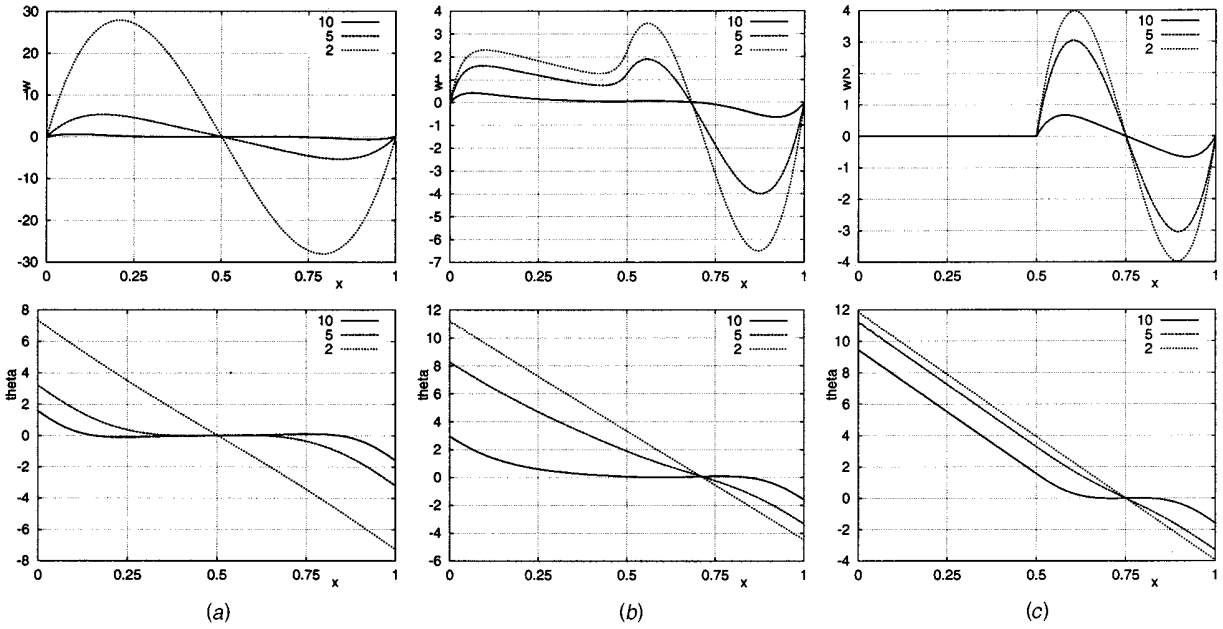

Fig. 5 Steady-state profiles $w_0(x)$ and $\theta_0(x)$ for Ra$=10^6$, $ep=0.5$, and γ varying in the range [2,15]: (*a*) Da$=1$, (*b*) Da $=10^{-3}$, and (*c*) Da$=10^{-6}$

main containing only fluid, and the one filled with the porous medium. Introducing $\Delta = 1/\mathrm{Da}^2 - 16\gamma^4$, when Δ is positive the solution reads

$$w_0(x) = A_1 e^{x\sqrt{1/2(1/\mathrm{Da}+\sqrt{\Delta})}} + A_2 e^{-x\sqrt{1/2(1/\mathrm{Da}+\sqrt{\Delta})}} + A_3 e^{x\sqrt{1/2(1/\mathrm{Da}-\sqrt{\Delta})}} + A_4 e^{-x\sqrt{1/2(1/\mathrm{Da}-\sqrt{\Delta})}}, \quad 0 < x < ep$$

$$w_0(x) = B_1 e^{(1+i)\gamma x} + B_2 e^{(1-i)\gamma x} + B_3 e^{(-1+i)\gamma x} + B_4 e^{(-1-i)\gamma x}, \quad ep < x < 1. \tag{13}$$

When Δ is negative, the previous formulas are still valid replacing $\sqrt{\Delta}$ with $i\sqrt{-\Delta}$. The temperature field $\theta_0(x)$ is obtained from the velocity field derivatives according to Eq. 10. Using the boundary conditions and the interfacial conditions, the eight constants are calculated by solving a 8×8 linear system. This analytical solution has been compared with a numerical solution obtained by direct simulation in a two-dimensional configuration, and excellent agreement has been obtained (Weisman et al. [7]). It is interesting to note that the stationary solution does not depend on the Prandtl number $Pr = \nu/\kappa$, which is not the case for the perturbations of this base flow for example.

Our results could be generalized to the case of a ratio $r(=\nu_{\mathrm{eff}}/\nu)$ different from 1, by changing equation (9) into

$$\alpha D^4 w_0 - \frac{\epsilon}{\mathrm{Da}} D^2 w_0 + 4\gamma^4 w_0 = 0, \tag{14}$$

where a new function $\alpha(\epsilon) = 1 - \epsilon + r\epsilon$ has been introduced. Then the interface condition would be the continuity of w_0 and of $\alpha D w_0$, keeping the continuity of temperature and heat flux.

The stationary velocity and temperature profiles depend on numerous parameters: the Rayleigh and Darcy numbers, the dimensionless width *ep* of the porous layer and also the parameter γ. In the case of a cavity of infinite vertical extent considered here, the stratification parameter γ is a free parameter. γ will be calculated in the next section in the case of a closed cavity. Before that, the influence of all four parameters previously mentioned on the velocity and temperature profiles will be discussed.

4.1 Influence of the Darcy Number. In order to illustrate the effect of the Darcy number, we will first consider the case Ra$=10^6$ and $ep=0.5$, i.e., the porous layer filling half of the cavity. The Darcy number used here, $\mathrm{Da} = K/L^2$, is defined using the macroscopic reference length L. A "microscopic" Darcy number, Da′ would be multiplied by a factor typically of $\approx 10^4$, since $\mathrm{Da}' = K/l^2 = (K/L^2).(L^2/l^2)$. Da′ should vary in the range $10^{-11} \leqslant \mathrm{Da}' \leqslant 10^5$ (values for fiber glass [25] p. 9, p. 26), corresponding to $10^{-15} \leqslant \mathrm{Da} \leqslant 10$. A porous medium characterized by a very low Darcy number is very impermeable, and should act like a solid medium. On the contrary, very high values of the Darcy number are characteristic of a very permeable medium, which should behave like a solely fluid phase. The effects of variation of the Darcy number upon the velocity and temperature profiles differ according to the range of γ, and two main ranges are presented:

Large Values of γ: $15 \leqslant \gamma \leqslant 35$. Variations of the velocity w_0 and of the temperature distribution θ_0 versus the horizontal coordinate x are represented on Fig. 4 for three values of the Darcy number belonging to the range $[10^{-6},1]$. As expected when the value of the permeability is large (Da$=1$), the porous layer behaves like a fluid medium and the flow develops in the whole width of the cavity. The flow takes the form of two separated boundary layer flows, one flow going upward near the heated wall and the return flow moving downward near the cooled wall. In the core between the two boundary layer flows, the velocity is nearly equal to zero. For larger Da numbers, the same curves are obtained. For intermediate values of the permeability (Da$=10^{-4}$), the upward flow splits into two flows: one developing in the porous part, the other one appearing in the fluid part in contact with the porous layer. Last in the case of a low value of the porous medium permeability (Da$=10^{-6}$ or smaller), the porous layer is equivalent to a solid layer and the flow just develops in the fluid part, $ep \leqslant x \leqslant 1$. Therefore we observe that the upward boundary layer becomes located next to the porous layer, which behaves like a solid boundary. We also observe that the effect of the decrease of the Darcy number is to bring the upward boundary layer

closer to the downward boundary layer, and thus to reduce the independence between the two boundary layers. The effect of the increase in γ is an increase of the absolute maximum velocity in the boundary layers.

Now for the horizontal temperature distribution $\theta_0(x)$, it must be stated that given the heat flux boundary conditions, the temperature field is defined except for one constant value θ_c. We take that constant to be zero in the middle part of the purely fluid layer. The temperature is then found to be constant (equal to zero) throughout the fluid, except in the boundary layers, and that holds for all values of Da or γ. In the purely fluid part, to the upward and downward boundary layer flows are associated small variations of θ_0. In the porous medium, the temperature variation is larger and increases continuously when the permeability decreases or when γ increases. In the case of a low value of the permeability of the porous medium ($Da=10^{-6}$), heat transfer in the porous layer is quasi conductive and the temperature consequently varies linearly.

It is useful to note that whatever the value of the Darcy number is, the same downward flow and associated temperature distributions are observed near the cooled vertical wall. This is due to the fact that the medium is still purely fluid in contact of the cold wall, and also that the two boundary layers do not interact. The temperature gradient over the fluid medium is the same for all permeability values.

Small Values of γ: $2 \leqslant \gamma \leqslant 15$. Profiles of the velocity w_0 and of the temperature distribution θ_0 versus the horizontal coordinate x are represented on Fig. 5 for three values of the Darcy number. The case $\gamma=5$ summarizes the effect of changes in the value of the Darcy number for small values of γ: it appears that the decrease in Da induces a transition from a double boundary layer regime to a conduction regime flow. This last flow is associated to a temperature profile varying linearly on the whole width of the cavity.

4.2 Influence of the Rayleigh Number. It should be noted that the widths of the boundary layers are independent of the Rayleigh number, once γ, *ep*, and Da are specified. The effect of varying the Rayleigh number is to modify the maximum value of the velocity and of the temperature. More precisely when the value of Ra is increased by a factor of 10, the maximum value of the velocity is multiplied by four and the maximum value of the temperature (at $x=0$) is multiplied by a factor close to 5/3. It should also be noted that this study focuses on stationary solutions, and that therefore these calculations only hold for Rayleigh numbers below the critical Ra number for the first bifurcation.

4.3 Influence of *ep* and of γ. The influence of the width of the porous layer *ep* and of the value of the vertical temperature stratification γ appears more clearly for a value of the Darcy number $Da=10^{-6}$. On Fig. 6 are represented the variations of the velocity profile for the following parameter values: $Ra=10^6$, $Da=10^{-6}$, $\gamma=15$, the value of the porous layer width varying between $ep=0.25$ and $ep=0.75$. It appears that an increase in the width of the porous layer induces a transition from a separated boundary layers flow to a dependent boundary layers flow and last to a conduction regime flow.

The same transitions take place when the stratification parameter γ decreases. This can be seen on Fig. 7, showing the variations of the velocity profile for $Ra=10^6$, $Da=10^{-6}$, $ep=0.25$, with γ increasing from $\gamma=5$ to $\gamma=20$.

As already mentioned in the introduction, the stratification parameter γ is a free parameter for the natural convection flow within an infinite vertical slot. But when dealing with a finite cavity, the vertical extent of the flow is bounded by horizontal walls, and that may be taken into account to determine the value of the stratification parameter, as shown in the next paragraph.

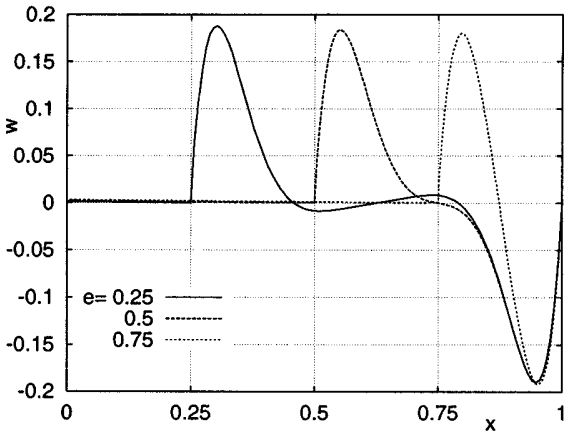

Fig. 6 Velocity profiles $w_0(x)$ for $Ra=10^6$, $Da=10^{-6}$, $\gamma=15$ and three values of *ep*: *ep*=0.25, *ep*=0.5, and *ep*=0.75

5 Determination of the Stratification Parameter

5.1 Energy Balance Method. The method, apparently first developed by Kimura and Bejan [9], consists in defining a control volume incorporating the upper horizontal boundary of the cavity, located at $z=H$, and part of the vertical walls, as represented on Fig. 8. Conservation of energy inside the control volume leads to equality between convective and conductive heat fluxes through the control volume surface S:

$$\int_S \rho_c c_p \tilde{T}\vec{U}.d\vec{S} = \int_S \lambda \vec{\nabla}\tilde{T}.d\vec{S}. \tag{15}$$

In a non-dimensional form Eq. 15 becomes

$$\mathrm{Ra}^{2/5} \int_S T\vec{u}.d\vec{S} = \int_S \vec{\nabla}T.d\vec{S}. \tag{16}$$

Replacing T with $T=T_c+\delta z+\theta_0(x)$ and using mass conservation through any horizontal plane

$$\int_0^1 w_0 dx = 0,$$

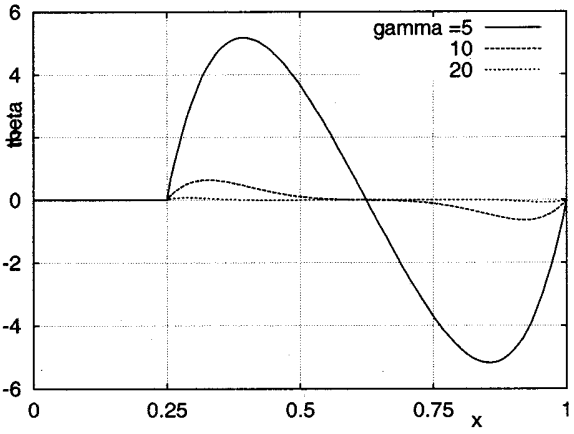

Fig. 7 Velocity profiles $w_0(x)$ for $Ra=10^6$, $Da=10^{-6}$, *ep* =0.25 and three values of γ: $\gamma=5$, $\gamma=10$ and $\gamma=20$

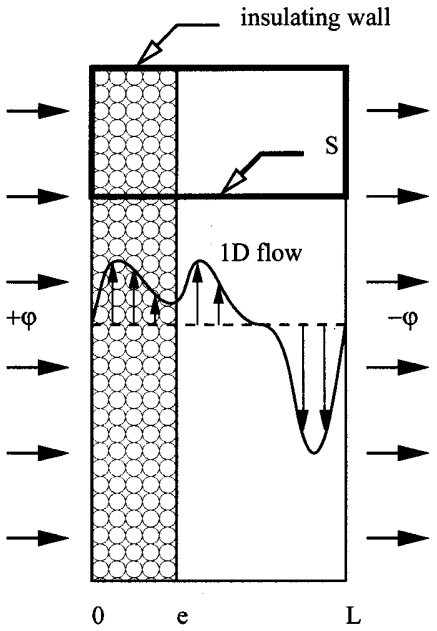

Fig. 8 Location of the control volume, with boundary *S* shown in bold line

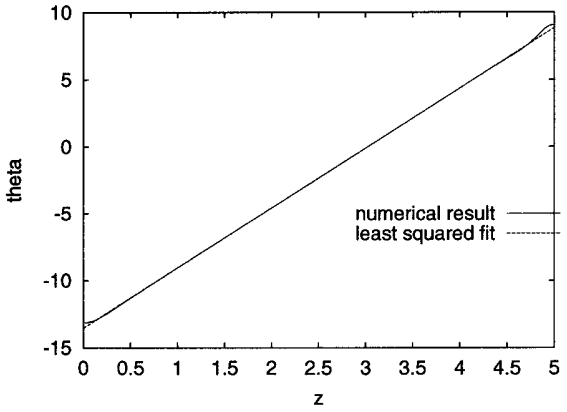

Fig. 9 Vertical temperature profile obtained from two-dimensional numerical simulations at mid-width of the cavity for Da$=10^{-4}$, $ep=0.25$, Ra$=10^6$, $A=5$. A least squared approximation for the central linear region is shown.

the left hand side of Eq. 16 can be simplified. Also the upper horizontal boundary is insulating, and the fluid velocity is zero on all cavity walls. Consequently, the following energy balance is obtained:

$$\int_0^1 w_0 \theta_0 dx = \frac{4\gamma^4}{\mathrm{Ra}^{6/5}}. \tag{17}$$

Once the Rayleigh and Darcy numbers are chosen, Eq. 17 is solved for γ using a bisection method. The solution for the vertical velocity and for the temperature is then completely determined using the analytical expressions for w_0 and θ_0 previously detailed.

5.2 Comparison With Numerical Simulations. The values of the stratification parameter γ obtained using the analytical expressions of Eqs. 10 and 13 and the energy balance method described in the previous paragraph were compared with those issued from direct integration of the two-dimensional time dependent Navier-Stokes and energy equations. For a given set of the aspect ratio $A=H/L$, the porous layer width *ep*, the Ra number and the Da number, the equations were integrated until a steady state was reached using a projection method and a second order backward Euler scheme, on a 128×256 regular mesh. The algorithm of march in time is based on a projection method, known as a modified fractional time step method and introduced by [26]. The algorithm involves implicit treatment of the viscous and Darcy penalty terms as well as explicit treatment of the convective term and the pressure gradient. The spatial discretization is based on a staggered mesh where the discrete equations are based on finite volume formulation. The resulting sparse pentadiagonal systems are solved by an ADI factorization. For solving the Poisson equation (in solving for the pressure field), a multigrid method is used. It was proven that the convergence of the numerical method is of order 2 in space and in time. The numerical results were examined by varying the number of grid points from 32×64 to 128×256. Refining the grid allowed to obtain grid independent results. In the case of a cavity filled with fluid (i.e., for $D_a>10$), results are in exact agreement with results of [27]. It should be noted that reaching truly steady state solution in the case of Neumann type boundary conditions (given heat flux on the boundaries) requires integrating the equations over very long times (typically one to two hours on NEC SX5 are needed). The calculation is much faster for Dirichlet boundary conditions (given temperature).

The vertical temperature profile (see the example shown in Fig. 9, corresponding to $A=5$, $ep=0.25$, Ra$=10^6$, and Da$=10^{-4}$) on the section $x=0.5$ was then plotted. For large enough aspect ratios ($A>1$), there is a large linear section away from the boundary coordinates ($z=0$ and $z=H/L=A$). The corresponding slope δ was calculated using a least squared error approximation, from which the value of the corresponding value of γ was calculated using Eq. 11, $\gamma=(\mathrm{Ra}^{4/5}\delta/4)^{1/4}$. The value found for γ does not depend on the vertical section selected for plotting the temperature profile.

Excellent agreement results from the comparison between values of γ determined numerically and semi-analytically using the energy balance: for a heating of the fluid corresponding to Ra $=10^6$, and a porous width $ep=0.25$ the values of the vertical temperature stratification found from the energy balance are $\gamma=14.787$, $\gamma=16.299$, and $\gamma=14.736$ for, respectively, the Darcy number values Da$=10^{-2}$, 10^{-4}, and 10^{-6}. From the two-dimensional temperature distributions numerically obtained, the values $\gamma=14.79$, 16.30, and 14.74 were determined for a fluid of Prandtl number $\mathrm{Pr}=\nu/\kappa=0.71$ and for the same values of the Darcy number than previously. The agreement is convincing.

Relation (17) is independent of the cavity's height *H*. Therefore the stratification parameter γ is independent of the aspect ratio *A* of the cavity, as soon as *H* is large compared to the width *L* of the cavity. We verified this property on the solution obtained numerically. We performed a test on a completely fluid cavity (see Fig. 10(*a*)) as well as on a fluid-porous cavity (see Fig. 10(*b*)), for several aspect ratios ranging from 1 to 8. In both cases, the Rayleigh number was equal to 10^6. The vertical temperature profiles shown correspond to the $x=1/2$ section. On the figures the central linear portion of the profiles seem to be parallel for all shown aspect ratios. We calculated the corresponding values of γ. In the first case (fluid cavity, Ra$=10^6$) the values obtained are as follows: $\gamma=14.821$ (for an aspect ratio $A=1$), $\gamma=14.640$($A=2$), $\gamma=14.663$ ($A=4$), $\gamma=14.661$ ($A=6$), $\gamma=14.660$ ($A=8$). The value found analytically is $\gamma=14.659$. In the second case (Da$=10^{-4}$, $ep=0.25$, Ra$=10^6$), the obtained numerical values are $\gamma=16.301$ ($A=2$), $\gamma=16.301$ ($A=4$), and $\gamma=16.300$ ($A=6$), the analytical value being $\gamma=16.298$. The aspect ratio $A=1$ is too small to be able to neglect the effect of the horizontal boundaries. The result of these comparisons is clear and confirms

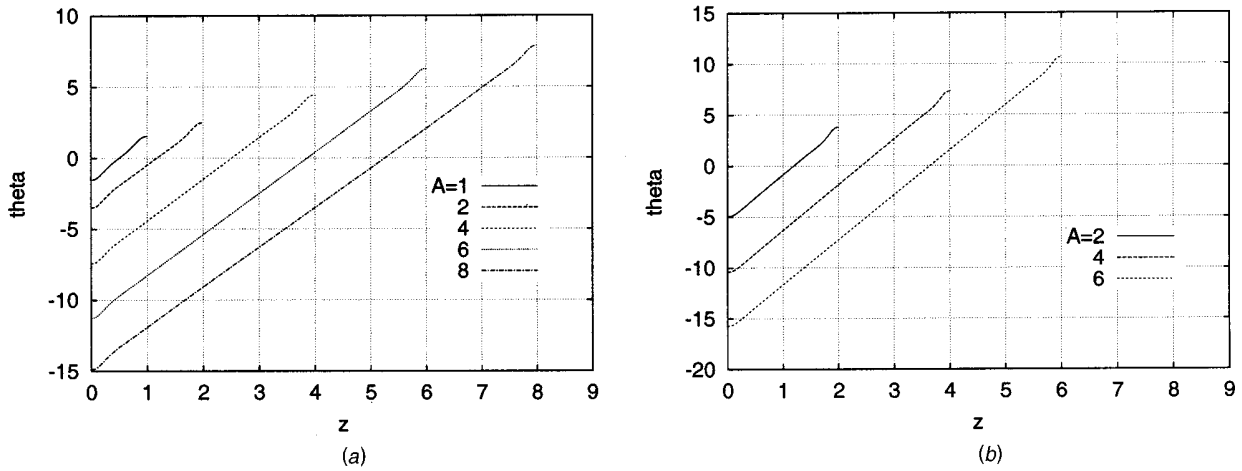

Fig. 10 Vertical temperature profile obtained from two-dimensional numerical simulations at mid-width of the cavity for several aspect ratios: (*a*) fluid cavity, Ra=10^6; (*b*) Da=10^{-4}, *ep*=0.25, Ra=10^6.

that γ is independent of the aspect ratio A. We next present a parameter study of the stratification parameter γ, calculated using the analytical solution and the energy balance.

5.3 Results for a Porous Layer of Width *ep*=0.5. On Fig. 11(*a*) and (*b*) are drawn the variations of the stratification parameter γ with respect to the Darcy number for several values of the Rayleigh number, and a constant width of the porous layer width $ep=0.5$.

First of all, one can note that for large Darcy number values γ is approximately constant: $\gamma(\mathrm{Da})\approx\gamma(1)$ for $\mathrm{Da}\geqslant 1$. This value of γ will be noted γ_f since the porous medium is then very permeable and behaves like a fluid. Similarly, for small Darcy number values, γ is also approximately constant: $\gamma(\mathrm{Da})\approx\gamma(10^{-9})$ for $\mathrm{Da}\leqslant 10^{-9}$. This value of γ will be noted γ_s, since the porous medium is then very impermeable and behaves like a solid. Therefore our results obtained for the range $10^{-9}\leqslant\mathrm{Da}\leqslant 1$ can be easily extended to the range $10^{-15}\leqslant\mathrm{Da}\leqslant 10^{6}$.

Furthermore looking at large values of the Rayleigh number in Fig. 11(*a*), one can see that $\gamma_f\approx\gamma_s$. This means that when the porous layer fills half of the cavity, the vertical temperature stratification does not change whether the flow develops either through the whole width of the cavity or only through only half of the cavity. This property remains true for all *ep* values. However when Ra decreases, differences between the values of γ for extreme values of the permeability appear (Fig. 11(*b*)). For Ra $>2.10^4$ we note that γ_s is slightly larger than γ_f, whereas for Ra$<2.10^4$, we note that γ_s is slightly smaller than γ_f. For instance when $ep=0.5$ and Ra=10^4, we obtained $\gamma_f=5.322$ and $\gamma_s=5.012$.

The transition between γ_s and γ_f takes place on a fairly narrow Da range. In that transition, γ increases and reaches a maximum value noted $\gamma_{\max}$ for a value of the Darcy number denoted by $\mathrm{Da}_{\max}$ (located roughly between Da=10^{-3} and Da=10^{-6}). Thus, the influence of the porous medium permeability on the vertical temperature gradient is concentrated around this point ($\gamma_{\max}$,$\mathrm{Da}_{\max}$). The two values $\gamma_{\max}$ and $\mathrm{Da}_{\max}$ just depend upon the Rayleigh number and the width of the cavity, and it appears that the location of the maximum $\mathrm{Da}_{\max}$ decreases when the Rayleigh number takes larger values.

Last we observe that when the heating strength, measured by the Rayleigh number, is increased, the value of the stratification parameter follows the same behavior. This can be understood considering the heat conservation equation Eq. 16, where it appears

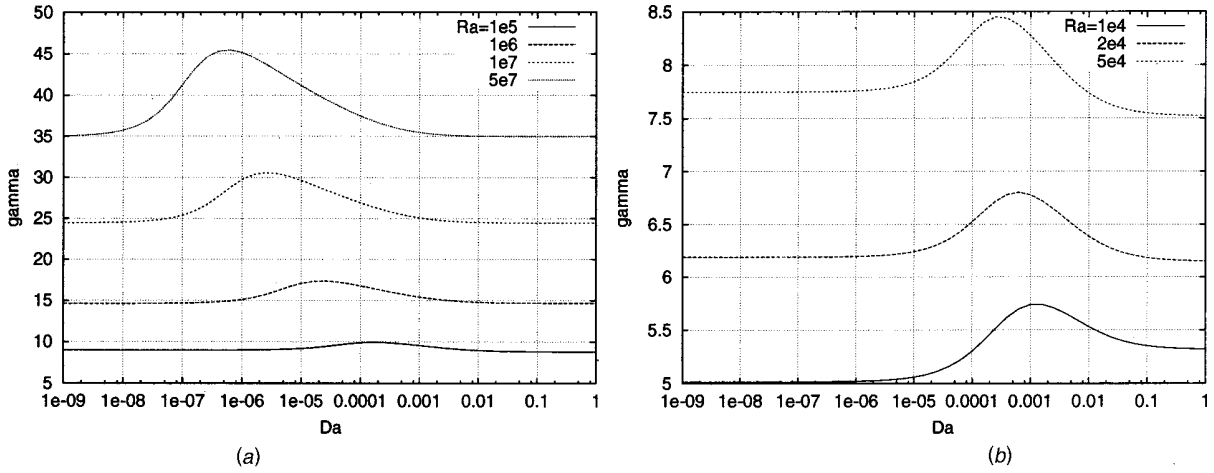

Fig. 11 Vertical temperature gradient γ versus the Darcy number Da for different heating strengths Ra, *ep*=0.5: (*a*) Ra $\in[10^5,5.10^7]$; and (*b*) Ra$\in[10^4,5.10^4]$.

that the vertical conductive heat transport term in the right hand side of the equation is proportional to a power law of the Rayleigh number.

The cavity studied here is characterized by parameters Ra and *ep*, and by the parameters γ_{max} and Da_{max} that we have just introduced. Useful relations between these four parameters can be found, and are presented in the following sections.

5.4 Case of a Purely Fluid Cavity Da=∞. The values of γ (denoted γ_f) for large values of the Darcy number are interesting, since in this case the cavity remains purely fluid, whatever the value of the width of the porous layer is. Thus this value depends only on the Rayleigh number.

Figure 12 shows the variations of $\log(\gamma_f)$ versus log(Ra) where log denotes the decimal logarithm, for twelve values of the Rayleigh number. γ_f is found to depend on the Rayleigh number according to the law

$$\gamma_f = 0.681\ \ \mathrm{Ra}^{2/9}. \tag{18}$$

Also in the same case of a purely fluid cavity, Kimura and Bejan [9] have found a power law between the vertical temperature gradient in the core of the base flow, the Rayleigh number Ra_{KB} and the aspect ratio A of the cavity: $\partial T/\partial z = \mathrm{CA}^{4/9}\mathrm{Ra}_{KB}^{8/9}$. Contrary to us, their result depends on the aspect ratio because they have used a Rayleigh number depending on the height of the cavity. Using our definition of the Rayleigh number, their law becomes: $\partial T/\partial z = C'\mathrm{Ra}_{KB}^{2/9}$, as in Eq. 18.

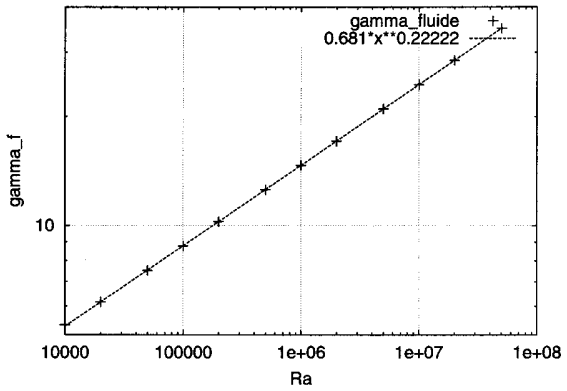

Fig. 12 log(γ_f) versus log(Ra), with 12 values of Ra shown

When the porous layer is no more perfectly permeable, there is a point of maximum γ called γ_{max}, with corresponding Da called Da_{max}. γ_{max} and Da_{max} are functions of Ra and *ep*. Expressions of these functions will be determined now.

5.5 Evolution of γ_{max} Versus Ra and *ep*. Figure 13(a) represents the variations of $\ln(\gamma_{max})$ versus the logarithm of the porous layer width for several values of the Rayleigh number. There

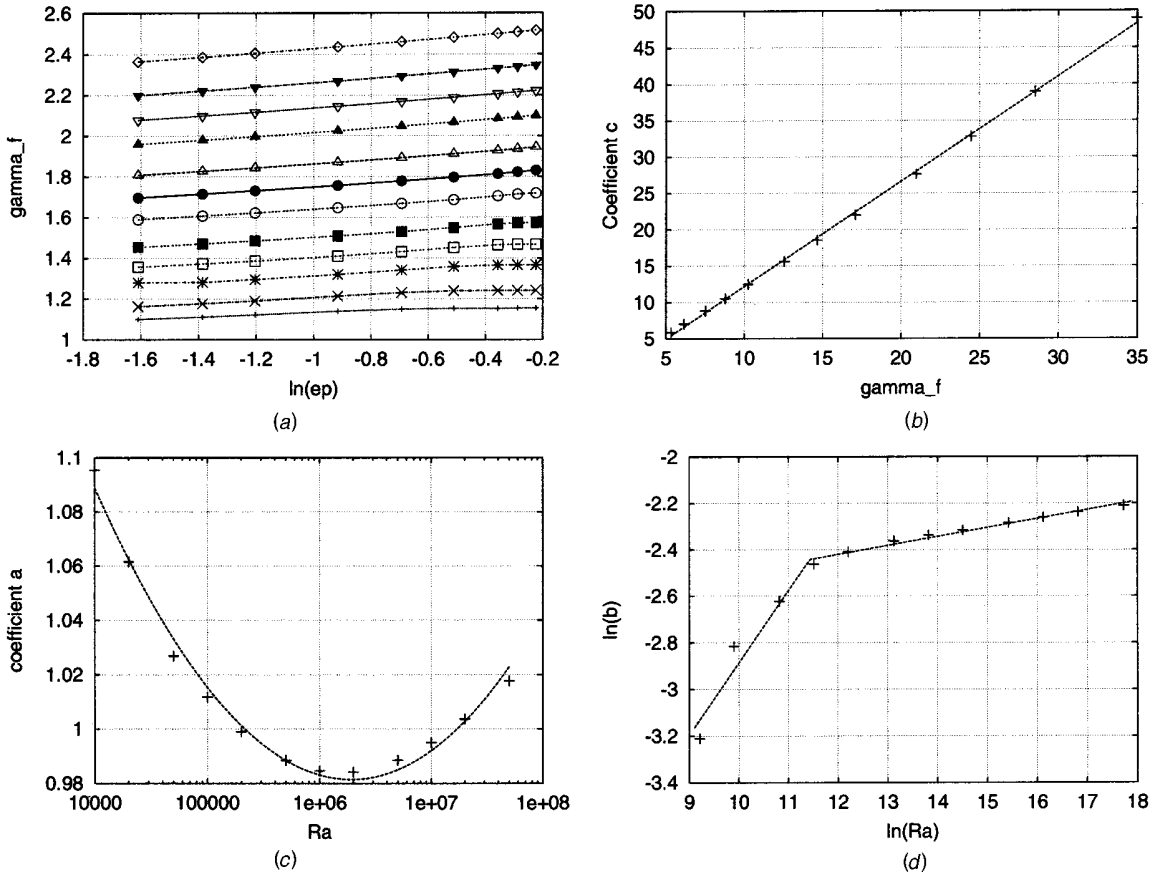

Fig. 13 (*a*) $\ln(\gamma_{max})$ versus ln(*ep*). Each line corresponds to a value of Ra, and on each line, each point corresponds to a value of *ep*. There are twelve Ra values in the $[10^4,5.10^7]$ range, and eight *ep* values in the [0.25,0.8] range; (*b*) *c*(γ_f) versus the stratification parameter γ_f in the entirely fluid layer, each point corresponds to one of the 12 Ra values of (*a*); (*c*) *a* versus ln(Ra), each point corresponds to one of the 12 Ra values of (*a*); (*d*) *b* versus Ra, each point corresponds to one of the 12 Ra values of (*a*).

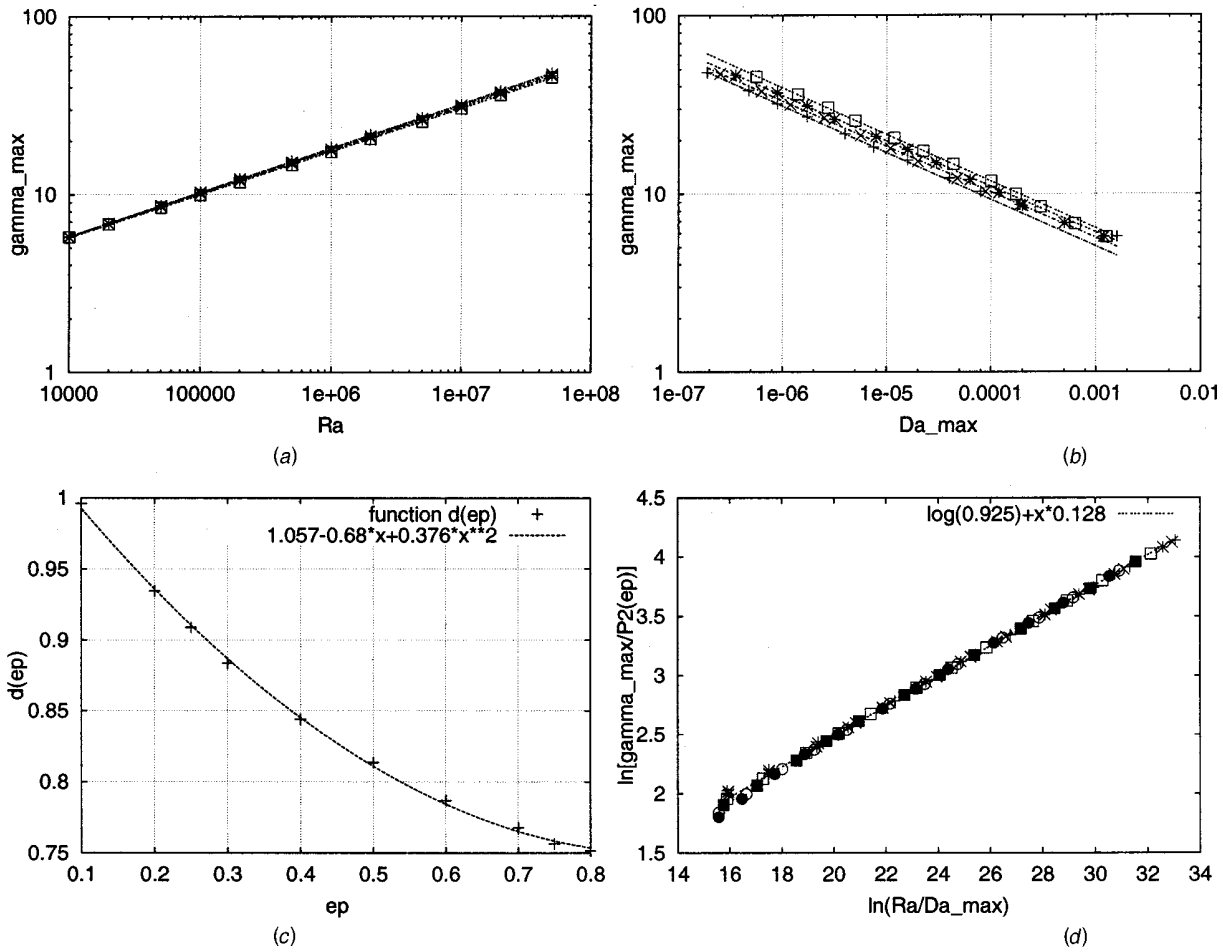

Fig. 14 (*a*) $\log(\gamma_{max})$ versus $\log(Ra)$. Each line corresponds to a value of *ep*, and on each line, each point corresponds to a value of Ra. There are twelve Ra values in the $[10^4,5.10^7]$ range, and five *ep* values in the [0.5,0.8] range; (*b*) $\log(\gamma_{max})$ versus $\log(Da)$, same *ep* values and Ra values as in (*a*); (*c*) function $d(ep)$ versus *ep*, all eight *ep* values in the [0.25,0.8] range; (*d*) $\ln(\gamma_{max}/P_2(ep))$ versus $\ln(Ra/Da_{max})$, all *ep* values and Ra values.

are twelve values of Ra: $Ra=10^4$, 2.10^4, 5.10^4, 10^5, 2.10^5, 5.10^5, 10^6, 2.10^6, 5.10^6, 10^7, 2.10^7, 5.10^7, and eight values of *ep*: $ep=0.25$, 0.3, 0.4, 0.5, 0.6, 0.7, 0.75, 0.8. At first glance, approximately parallel straight lines are obtained, leading to the law $\gamma_{max}=c(Ra)ep^{1/10}$. For each line the coefficient c was obtained using a least squared error fit. Instead of determining $c(Ra)$, variations of c versus the stratification parameter γ_f in the entirely fluid layer may be studied, since we have just shown that γ_f is linked to the Rayleigh number (Eq. (18). Figure 13(*b*) giving the variation of c versus γ_f, indicates that $c(Ra)=P_1(\gamma_f)$ where P_1 is a first order polynomial. More careful analysis showed that the straight lines observed on Fig. 13(*a*) are not perfectly parallel nor straight, and that $\gamma_{max}/c(Ra)$ is not exactly equal to $ep^{1/10}$. Writing the law in the form $\gamma_{max}/c(Ra)=a(Ra)ep^{b(Ra)}$, the functions $a(Ra)$ and $b(Ra)$ were fitted. Variations of a and $\ln(b)$ versus $\ln(Ra)$ are represented respectively on Fig. 13(*c*) and (*d*). The results are that function a takes the form of a second order polynomial of $\ln(Ra)$, and that b varies exponentially with Ra. As a summary, the analytical fit that found for evaluation of γ_{max} as a function of Ra and *ep* is

$$\begin{cases} \gamma_{max}=P_1(\gamma_f)a(Ra)ep^{b(Ra)}, \\ P_1(\gamma_f)=-2.27+1.44\gamma_f \\ a=1.769-0.113\ln(Ra)+3.891\ \ 10^{-3}(\ln(Ra))^2. \\ b=2.512\ \ 10^{-3}\times Ra^{0.310}\ \text{ for } Ra\leqslant 10^5 \\ \quad =5.604\ \ 10^{-2}\times Ra^{0.0385}\ \text{ for } Ra>10^5 \end{cases} \quad (19)$$

The above expression uses γ_f, which is a function of Ra, as written in Eq. 18. In the following chapter, another fit is found for the expression of γ_{max} as a function of Ra, Da_{max}, and *ep*.

5.6 Evolution of γ_{max} Versus Ra, Da_{max}, and *ep*. On Fig. 14(*a*) are represented the variations of the decimal logarithm $\log(\gamma_{max})$ versus $\log(Ra)$ for different values of the width of the porous layer. The same twelve values of Ra as in the previous section are used, and only 5 values of *ep* are shown on Fig. 14(*a*) and (*b*): $ep=0.5$, 0.6, 0.7, 0.75, 0.8. It appears that γ_{max} varies like $Ra^{1/4}$. In addition Fig. 14(*b*) gives the evolution of $\log(\gamma_{max})$ versus $\log(Da_{max})$, still for different values of *ep*. Here γ_{max} is found to vary like $Da_{max}^{-1/4}$. Thus the maximum value of γ depends upon the ratio of the Rayleigh number to Da_{max}, according to the law $\gamma_{max}=d(ep)(Ra/Da_{max})^{1/8}$. Values of $d(ep)$ were obtained using a least squared fit using all Ra values for a given *ep* value. The function $d(ep)$, represented on Fig. 14(*c*), is found to be well fitted with a second order polynomial: $d(ep)=P_2(ep)$. Similarly to the previous section, the power of 1/8 may be improved. From Fig. 14(*d*), giving the variations of $\ln(\gamma_{max}/P_2(ep))$ versus $\ln(Ra/Da_{max})$ for all eight values of the porous layer's width, and all twelve values of Ra, we deduce the law $\gamma_{max}/P_2(ep)=0.925\times(Ra/Da_{max})^{0.128}$.

As a summary, the analytical fit found for the evaluation of γ_{max} as a function of Ra, Da_{max}, and *ep* is:

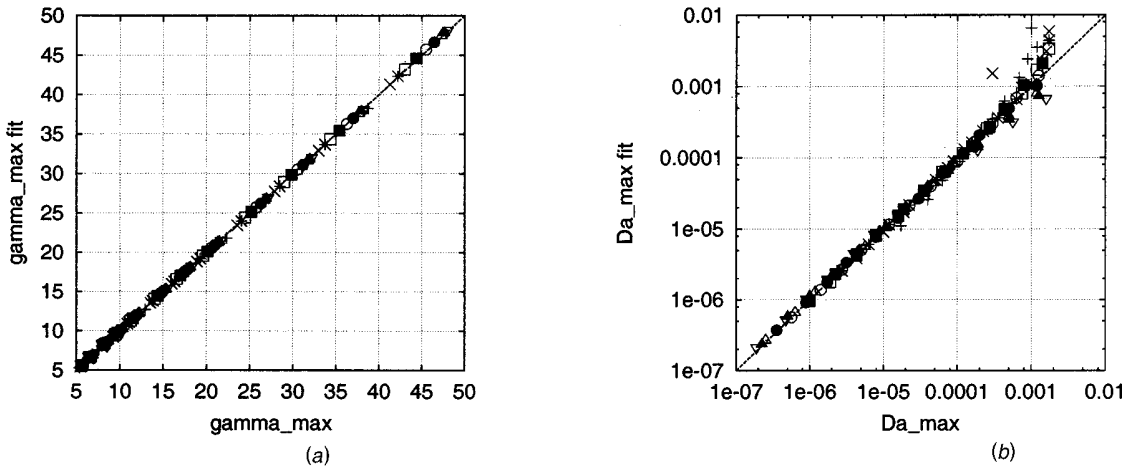

Fig. 15 γ_{max} (*a*) and Da_{max} (*b*) calculated from the analytical fit versus the same quantities calculated directly from the model equations. All points shown (12 values of Ra and 8 values of *ep*).

$$\begin{cases} \gamma_{max} = P_2(ep) \times 0.925 \times \left(\dfrac{Ra}{Da_{max}} \right)^{0.128} \\ P_2(ep) = 1.057 - 0.68 \times ep + 0.376 \times ep^2 \end{cases} . \quad (20)$$

From Eqs. 18, 19, and 20, the following law relating Da_{max} and the Rayleigh number and the porous layer's width may be deduced, where $P_1(\gamma_f)$, $P_2(ep)$, $a(Ra)$, and $b(Ra)$ are given in the referenced equations:

$$Da_{max} = Ra \times \left(\frac{P_2(ep) \times 0.925}{P_1(0.681 Ra^{2/9}) a(Ra) ep^{b(Ra)}} \right)^{7.8} . \quad (21)$$

This relation indicates which porous material must be used (more precisely which permeability should be chosen) in order to obtain maximum vertical heat transfer in the porous medium, for a given width of the porous layer (the width of the fiberglass layer in an insulating wall for example) and a given amount of energy supplied to the material.

According to the previous study, one can now determine γ_{max} and Da_{max} from the knowledge of Ra and *ep*, according to Eqs. 19 and 21 that summarize the fits that were performed. Figure 15 shows the quality of these fits for determining γ_{max} and Da_{max}. On the figure are shown on the *x* axes the values calculated from the analytical formulas giving $w_0(x)$ and $\theta_0(x)$ and from Eq. 17 for the energy balance, and on the *y* axes the values given from the fits of Eqs. 19 and 21. If the fits are correct, all points should fall on the $y=x$ line. Figure 15(*a*) shows the γ_{max} values and Fig. 15(*b*) shows the Da_{max} values. All points are shown (12 values of Ra and 8 values of *ep*). The fits seem to be correct, except for the estimate of Da_{max} for small Ra values (largest values of Da_{max}, for all *ep* values).

One interesting quantity is the ratio of γ_{max} versus γ_f: it measures the efficiency of the presence of a porous layer on the heat transfer in the cavity. On Fig. 16 are reported the variations of this ratio versus the Ra number or the Da_{max} number.

Results show that for a given porous width the presence of a porous layer improves the vertical heat transfer in the cavity in two specific situations: when external heating is intense (large Rayleigh number) or when the porous medium is more impermeable (small Da_{max}).

After having studied vertical transport of heat, the next paragraph will be devoted to the determination of horizontal heat transfer between the two vertical walls of the cavity, and the calculation of Nusselt numbers.

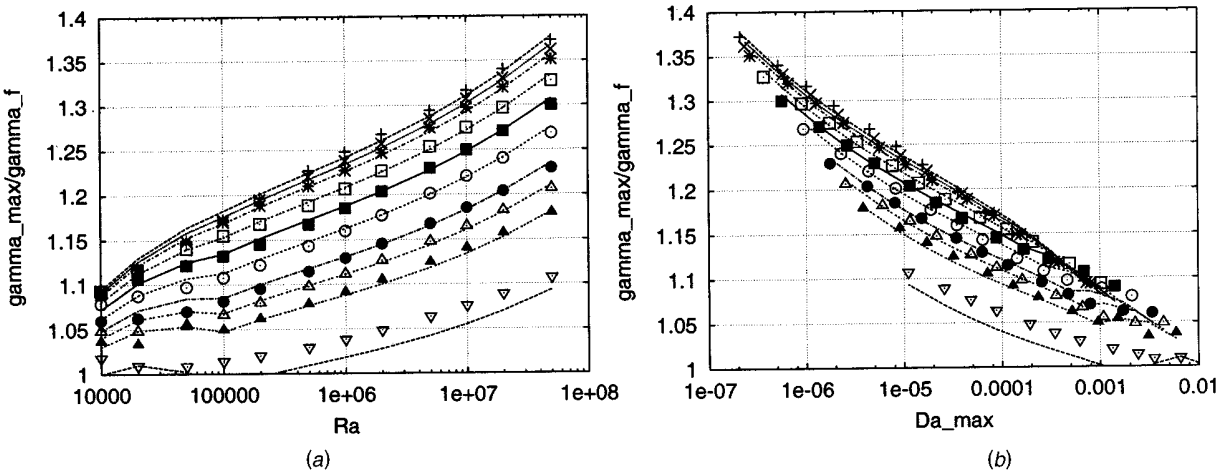

Fig. 16 γ_{max}/γ_f calculated from the analytical fit (solid curves) and calculated directly from the model equations (points) versus (*a*) Ra and (*b*) Da_{max}. All points shown (12 values of Ra and 8 values of *ep*, bottom *ep*=0.1 to top *ep*=0.8).

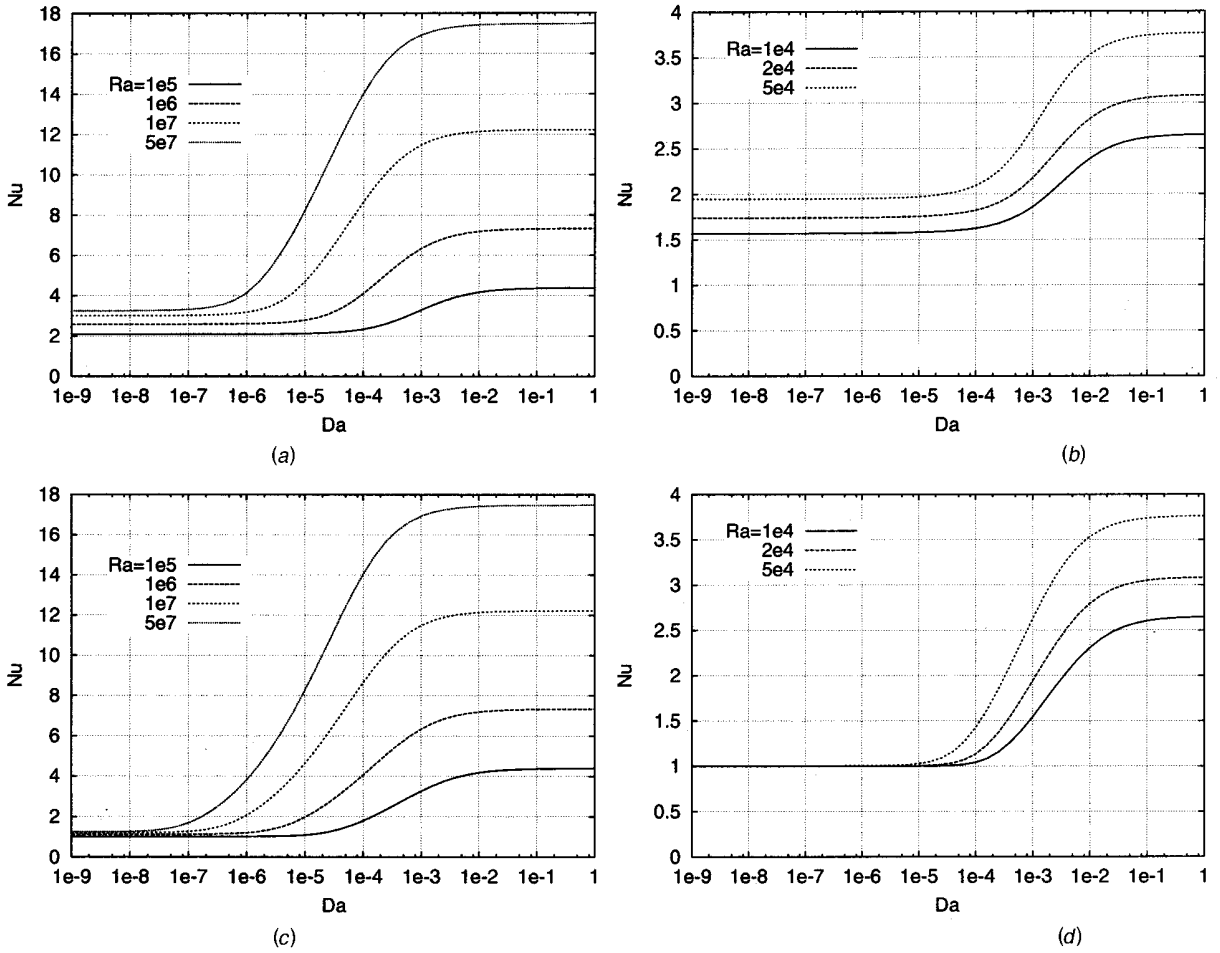

Fig. 17 Nusselt number Nu versus Da, top: $ep=0.25$, bottom: $ep=0.75$; (left) $Ra\in[10^5,5.10^7]$ (right): $Ra\in[10^4,5.10^4]$.

6 Nusselt Numbers

The cavity is submitted to a horizontal heat flux of density φ, and we saw in the previous paragraph that part of this injected energy is convected vertically. Now we are interested in the horizontal propagation of the energy through the width of the cavity. Once a horizontal heat flux φ is imposed, the horizontal heat transfer capacity of the cavity is characterized by the resulting horizontal temperature difference between the vertical boundaries $\Delta T=T(x=0)-T(x=L)$. As usual, the Nusselt number is defined as

$$\mathrm{Nu}=\frac{\varphi L}{\lambda \Delta T}, \tag{22}$$

which in dimensionless form, using $\Delta\theta_0=\theta_0(x=0)-\theta_0(x=1)$, is

$$\mathrm{Nu}=\frac{\mathrm{Ra}^{1/5}}{\Delta\theta_0}. \tag{23}$$

The efficiency of the horizontal heat transfer through the cavity is measured by the Nusselt number. When the width *ep* of the porous layer is fixed, variations of Nu versus the Darcy number for a fixed Rayleigh number are drawn on Fig. 17. In complement, when the Rayleigh number is fixed the variation of the Nusselt number versus Da for several porous layer thicknesses are presented on Fig. 18. From the two figures a predominant tendency in the behavior of the Nusselt number can be deduced: Nu increases with the Darcy and Rayleigh numbers, but decreases with *ep*. Therefore heat transfer is more efficient when the porous layer is permeable or thin, and when Ra is high. For small Da numbers, Nu is close to 1 (conductive heat transfer) and variation of Ra does not affect the value of Nu. This is especially true for larger porous layer widths *ep* (corresponding to an almost totally solid cavity).

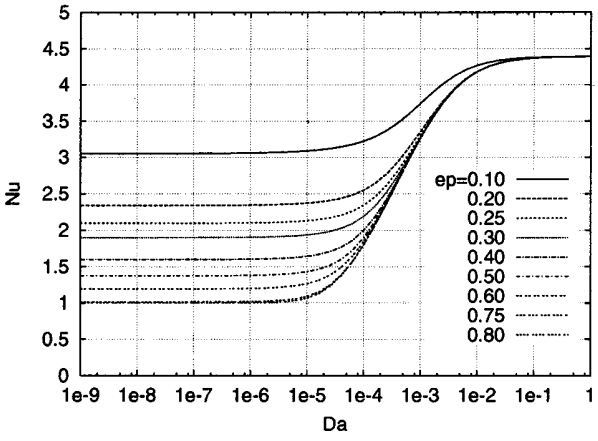

Fig. 18 Nusselt number versus Darcy number for various *ep* values, $Ra=10^5$

These results can be understood, looking back at the horizontal temperature profiles presented on Fig. 4 and Fig. 5. On these figures one can see the temperature difference $\Delta\theta_0$, which is inversely proportional to the Nusselt number through Relation 23. It clearly appears that the horizontal temperature distribution presents a large decrease essentially in the porous part. Moreover the temperature difference through the porous medium is proportional to the width of the porous layer, and is larger when the porous medium is impermeable (with a linear temperature variation): when strong vertical flow develops in the cavity, a large convective heat transport is induced, leading to a small horizontal temperature difference. Therefore horizontal heat transfer is essentially affected by the presence or the absence of flow. To strong vertical flow is associated large heat transfer. Then the influence of the Darcy number and of the porous part width previously described is directly deduced from the base flow characteristics, which are: the flow is stronger in the fluid layer, and is decelerated in the porous part as this layer becomes impermeable.

Concerning the influence of the Rayleigh number, one can look at the heat conservation equation Eq. 5 written in the case of a stationary flow $\Delta T = \mathrm{Ra}^{2/5}(\vec{u}.\vec{\nabla})T$. Thus an increase in the value of the Rayleigh number induces stronger vertical heat transport. Small horizontal temperature difference is then induced in the cavity.

7 Conclusion

We have presented the complete calculation of the one-dimensional buoyancy-induced flow developing in a rectangular cavity, where the vertical boundaries are submitted to a horizontal and uniform heat flux, and a vertical porous layer is placed close to the heated wall. Our aim was to improve the analytical determination of the one-dimensional flow (Weisman et al. [7]) by calculating the stratification parameter γ associated to the plan-parallel flow.

In the case of a vertically infinite cavity, γ is a free parameter and we have presented the influence of the characteristic parameters of the cavity (Da, Ra, *ep*, and γ) on the stationary flow. According to the values of these parameters, we can observe a transition from a double boundary layer flow (with boundary layers independent or linked) to a conductive regime flow.

In the case of a closed cavity, we have calculated the value for the stratification parameter. The method is based on the use of the balance between vertical convective and conductive heat transfer both in the fluid and in the porous medium. The obtained values of γ are also in perfect agreement with the values found with the two-dimensional numerical simulations. We have shown that the stratification parameter reaches a maximum value $\gamma_{\max}$ for an intermediate value of the porous medium permeability, $\mathrm{Da}_{\max}$. We have determined by fitting some simple relations between $\gamma_{\max}$, $\mathrm{Da}_{\max}$, *ep* and Ra. With these relations we can now determine the permeability of the porous material leading to maximal vertical heat transfer for a given heating strength, and a given porous layer width.

Moreover we have characterized the horizontal heat transfer through the cavity by calculating the temperature difference between the vertical walls of the cavity, once a given heat flux between the vertical boundaries is prescribed. This temperature difference is found to develop essentially in the porous part and therefore Nusselt numbers are larger when the porous layer becomes permeable or thin.

Now that we have completely characterized the base flow in the cavity, the linear stability analysis of this flow can be performed. This work, where perturbations are sought under the form of transverse propagating waves, is under progress.

Acknowledgments

Numerical simulations were performed on the SX5-NEC of the laboratory IDRIS-CNRS.

Nomenclature

A = aspect ratio $= H/L$
c_p = isobaric specific heat, J/kgK
Da = Darcy number $= K/L^2$
d = porous layer thickness, m
$\vec{dS}$ = surface vector
ep = dimensionless porous layer thickness
$\vec{g}$ = gravitational acceleration, m^2/s
H = cavity height, m
K = permeability of the porous medium, m^2
L = cavity width, m
Nu = Nusselt number $= \varphi L/\lambda\Delta T$
P = pressure, Pa
p = dimensionless pressure
Pr = Prandtl number $= \nu/\kappa$
r = ratio ν_{eff}/ν
Ra = Rayleigh number $= g\beta L^4\varphi/\lambda\nu\kappa$
t = time, s
$\tilde{T}$ = temperature, K
T = dimensionless temperature
T_c = reference temperature, K
ΔT = horizontal temperature difference, K
$\Delta T^\star$ = temperature difference scale $= \varphi L\,\mathrm{Ra}^{-1/5}/\lambda$, K
$\vec{U}$ = velocity vector, m/s
$\vec{u}$ = dimensionless velocity vector
u = dimensionless x component of the velocity
w = dimensionless z component of the velocity
x = horizontal coordinate
z = vertical coordinate
α = vertical temperature gradient, $\mathrm{K\,m^{-1}}$
β = fluid thermal expansion coefficient, $\mathrm{K^{-1}}$
δ = dimensionless vertical temperature gradient
$\Delta\theta_0$ = dimensionless horizontal temperature difference
ϵ = porous layer characteristic function
γ = stratification parameter $= (\mathrm{Ra}^{4/5}\delta/4)^{1/4}$
γ_s = stratification parameter for an almost solid porous medium
κ = thermal diffusivity $= \lambda/\rho_c c_p$, $\mathrm{m^2 s^{-1}}$
λ = fluid thermal conductivity, W/mK
μ = dynamic viscosity, $\mathrm{kg\,m^{-1}\,s^{-1}}$
ν = kinematic viscosity, $\mathrm{m^2\,s^{-1}}$
ρ = fluid density, $\mathrm{kg\,m^{-3}}$
ρ_c = fluid reference density, $\mathrm{kg\,m^{-3}}$
θ_0 = dimensionless horizontal temperature
θ_c = reference dimensionless temperature
φ = prescribed heat flux density, W/m^2
ϕ = porosity

Subscripts

0 = refers to stationary state
eff = refers to effective properties for a fluid-saturated porous medium
f = refers to the fluid
p = refers to the porous medium

References

[1] Lauriat, G., and Prasad, V., 1987, "Natural Convection in a Vertical Porous Cavity: A Numerical Study for Brinkman-Extended Darcy Formulation," ASME J. Heat Transfer, **109**, pp. 688–696.
[2] Vafai, K., and Kim, S. J., 1990, "Fluid Mechanics of the interface Region Between a Porous Medium and a Fluid Layer—An Exact Solution," Int. J. Heat Fluid Flow **11-3**, pp. 254–256.
[3] Beckerman, C., Viskanta, R., and Ramadhyani, S., 1988, "Natural Convection in Vertical Enclosures Containing Simultaneously Fluid and Porous Layer," J. Fluid Mech., **186**, pp. 257–284.
[4] Le Breton, P., Caltagirone, J. P., and Arquis, E., 1991, "Natural Convection in a Square Cavity With Thin Porous Layers on its Vertical Walls," ASME J. Heat Transfer, **113**, pp. 892–898.
[5] Gobin, D., Goyeau, B., and Songbe, J.-P., 1998, "Double Diffusive Natural

Convection in a Composite Fluid-Porous Layer,'' ASME J. Heat Transfer, **120**, pp. 234–242.
[6] Nield, D., and Bejan, A., 1998, *Convection in Porous Media*, 2nd edition, Springer-Verlag, New York.
[7] Weisman, C., Le Quéré, P., and Firdaouss, M., 1999, ''Sur une solution exacte de la convection naturelle en cavité partiellement remplie d'un milieu poreux,'' C. R. Acad Sc. Paris, Vol. 327-II B, pp. 235–240.
[8] Bergholz, R. F., 1978, ''Instability of Steady Natural Convection in a Vertical Fluid Layer,'' J. Fluid Mech., **84**, pp. 743–768.
[9] Kimura, S., and Bejan, A., 1984, ''The Boundary Layer Natural Convection Regime in a Rectangular Cavity with Uniform Heat Flux from the Side,'' ASME J. Heat Transfer, **106**, pp. 98–103.
[10] Trevisan, O. V., and Bejan, A., 1986, ''Mass and Heat Transfer by Natural Convection in a Vertical Slot Filled With Porous Medium,'' Int. J. Heat Mass Transf., **29**, pp. 403–415.
[11] Gill, A. E., 1966, ''The Boundary-Layer Regime for Convection in a Rectangular Cavity,'' J. Fluid Mech., **26**, pp. 515–536.
[12] Weber, J. E., 1974, ''The Boundary-Layer Regime for Convection in a Vertical Porous Layer,'' Int. J. Heat Mass Transf., **18**, pp. 569–573.
[13] Amiri, A., and Vafai, K., 1994, ''Analysis of Dispersion Effects and Non-Thermal Equilibrium, Non-Darcian, Variable Porosity Incompressible Flow Through Porous Media,'' Int. J. Heat Mass Transf., **37**, No. 6, pp. 939–954.
[14] Amiri, A., Vafai, K., and Kuzay, T. M., 1995, ''Effects of Boundary Conditions on Non-Darcian Heat Transfer Through Porous Media and Experimental Comparisons,'' Numer. Heat Transfer, Part A, **27**, pp. 651–664.
[15] Beck, J. L., 1972, ''Convection in a Box of Porous Material Saturated With Fluid,'' Phys. Fluids, **15**, No. 8, pp. 1377–1383.
[16] Alazmi, B., and Vafai, K., 2000, ''Analysis of Variance Within the Porous Media Transport Models,'' ASME J. Heat Transfer, **122**, pp. 303–326.
[17] Amahmid, A., Hasnaoui, M., and Vasseur, P., 1999, ''Etude analytique et numérique de la convection naturelle dans une couche poreuse de Brinkman doublement diffusive,'' Int. J. Heat Mass Transf., **42**, pp. 2991–3005.
[18] Givler, R. C., and Altobelli, S. A., 1994, ''A Determination of the Effective Viscosity for the Brinkman-Forchheimer Flow Model,'' J. Fluid Mech., **258**, pp. 355–370.
[19] Alazmi, B., and Vafai, K., 2001, ''Analysis of Fluid Flow and Heat Transfer Interfacial Conditions Between a Porous Medium and a Fluid Layer,'' Int. J. Heat Mass Transf., **44**, pp. 1735–1740.
[20] Ochoa-Tapia, J., and Whitaker, S., 1995, ''Momentum Transfer at the Boundary Between a Porous Medium and a Homogeneous Fluid: I—Theoretical Development,'' Int. J. Heat Mass Transf., **38**, No. 14, pp. 2635–2646.
[21] Ochoa-Tapia, J., and Whitaker, S., 1995, ''Momentum Transfer at the Boundary Between a Porous Medium and a Homogeneous Fluid: II—Comparison With Experiment,'' Int. J. Heat Mass Transf., **38**, No. 14, pp. 2647–2655.
[22] Le Breton, P., 1991, ''Etude numérique et expérimentale de la convection naturelle laminaire et turbulente en cavité partiellement occupée d'un milieu poreux,'' Ph.D., Univ. Bordeaux.
[23] Bejan, A., 1984, *Convection Heat Transfer*, John Wiley and Sons, New York.
[24] Straughan, B., 2001, ''A Sharp Nonlinear Stability Threshold in Rotating Porous Convection,'' Proc. R. Soc. London, Ser. A, **457**, pp. 87–93.
[25] Kaviany, M., 1991, *Principles of Heat Transfer in Porous Media*, Springer-Verlag, New York.
[26] Temam, R., 1979, *Navier-Stokes Equations*, North-Holland, Amsterdam.
[27] Le Quéré, P., 1991, ''Accurate Solutions to the Square Differentially Heated Cavity at High Rayleigh Number,'' Comput. Fluids, **20**, pp. 19–41.

.

O. Hireche, I. Ramadan, **C. Weisman**, D. Baltean-Carlès, V. Daru, H. Bailliet, Y. Fraigneau, « Experimental and numerical investigation of natural convection flows in two horizontal thermoacoustic cavities », Int. J. Heat Mass Transfer 149, 119195, 2020.

International Journal of Heat and Mass Transfer 149 (2020) 119195

Contents lists available at ScienceDirect

International Journal of Heat and Mass Transfer

journal homepage: www.elsevier.com/locate/hmt

Experimental and numerical investigation of natural convection flows in two horizontal thermoacoustic cavities

Omar Hireche[a], Islam Ramadan[b], Catherine Weisman[a,c,*], Hélène Bailliet[b], Yann Fraigneau[a], Diana Baltean-Carlès[a,c], Virginie Daru[a,d]

[a] Laboratoire LIMSI, CNRS, Campus universitaire bât. 507, Rue du Belvedère, Orsay Cedex F-91405, France
[b] Institut Pprime, CNRS - Université de Poitiers - ENSMA, ENSIP, 6 rue Marcel Doré, Bât. B17 - BP 633, Poitiers Cedex 86022, France
[c] Sorbonne Université, Faculté des Sciences et Ingénierie, 4 Place Jussieu, Paris 75005, France
[d] DynFluid Lab., ENSAM, 151 Bd de l'Hôpital, Paris 75013, France

ARTICLE INFO

Article history:
Received 1 August 2019
Revised 22 November 2019
Accepted 8 December 2019

Keywords:
Natural convection
Thermoacoustics
Porous medium
Particle image velocimetry
Numerical simulation

ABSTRACT

This study aims at exploring the potential generation of natural convective flows in thermoacoustic devices. To this effect, two thermoacoustic setups are considered without acoustic oscillations, each setup thus constituting a cavity filled with air and comprising a porous medium heated on one of its ends. In the first configuration, the porous medium is a ceramic stack. In the second configuration, an ambient heat exchanger using circulating ambient water is placed on the other end of the porous medium (which is a regenerator). The wall temperature is measured in several points using thermocouples and natural convection flows developing in these cavities are measured in a vertical plane using Particle Image Velocimetry. Moreover numerical calculations are performed based on simplified 3D configurations, using immersed solid bodies at prescribed temperature to represent the heating or cooling elements and describing the porous media as homogeneous and either isotropic or anisotropic. Navier-Stokes equations under Boussinesq assumption are solved in the entire domain with the addition of a Darcy correction term in the porous media. Excellent qualitative and quantitative agreement on velocity fields is obtained between experimental and numerical simulation results for both configurations, which validates the model description. It is shown that the observed natural convection flows are fully three-dimensional and of significant magnitude so that they could potentially interfere with thermoacoustic effects.

1. Introduction

Thermoacoustic devices use thermal and dynamic interactions between the acoustic oscillations of a working inert gas and conducting solid walls to generate either heat pumping for refrigerating purposes or mechanical work for engine operating purposes [1]. These interactions are called the thermoacoustic effect. They occur nearby the solid walls, in a thermal boundary layer area: the gas experiences acoustic oscillations, while exchanging heat with the solid wall. In order to increase the exchange surface area, a porous medium is used. This porous medium is placed between two heat exchangers, forming the thermoacoustic core (TAC). The heat exchangers enable to either impose a temperature gradient along the porous medium, in order to produce acoustic power (engine), or to benefit from the heat pumping effect steered by an imposed acoustic oscillation (refrigerator). The thermoacoustic core represents the active part of the device, where the energy conversion takes place. Usually, thermoacoustic devices also include an acoustic resonator for sustaining the acoustic wave, and potentially an acoustic source or a linear electric generator, depending on the desired conversion effect. Thermoacoustic devices represent an interesting ecological alternative (almost no moving parts, the use of inert gas, simplicity) for industrial applications: cryogenics [2], air conditioning [3], domestic refrigeration, solar powered thermoacoustic engines [4], electric energy generators (conversion of the acoustic power into electric power) [5], waste heat recovery (for example, thermoacoustic heat pumps are used to upgrade the waste heat for renewed use in the industrial process) [6]. However thermoacoustic devices still suffer from poor performance generally caused by the existence of several nonlinear phenomena interfering with the process of energy transfer and deteriorating the global performance of the device. These nonlinear phenomena are related to jet-driven streaming, acoustic streaming, harmonic generation, end-effects and natural convection, and are not well described or just partially. Among these phenomena, natural con-

* Corresponding author.
E-mail address: weisman@limsi.fr (C. Weisman).

https://doi.org/10.1016/j.ijheatmasstransfer.2019.119195
0017-9310/

vection has been the least investigated. The present study focuses on the effect of natural convection flows.

The influence of natural convection on starting conditions for a thermoacoustic engine was pointed out in an early paper of Gardner and Swift [7]. They observed that in the engine under study, the acoustic oscillation did not start although the design parameters were respected. This appeared to be due to a distortion of the mean temperature field, which was identified by the authors as originating from gravity-driven convection in the stack. The experimental procedure was modified, in order to reduce the convection flow, by decreasing the mean pressure and start the oscillation at a lower pressure. Once the oscillation was stabilized, the mean pressure was changed to its designed value. This is the option generally chosen by thermoacousticians: try to avoid or to reduce natural convection; but most of the time it is impossible to completely avoid it, since the devices come in a variety of geometries. The influence of the tilt angle on the starting condition of a solar powered thermoacoustic engine was analyzed more recently using Thermal Infrared Imager temperature measurements in the TAC [8]. In cousin devices that are pulse tube refrigerators, natural convection was also pointed out as a major source of losses [9,10] but no detailed analysis was performed and no estimate or measurement of the natural convection velocity field is available.

Apart from these few experimental evidence of natural convective flows in real devices, some experimental studies aimed at characterizing natural convection in simplified academic configurations. Natural convection and heat transfer inside a horizontal empty resonator, taking place between a hot heat exchanger and a cold heat exchanger, was investigated experimentally using thermal infrared imaging and particle image velocimetry (PIV) [11], and for different tilt angles [12]. It was shown that heat transfer mode changed from natural convection to forced convection with the addition of acoustic oscillation.

The role of natural convection on the distortion of Rayleigh streaming flow was exhibited in some recent experimental studies [13–15]. Measurement of the sole convection velocity field along a vertical section of the resonator under a temperature gradient was performed in [14] in order to explain the distorted streaming velocity field observed, but the measurement was very localized and there was no theoretical explanation of the complex velocity measurements obtained. Measurements of the mean velocity field in the entire cold resonator part of a simple standing-wave thermoacoustic engine were recently performed by Ramadan et al. [15]. Using both PIV and LDV techniques, they showed the existence of a mean flow with or without thermoacoustic oscillations. This flow was identified as natural convection combined, when acoustic waves are present, with Rayleigh streaming. However, in this preliminary study, measurements were performed only in the central horizontal plane, which is limiting for the study of natural convection. More generally, a characterization of the 3D nature of the natural convection velocity field suggested by all above-cited studies is still lacking and its influence on the overall thermoaoustic heat transfer not yet quantified. This is because dedicated adequate measurements of natural convection flow and temperature distribution are difficult in real devices, due to the many coupled intricate physical phenomena.

From the numerical point of view, natural convection is not yet included in thermoacoustic designing tools. It is therefore necessary to develop a numerical tool that can predict the magnitude and flow pattern of natural convection flows as well as the associated temperature distribution. So far it is unrealistic to integrate all effects in one complete numerical code, for a given complex device: acoustics, thermoacoustic energy conversion, acoustic streaming, natural convection without powerful computing resources. This is due to the existence of several distinct time scales (acoustic, thermal diffusion) and spatial scales (wavelength, viscous and thermal boundary layer thickness, device's characteristic scales). Such simulations would therefore be very time consuming, since long physical times would have to be discretized in small time steps, and extended physical domains discretized with fine mesh. Morever, for a better understanding of how several physical processes interact, it seems relevant to study them separately in a first approach. Therefore, this study focuses on the natural convection flow in thermoacoustic device configurations, with no acoustic oscillation. As will be shown further, the geometrical configuration of thermoacoustic devices can generally be considered as a series of heated cavities, some of which are filled with a porous medium. Each cavity is submitted to a temperature difference, which can generate a heat-driven flow.

Convection flows through non homogenous and anisotropic porous media in cavities heated from the side are quite well described, with studies started in the 1980s [16]. The same problem in mixed fluid and porous cavities was treated extensively in the literature [17,18]. The convection flow depends strongly on the geometry of the cavities and the previous general studies cannot be directly applied to the specific case of a thermoacoustic engine. The specific geometry of a thermoacoustic stack was considered in [19], where natural convection in a 2D differentially heated horizontal cavity, filled with a stack of plates, was considered. This study showed that a Darcean porous model gives correct orders of velocity scales, and allows for a qualitative description of the solutions. A preliminary 3D numerical study of the effects of natural convection in a cylindrical guide containing an assembly of a hot heat exchanger and porous medium was conducted recently [20]. The influence of the porous medium's physical characteristics (permeability, thermal conductivity, anisotropy) on the flow and temperature fields was investigated.

The numerical approach of [20] is pursued in this paper on realistic configurations, and confronted with experiments resulting from extending the preliminary study in [15]. In the present analysis, the experimental and numerical models were elaborated and calibrated jointly in order to improve the description of natural convection flows in a thermoacoustic system. The first objective of this paper is to predict natural convection flows in configurations that are representative of such systems. The second objective is to show that the model works well by comparison with possible measurements in parts of the device.

As mentioned above, to isolate natural convection from other phenomena, we chose to work with a thermoacoustic cavity but not with a thermoacoustic device; i.e. no acoustic oscillation was generated in the cavity. Whether or not natural convection should be accounted for in the design of a thermoacoustic device is going to depend highly on the device's geometry and its orientation with respect to gravity. It is also going to depend particularly on the thermo-physical parameters of all constituting elements, and specifically the thermoacoustic core. Therefore, and in order to explore increasingly realistic geometries, we investigate two different configurations: the first one consists in a very simplified thermoacoustic core that is composed of an electric heater attached to a ceramic stack; the second one is composed of the same two elements followed by an ambient heat exchanger. These two configurations are further referred to as horizontal cavity without ambient heat exchanger (or 1st configuration), and horizontal cavity with ambient heat exchanger (or 2nd configuration).

In the following, the first configuration is investigated in Section 2. The experimental setup and method are described (Section 2.1) and the numerical method is presented (Section 2.2). Experimental and numerical results are then compared and discussed, and the potentiality of the numerical model for predicting purposes is assessed (Section 2.3). The configuration with ambient heat exchanger is considered in Section 3, following the same approach.

2. Horizontal cavity without ambient heat exchanger (1st configuration)

2.1. Experimental setup, measurement systems and procedure

For this first comparison between experimental and numerical approaches, a very simple thermoacoustic cavity is used. As shown in Fig. 1a, the resonator is made of a glass tube with inner and outer diameters of 39 mm and 44 mm, respectively. The total length of the resonator is 738 mm and the thermoacoustic core is placed at a distance of 129 mm away from one end of the resonator. The thermoacoustic core consists of an electric heater attached to one side of a 400 CPSI (Cell Per Square Inch) ceramic stack that has length of 60 mm. The axial coordinate is also defined in Fig. 1a, with $x = 0$ corresponding to the right end of the ceramic stack. In such a simple thermoacoustic engine, applying high enough temperature gradient along the stack generates sustainable standing acoustic waves. A more detailed description for the experimental setup can be found in [15]. In order to isolate the natural convection flow, the two small plugs at the ends of the resonator tube were removed to cease any acoustic oscillations and velocity measurements were performed in the central vertical plane. It was checked previously [15] that the removal of the plugs does not affect the natural convection flow.

A PIV system is used to measure the natural convection flow in the central vertical plane. The PIV system consists of a double pulse Nd:YAG laser source that illuminates the vertical plane. Two cameras (Imager Pro X) with spatial resolution of 2048 $\times$ 2048 pixels^2 and maximum repetition rate of 15 Hz are used to record the images. Each camera is equipped with a Nikon lens (Model: Sigma 105 mm). The two cameras are placed next to each other in order to increase the size of the measurement Field Of View (FOV). An atomizer aerosol generator (Model: TOPAS ATM 210) is used to atomize oil to produce seeding particles with a mean particle diameter of 0.4 µm. In order to achieve better correlation between the acquired double-images, the time between laser pulses is adjusted to allow the seeding particles to displace a distance of about 1/4 the size of the interrogation area [21].

The measurement procedure followed in the current study is similar to the procedure we followed in our previous work [15]. In order to have enough seeding particles after the system reaches to the steady-state conditions (i.e. the change in the temperature over the PIV measurement period does not exceed 5%), the preheating technique is followed. A 31.5 W $\pm$ 1% electrical power is applied to the hot heat exchanger (coiled resistance). After the preheating of the system, the seeding particles are introduced from one extremity and flow until reaching the other extremity of the duct so that the seeding particles are dispersed over the whole duct. The system is left for 3 min in order to eliminate the effects of the seeding introduction on the natural convection flow. Finally, the PIV measurements are started and 100 double-images captured. The natural convection flow distribution is measured in the central vertical plane, covering the axial distance from $x = 0$ mm (end of ceramic stack) to $x = 520$ mm. Since wall temperatures are very important for the study of the natural convection flow, several thermocouples are used to measure the wall temperatures and the temperatures at the center of the two side sections of the ceramic stack. As shown by Fig. 1b (large dots), on the tube wall for each axial position there are two temperature measurements corresponding to the top and bottom of the tube wall.

The uncertainty of the measured quantities (i.e. temperature and the velocity) is estimated by repeating the measurements (3 times) under the same input electric power to the electrical heater and calculating the standard deviation of these quantities. The estimated value of the uncertainty in the temperature measurements is thus found to be $\pm$ 1 % of the reported mean temperatures. For the velocity measurements, the uncertainty of the measurements is calculated over the whole measurement area and then the spatial-average uncertainty is calculated. The spatial-average uncertainty is found to be $\pm$ 13 % of the reported velocities.

2.2. Numerical model

2.2.1. Numerical simulation parameters

A simplified 3D configuration is introduced in order to model the experimental configuration described in the previous section (Fig. 2a). The domain under study is a horizontal cylindrical tube of length L and radius R, filled with air and closed at both ends.

The ceramic stack, constituted of horizontal capillaries of square cross section with side length $a = 1$ mm, is modeled as a homogeneous and anisotropic porous medium of length L_p and radius R (see Fig. 2a and Table 1a). Its porosity ϵ, defined as the ratio of gas volume to total volume is calculated based on the given geometry. The equivalent permeability in the axial direction is $K_{xx} = \frac{a^2\epsilon}{8}$ (calculated using [18]), its permeability in the radial and azimutal directions are approximately zero (in the code they are set to 10^{-12} m^2). The equivalent thermal conductivity is assumed isotropic and homogeneous, of scalar value $k_p = \epsilon k_{fluid} + (1-\epsilon)k_{solid}$ (again based on [18]). The numerical values of these parameters are given by Table 1b.

The hot exchanger (coiled resistance), placed at a distance L_L from the left end, is modeled as 2 solid rings of width e_h

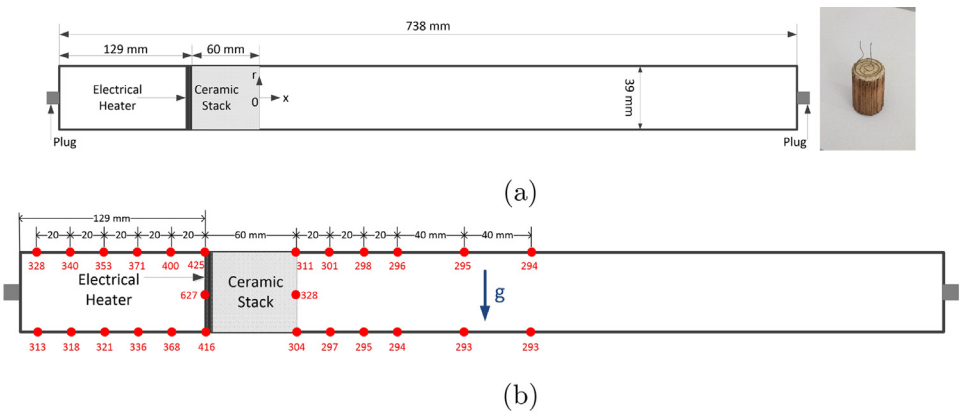

Fig. 1. (a): Schematic for the thermoacoustic resonator and image of the thermoacoustic core. (b): Thermocouples locations and results of measurements (in K) in the 1st configuration.

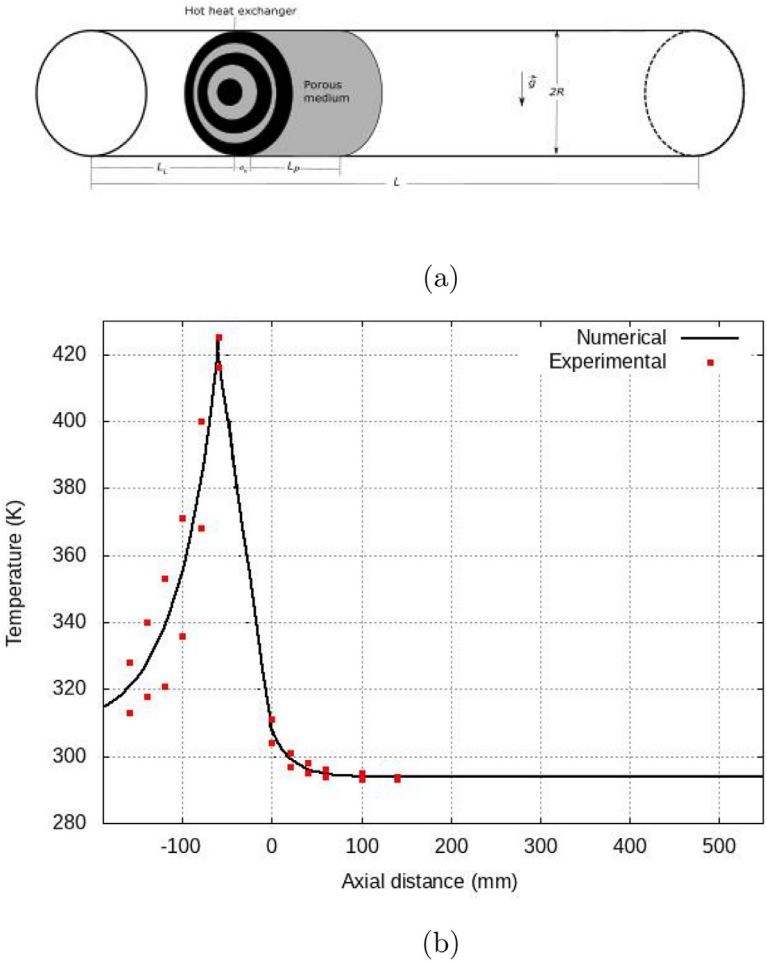

(a)

(b)

Fig. 2. (a): Numerical configuration for the 1st configuration, (b): temperature prescribed in the numerical model along the tube wall, as a function of axial position (solid line), and measurements on top/bottom of the outside tube wall (squares) reported from Fig. 1b.

Table 1
(a): Geometrical and thermal parameters, (b): Thermophysical parameters for air and porous medium, 1st configuration.

R	L	L_L	e_h	L_p	T_{hot}	T_{cold}
mm	mm	mm	mm	mm	K	K
39	738	129	5.8	60	520	293
			(a)			
ρ	μ	k	c_p	ϵ	K_{xx}	k_p
kg m^{-3}	kg m^{-1} s^{-1}	W m^{-1} K^{-1}	J kg^{-1} K^{-1}		m^2	W m^{-1}K^{-1}
1.07	1.9×10^{-5}	2.8×10^{-2}	1004	0.64	8.10^{-8}	$9.18.10^{-1}$
			(b)			

and a central core maintained at certain hot temperature (the central core being hotter than the outside ring). Temperature values prescribed in this hot heat exchanger are: 420 K on the outside ring, 523 K on the middle ring, and 627 K in the central core. Therefore the "average" hot temperature is estimated as $T_{hot} = 520$ K. Along the tube wall, temperature is imposed as a function of the axial coordinate only, based on the measured temperature distribution, as shown by Fig. 2b. Since for each axial position there are two measures of temperature (at the top and bottom of the outside wall) reported in Fig. 1b, the average value between the two measured values was calculated and prescribed for the corresponding axial position. On the left of the HHX, the temperature distribution is then fit with an exponential function. Along the porous medium a linear variation is used. Finally on the right of the porous medium the temperature distribution is fit with another exponential function (Fig. 2b).

The thermophysical parameters for air are calculated for atmospheric pressure and at a reference temperature chosen to be $T_{ref} = 320$ K which is the global mean temperature of the air.

2.2.2. Governing equations

In the fluid domain, the Navier-Stokes equations are written as classically under Boussinesq assumptions. The reference air density ρ, thermal conductivity k, heat capacity c_p, dynamic viscosity μ, and volume expansion coefficient at constant pressure $\beta = 1/T_{ref}$ for an ideal gas are constant and equal to their value for a reference temperature T_{ref} and atmospheric pressure.

The thermophysical characteristics of the porous medium are its porosity ϵ, its permeability tensor **K**, and its equivalent thermal conductivity k_p. A scalar phase variable X is introduced to identify the nature of the medium (X = 1 for gas, X = 0 for the porous medium) so that a Darcy term appears as additional term in the

right hand side of the momentum equation in the case of the porous medium zone. Therefore the equations can be written in a unified form as:

$$\nabla.\mathbf{V} = 0$$

$$\frac{\partial(\rho\mathbf{V})}{\partial t} + \nabla.(\rho\mathbf{V}\otimes\mathbf{V}) = -\nabla p + \mu\Delta\mathbf{V} - \rho\beta(T - T_{ref})\,\mathbf{g} - (1-X)\mu\mathbf{K}^{-1}\mathbf{V}$$

$$\rho c_p\left(\frac{\partial T}{\partial t} + (\mathbf{V}.\nabla)T\right) = \nabla.[(X\,k + (1-X)\,k_p)\nabla T]$$

In the above equations $\mathbf{V}$ is the velocity vector, p is the nonhydrostatic pressure, T is the temperature, t is time and $\mathbf{g}$ is the acceleration of gravity.

On all solid boundaries (i.e. the cylinder walls and the heat exchanger solid parts), a no-slip condition is imposed, and the temperature is prescribed as detailed in the previous section.

2.2.3. Numerical method

Computations are performed with the in-house code SUNFLUIDH, which has been developed at LIMSI for simulations of unsteady incompressible flows. The previous governing equations are solved in the entire domain using a finite volume approach with a second order discretization in space and time. An implicit treatment of the viscous and thermal conductive terms ensures better numerical stability with regard to the time step which only depends on the CFL criterion. The equation set is solved by means of an ADI method [22]. An incremental projection method is used in order to ensure the divergence-free velocity field [23,24]. This implies to solve a Poisson's equation at each time step which is carried out with a multigrid-SOR algorithm [25]. The solution corresponds to the time-variation of pressure from which the correction term is estimated in order to get the divergence-free velocity field. The mesh is body-fitted regular.

The numerical domain is meshed using 64 points regularly spaced along the radial direction, 64 points regularly spaced along the azimutal direction, and 512 points placed regularly along the axis. The mesh size in the axial direction is $\Delta x = 1.4$ mm. In the radial direction, $\Delta r = 0.61$ mm. It was checked through a mesh-refinement study that this spatial resolution is adequate for the given configuration. The time step is adjusted throughout the simulation in order to satisfy a CFL < 0.5 criterion.

2.3. Results and discussion

Fig. 3 shows the experimental and numerical velocity vector maps and colored contours of the axial velocity component for the central vertical plane at the right side of the porous medium, which corresponds to the measurement field of view (close-up views for the figures near the porous medium (i.e. $x = 0$) are also shown in Fig. 3). Fig. 4 shows the numerical temperature field over the same region. The vortex flow observed is indeed that of natural convection of air in a cylindrical fluid cavity, triggered by a horizontal temperature gradient (the temperature of the right side of the porous medium is still much higher than the ambient temperature, as shown on Fig. 4). The numerical temperature at the center of the right end section of the porous medium is found to be equal to 320 K, in good agreement with the measured value of 328 K (see Fig. 1b). Experimental and numerical results agree remarkably well (Fig. 3), considering the numerous simplifications and approximations made in the numerical model. It should be pointed out that the numerical calculation converges to a steady solution, in agreement with experimental results (in which the temperature and thus velocity fields only change very slowly in time). The main difference lies in that for $x > 150$ mm a small flow remains observable along the whole experimental field of view, while in the numerical simulation it becomes negligible. This could be due to the fact that the temperature imposed on the tube boundary is based on the measurement of the outside temperature and not on the inside, which should be slightly higher, therefore extending the natural convection flow. Also the presence of the openings on the tube ends (open plugs) is not modeled (a closed end with no slip condition is imposed in the numerical domain). In addition, the maximum amplitude and the extent of the convection flow in the field of view are highly dependent on the value of the driving ΔT imposed through prescribed boundary temperature values. The temperature on the glass tube is not controlled and the ambient temperature varied slightly during the experiment (about 2 degrees). The effect of changing ΔT by $\pm$ 2 K (i.e. representing 12% of $\Delta T = 17$ K for the experimental field of view) could also explain the observed discrepancy between the measurements and the numerical results : A rough model gives the max velocity amplitude as a linear function of ΔT. The corresponding variation of the extent of the convection cell is harder to estimate. Fig. 5 shows the axial profile of the vertical velocity component obtained from experiments and numerical simulations at the central vertical plane, again on the right side of the porous medium, for several values of the radial coordinate r (which on this plane measures the height). Here again the agreement between experimental and numerical results is very good, except for the limit $x \to 0$ (end of the porous medium) where the local geometry changes are not accounted for in the model (the porous medium being considered homogeneous). Also, the porous medium being very anisotropic, the model used for the hot exchanger (and particularly its solid-fluid geometry shown on Fig. 2a) influences the velocity near $x = 0$. As expected, the velocity profiles are not symmetric with respect to the x-axis, and show the development of the convection boundary layer along the "hotter" section $x = 0$, in the bottom half between $r = -15$ mm until $r = 0$. The maximum velocity then decreases because when the flow reaches the top tube wall it is forced to turn. Fig. 6 shows the axial profiles of the axial velocity component obtained from experiments and numerical simulations in the same locations as Fig. 5. Here again the agreement between experimental and numerical results is very good, except for the limit $x \to 0$ (end of the porous medium). As expected, the velocity is negative for the lower part of the tube, and positive for the upper part, forced by the upward flow along the hotter porous medium end $x = 0$. Fig. 7 shows the vertical profile of the axial velocity component obtained from experiments and numerical simulations on the central vertical plane, on the right side of the porous medium, for several values of the axial position. The agreement between experiments and numerical simulations is good, but the maximum values are about 20% off. Also, as noted on Fig. 3, for $x > 150$ mm, there is a small discrepancy between numerical and experimental results.

Fig. 8 a and b show velocity vector maps and colored contours of the axial velocity component obtained from numerical simulations and experimental data from [15] on the central horizontal plane, on the right side of the porous medium. There is again excellent agreement between experiments and numerical simulations. Convective velocities are of course a lot smaller on that plane than on the central vertical plane. Fig. 8c shows the numerical and experimental transverse profile (as a function of the radial coordinate) of the axial velocity component on the central horizontal plane at $x = 60$ mm. On this plane the flow is symmetric with respect to the x-axis.

In order to better understand the convective flow observed in the measurement field of view, contours of the axial velocity component and temperature in the central vertical plane obtained from numerical simulations are shown within the porous medium on Fig. 9a and b, and left of the hot heat exchanger on Fig. 9c and d. The flow inside the porous medium is indeed character-

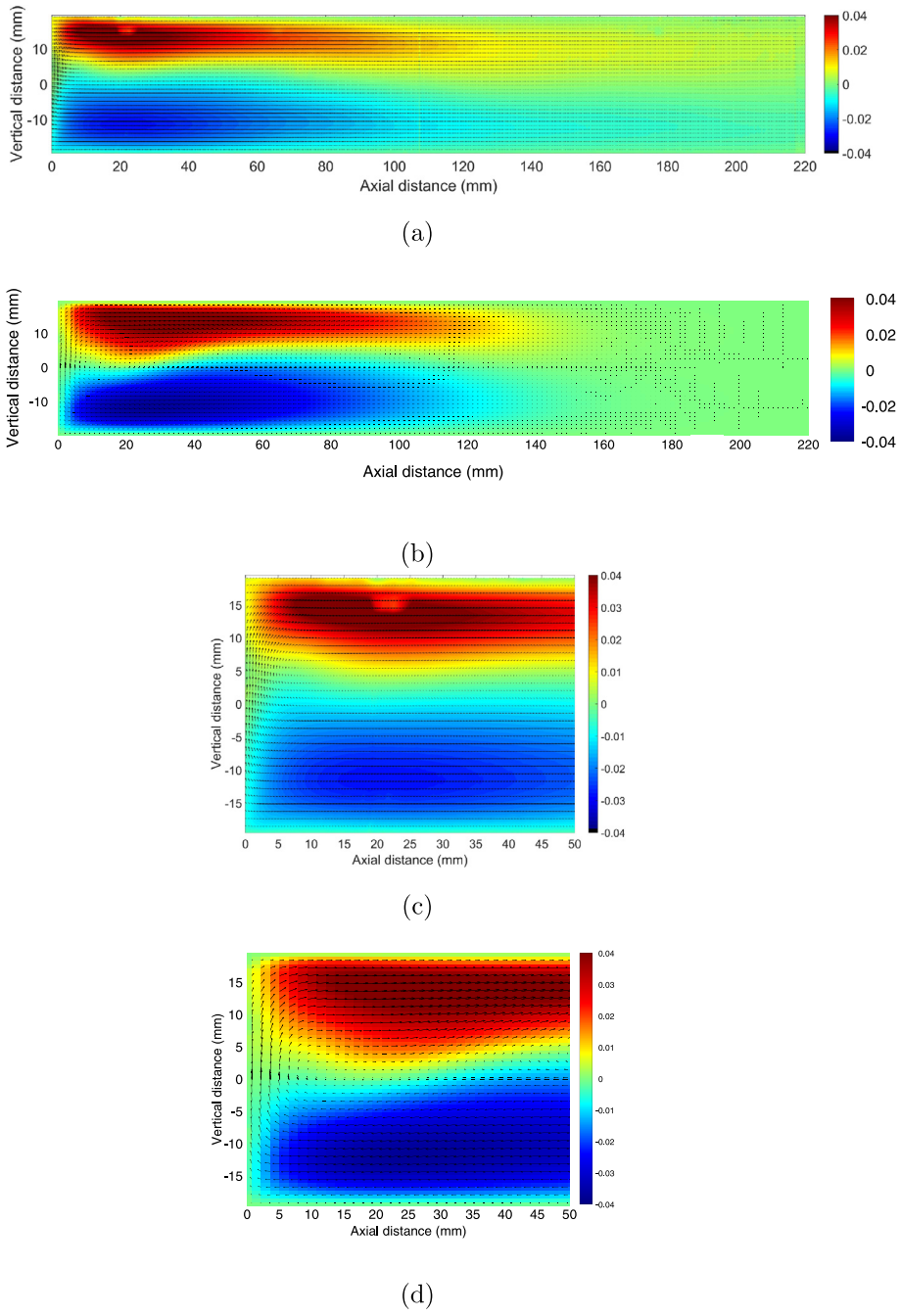

Fig. 3. Velocity vector maps and colored contours of the axial velocity component obtained from experiments (a) and numerical simulations (b) on the central vertical plane, on the right side of the porous medium. Zooms on the left part of the figures, for experimental results (c) and numerical simulations (d).

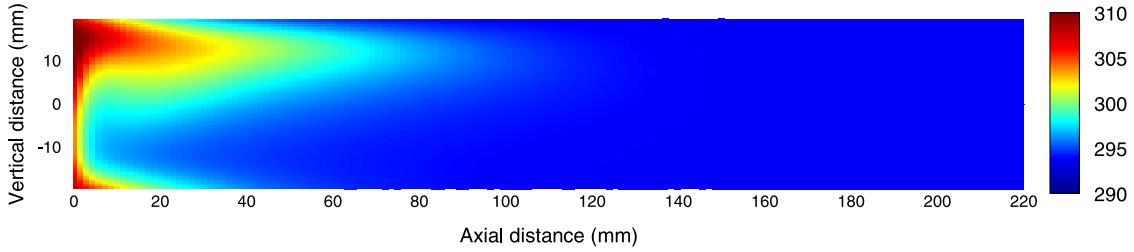

Fig. 4. Calculated temperature map on the central vertical plane, on the right side of the porous medium.

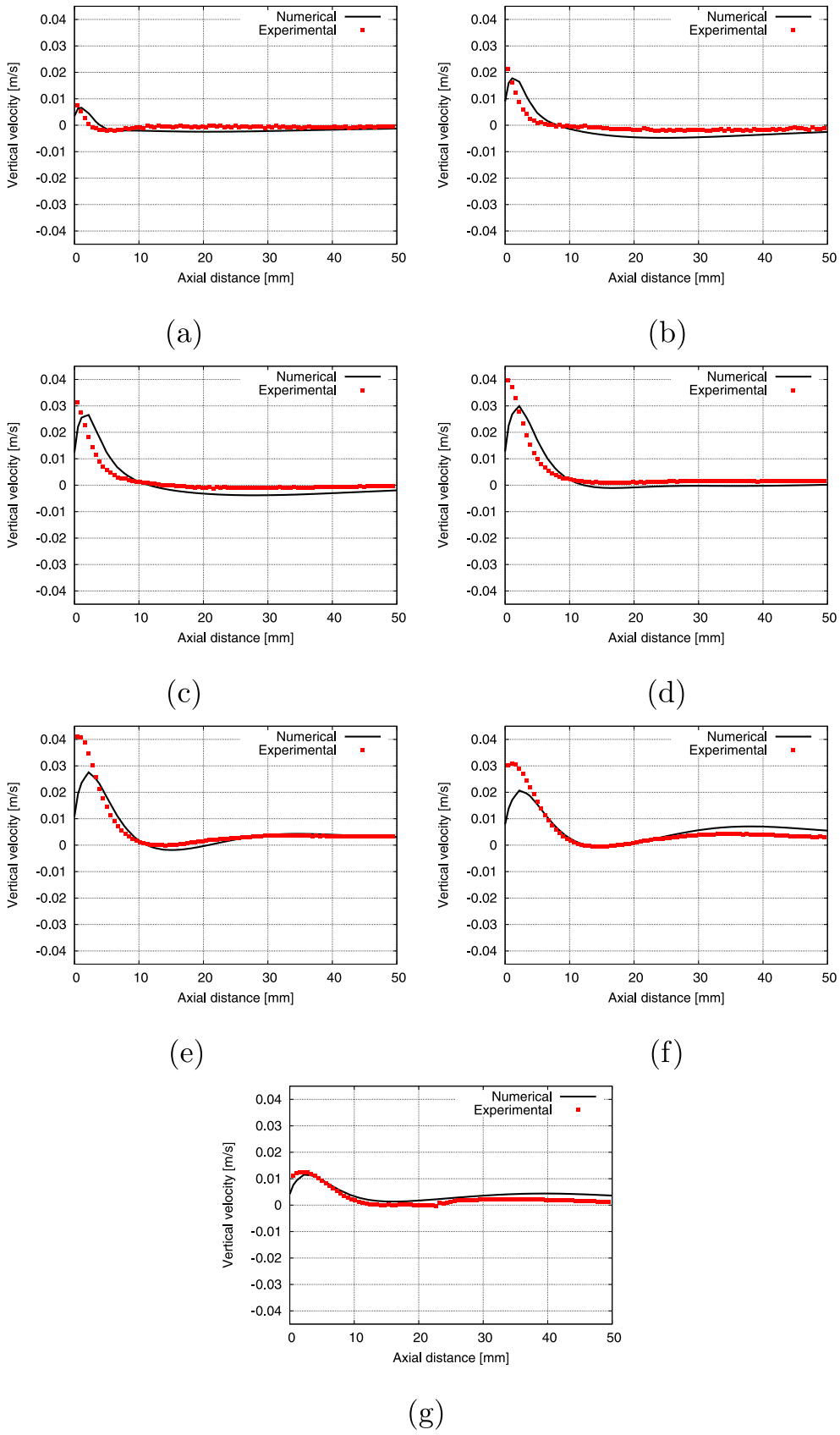

Fig. 5. Axial profile of the vertical velocity component on the right of the porous medium (squares: experiments, solid line : numerical simulation) on the central vertical plane at (a): $r = -15$ mm, (b): $r = -10$ mm, (c): $r = -5$ mm, (d): $r = 0$, (e): $r = 5$ mm, (f): $r = 10$ mm, (g): $r = 15$ mm.

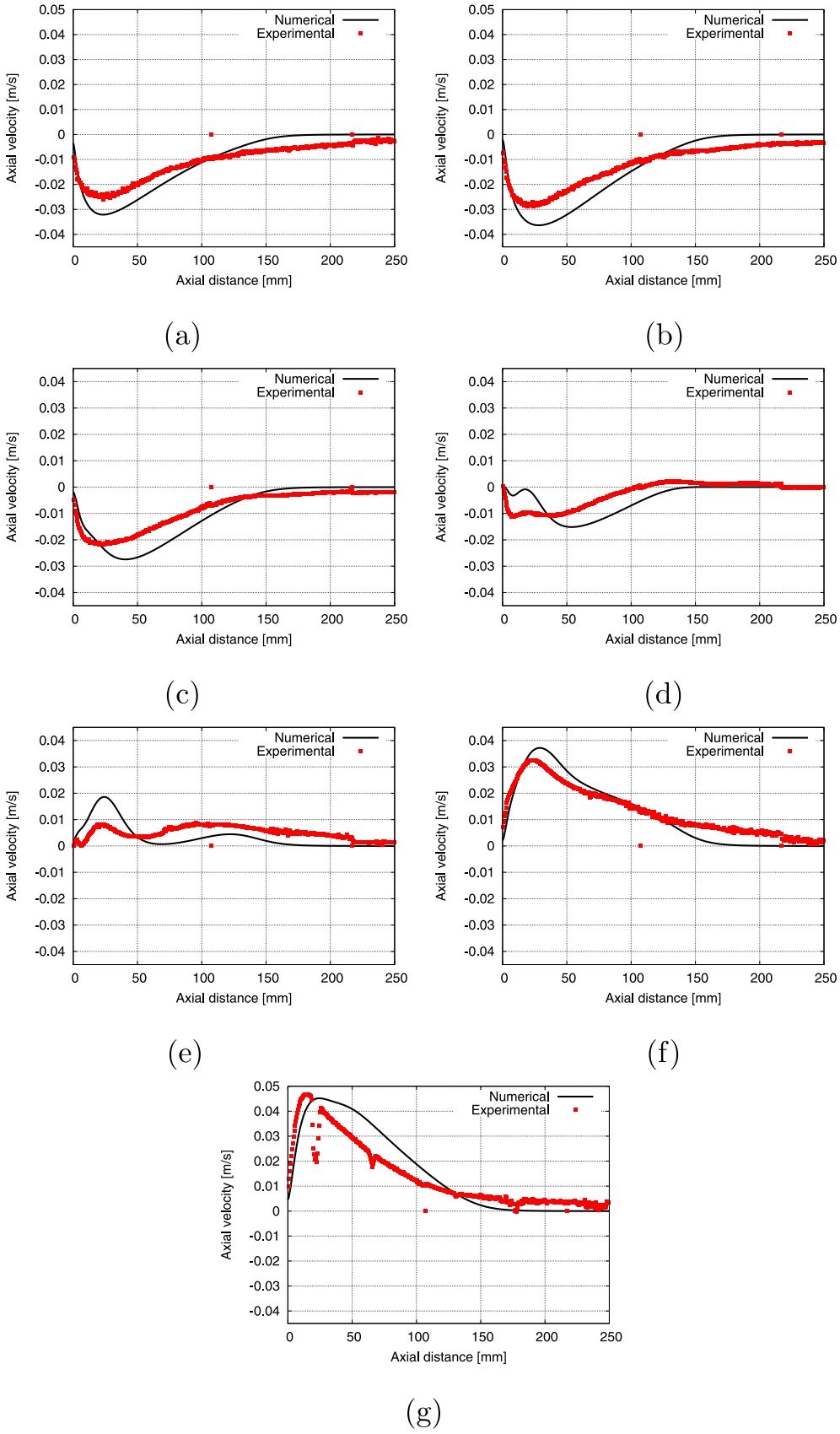

Fig. 6. Axial profile of the axial velocity component on the right of the porous medium (squares: experiments, solid line: numerical simulation) on the central vertical plane at (a): $r = -15$ mm, (b): $r = -10$ mm, (c): $r = -5$ mm, (d): $r = 0$, (e): $r = 5$ mm, (f): $r = 10$ mm, (g): $r = 15$ mm.

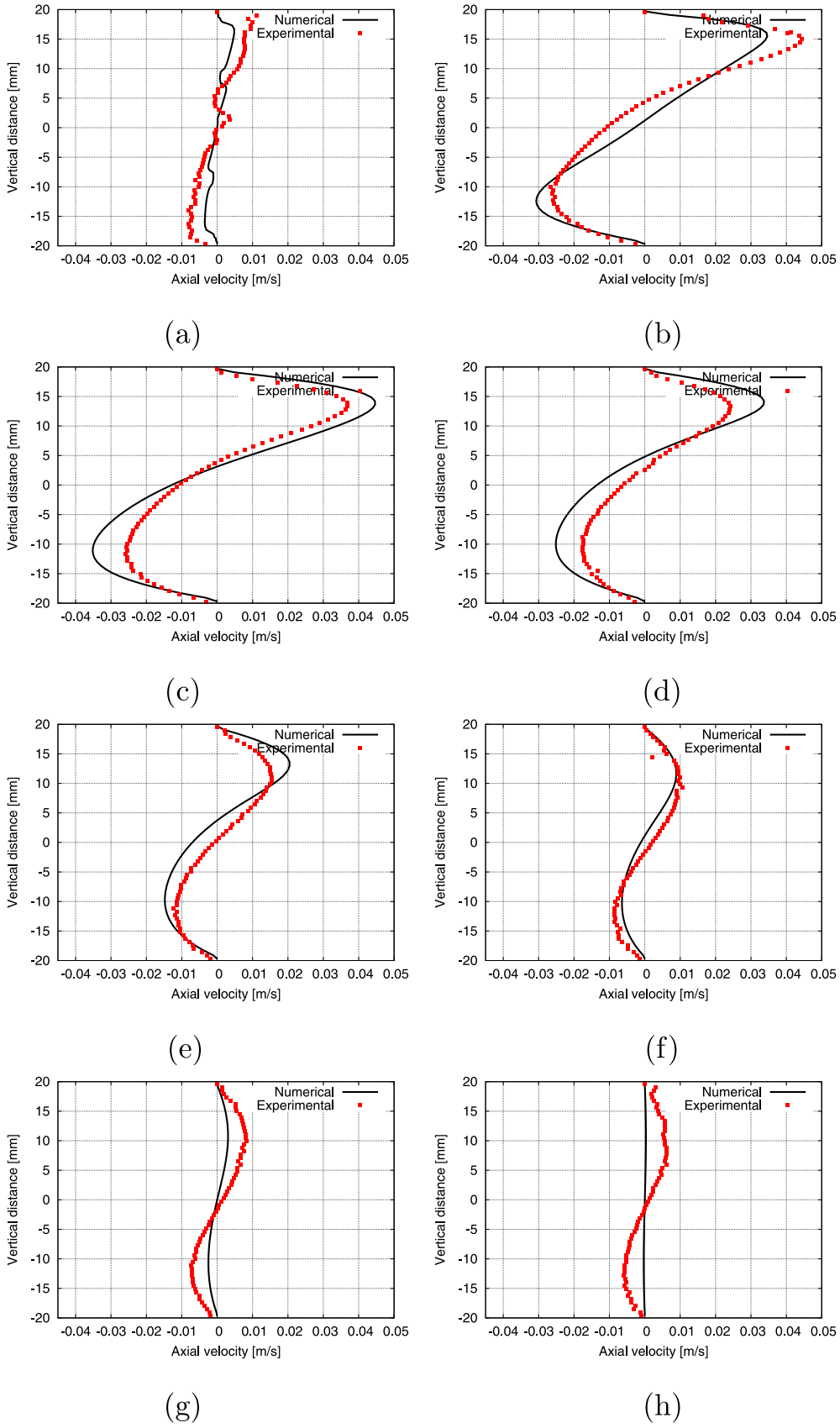

Fig. 7. Vertical profile of the axial velocity component on the right of the porous medium (squares: experiments, solid line: numerical simulation) on the central vertical plane at (a): $x = 0$ mm, (b): $x = 10$ mm, (c): $x = 40$ mm, (d): $x = 70$ mm, (e): $x = 100$ mm, (f): $x = 130$ mm, (g): $x = 150$ mm (h): $x = 180$ mm.

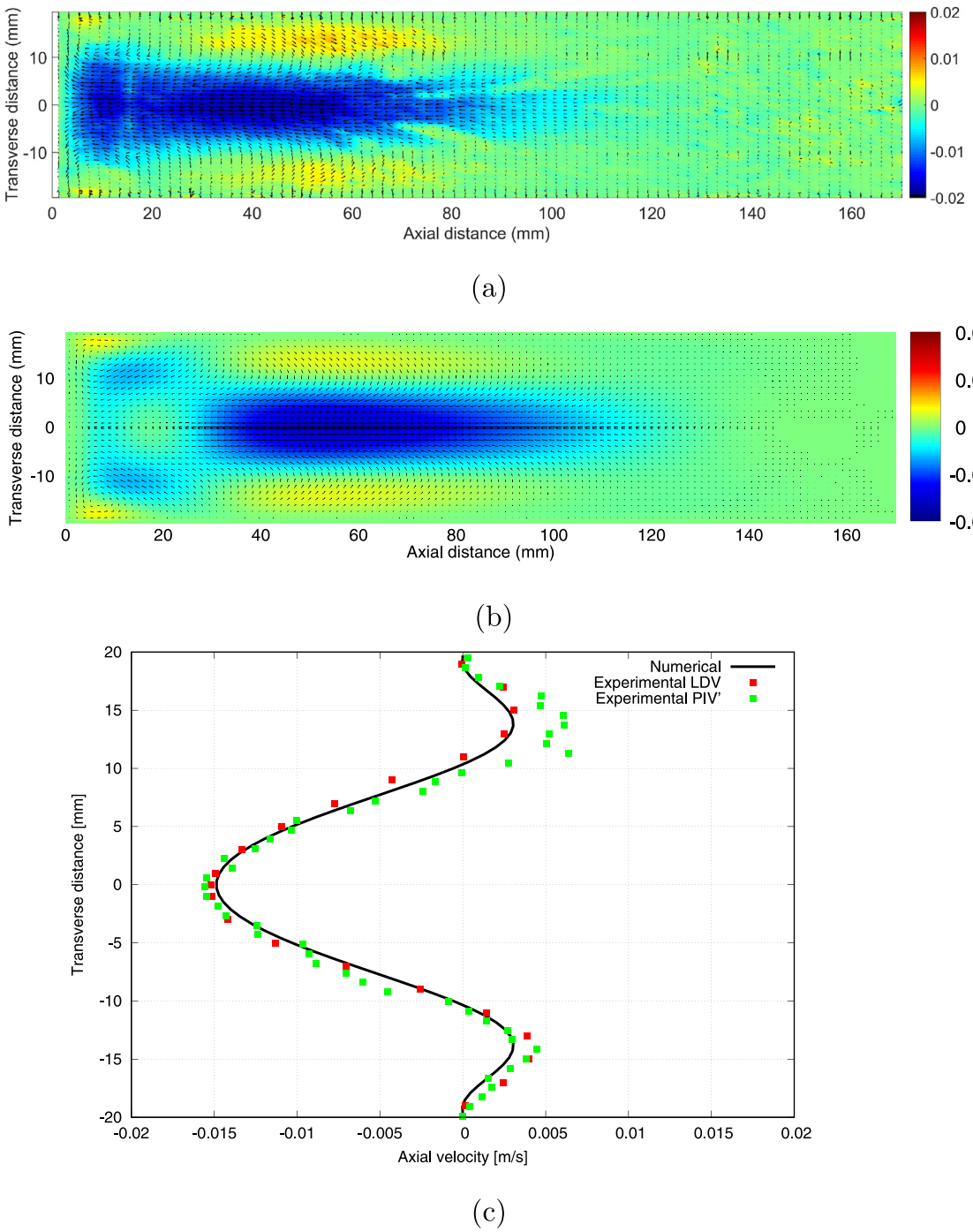

Fig. 8. Velocity vector maps and colored contours of the axial velocity component (a): experiments, (b): numerical simulations on the central horizontal plane, on the right side of the porous medium. (c): Distribution of the axial velocity component as a function of the radial coordinate (squares: experiments, solid line : numerical simulation) on the central horizontal plane at $x = 60$ mm.

istic of natural convection flow in a cavity filled with a strongly anisotropic porous medium (Fig. 9a). The flow is constrained to remain in the horizontal plane, and the permeability being very small, conduction dominates convection (with mostly horizontal stratification of temperature), and the flow is very slow. Also, because of the porous medium's anisotropy, the model used for the hot heat exchanger influences the flow in the right fluid cavity, i.e. in the measurement field of view: For example the no-slip condition on the solid core and rings and the zero permeability in the radial and azimutal directions put high constraints on the development of the flow in the porous medium. The flow thus retains the geometry of the hot heat exchanger (Fig. 9a). In the left fluid cavity the convection vortex turns in the opposite direction, because the cooler boundary is on the left (Fig. 9c).

In order to get an insight in driving effects in the thermoacoustic cavity, the maximum velocity in different regions is examined thereafter in light of classically defined reference Rayleigh numbers and associated velocity scales. On the right side of the hot heat exchanger, the flow is driven by the temperature difference $\Delta T = T_{hot} - T_{cold}$. The flow in this region should then be that of a differentially heated cavity partly filled with an anisotropic porous medium. Using the axial permeability K_{xx} and equivalent thermal

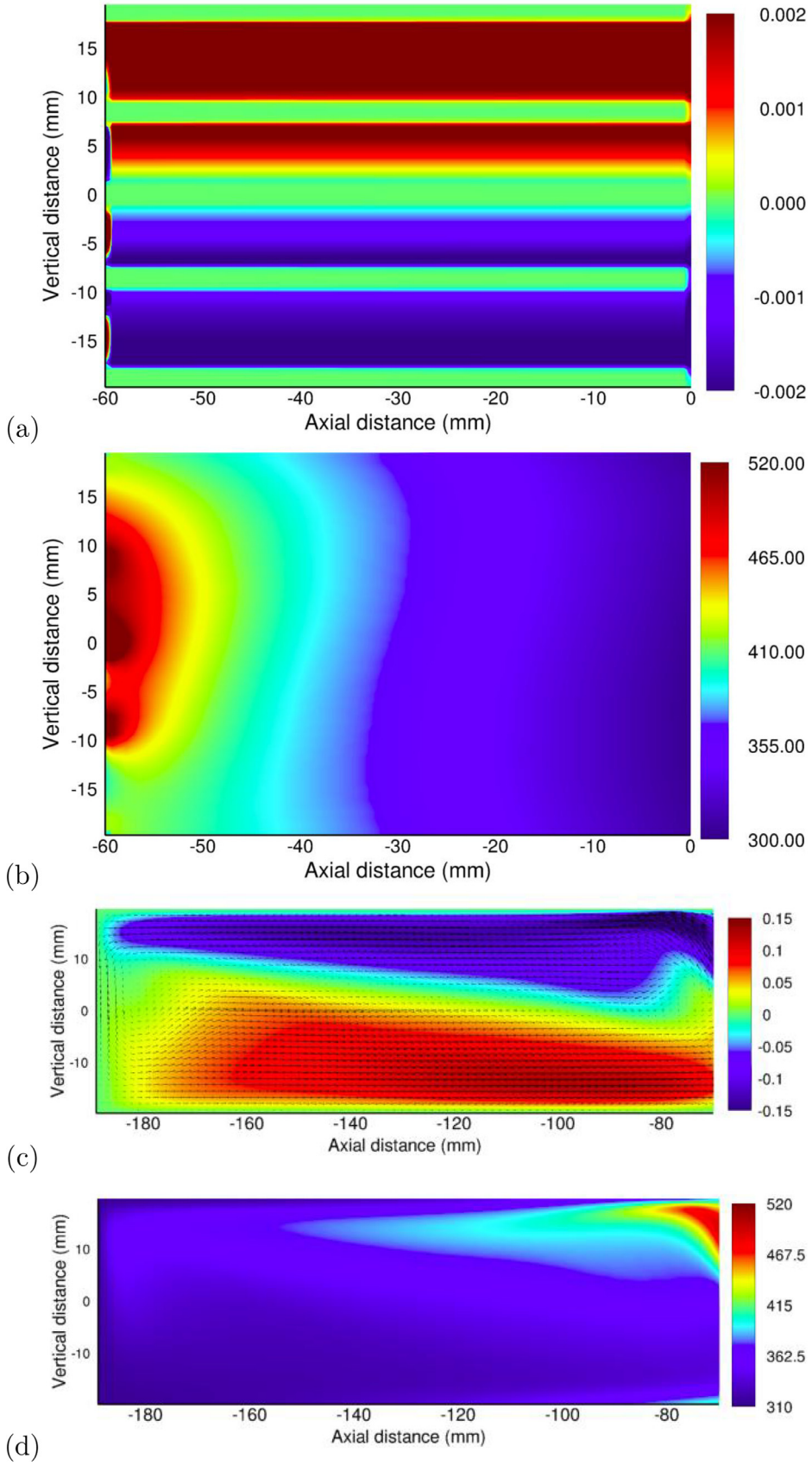

Fig. 9. Contour of the axial velocity component (a) and temperature (b) in the central vertical plane in the porous medium region. Contour of the axial velocity component (c) and temperature (d) in the central vertical plane in the cavity left of the hot heat exchanger.

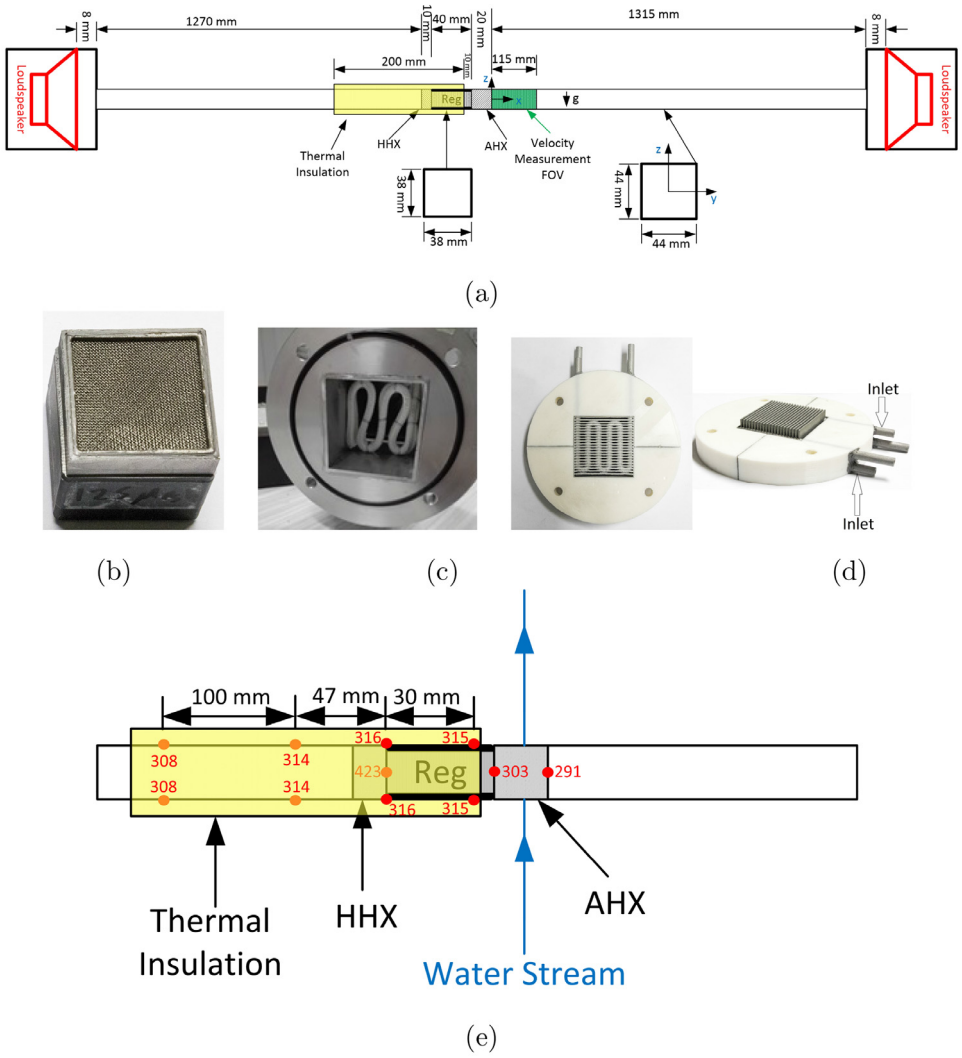

Fig. 10. (a): Schematic for the 2nd experimental setup. Photos for (b): The regenerator, (c): The hot heat exchanger, (d): The ambient heat exchanger, (e): Thermocouples locations and results of measurements.

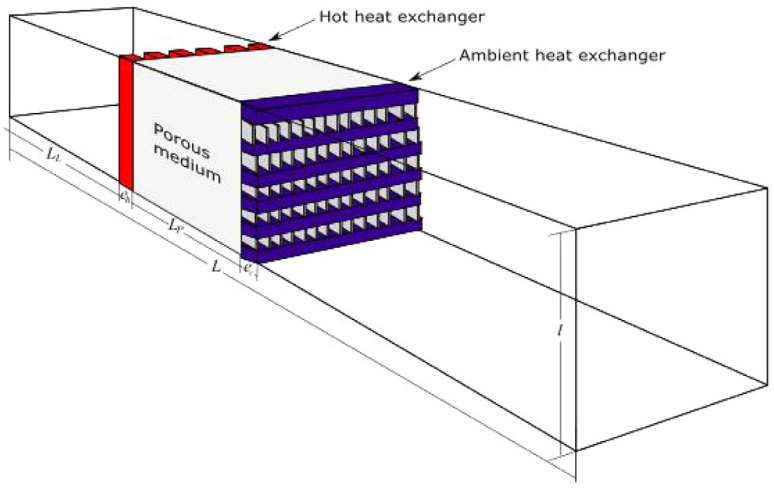

Fig. 11. Numerical configuration for the 2nd configuration.

conductivity k_p, the porous medium Rayleigh number is $Ra_p = \frac{\rho g \beta \Delta T H K_{xx}}{\mu \alpha_p}$, with $\alpha_p = \frac{k_p}{\rho c_p}$ the porous medium equivalent thermal diffusivity, and H a reference height [18]. Using all geometrical and thermophysical parameters presented previously (Table 1), and taking the reference height $H = R$, this porous Rayleigh number is $Ra_p = 1.1$. The associated velocity scale is $V_{refp} = \frac{\alpha_p}{H} Ra_p = 0.02$ m/s [18]. The maximum velocity in the region on the right of the hot heat exchanger is about 0.04 m/s, which is indeed on the order of this velocity scale. The characteristics of the porous medium therefore determine the strength of the convection flow.

On the left of the hot heat exchanger, the flow is driven by the temperature difference between the left end of the cylindrical tube and the heat exchanger (imposed based on the experiments and equal to about $\Delta T_l = 110$ K). The flow in this region should then be that of a differentially heated fluid cavity. The reference fluid Rayleigh number is classically given as $Ra = \frac{\rho g \beta \Delta T_l H^3}{\mu \alpha}$, with $\alpha = \frac{k}{\rho c_p}$ the fluid thermal diffusivity, and H a reference height [17]. Using the same reference height $H = R$, this fluid Rayleigh number is $Ra = 3.36 \times 10^5$. The associated velocity scale is $V_{ref} = \frac{\alpha}{H} Ra^{1/2} = 0.38$ m/s [17]. The maximum velocity in the region on the left of the hot heat exchanger is about 0.15 m/s (Fig. 9c), which is indeed on the order of this velocity scale. The strength of the convection flow in this region will then be determined by the effectiveness of the isolation of this "hot" part of the tube.

When this simple thermoacoustic engine is functioning (with plugs in place), acoustic velocities of about 2 m/s and streaming velocities of about of 1 cm/s have been observed for the same applied electrical power [15]. Therefore the present results confirm that natural convection is significant and that this phenomenon is important in understanding mean velocity measurements in such a device. This phenomenon, as acoustic streaming and jet streaming, is a source of heat flux that should be taken into account for a realistic thermal balance in such a device. Moreover, the above presented results show that a simple model as the one proposed here gives realistic results, meaning that a thermoacoustic core is satisfactorily described as a homogeneous porous medium in terms of natural convection effects. Finally, it was found that the use of Rayleigh numbers give a correct order of magnitude for the convective velocity, that can be used for a preliminary estimate. In the following section we consider a configuration slightly more complicated and more representative of an optimized system because an ambient heat exchanger is added. Our aims here are the same as above, i.e. investigate the natural convection flows in such a system both experimentally and numerically.

3. Natural convection flow in a cavity with ambient heat exchanger

3.1. Experimental setup, measurement systems and procedure

In this second experimental setup, many factors were taken into considerations in the design process to overcome difficulties encountered in the 1st configuration. First, the resonator duct is chosen to have a square cross-sectional area to facilitate the PIV measurements in the vertical plane ($x - z$ plane in Fig. 10a) at different transverse locations (y-direction). Second, an Ambient Heat Exchanger (AHX) is added on the right side of the regen-

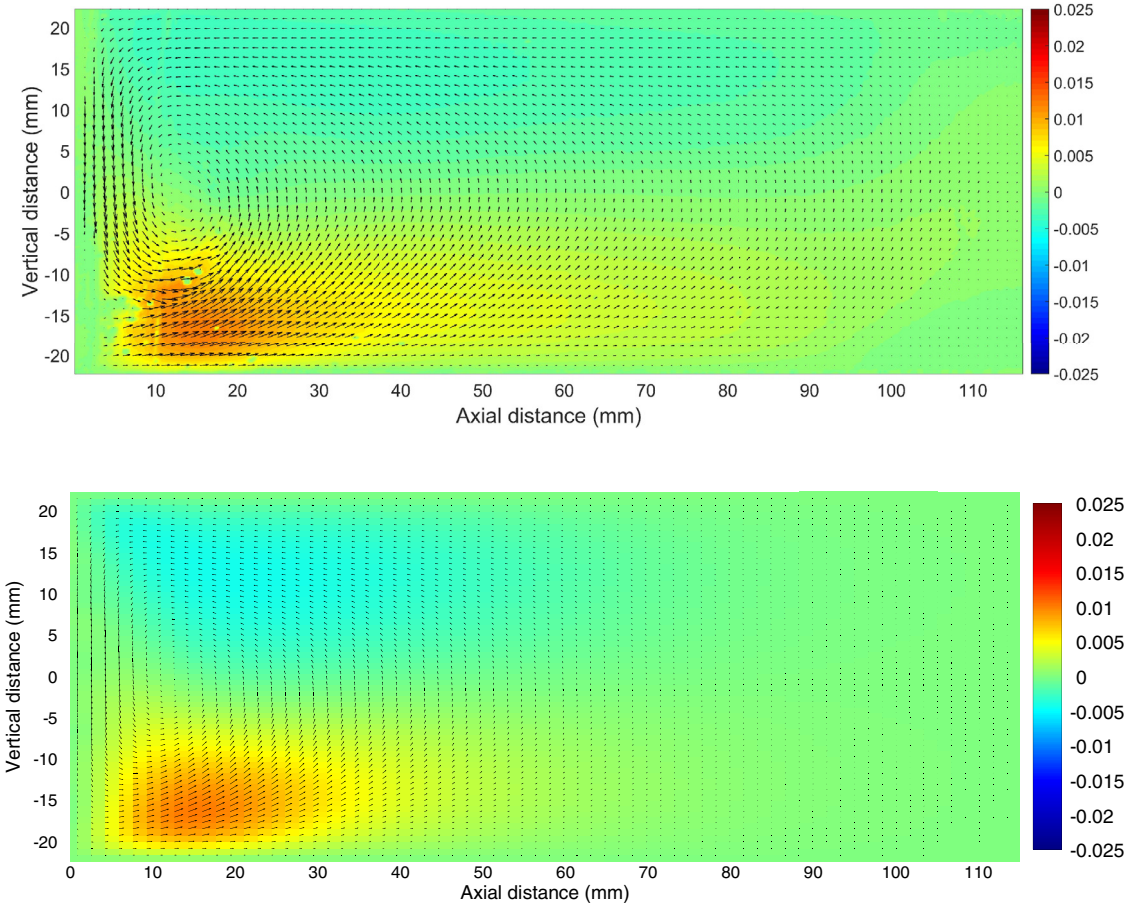

Fig. 12. Velocity vector map overlapped on the color map of the axial velocity component at the exit of the AHX on vertical plane at $y = -19$ mm (top: experiments, bottom: numerical simulations).

erator to keep its temperature constant. At the left side of the regenerator ends is placed an electric resistance as in the 1st configuration. Third, a thermal insulation is used to cover the hot part of the resonator and hence to reduce the heat loss through the walls of the resonator tube. As shown in Fig. 10a, the setup consists of a square duct with inner side length of 44 mm and the total length of the duct is 2655 mm. The left part of the duct is made of aluminum whereas the right part of the duct is made of acrylic to grant an optical access for the laser measurements. Two loudspeakers (Model: PHL - B20/2410) are attached to the ends of the duct. As before, in order to isolate the natural convection flow, no acoustic wave was generated in the resonator, that is the loudspeakers were turned off. The thermoacoustic core consists of a regenerator placed between the Hot Heat Exchanger (HHX) and the AHX. The coordinate system is also defined in Fig. 10a, with $x = 0$ corresponding to the right end of the AHX. As shown in Fig. 10b, the regenerator is made of stainless steel wire meshes stacked in a steel canister with a total length of 40 mm. The volumetric porosity (i.e. the ratio of the gas volume to the total volume) of the regenerator is 80%. The HHX is made of an insulated electric heater wire with total length of 450 mm and an outer diameter of 5 mm. The electrical wire is formed as shown in Fig. 10c, yielding a porosity of the hot heat exchanger of 43% and a length in the axial direction (i.e. x-axis) of 10 mm. As shown in Fig. 10d, the AHX is made of three parts. The central part, which is responsible for the heat exchange between the gas and the water, is printed (using 3D printing technology) from steel powder. The other two parts (white in Fig. 10d) are printed from plastic to avoid the heat transfer through the walls. The three parts are glued together and assembled with the resonator duct. The central part of the AHX is made of fins with thickness of 1 mm and plate spacing of 1 mm. Also, there are two water paths where the water flow direction in one of them is in the opposite direction to the other to achieve a temperature uniformity over the cross-section of the AHX. The inner and outer diameters of the water tubes are 3 mm and 5 mm, respectively. The total length of the AHX in the axial direction (i.e. x-axis) is 20 mm and its porosity is 40.5%.

The same PIV system as for the first setup was used and a similar experimental procedure was followed. Here the input electrical power was 30 W ± 1% and the temperatures of the walls of the aluminum duct are measured (see Fig. 10e). Thermocouples are placed beneath the thermal insulation and in contact with the walls of the duct to accurately measure the wall temperatures. It was checked that thanks to the AHX, the temperature of the right part of the resonator duct (i.e. acrylic duct) remains at the ambient temperature therefore, no temperature measurements were conducted on the walls of the acrylic duct. The PIV measurements performed in this system focus on measuring the natural convection flow at the end of the AHX in the vertical plane (i.e. $x - z$ plane) and at 7 different transverse locations (i.e. $y = 0, \pm 5$ mm, ± 15 mm and $\pm$ 19 mm).

The uncertainty in the temperature measurements is ± 1 % of the reported mean temperatures. The value of the spatial-average uncertainty in the velocity measurements is reduced to ± 6 % (compared to ± 13 % in the first experimental setup in which a circular duct is used) because the laser light reflections are less when the duct walls are flat (i.e. square duct).

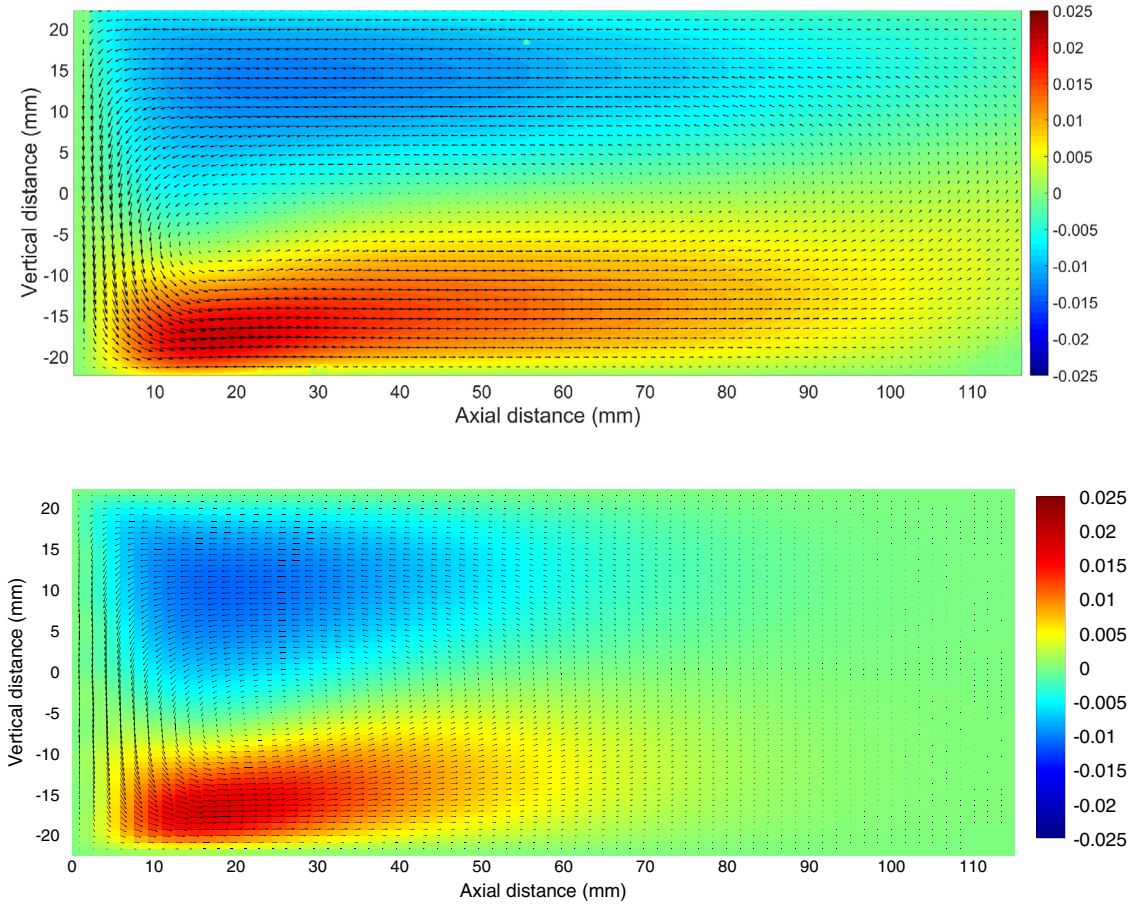

Fig. 13. Velocity vector map overlapped on the color map of the axial velocity component at the exit of the AHX on vertical plane at $y = -5$ mm (top: experiments, bottom: numerical simulations).

3.2. Numerical model

As previously, a simplified 3D configuration is introduced in order to model the experimental configuration (Fig. 11). The horizontal duct has a square cross-section (with side length equal to the inner side length of the experiment $l = 44$ mm).

The regenerator is modeled as a homogeneous parallelepipedic isotropic porous medium block of length $L_p = 40$ mm and cross-section width 38 mm, inserted in a steel case (as in the experiment). Its thermophysical characteristics are its porosity $\epsilon = 0.8$, its permeability $K_{xx} = K_{yy} = K_{zz} = K = 10^{-8}$ m^2 (based on experimental work performed on similar materials [26]), and its equivalent thermal conductivity $k_p = 3.16$ W m^{-1} K^{-1} (calculated as $k_p = \epsilon k_{fluid} + (1-\epsilon)k_{solid}$).

The hot heat exchanger (electric wire) is modeled as 6 vertical solid plates of axial width $e_h = 10$ mm (as in the experiment) and transverse width equal to 4 mm, maintained at given hot temperature $T_{hot} = 438$ K.

The ambient heat exchanger, placed on the right side of the porous medium, is modeled as 6 horizontal solid plates of axial width $e_c = 20$ mm (as in the experiment) and transverse width equal to 4 mm maintained at given cold (water) temperature $T_{cold} = 291$ K. In between the solid plates, the vertical fins are modeled as a homogeneous anisotropic porous medium (i.e. stack of thin plates). The characteristics of that porous medium are its porosity $\epsilon = 0.4$ (as in the experiment), its permeability assumed anisotropic $K_{xx} = K_{zz} = d_1^3/(12d_1 + d_2) = 10^{-8}$ m^2 (where d_1 is the plate's interspace and d_2 the plate's width, based on [18]), $K_{yy} \approx 0$, and its thermal conductivity $k_p = 27.4$ W m^{-1} K^{-1} (calculated from the porosity and thermal conductivities of gas and plates).

On the left of the HHX, in order to model the thermal insulation, the duct walls are adiabatic. Therefore the steady temperature in that region should be homogeneously equal to the hot temperature T_{hot}, and the natural convection flow should not extend very far. For that reason and in order to lower computational costs, the length of the duct left of the HHX is reduced to $L_l = 160$ mm.

Since the thermal insulation also covers part of the regenerator, the duct walls are adiabatic along the insulation (with axial extension identical to that used in the experiment). The temperature of the remainder of the duct wall along the regenerator is prescribed equal to $T_{amb} = 294$ K. The ambient temperature T_{amb} is prescribed along the duct walls on the right side of the AHX.

The temperature difference $T_{amb} - T_{cold} = 3$ K being quite small, the natural convection flow should not extend very far. For that reason and in order to lower computational costs, the length of the duct right of the AHX is reduced so that the total computational length is smaller than that of the experiment and equal to $L = 430$ mm. The reference ambient temperature T_{amb} is used to calculate the thermophysical parameters of the fluid.

The numerical domain is meshed using 64 points regularly spaced along the cross sectional sides in the y and z directions. The mesh size in the axial direction is $\Delta x = 1.6 \times 10^{-3}$ m. This spatial resolution is adequate for the given problem configurations. The time step is adjusted throughout the simulation in order to satisfy a CFL < 0.5 criterion.

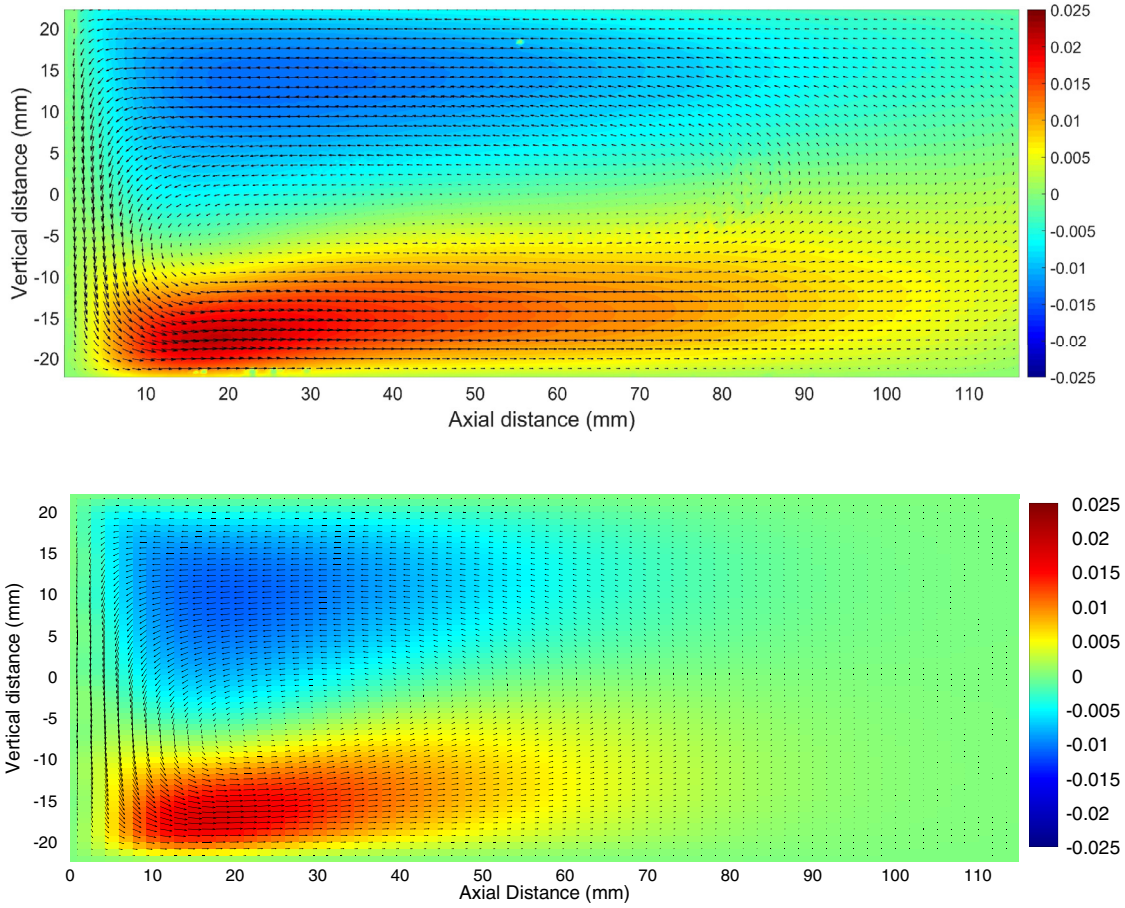

Fig. 14. Velocity vector map overlapped on the color map of the axial velocity component at the exit of the AHX on vertical plane at $y = 0$ (top: experiments, bottom: numerical simulations).

3.3. Results and discussion

As for the previous configuration both simulation and experiments reach a steady state. Figs. 12–14 show the velocity vector map overlapped on the color map of the axial velocity component of the natural convection flow obtained from experiments and numerical simulations at the exit of the AHX on vertical plane for 3 different transverse locations $y = -19$ mm (Fig. 12), $y = -5$ mm (Fig. 13), and $y = 0$ (center plane, Fig. 14). Experimental and numerical results agree remarkably well, both qualitatively and quantitatively, considering the numerous simplifications and approximations made in the numerical model. As in the case of the first experiment -without AHX-, the natural convection vortices extend for a longer axial distance in the experiments than in numerical calculation. Again, this could be due to the fact that the temperatures imposed on the tube boundary are based on the measurement of the outside temperature instead of the inside. The convection vortex is in the opposite direction than in the configuration without ambient heat exchanger, and the maximum axial velocity component is about half. The direction of the flow comes from the fact that the ambient heat exchanger is very effective, so that the tubes containing the cold water are cooler than the ambient temperature on the right fluid cavity. Therefore the fluid tends to move downward in the vicinity of the AHX and then is forced to turn right at the bottom of the duct. The order of magnitude of the velocity can be compared to the natural convection reference velocity in a fluid cavity calculated using $\Delta T_r = T_{amb} - T_{cold} = 3$ K and a reference height $H = 44$ mm. The calculation gives the Rayleigh number $Ra = 1.63 \times 10^4$ and $V_{ref} = 0.07 \times 10^{-3}$ m/s. The maximum velocity in that region is about 0.025 m/s (Figs. 12–14), which is indeed on the order of this velocity scale. In order to better understand the convection flow, contours of the calculated axial velocity component and temperature in the central vertical plane around the regenerator (the measurement field of view does not extend left of $x = 0$) are shown on Fig. 15. Analysis of this figure and of Fig. 12 shows that in this experiment the AHX prevents the development of a strong natural convection flow on the right part of the duct. Therefore the duct is clearly separated in two parts, left of the AHX and right of the AHX.

Since the regenerator is placed between the heat exchangers, the flow is similar to the natural convection flow in a porous differentially heated cavity (Fig. 15). However the regenerator's permeability being very small, so are velocities (on the order of 0.002 m/s) and isothermal lines are almost vertical, i.e. the regenerator acts like a conducting solid. The order of magnitude of the velocity can be compared to the porous natural convection reference calculated using $\Delta T = T_{hot} - T_{cold} = 147$ K, $H = 44$ mm. The calculation gives the porous Rayleigh number $Ra_p = 1.26 \times 10^{-1}$ and $V_{refp} = 2.2 \times 10^{-3}$ m/s. The maximum velocity in the regenerator is about 0.002 m/s (Fig. 15), which is indeed on the order of this velocity scale. Both the ambient heat exchanger and the isolation of the hot duct contribute to the concentration of temperature gradients in the regenerator only. The convection flow inside the regenerator depends then mostly on its permeability.

On the left of the HHX the flow is clearly driven by the flow between the mesh wires of the regenerator (Fig. 15). The temperature in that region is almost homogeneously hot.

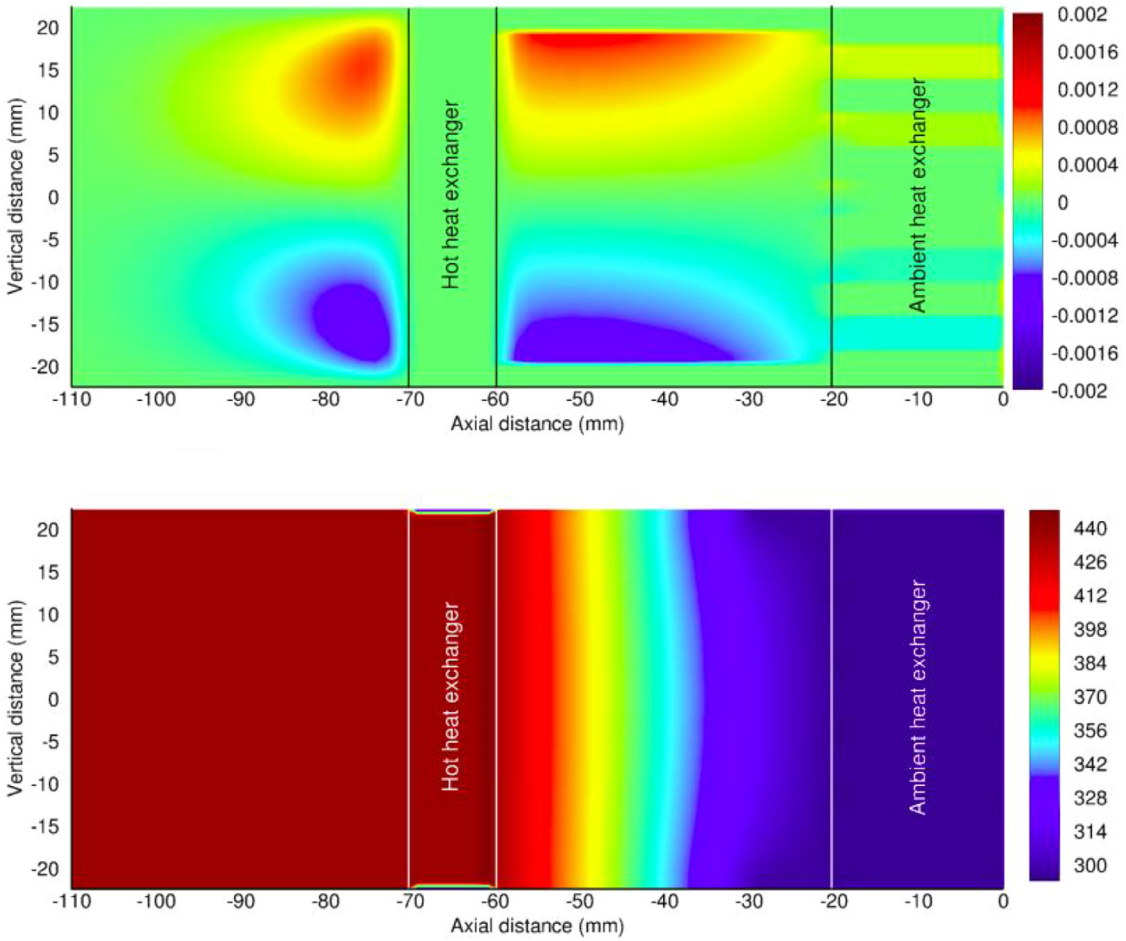

Fig. 15. Contours of the axial velocity component (top) and temperature (bottom) in the vertical central plane (numerical simulation results).

In sum, the simple model proposed here predicts the natural convection flow inside the entire device, with good agreement with measurements in the field of view.

4. Conclusion

Natural convection flows were analyzed both experimentally and numerically for two different horizontal thermoacoustic cavities, when no acoustic oscillations were present. The first cavity consisted of a cylindrical resonator filled with air and containing a thermoacoustic core made of a ceramic stack placed next to a wire resistance (hot heat exchanger). The second cavity consisted of a duct with square cross-section filled with air and containing a thermoacoustic core made of a regenerator placed between a wire resistance (hot heat exchanger) and an ambient heat exchanger (using a water stream for the heat exchange). Temperature was measured by thermocouples in several points along the cavities, and velocity fields were obtained from PIV measurements in several vertical planes (only the central vertical plane in the first experiment). The numerical model consisted in solving Navier-Stokes equations under Boussinesq assumptions inside a simplified cavity based on each experimental setup. In the first experiment, the cylindrical cavity was of similar geometry and dimensions as the experiment, the hot heat exchanger was modeled as several immersed solid bodies at given temperature, and the ceramic stack was modeled as a homogeneous anisotropic porous medium. The temperature along the cylindrical tube was prescribed as a boundary condition based on the experimental measurements. In the second experiment, the cavity was also modeled based on experiments, the regenerator being modeled as a homogeneous isotropic porous medium and the ambient heat exchanger as an immersed solid body at given temperature inside a homogeneous anisotropic porous medium. The temperature boundary conditions were also based on experimental measurements.

It was shown that the flow and temperature distributions are fully three-dimensional. They depend on the thermophysical properties of the working gas and of the porous media constituting the thermoacoustic stack or regenerator and heat exchangers, as well as on the geometrical characteristics of the device and the temperature conditions. There was excellent qualitative and quantitative agreement on the velocity fields between experimental and numerical simulation results for both configurations. Also the velocity scales observed in the different regions of the thermoacoustic cavities were in good agreement with classical scales for natural convection flows within a porous or fluid cavity. It should therefore be possible to predict the strength and patterns of natural convection flows inside functioning thermoacoustic devices using an approach similar to the one proposed here. It was noted that the observed natural convection flows could be quite significant in such devices and potentially interfere with thermoacoustic effects. We hope the fairly simple models used here will be further used by others to assess potential natural convection effects and contribute to optimal design of thermoacoustic devices. However, possible interaction and coupling between thermoacoustic and natural convection effects was not studied here and is the topic of ongoing work.

CRediT authorship contribution statement

Omar Hireche: Formal analysis, Writing - original draft. **Islam Ramadan:** Conceptualization, Visualization, Writing - original draft. **Catherine Weisman:** Supervision, Validation, Writing - review & editing. **Hélène Bailliet:** Project administration, Writing - original draft. **Yann Fraigneau:** Software. **Diana Baltean-Carlès:** Project administration, Writing - original draft. **Virginie Daru:** Validation, Supervision.

Acknowledgments

This research is financially supported by Agence Nationale de la Recherche (Projet ANR-17-CE06-0007-01). The authors also appreciate the technical assistance provided by Pascal Biais, Laurent Philippon and Philippe Szeger.

Supplementary material

Supplementary material associated with this article can be found, in the online version, at 10.1016/j.ijheatmasstransfer.2019.119195

References

[1] G.W. Swift, Thermoacoustics: a unifying perspective for some engines and refrigerators, ASA Press, Springer, 2002.
[2] W. Dai, E. Luo, J. Hu, H. Ling, A heat driven thermoacoustic cooler capable of reaching liquid nitrogen temperature, Appl. Phys. Lett. 86 (2005) 224103.
[3] L. Zoontjens, C. Howard, A. Zander, B. Cazzolato, Feasibility study of an automotive thermo acoustics refrigerator, in: Proceedings of Acoustics, Busselton, Australia, 2005.
[4] J.A. Adeff, T.J. Hofler, Design and construction of a solar-powered, thermoacoustically driven, thermoacoustic refrigerator, J. Acoust. Soc. Am. 107 (6) (2005) L37–L42.
[5] S. Backhaus, E. Tward, M. Petach, Traveling wave thermoacoustic electric generator, Appl. Phys. Lett. 85 (2004) 1085.
[6] S. Spoelstra, M.E.H. Tijani, Thermoacoustic heat pumps for energy savings, in seminar “boundary crossing acoustics”, in: Proceedings of the Acoustical Society of the Netherlands, 2005.
[7] D.L. Gardner, G.W. Swift, A cascade thermoacoustic engine, J. Acoust. Soc. Am. 114 (4) (2003) 1905–1919.
[8] Y.-L. He, H.-B. Ke, F.Q. Cui, W.Q. Tao, Explanations on the onset and damping behaviors in a standing-wave thermoacoustic engine, Appl. Therm. Eng. 58 (2013) 298–304.
[9] G. Thummes, M. Schreiber, R. Landgraf, C. Heiden, Convective heat losses in pulse tube coolers: effect of pulse tube inclination, in: R.G. Ross (Ed.), Cryocoolers 9, Springer, Boston, 1997.
[10] M.E. Poese, R.M. Keolian, R.W.M. Smith, S.L. Garrett, E.C. Mitchell, Performance estimates of a helium-based thermoacoustic-Stirling chiller, Int. J. Low-Carbon Technol. 8 (2013) i79–i84.
[11] N. Pan, S. Wang, C. Shen, Visualization investigation of the flow and heat transfer in thermoacoustic engine driven by loudspeaker, Int. J. Heat Mass Transf. 55 (2012) 7737–7746.
[12] N. Pan, S. Wang, C. Shen, A fundamental study on characteristic of thermoacoustic engine with different tilt angles, Int. J. Heat Mass Transf. 74 (2014) 228–237.
[13] P. Debesse, D. Baltean-Carlès, F. Lusseyran, M.X. François, Oscillating and streaming flow identification in a thermoacoustic resonator from under-sampled PIV measurements, Meas. Sci. Technol. 25 (16pp) (2014) 25005.
[14] E. Saint Ellier, Y. Bailly, L. Girardot, D. Ramel, P. Nika, Temperature gradient effects on acoustic and streaming velocities in standing acoustic waves resonator, Exp. Therm. Fluid Sci. 66 (2015) 1–6.
[15] I. Ramadan, H. Bailliet, J.C. Valière, Experimental investigation of the influence of natural convection and end-effects on Rayleigh streaming in a thermoacoustic engine, J. Acoust. Soc. Am. 143 (1) (2018) 361–372.
[16] D. Poulikakos, A. Bejan, Natural convection in vertically and horizontally layered porous media heated from the side, Int. J. Heat Mass Transf. 26 (1983) 1805–1814.
[17] A. Bejan, Convection Heat Transfer, Mac Graw Hill, 1985.
[18] D.A. Nield, A. Bejan, Convection in Porous Media, Springer and Business Media, New York, 2006.
[19] C. Weisman, D. Baltean-Carlès, P. Duthil, P.L. Quéré, Natural convection in a stack of horizontal plates in a differentially heated cavity, in: Proceedings of the 19th International Symposium on Transport Phenomena (ISTP-19), Reykjavik, Island, 2008.
[20] O. Hireche, C. Weisman, D. Baltean-Carlès, V. Daru, Y. Fraigneau, Numerical study of the effects of natural convection in a thermoacoustic device, in: Proceedings of the 24th Congres Francais de Mecanique, Brest, France, 2019.
[21] A.K. Prasad, Particle image velocimetry, Curr. Sci. 79 (1) (2000) 51–60.
[22] D.W. Peaceman, H.H. Rachford, The numerical solution of parabolic and elliptic differential equations, J. Soc. Indust. Appl. Math. 3 (1) (1955) 28–41.
[23] K. Goda, A multistep technique with implicit difference schemes for calculating two or three-dimensional cavity flows, J. Comput. Phys. 30 (1979) 76–95.
[24] J.L. Guermond, P.D. Minev, J. Shen, An overview of projection methods for incompressible flows, Comp. Meth. Appl. Mech. Eng. 195 (2006) 6011–6045.
[25] Y. Saad, Iterative methods for sparse linear systems, Society for Industrial and Applied Mathematics, second ed., 2003.
[26] S.H. Tasnim, Porous Media Thermoacoustic Stacks: Measurements and Models, University of Waterloo, Ontario, Canada, 2011 Thesis.

.

P. Le Quéré, C. Weisman, H. Paillère, J. Vierendeels, E. Dick, R. Becker, M. Braack, J. Locke, "Modelling of natural convection flows with large temperature differences : A Benchmark problem for low Mach number solves. Part 1. Reference solutions", ESAIM : Mathematical Modelling and Numerical Analysis, vol. 39 (3), 609-616, 2005.

ESAIM: M2AN
Vol. 39, N° 3, 2005, pp. 609–616
DOI: 10.1051/m2an:2005027

ESAIM: Mathematical Modelling and Numerical Analysis

MODELLING OF NATURAL CONVECTION FLOWS WITH LARGE TEMPERATURE DIFFERENCES: A BENCHMARK PROBLEM FOR LOW MACH NUMBER SOLVERS. PART 1. REFERENCE SOLUTIONS

Patrick Le Quéré[1], Catherine Weisman[1], Henri Paillère[2], Jan Vierendeels[3], Erik Dick[3], Roland Becker[4], Malte Braack[4] and James Locke[5]

Abstract. There are very few reference solutions in the literature on non-Boussinesq natural convection flows. We propose here a test case problem which extends the well-known De Vahl Davis differentially heated square cavity problem to the case of large temperature differences for which the Boussinesq approximation is no longer valid. The paper is split in two parts: in this first part, we propose as yet unpublished reference solutions for cases characterized by a non-dimensional temperature difference of 0.6, Ra = 10^6 (constant property and variable property cases) and Ra = 10^7 (variable property case). These reference solutions were produced after a first international workshop organized by CEA and LIMSI in January 2000, in which the above authors volunteered to produce accurate numerical solutions from which the present reference solutions could be established.

Mathematics Subject Classification. 65M50, 76M10, 76M12, 76M20, 76M22, 76R10.

Numerical workshop, Low Mach Number Flows Conference, June 21-25, 2004, Porquerolles, France.

Introduction

Heat transfer by natural convection and conduction in enclosures occurs in numerous practical situations: solar collectors, cooling of nuclear reactors, heat management in electronic equipment, etc. In many of these situations, the temperature difference is small enough that the flow may be modelled assuming that the flow is incompressible with constant physical properties and buoyancy effects modelled as a linear function of the temperature, the so-called Boussinesq approximation. However, for large temperature differences, the flow becomes compressible with a strong coupling between the continuity, the momentum and the energy equations through the equation of state, and its properties (viscosity, heat conductivity) also vary with the temperature, making the Boussinesq flow approximation inappropriate and inaccurate. Most references in the literature deal with Boussinesq type natural convection flows. There is a clear need therefore to have reference data (*i.e.* to validate CFD codes) for natural convection flows with large temperature differences, where low Mach number

Keywords and phrases. Natural convection, non-Boussinesq, low Mach number.

[1] LIMSI, BP 133, 91403 Orsay Cedex, France. plq@limsi.fr; weisman@limsi.fr

[2] CEA Saclay, DEN/DM2S/SFME,91191 Gif-sur-Yvette Cedex, France. henri.paillere@cea.fr

[3] Ghent University, B-9000 Gent, Belgium. Jan.Vierendeels@UGent.be; erik.dick@UGent.be

[4] Heidelberg University, Germany. malte.braack@iwr.uni-heidelberg.de

[5] U. Warwick and British Energy Generation Ltd.

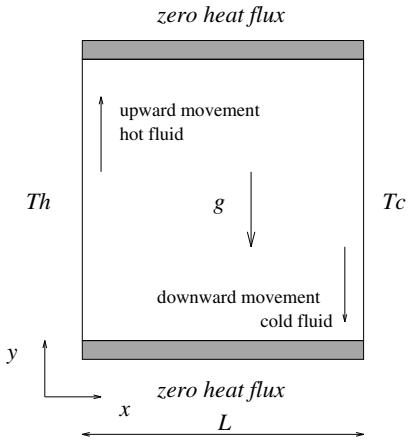

FIGURE 1. Differentially heated square cavity problem.

effects come into play. A test case was designed, extending the well-known de Vahl Davis benchmark problem [5] to cases with large temperature differences.

In January 2000, CEA and LIMSI organized a first international benchmark [11] dealing with this test case, with the objective of establishing reference (*i.e.* grid and model independent) solutions from a code-to-code comparison of various flow models and solvers. Twenty-two contributions were received and they enabled to point out several numerical difficulties – such as mass and energy conservation issues, post-processing of Nusselt numbers and CPU performance constraints. Following this benchmark, several participants performed further calculations to derive reference solutions. Their results which were not published, are presented here. In the second part of the paper, we will describe the results obtained in the framework of the conference on "Mathematical and numerical aspects of low Mach number flows" organized by INRIA and MAB in June 2004.

1. A NATURAL CONVECTION TEST-CASE

1.1. **Description**

The test-case selected for the numerical conference organized by INRIA and MAB in June 2004 is the differentially heated square cavity problem depicted in Figure 1. It is similar to the well-known benchmark [5] for incompressible flow solvers which produced a set of reference solutions for different Rayleigh numbers Ra, ranging from 10^3 to 10^6 [4], later extended up to 10^8 close to the end of the steady laminar regime [8]. We recall that for a perfect gas, the Rayleigh number is defined as

$$\mathrm{Ra} = \mathrm{Pr}\,\frac{g\rho_o^2(T_h - T_c)L^3}{T_o\,\mu_o^2} \tag{1}$$

where Pr is the Prandtl number (0.71 for air), g is the gravity, L the height of the cavity, T_h and T_c the hot and cold temperatures applied to the vertical walls, T_o a reference temperature equal to $(T_h + T_c)/2$, ρ_o reference density corresponding to T_o, and μ the coefficient of viscosity at T_o. The temperature differences may be defined by the non-dimensional parameter ϵ:

$$\epsilon = (T_h - T_c)/(T_h + T_c). \tag{2}$$

For small enough ϵ, compressibility effects may be neglected, and incompressible flow models with the Boussinesq approximation are valid and accurate enough to compute the flow and the heat transfer to the walls [7].

The latter is characterized by the local and average Nusselt numbers Nu and $\overline{\mathrm{Nu}}$,

$$\mathrm{Nu}(y) = \frac{L}{k_o(T_h - T_c)}\, k\frac{\partial T}{\partial x}\bigg|_w, \qquad \overline{\mathrm{Nu}} = \frac{1}{L}\int_{y=0}^{y=L} \mathrm{Nu}(y)\,\mathrm{d}y$$

where $k(T)$ is the thermal conductivity and $k_o = k(T_o)$. For large temperature differences, the Boussinesq assumptions break down and one needs to resort to a compressible flow model, or since the Mach numbers remain small, to a low Mach number approximation model. Chenoweth and Paolucci [3] have studied in detail the effects of Ra and ϵ on flow patterns and heat transfer, but used temperature-dependent properties as well as varying Prandtl number. Polezhaev [14] studied the $\epsilon = 0.2$ case with temperature-dependent properties and constant Prandtl number. Le Quéré *et al.* [9] have also studied the non-Boussinesq cases (up to $\epsilon = 0.6$) with Sutherland's laws for viscosity and thermal conductivity.

1.2. **Governing equations**

We consider in this study the Navier-Stokes equations describing the flow of a compressible, calorically and thermally perfect gas, with constant Prandtl number. In conservative form, they read:

$$\begin{aligned}
&\frac{\partial}{\partial t}\rho + \nabla\cdot(\rho\underline{u}) = 0\\
&\frac{\partial}{\partial t}(\rho u) + \nabla\cdot(\rho\underline{u}\otimes\underline{u} + p\underline{\underline{I}}) = \rho\underline{g} + \nabla\cdot\underline{\underline{\tau}}\\
&\frac{\partial}{\partial t}(\rho E) + \nabla\cdot(\rho\underline{u}H) = \nabla\cdot(k\nabla T) + \rho\underline{g}\cdot\underline{u}\\
&p = \rho RT = (\gamma-1)\rho(E - \frac{1}{2}\|\underline{u}\|^2)
\end{aligned} \tag{3}$$

where ρ, u, p, E and H are respectively the density, velocity, pressure, specific total energy and specific total enthalpy. $\underline{g}$ and $\underline{\underline{\tau}}$ represent respectively the gravity and the viscous stress tensor,

$$\underline{\underline{\tau}} = \mu\left(\nabla\underline{u} + \nabla^T\underline{u} - \frac{2}{3}(\nabla\cdot\underline{u})\underline{\underline{I}}\right).$$

μ and k are respectively the dynamic viscosity and the heat conduction coefficients. At low Mach numbers, the dissipation term $\nabla\cdot(\underline{\underline{\tau}}\cdot\underline{u})$ in the energy equations may be neglected, and was omitted in the equation.

For non-conservative solvers based on low Mach number asymptotic approximations of the Navier-Stokes equations, the energy equation may be written in different forms, in terms of specific internal energy, enthalpy or temperature. For a perfect gas, and neglecting the energy dissipation term, the following form is advocated:

$$\rho c_p\left(\frac{\partial}{\partial t}T + \underline{u}\cdot\nabla T\right) = \nabla\cdot(k\nabla T) + \frac{\mathrm{d}\overline{P}(t)}{\mathrm{d}t}$$

where $\overline{P}(t)$ is the (spatially uniform) thermodynamic pressure in the domain, and c_p is the specific heat at constant pressure, which may be expressed in terms of the ratio of specific heats γ and the gas constant R, $c_p = \gamma R/(\gamma-1)$.

In the general case the evolution of $\overline{P}(t)$ is governed by a first order equation invoking the mass and heat fluxes at the boundary [12]. In the case of a cavity with impervious walls, this equation of evolution reduces to

$$\frac{d\overline{P}}{dt} = (\gamma-1)\int_{\partial\Omega}\kappa\nabla T.\mathbf{n}\; d\sigma\;. \tag{4}$$

Alternatively, $\overline{P}(t)$ can be obtained directly from the constraint of global conservation of mass contained in the cavity at initial time

$$\overline{P}(t) = P_0 \frac{\int \frac{1}{T_0} dv}{\int \frac{1}{T} dv} \ . \tag{5}$$

In this study, we shall assume either constant or temperature-dependent transport coefficients $\mu(T)$ and $k(T)$, given by Sutherland's law:

$$\frac{\mu(T)}{\mu^*} = \left(\frac{T}{T^*}\right)^{\frac{3}{2}} \frac{T^* + S}{T + S}, \quad k(T) = \frac{\mu(T)\gamma R}{(\gamma - 1)\mathrm{Pr}}$$

with $T^* = 273$ K, $S = 110.5$ K, $\mu^* = 1.68 \times 10^{-5}$ kg/m/s, $\gamma = 1.4$ and $R = 287$ J/kg/K, and $\mathrm{Pr} = 0.71$.
It is noted that at steady state, integration of the energy equation over the volume of the cavity represented in Figure 1 implies that the average Nusselt numbers on the vertical walls denoted by L (left wall at T_h) and R (right wall at T_c) are equal:

$$\overline{\mathrm{Nu}}_L = \overline{\mathrm{Nu}}_R. \tag{6}$$

1.3. **Initial conditions**

In each case, the problem is completely defined by the Rayleigh number, the value of ε and the following coefficients:

$$\begin{aligned} P_o &= 101325 \text{ Pa} \\ T_o &= 600 \text{ K} \\ R &= 287 \text{ J/kg/K} \\ \rho_o &= \frac{P_o}{RT_o} \\ Pr &= 0.71 \\ \gamma &= 1.4 \\ g &= 9.81 \text{ m/s}^2. \end{aligned}$$

Spatially uniform initial conditions are imposed, $\forall (x, y) \in [0, L]^2$,

$$\begin{aligned} T(x, y) &= T_o \\ \rho(x, y) &= \rho_o \\ \overline{P}(t = 0) \quad &= P_o \\ u(x, y) = v(x, y) &= 0. \end{aligned}$$

1.4. **Boundary conditions**

On the hot wall, a temperature of $T_h = T_o(1 + \varepsilon)$ is imposed, and on the cold wall, a temperature of $T_c = T_o(1 - \varepsilon)$ is imposed. On the horizontal walls, adiabatic conditions are applied. On all walls, the no-slip condition is imposed for the velocity.

1.5. **Required results and workshop contributions**

Participants were asked to produce solutions for several test cases in a given format so as to be easily manipulated for the purpose of comparison. More than 25 contributions were received, which are reported in [11] and will not be discussed here.

2. Reference test cases and contributors

During the round table discussion that took place in the January 2000 workshop, it was suggested that the comparison exercise would be incomplete if the opportunity was not taken to try to establish reference solutions for a few of the test cases. It was also proposed that these solutions should be established from a consensus between different contributors, rather than imposed from a single contributor, given the uncertainties in the underlying modelling approaches. Several contributors volunteered to perform additional calculations with the challenge to provide results of assessed quality that could be used to derive these reference solutions. These participants were asked to produce "grid-converged" results, or to ensure that their numerical results were sufficiently accurate by refining the mesh until the solutions varied no more (at least for the first four digits).

The three test cases which were selected are the following.

- Test case T1: $\mathrm{Ra} = 10^6$, $\epsilon = 0.6$ and constant properties $\mu = \mu^*$.
- Test case T2: $\mathrm{Ra} = 10^6$, $\epsilon = 0.6$ and Sutherland law $\mu = \mu(T)$.
- Test case T3: $\mathrm{Ra} = 10^7$, $\epsilon = 0.6$ and Sutherland law $\mu = \mu(T)$.

2.1. **Contributors**

2.1.1. *J. Locke, British Energy Generation Ltd and U. Warwick, UK*

The solutions were obtained by solving the steady-state equations, and using iteration to maintain the correct mass of fluid. The work was carried out using FEAT [6], a fluid modelling program developed by British Energy Generation Ltd. FEAT is a Finite Element code, which uses quadratic elements for accurate and smooth solutions. Upwinding is not usually needed, which allows h^4 truncation errors, and very fast mesh-convergence. The method of solution for a steady state of a non-linear equations system is based on Newton-Raphson iteration, and uses the frontal algorithm to solve the linearized system for each iteration. FEAT is used for low Mach number flows, but implements the full compressible form of the Navier-Stokes equations in order to deal with property dependence due to large temperature differences. The local pressure gradients in the equation for thermal energy conservation are ignored and, as well as this, the enthalpy is assumed to be a function of temperature alone. This means that the thermal energy is effectively decoupled from the energy in the flow field, and that FEAT cannot model sound waves.

2.1.2. *R. Becker and M. Braack, Heidelberg University, Germany*

The authors apply flow equations valid for low Mach number flow, and formulated in primitive variables where the total pressure is split in a hydrodynamical part and a thermodynamic part [1]. The hydrodynamical pressure is neglected in the equation of state, because it is several orders of magnitude smaller than the thermodynamic pressure, which is constant in space. The gas law becomes an algebraic equation for the density, in contrast to the full compressible formulation where it is the equation for the total pressure. The discretization is based on conforming bilinear Finite Elements on quadrilateral meshes. The Galerkin formulation is stabilized by introducing additional least-square terms. The discretized non-linear equations are solved by a quasi-Newton method and the resulting linear equations by multigrid iterations (V-cycle), with block-ILU smoothing. The results are obtained on equidistant tensor grids. Further details are available in [2].

2.1.3. *J. Vierendeels and E. Dick, Ghent University, Belgium*

An AUSM (Advection Upwind Splitting Method) based discretization method is implemented, with an explicit third-order upwind discretization for the convective part, a line-implicit central discretization for the acoustic part and for the normal diffusive fluxes. The tangential fluxes are discretized centrally and treated explicitly [15]. For vanishing Mach number, stabilization terms are added to the mass flux. A low Mach number preconditioning of the convective fluxes is also used. A semi-implicit line method in multistage form is used because of the explicit third-order discretization of the convective part. The multistage semi-explicit method is accelerated with the multigrid method, using a full approximation scheme in a W-cycle with six levels of grids. The pressure in each node is re-scaled after each MG cycle so as to enforce the mass conservation.

2.1.4. *C. Weisman and P. Le Quéré, LIMSI, France*

The algorithm integrates in time the low Mach number equations formulated in primitive variables where the total pressure is split in a hydrodynamical part and a thermodynamic part. Time advancement is performed using a fractional time step method derived from the projection method used to compute incompressible flows. Spatial discretization uses a second order spatial approximation for both convective and diffusive fluxes on a standard finite volume staggered mesh. The momentum equations are advanced in time using an incremental ADI solver, using the old pressure field. A projection step is used to compute the velocity field with given divergence. This step involves the solution of a non separable Poisson equation, which is done using a multigrid algorithm. Spatial care was taken to ensure that all compatibility conditions were satisfied at the discrete level. Steady solutions were obtained by integrating long enough, and it was checked that the steady solutions were independent of the time step, thanks to the use of the incremental ADI solvers. Most computations were performed with Chebyshev and uniform grids in the horizontal and vertical direction, respectively.

2.1.5. *P. Le Quéré, LIMSI, France*

The test cases were computed using the algorithm described in [9]. This algorithm integrates the Low Mach number equations in unsteady form. The spatial approximation uses Chebyshev pseudo-spectral approximations in both spatial directions. The time stepping is second order and combines an explicit treatment of the convective terms with and implicit treatment of the diffusive terms. The resulting non separable Helmholtz equations are solved iteratively within each time step using an approximate factorization of the finite difference approximation of the Helmholtz operator as preconditioning. The divergence constraint is imposed using an Uzawa type iterative algorithm. Steady state solutions are obtained by integrating long enough.

2.2. **Accuracy assessment**

Assessing the quality and quantifying the accuracy of numerical solutions is a matter of utmost importance which is drawing increasing attention under the name of verification and validation. For most general programs and configurations this is a very complex process which is described for instance in [10]. The problem at hand belongs to a class of configurations for which the process of accuracy assessment involves three different aspects:

- making sure that the computer program is bug free;
- making sure that the steady state solution has been obtained;
- quantifying the spatial discretization error.

Aside from obvious coding mistakes which should never be overlooked, the first point is related to the consistency of the overall discrete algorithm with the continuous equations, and will not be discussed here.

The second point is particularly important for unsteady algorithms where steady states are obtained by letting time run to infinity. Infinity corresponds to the time scale for the flow establishment in the cavity and it is known [13] that this time scale is a diffusive time scale corresponding to the time needed to damp the internal waves in the cavity core which scales like $\mathrm{Ra}^{1/2}$ in the dimensionless units considered here. For explicit or semi-implicit schemes with the usual stability strains, integrating for such a long time can require hundreds of thousands of time steps, resulting in very long CPU times.

Quantifying the spatial discretization error in order to produce a solution of increased accuracy can usually be done through a Richardson extrapolation. Richardson extrapolation consists of computing solutions on different meshes, determining the leading order of the truncation error and extrapolating these solutions to zero mesh size. Let f_h, $f_{h'}$, $f_{h''}$ be the numerical approximations for a given scalar quantity f computed on three corresponding grids of of mesh size $h \leq h' \leq h''$ respectively with $\frac{h}{h'} = \frac{h'}{h''}$. Assuming that these grid meshes fall within the asymptotic convergence region with the truncation error at leading order characterized by h^α, it follows that:

$$\begin{aligned} f_h &= f + Ch^\alpha \\ f_{h'} &= f + Ch'^\alpha \\ f_{h''} &= f + Ch''^\alpha. \end{aligned}$$

TABLE 1. Reference results obtained in 2000.

	Locke (FE)	Becker & Braack (FE)	Vierendeels & Dick (FV)	Weisman & Le Quéré (FV)	Le Quéré (Spectral)	**Reference Solution**
Test case T1 ($\mathrm{Ra} = 10^6$, $\epsilon = 0.6$ and constant properties)						
Nu(h)	8.859785	8.859780	8.859783	8.859781	8.859777	**8.85978**
Nu(c)	8.859789	8.859780	8.859783	8.859780	8.859777	**8.85978**
P/Po	0.8563379	0.8563379	0.8563383	0.8563376	0.8563380	**0.856338**
Mesh	160×160	4×10^6 d.o.f.	512×512	512×512	80×80	
Test case T2 ($\mathrm{Ra} = 10^6$, $\epsilon = 0.6$ and Sutherland law)						
Nu(h)	8.686678	8.686605	8.686587	8.686583	8.686581	**8.6866**
Nu(c)	8.686617	8.686605	8.686611	8.686583	8.686581	**8.6866**
P/Po	0.9244872	0.9244874	0.9244877	0.9244872	0.9244873	**0.924487**
Mesh	160×160	4×10^6 d.o.f.	512×512	1024×1024	80×80	
Test case T3 ($\mathrm{Ra} = 10^7$, $\epsilon = 0.6$ and Sutherland law)						
Nu(h)	16.240740	16.241060	16.2409905	16.24097		**16.2410**
Nu(c)	16.240740	16.241060	16.2411507	16.24097		**16.2410**
P/Po	0.9226343	0.9226358	0.92263384	0.92263384		**0.92263**
Mesh	160×160	4×10^6 d.o.f.	512×512	1024×1024		

Combining these equation leads to the values of α and C:

$$\alpha = \frac{\ln\left(\frac{f_h - f'_h}{f'_h - f''_h}\right)}{\ln(\frac{h}{h'})}, \qquad C = \frac{f_h - f'_h}{h^\alpha(1 - (\frac{h'}{h})^\alpha)};$$

which allows for the computation of the extrapolated value for f. This procedure works if higher order terms are really negligible *i.e.* if $f_h = f + Ch^\alpha$ is a good approximation of the truncation error for the coarser grid (see [10] for a thorough discussion).

3. Reference solutions (2000)

Table 1 summarizes the converged results obtained for each of the three test cases from the 5 different contributions. As can be seen, an excellent agreement is obtained between the different contributions and the last column provides a reference solution with all digits exact given the usual rounding conventions. The accuracy of reference solution T1 is close to 10^{-6}, whereas that of solutions T2 and T3 is slightly lower and around 10^{-5}. It is to be noted that establishing these reference solutions has required computing solutions over very fine meshes in most cases (except for Locke) and that significant computing resources were involved. It should also be noted that the level of agreement is quite exceptional given the fact that all these contributions do not solve exactly the same physical model (some use the full compressible equations while others use the low-Mach number equations). The last comment is that one should not try to derive reference solutions of

infinite accuracy, because the differences in the models, fully compressible or low-Mach number, will eventually show up in the solutions, at accuracy levels of Ma^2, that is around 10^{-7} or 10^{-8}. This still leaves some room for improvement for cases T2 and T3.

4. Conclusion

Reference solutions have been derived for three test cases of steady natural convection flows of gases under large temperature differences. These reference solutions can be used in the process of validation and verification of CFD codes at the elementary level, before addressing more complex physical configurations.

References

[1] R. Becker, M. Braack and R. Rannacher, Numerical simulation of laminar flames at low Mach number with adaptive finite elements. *Combustion Theory and Modelling, Bristol* **3** (1999) 503–534.
[2] R. Becker, M. Braack, Solution of a stationary benchmark problem for natural convection with high temperature difference. *Int. J. Thermal Sci.* **41** (2002) 428–439.
[3] D.R. Chenoweth and S. Paolucci, Natural Convection in an enclosed vertical air layer with large horizontal temperature differences. *J. Fluid Mech.* **169** (1986) 173–210.
[4] G. de Vahl Davis, Natural convection of air in a square cavity: a benchmark solution. *Int. J. Numer. Methods Fluids* **3** (1983) 249–264.
[5] G. de Vahl Davis and I.P. Jones, Natural convection of air in a square cavity: a comparison exercice. *Int. J. Numer. Methods Fluids* **3** (1983) 227–248.
[6] FEAT User Guide, Finite Element Analysis Toolbox, British Energy, Gloucester, UK (1997).
[7] D.D. Gray and A. Giorgini, The Validity of the Boussinesq approximation for liquids and gases. *Int. J. Heat Mass Transfer* **15** (1976) 545–551.
[8] P. Le Quéré, Accurate solutions to the square differentially heated cavity at high Rayleigh number. *Comput. Fluids* **20** (1991) 19–41.
[9] P. Le Quéré, R. Masson and P. Perrot, A Chebyshev collocation algorithm for 2D Non-Boussinesq convection. *J. Comput. Phys.* **103** (1992) 320–335.
[10] W.L. Oberkampf and T. Trucano, *Verification and validation in Computational Fluid Dynamics*. Sandia National Laboratories report SAND2002-0529 (2002).
[11] H. Paillère and P. Le Quéré, *Modelling and simulation of natural convection flows with large temperature differences: a benchmark problem for low Mach number solvers*, 12th Séminaire de Mécanique des Fluides Numérique, CEA Saclay, France, 25–26 Jan., 2000.
[12] S. Paolucci, *On the filtering of sound from the Navier-Stokes equations*. Sandia National Laboratories report SAND82-8257 (1982).
[13] J.C. Patterson and J. Imberger, Unsteady natural convection in a rectangular cavity. *J. Fluid Mech.* **100** (1980) 65–86.
[14] V.L. Polezhaev, Numerical solution of the system of two-dimensional unsteady Navier-Stokes equations for a compressible gas in a closed region. *Fluid Dyn.* **2** (1967) 70–74.
[15] J. Vierendeels, K. Riemslagh and E. Dick, A Multigrid semi-implicit line-method for viscous incompressible and low-Mach number flows on high aspect ratio grids. *J. Comput. Phys.* **154** (1999) 310–341.

.

O. Hireche, **C. Weisman**, D. Baltean-Carlès, P. Le Quéré, L. Bauwens, "Low Mach number analysis of idealized thermoacoustic engines with numerical solution", J. Acoust. Soc. Am. 128 (6), 3438-3448, 2010.

Low Mach number analysis of idealized thermoacoustic engines with numerical solution

Omar Hireche
Laboratoire de Mécanique Appliquée, Université des Sciences et de la Technologie d'Oran Mohamed Boudiaf, BP 1523, EL-M'naouer Oran 31000, Algeria

Catherine Weisman[a] and Diana Baltean-Carlès[b]
Université Pierre et Marie Curie, 4 Place Jussieu 75252 Paris Cedex 05, France

Patrick Le Quéré
Laboratoire d'Informatique pour la Mécanique et les Sciences de l'Ingénieur, Centre National de la Recherche Scientifique UPR 3251, 91403 Orsay Cedex, France

Luc Bauwens
Department of Mechanical and Manufacturing Engineering, University of Calgary, Calgary, Alberta T2N 1N4, Canada

(Received 4 June 2009; revised 29 September 2010; accepted 4 October 2010)

A model of an idealized thermoacoustic engine is formulated, coupling nonlinear flow and heat exchange in the heat exchangers and stack with a simple linear acoustic model of the resonator and load. Correct coupling results in an asymptotically consistent global model, in the small Mach number approximation. A well-resolved numerical solution is obtained for two-dimensional heat exchangers and stack. The model assumes that the heat exchangers and stack are shorter than the overall length by a factor of the order of a representative Mach number. The model is well-suited for simulation of the entire startup process, whereby as a result of some excitation, an initially specified temperature profile in the stack evolves toward a near-steady profile, eventually reaching stationary operation. A validation analysis is presented, together with results showing the early amplitude growth and approach of a stationary regime. Two types of initial excitation are used: Random noise and a small periodic wave. The set of assumptions made leads to a heat-exchanger section that acts as a source of volume but is transparent to pressure and to a local heat-exchanger model characterized by a dynamically incompressible flow to which a locally spatially uniform acoustic pressure fluctuation is superimposed. © *2010 Acoustical Society of America*. [DOI: 10.1121/1.3506348]

PACS number(s): 43.35.Ud [RR] Pages: 3438–3448

I. INTRODUCTION

The nonlinear nature of the energy exchanges within the stack plays a crucial role in thermoacoustic engines, affecting power generation, development of thermoacoustic instability, frequency selection, and saturation. Classical linear theory[1–3] has been successful in predicting onset temperatures and stability curves for each acoustic mode that are in good agreement with experiments.[4–7] Quasi-one-dimensional linear codes[8] yield parameters such as temperature profile, frequency, power of the saturated regime for a fixed geometry, working gas, and mean pressure. Subsequent work based upon linear theory includes, for instance, approximate relations for the thermoacoustic gain and efficiency, damping coefficient, oscillation frequency, and onset temperature.[9,10] So far, extension to nonlinear regimes has either used simplified quasi-one-dimensional models[11,12] or if based upon multidimensional models,[13,14] these rely upon restrictive assumptions, or a rather coarse spatial resolution in the stack and heat exchangers. The current work presents a well-resolved model, in which the flow in the stack and heat exchangers remains fully nonlinear and multidimensional. Resonator and load are described by a standard linear one-dimensional acoustic model. Proper coupling between these two submodels results in a global model that is asymptotically consistent in the small Mach number approximation.

The classical thermoacoustic stability analysis by Rott[1] was based upon the standard assumptions leading to linear acoustics, i.e., a formulation in the small Mach number limit, with length and time in a ratio of the order of the speed of sound, which he also coupled with a boundary layer model. Rott proceeded by considering the limit case whereby temperature changes are reduced to a jump with zero thickness between two uniform values and introducing *ad-hoc* continuity conditions across that singularity. In order to obtain this limit solution, he thus considered a temperature gradient taking place over a length that becomes negligible compared with the wavelength, as the Mach number approaches zero.

In the "short engine" model, Swift[2] also assumed that the stack is short compared with the wavelength but long compared with the sweep by the fluid motion. Indeed, in the resulting model, pressure is time-dependent but with negligible phase shift over the stack length, while a linear

[a]Author to whom correspondence should be addressed. Present address: LIMSI, CNRS UPR 3251, 91403 Orsay Cedex, France. Electronic mail: catherine.weisman@upmc.fr
[b]Current address: LIMSI, CNRS UPR 3251, 91403 Orsay Cedex, France.

formulation is retained, hence the implicit assumption whereby the stack is longer than the sweep.

In the current model, the system is split into two different regions. The length of the stack and heat exchangers assembly is assumed comparable with the sweep by the fluid motion. While often realistic, this scaling is interesting because the resulting local model for the heat exchanger assembly retains all the physics included in Swift's short engine model to which it adds the physics of nonlinear advection (at the cost of additional complications). In the resonators, the usual assumption is made of a length of the order of the wavelength. With the local flow in the heat exchangers thus adequately modeled, consistent jump conditions across Rott's singularity are obtained, which, coupled with an acoustic formulation in the resonator, result in an asymptotically consistent global model. There is no *ad-hoc* assumption in this approach and no phenomenological imposed law.

The model can deal with complex and realistic heat exchanger and stack configurations, and it retains the essential advective nonlinearity. Although that nonlinearity remains fully reversible, it does result in the stack and heat exchangers behaving as a source in the acoustics, with a strength that will be reduced as the amplitude grows. It is thus suitable for transient operation and if the computation is pursued long enough it should result in a saturation and hence stationary operation.

Different scalings characterize different physics, which opens the door to a variety of singular perturbation or multiple scales studies. There are situations that require using a single length scale and multiple time scales, such as slowly varying acoustics.[11,15] Here, the presence of two distinct regions described by different length scales while sharing a single characteristic time lead to a singular perturbation problem (i.e., matched asymptotics or boundary layer methods).

The goal here is to demonstrate the effectiveness of the singular perturbation analysis. In doing so, the emphasis was placed on the flow in the stack and heat exchangers, which was coupled with the simplest meaningful consistent resonator model. On that basis, an exploration of the fundamental consequences of the current set of scaling assumptions is presented, but no attempt is made to obtain realistic results that could be used for practical purposes. To illustrate the power of the method, results were obtained focusing mainly upon startup and stability and also saturation due to nonlinear effects in the heat exchangers and stack, in a much idealized resonator and load configuration.

The two assumptions proposed for the stack and heat exchangers, of a small Mach number and a sweep of the order of the stack and heat-exchangers length, lead to a local model in which spatially uniform pressure fluctuations can still actually occur at up to leading order. Large temperature and density variations can also be dealt with, both in time and in space.[16] (If additionally the solution domain would be connected to a large pressure reservoir such as the atmosphere, and if the boundary conditions would restrict temperature variations to some small values, the standard incompressible Navier–Stokes equations would be obtained; however, these additional assumptions are not applicable in the current context.) The resulting model is more or less standard in Stirling engine and pulse-tube cryorefrigerator models, in which leading order pressure varies,[17] in contrast to the current situation, where due to the presence of the resonators, pressure fluctuations only occur at acoustic order. It has been used in an analysis in straight ducts,[18] and simulations motivated by thermoacoustic devices, either using a vortex method[19] or second-order accurate finite volume method,[20] that dealt with the heat exchangers alone, with boundary conditions meant to represent resonator acoustics.

In the current formulation, the computational fluid dynamics (CFD) solution for the local flow in the stack and heat exchangers is coupled with a consistent acoustic model in the resonators. Other recent CFD studies have been based upon a fully viscous, conductive, and compressible solution.[21] Some have relied upon commercial codes to simulate the thermoacoustic engine.[22] Given the broad range of scales present in the fully compressible problem, these approach leads to extremely large simulations[23] or simulation of devices of very small (miniature) size.[24] In contrast, the current approach allows focusing a smaller computational effort upon the heat exchangers and stack, where it is important because this is where small scales truly matter.

II. PHYSICAL MODEL

A. Geometry

The geometry of the device consists of a duct with rectangular cross-section within which a set of heat exchangers is placed. The set of heat exchangers is made up of a stack placed between a cold and a hot heat exchanger. This assembly is inserted within the resonator tube, which is closed at one end and terminates with a load at the other end, which thus undergoes a small amplitude oscillation. Dead space separates the stack from the heat exchangers. In this article, the expression "heat-exchanger section" is consistently used to refer to the entire region, including heater, stack, and cooler. The geometry is shown in Fig. 1 (top).

B. Formulation

The problem that is being addressed consists of an initial boundary value problem, on the spatial domain shown in Fig. 1 (top), characterized by the conservation laws of viscous, conducting, compressible fluid dynamics, together with conservation of energy in the stack walls. The working fluid is a known ideal gas with constant specific heats.

Boundary conditions include no-slip conditions on the heat exchanger and stack walls. Resonator walls are free slip and adiabatic. A temperature boundary condition is provided on the heat-exchanger walls. Both temperature and heat flux are continuous on the stack walls. The load is characterized by a known relationship between the local acoustic pressure and velocity, which is approximately the same at the mean load location and the actual load location, assuming its displacement is negligible compared with the wavelength. These initial conditions are discussed in detail in Sec. II G.

The problem thus described can be solved numerically without further simplification. However, this entails very large computations, while, clearly, as long as the Mach numbers remain small, flow in the resonators will differ very little from linear acoustics. In contrast, in the heat-exchanger

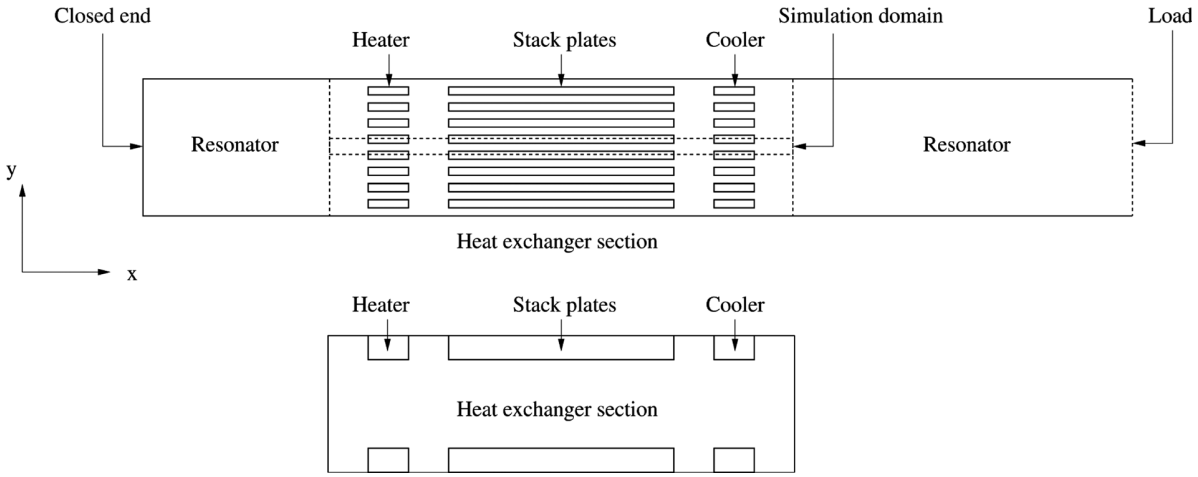

FIG. 1. Geometry of entire system (top) and of numerical simulation domain (bottom).

section, there is a need for a simulation that deals with transient and spatially resolved velocities and temperatures. Next, an appropriate simplified model is derived from asymptotic analysis, reducing the flow in the resonator to an acoustic model, eliminating the need for an acoustic Courant–Friedrichs–Lewy condition (time steps smaller than mesh size divided by the speed of sound) and focusing on the heat-exchanger section.

C. Scaling assumptions

Since temperatures must be properly resolved throughout the device, temperatures, hence the speed of sound, must be taken to be of the same order throughout. Although the presence of a load requires that one of the extremities of the resonator must be moving, the displacement will be small as long as fluid velocities are small. Thus one can introduce a reference resonator length $\tilde{L}_{\mathrm{res}}$, a reference temperature, which here, is set equal to the cold heat-exchanger temperature $\tilde{T}_{\mathrm{ref}}$, and consequently, a reference speed of sound $\tilde{c}_{\mathrm{ref}}$. Given that the period will be determined by an acoustic resonance, time is scaled by $\tilde{t}_{\mathrm{ref}} = \tilde{L}_{\mathrm{res}}/\tilde{c}_{\mathrm{ref}}$, which equals one half of the resonant period in an empty tube closed at both ends and at the cold end temperature. This provides a single time scale for the entire problem.

It is reasonable to expect the heat-exchanger section to be acoustically compact, i.e., its characteristic length is small compared with the resonator length. If the heat exchangers are not overly large compared to the stack, the length of the heat-exchanger section is of the same order as the stack length, which provides a suitable reference, and $\tilde{L}_{\mathrm{stack}} \ll \tilde{L}_{\mathrm{res}}$.

As to fluid velocities, very low initial values associated with initial conditions are not particularly representative and do not provide a meaningful scale. However, close to the stationary regime, the fluid motion should sweep a length comparable with the stack length, over which the temperature gradient takes place, hence velocities of order $\tilde{L}_{\mathrm{stack}}/\tilde{t}_{\mathrm{ref}}$. Taking into account the definition of $\tilde{t}_{\mathrm{ref}}$ above results in $\tilde{L}_{\mathrm{stack}}/\tilde{L}_{\mathrm{res}} = \tilde{U}_{\mathrm{ref}}/\tilde{c}_{\mathrm{ref}}$, so that

$$M = \frac{\tilde{U}_{\mathrm{ref}}}{\tilde{c}_{\mathrm{ref}}} = \frac{\tilde{L}_{\mathrm{stack}}}{\tilde{L}_{\mathrm{res}}} \ll 1. \tag{1}$$

Pressure is scaled by its value at rest $\tilde{P}_{\mathrm{ref}}$ and density by its value at reference pressure and temperature $\tilde{\rho}_{\mathrm{ref}} = \tilde{P}_{\mathrm{ref}}/R\tilde{T}_{\mathrm{ref}}$. All variables are scaled uniformly throughout the device except for the longitudinal coordinate $\tilde{x}$, which is scaled by $\tilde{L}_{\mathrm{stack}}$ in the heat-exchangers section but by $\tilde{L}_{\mathrm{res}}$ in the resonators. Perturbation series in the reference Mach number are introduced for all dependent variables, using the notation, for example, for pressure

$$p = p^{(0)} + Mp^{(1)} + M^2p^{(2)} + \mathcal{O}(M^3). \tag{2}$$

For velocity, however, the solution below only includes the leading order contribution so there is no need to introduce extra symbols. Below, u is used for the dimensionless longitudinal velocity and v for the transverse velocity; $\mathbf{u}$ represents the dimensionless velocity vector.

If the length of the heat-exchanger section is smaller than the resonator length by a factor of order M, then it only contributes to $O(M)$ on the overall length. The symbol $\hat{x}$ is used for the longitudinal coordinate as scaled in the resonators and setting its origin at the heat-exchangers location. Then at the closed end on the hot side, $\hat{x} = -l_L = -\tilde{l}_L/\tilde{L}_{\mathrm{res}}$. Likewise, at the mean load location, $\hat{x} = l_R = \tilde{l}_R/\tilde{L}_{\mathrm{res}}$. Both the stack plate thickness and the distance between plates are of the order of the viscous and heat penetration depth. In the heat-exchanger section, the dimensionless spatial coordinates scaled by the stack length are denoted as x and y, with the origin set at the stack center.

Next, the formulation is written in the dimensionless variables (without $\tilde{}$) introduced above, respectively, in the resonators and then in the heat-exchanger section.

D. Resonators

If the resonator cross-section is much wider than the viscous penetration depth, the wall boundary layer thickness is negligible compared to the resonator width. Furthermore, if the thermal boundary conditions are adiabatic, the flow is one-dimensional. Likewise, longitudinal diffusion results in negligible irreversibility. Thus, the flow is approximately isentropic, and as long as the Mach number remains small, temperature, density, and pressure remain constant at leading

order, hence equal to their spatially uniform initial values: $p^{(0)}=1$ and $\rho^{(0)}=1/T^{(0)}$. The temperature is $T^{(0)}=T_{\text{cold}}=1$ on the cold side while it equals $T^{(0)}=T_{\text{hot}}=\tilde{T}_{\text{hot}}/\tilde{T}_{\text{cold}}$ on the hot side. At leading order, these assumptions lead to linear acoustics. Indeed, the mass and momentum conservation equations become

$$\frac{\partial \rho^{(1)}}{\partial t}+\rho^{(0)}\frac{\partial u}{\partial \hat{x}}=0, \qquad \rho^{(0)}\frac{\partial u}{\partial t}+\frac{1}{\gamma}\frac{\partial p^{(1)}}{\partial \hat{x}}=0, \tag{3}$$

in which $\rho^{(1)}$ and $p^{(1)}$ are related by the isentropic relation: $p^{(1)}=\gamma T^{(0)}\rho^{(1)}$, where γ is the ratio of specific heats.

Boundary conditions at the two resonator ends correspond, respectively, to a closed end at $\hat{x}=-l_L$ and a load at the other extremity, instantaneously located at $\hat{x}_R=l_R+\mathcal{O}(M)$, and characterized by some differential relationship between velocity and pressure, which becomes linear in the small Mach number limit. A purely dissipative load is then represented by a reflection coefficient, applied at the fixed location $\hat{x}=l_R$ and denoted by f in dimensionless form. (The current formulation can readily be extended to more realistic loads.) Thus,

$$u(-l_L,t)=0, \qquad p^{(1)}(l_R,t)=fu(l_R,t). \tag{4}$$

The acoustic problem depends upon continuity or jump conditions at the heat-exchanger location, yet to be determined. However, based upon the current information, the problem can be reduced to a single relationship between acoustic pressure and velocity at the location $\hat{x}=0$, on each side, based upon a d'Alembert solution on characteristics.

Eliminating density,

$$\frac{\partial p^{(1)}}{\partial t}+\gamma\frac{\partial u}{\partial \hat{x}}=0, \qquad \gamma\frac{\partial u}{\partial t}+T^{(0)}\frac{\partial p^{(1)}}{\partial \hat{x}}=0. \tag{5}$$

This system is readily diagonalized, adding and subtracting the second equation to the first one multiplied by $\sqrt{T^{(0)}}$, yielding the Riemann variables, which remain constant on characteristics moving at the speed of sound $\sqrt{T^{(0)}}$, respectively, left and right:

$$\mathcal{L}=\gamma u-\sqrt{T^{(0)}}p^{(1)}, \qquad \mathcal{R}=\gamma u+\sqrt{T^{(0)}}p^{(1)}. \tag{6}$$

At the hot (left) side, the boundary condition is $u=0$, which, since $\mathcal{L}+\mathcal{R}=2\gamma u$ determines a reflection whereby $\mathcal{R}_L(-l_L,t)=-\mathcal{L}_L(-l_L,t)$. Since acoustic waves move at the speed of sound, $\mathcal{L}(\hat{x},t)=\mathcal{L}(0,t+\hat{x}/\sqrt{T^{(0)}})$ and $\mathcal{R}(\hat{x},t)=\mathcal{R}(0,t-\hat{x}/\sqrt{T^{(0)}})$, so that $\mathcal{R}_L(0,t+l_L/\sqrt{T^{(0)}})=-\mathcal{L}_L(0,t-l_L/\sqrt{T^{(0)}})$. Shifting time by $2l_L/\sqrt{T^{(0)}}$, at the heat-exchanger location, $\hat{x}=0^-$, taking into account that $T^{(0)}=T_{\text{hot}}$, one finds

$$\mathcal{R}_L(0^-,t)=-\mathcal{L}_L\left(0^-,\frac{t-2l_L}{\sqrt{T_{\text{hot}}}}\right). \tag{7}$$

Likewise, on the cold side, taking into account that $\mathcal{L}+\mathcal{R}=2\gamma u$ and $\mathcal{R}-\mathcal{L}=2\sqrt{T^{(0)}}p^{(1)}$, and in view of the boundary condition of Eq. (6), at the heat-exchangers location $\hat{x}=0^+$, and since $T^{(0)}=1$,

$$\mathcal{L}_R(0^+,t)=Z\mathcal{R}_R(0^+,t-2l_R), \tag{8}$$

in which

$$Z=\frac{\gamma-f}{\gamma+f}. \tag{9}$$

An open end corresponds to $f=0$ hence $Z=1$ while at a closed end, f is infinite and $Z=-1$. Both cases result in a zero load since the power developed is the time-averaged value of $up^{(1)}$.

E. Heat-exchanger section

Within the heat-exchanger section, the problem is not amenable to analytical solution. A numerical simulation is required.

The stack is made up of a large number of identical uniformly spaced plates. It is thus reasonable to assume vertical periodicity, i.e., flow and heat transfer are identical in all gaps. The flow in only one slot between two contiguous plates needs being simulated, as shown in Fig. 1 (bottom). The same scaling as described above is used but, in contrast with the resonator model, length is now scaled by $\tilde{L}_{\text{stack}}$. The perturbation series equations, Eq. (2), are then introduced in the compressible, viscous, and conductive Navier–Stokes equations, respectively, conservation of mass, momentum, and energy. The system equations become

$$\frac{\partial \rho^{(0)}}{\partial t}+\nabla\cdot(\rho^{(0)}\mathbf{u})=0, \tag{10}$$

$$\begin{cases}\nabla p^{(0)}=0,\\ \nabla p^{(1)}=0,\\ \dfrac{\partial(\rho^{(0)}\mathbf{u})}{\partial t}+\nabla\cdot(\rho^{(0)}\mathbf{u}\otimes\mathbf{u})=-\nabla p^{(2)}+\dfrac{1}{\mathrm{Re}}\nabla\cdot\tau,\end{cases} \tag{11}$$

$$\rho^{(0)}\left[\frac{\partial T^{(0)}}{\partial t}+(\mathbf{u}\cdot\nabla)T^{(0)}\right]=\frac{\gamma-1}{\gamma}\left[\frac{\partial p^{(0)}}{\partial t}+(\mathbf{u}\cdot\nabla)p^{(0)}\right]+\frac{1}{\mathrm{Pe}}\nabla\cdot(k\nabla T^{(0)}), \tag{12}$$

where $\tau=\mu[\nabla\mathbf{u}+(\nabla\mathbf{u})^t-\frac{2}{3}(\nabla\cdot\mathbf{u})\mathbf{I}]$, Re is the reference Reynolds number $\mathrm{Re}=\tilde{\rho}_{\text{ref}}\tilde{U}_{\text{ref}}\tilde{L}_{\text{stack}}/\tilde{\mu}_{\text{ref}}$, Pe is the reference Péclet number $\mathrm{Pe}=\tilde{U}_{\text{ref}}\tilde{L}_{\text{stack}}/\tilde{\alpha}_{\text{ref}}$, and μ, k, and α are the dynamic viscosity, thermal conductivity, thermal diffusivity, respectively, scaled by their value at the reference state $\tilde{\mu}_{\text{ref}}$, $\tilde{k}_{\text{ref}}$, and $\tilde{\alpha}_{\text{ref}}$. Gravity has been neglected. k and μ are assumed to be independent of temperature.

From momentum at leading order, $p^{(0)}$ is a function of time only. However, this value has to equal the pressure $p^{(0)}=1$ in the resonator. At order M, likewise, $p^{(1)}$ is a function of time only, but given that in the resonator $p^{(1)}$ fluctuates, it remains a function of time. Taking the leading order equation of state into account, $\rho^{(0)}=1/T^{(0)}$, the problem becomes

$$\frac{\partial \rho^{(0)}}{\partial t}+\nabla\cdot(\rho^{(0)}\mathbf{u})=0, \tag{13}$$

$$\frac{\partial(\rho^{(0)}\mathbf{u})}{\partial t} + \nabla\cdot(\rho^{(0)}\mathbf{u}\otimes\mathbf{u}) = -\nabla p^{(2)} + \frac{H}{\mathrm{Re}_{\tilde{H}}}\nabla\cdot\tau, \quad (14)$$

$$\rho^{(0)}\left[\frac{\partial T^{(0)}}{\partial t} + (\mathbf{u}\cdot\nabla)T^{(0)}\right] = \frac{H}{\mathrm{Pe}_{\tilde{H}}}\nabla^2 T^{(0)}, \quad (15)$$

$$\rho^{(0)}T^{(0)} = 1, \quad (16)$$

introducing $\mathrm{Re}_{\tilde{H}}$, $\mathrm{Pe}_{\tilde{H}}$, based on the distance $\tilde{H}$ separating two successive plates centerlines, and H being the corresponding dimensionless distance, $H = \tilde{H}/\tilde{L}_{\mathrm{stack}}$.

In the solid plates, the heat conduction equation written in dimensionless form is

$$\frac{\partial T}{\partial t} = \frac{1}{\mathrm{Pe}_s}\nabla^2 T, \quad (17)$$

where $\mathrm{Pe}_s = \mathrm{Pe}_{\tilde{H}} H\,\alpha_{\mathrm{ref}}/\alpha_s$ is the Péclet number in the wall.

Boundary conditions on symmetry lines (due to vertical periodicity of the stack) include zero normal velocities within the fluid domain and zero normal temperature gradients on all symmetry lines. Fixed temperatures are imposed at the heat-exchanger walls, while continuity of temperature and normal heat flux are imposed at the interface between fluid and stack. Both velocity components vanish on all solid walls. Boundary conditions at the left and right ends are dealt with below and so are the initial conditions.

F. Matching

In the resonator scaling, the heat-exchanger section shrinks to zero thickness as $M = \tilde{L}_{\mathrm{stack}}/\tilde{L}_{\mathrm{res}} \to 0$. In the heat-exchanger scaling, the resonator length becomes infinity. In other words, in the limit of $M \to 0$, the location $\hat{x} = 0^-$, i.e., the right end of the left resonator section corresponds to $x \to -\infty$ in the heat-exchanger section. Likewise, $\hat{x} = 0^+$, the left end of the right resonator section corresponds to $x \to +\infty$ in the scaling used in the heat-exchanger section. Thus, velocity, pressure, and temperature values must approach the same values at these locations in both solutions.

First, according to the formulation in the heat-exchanger section, pressure is spatially uniform to order M; thus, for acoustic pressures,

$$p^{(1)}(0^-) = p^{(1)}(0^+) = p^{(1)}(0). \quad (18)$$

Leading order temperatures are constant and uniform in each resonator side. Thus, leading order temperatures in the heat exchangers must approach these fixed values for both $x \to -\infty$ and $x \to +\infty$. The acoustic solution in the resonators provides one equation on each side relating the acoustic pressure $p^{(1)}(0)$, respectively, to longitudinal velocity for $x \to -\infty$, Eq. (7), and $x \to +\infty$, Eq. (8). Transverse velocities vanish in the resonators, hence also for $x \to \pm\infty$.

Finally, integrating the energy equation, Eq. (15), over the entire heat-exchanger section and making use of continuity, a global energy balance is obtained, relating velocities at the two ends to heat transfer (with the end boundaries set to be adiabatic $\partial T/\partial n = 0$). Taking into account that $u(0^-) = \lim_{x\to-\infty} u$, $u(0^+) = \lim_{x\to+\infty} u$,

$$[u(0^-) - u(0^+)] + \frac{1}{\mathrm{Pe}_{\tilde{H}}}\int \nabla T^{(0)}\cdot\mathbf{n}\,ds = 0. \quad (19)$$

Finally, solving Eqs. (7), (8), and (19) determines $u(0^-)$, $u(0^+)$, and $p^{(1)}(0)$, providing boundary conditions for both resonators and for the low Mach number problem in the heat-exchanger section. These results show that the heat-exchanger section is transparent to acoustic pressure but appears in the acoustics as a point source of volume.

G. Initial conditions

The onset problem is a stability problem, in which the issue is the growth of initial perturbations. When using numerical simulation, it is often the case that numerical errors provide an initial perturbation which triggers the instability. However, here, for initial conditions in which the fluid is initially at rest, the initial field is uniform. Since our code is, appropriately, symmetrically implemented, subtracting, however, approximate but identical binary representations at neighboring spatial locations yields differences with a binary representation that is exactly zero; likewise, the value of the initial velocities is zero, which likewise has an exact binary representation. As a result, numerical errors do not provide an initial perturbation. For initial conditions in which the fluid is initially at rest, it stays at rest, as long as the temperature in the heat exchangers and the fluid corresponds to a steady solution. However, if the initial temperature field is not uniform lengthwise, round-off errors result in an initial numerical value of the integral in Eq. (19) that is not exactly zero.

The current model being nonlinear, different initial conditions might trigger different results, and it might be worthwhile testing different initial models. Since the acoustic solution in the resonators, Eqs. (7) and (8), relates the current solution to solutions at earlier times, defining initial conditions is equivalent to defining the previous acoustic history. Likewise, specific temperature distributions can be tested. These issues are discussed in detail below.

III. NUMERICAL SOLUTION

A finite volume solver suitable for low Mach number flows with large temperature gradients and large pressure fluctuations[25] was adapted to deal with the present configuration. The solver has been validated on a benchmark problem of non-Boussinesq natural convection. Time discretization combines an implicit treatment of the viscous and diffusive terms with an explicit discretization for the convective terms. The algorithm implements a second-order spatial and time discretization on a uniform mesh.

The simulation domain is extended beyond the heat-exchanger section by a length equal to twice the stack length. In the matching equations, values on the left and right boundaries are used, where the flow is forced to be one-dimensional. An additional phase variable is used, specifying whether a given cell is to be treated as solid or fluid. The equations are then solved through the whole domain, using appropriate tests

of the phase variable, ensuring continuity of both temperature and heat flux through the plate-fluid interfaces.

Spatial discretization is based upon a staggered mesh. Velocities are defined on cell faces, while density, temperature, and phase are defined on cell centers. In the continuity equation, the divergence of the velocity field is adjusted at each time step using a fractional time step method derived from the projection method for incompressible flows.

The sequence of steps for advancing in time from time t^n to time t^{n+1} is as follows:

(1) The energy equation, Eq. (15), is solved for the new temperature field T^{n+1}, using density at time t^n, by either a nonincremental alternating direction implicit (ADI) algorithm or the generalized minimal residual method (GMRES).[26]
(2) The linear system of Eqs. (7), (8), and (19) is solved, determining $u(0^-)^{n+1}$, $u(0^+)^{n+1}$, and $p^{(1)}(0)^{n+1}$, based upon values at previous times. The velocity values provide boundary conditions in the calculation of the velocity field. These values and the new value of the acoustic pressure are stored since they will be needed at future time steps.
(3) The new density is determined from the equation of state, Eq. (16).
(4) The new divergence, at time t^{n+1}, is obtained by combining the energy equation and the continuity equation, yielding $\nabla \cdot \mathbf{u}^{n+1} = (H/\mathrm{Pe}_{\tilde{H}})\Delta T^{n+1}$.
(5) An intermediate velocity vector is calculated which does not satisfy continuity, from momentum, Eq. (14), using ADI or GMRES, with dynamic pressure at t_n.
(6) The dynamic pressure correction is determined using the multigrid method.[27] Numerical parameters in the multigrid algorithm are adjusted for optimal convergence.
(7) Respective arrays are updated with the new velocity field $\mathbf{u}^{n+1}$ and dynamic pressure.

IV. RESULTS

A. Device and configurations simulated

The various cases that were simulated correspond to a single engine geometry, based upon an existing experimental set-up.[28] The overall length is $\tilde{L}_{\mathrm{res}} = 7.57\,\mathrm{m}$, with a stack $\tilde{L}_{\mathrm{stack}} = 150\,\mathrm{mm}$ long, made up of stainless steel plates 0.20 mm thick separated by a spacing $\tilde{h} = 0.77\,\mathrm{mm}$ wide. The stack porosity is $\tilde{h}/\tilde{H} = 0.794$, where $\tilde{H}$ is the distance separating two successive plate centerlines, and $\tilde{h}$ is the gap or flow passage between two successive stack plates. The distance between the heat exchangers and the ends of the stack plates equals $\tilde{h}$, and the heat-exchanger length is taken to be $\tilde{L}_{\mathrm{stack}}/20$. The length of the left resonator section is $\tilde{l}_L = 676$ mm. The device is filled with helium at 1 MPa and a temperature of 293 K on the cold side. The heat exchangers are taken to be made of the same material as the stack plates. The resonant frequency of the device is 66.6 Hz when filled with helium at 293 K in both cold and hot sections, no thermoacoustic heat pumping, and no load. These data result in a ratio of 0.38 between thermal boundary layer and spacing between two successive stack plates, which is appropriate for thermoacoustic energy transfer.[2]

Using the scalings previously defined, the reference Mach number is equal to $M = 0.02$, so that $\tilde{L}_{\mathrm{res}} = 50\,\tilde{L}_{\mathrm{stack}}$ [Eq. (1)]. The Péclet and Reynolds numbers, based on $\tilde{H}$ are $\mathrm{Pe}_{\tilde{H}} = 1093$ and $\mathrm{Re}_{\tilde{H}} = 1584$. The solid Péclet number for the stack plates and the heat exchangers is $\mathrm{Pe}_s = 4.485 \times \mathrm{Pe}_{\tilde{H}} = 31.7$.

A combination of values of the dimensionless temperature in the hot heat exchanger ($T_{\mathrm{hot}} = 1.2$, 1.3, and 2) and of the load ($f = \infty$, 90) were simulated. Two initial conditions were tested, with initial velocities and acoustic pressures in a resonator excited by either: (1) A random noise or (2) a standing wave at the cold resonator frequency, with no load and no thermoacoustics. In the heat-exchanger section, both initial dynamic pressure and velocity were set to zero. Two sets of initial temperature conditions in the stack and the fluid in the gap were also considered: A longitudinally linear distribution between heat exchangers, in both solid and fluid, or a distribution corresponding to steady-state heat conduction, with the fluid at rest. The latter was calculated numerically, taking into account the geometry of the heat-exchanger section, including the gas layer between heat exchangers and stack plates, and the thermal conductivities in the wall and the gas.

B. Convergence analysis

A convergence analysis was performed for $T_{\mathrm{hot}} = 1.2$, with a closed cold end, starting from random noise, and assuming balanced initial temperatures due to conduction in the heat-exchanger section, with spatial resolutions of 1024×32, 2048×32, and 2048×64 grid points. The coarse mesh allows for three grid points inside each half-plate width and three grid points in the fluid gap between heat exchanger and plate end. The time step was chosen as large as possible, maximizing the Courant number while ensuring stability. The coarsest resolution used was about 600 time steps per dimensionless unit of time, which, since initially velocities are small, is appropriate. As velocities increased, the time step was decreased by a factor of 10, to a value of 1/6000. The CPU (Central Processing Unit) time was about 1 μs per time step and per mesh point on a NEC SX8. The numerical parameters for the multigrid algorithm dealing with pressure correction and the divergence of the velocity field are adjusted so that for the coarsest grid, an average of only three or four iterations is needed. On the coarsest grid, the average CPU time per run is 2 h when only simulating the early phase of the process, showing amplification of the initial perturbation. It took about 50 h until saturation was observed, when the wave amplitude no longer increases. These are good performance figures when compared with current literature reports.[23]

While qualitatively the results were observed to be independent of the grid size, quantitative differences of about 10% in the growth rates were noted between coarse and fine mesh, but only of 1% between the two finest meshes. For each spatial grid, solutions were obtained using three different time steps, from 1/600th to 1/6000th of the unit time. In order to

assess any effect of the truncation error inherent to the ADI solver, while GMRES yields an exact solution of the discretized equations, results using both solvers were compared. For all the time steps that were used, they were nearly identical. Since GMRES is more costly, all results below were obtained using the ADI solver, and for the coarsest mesh.

V. DISCUSSION

A. Initial amplification

Figures 2 and 3 show results obtained for an initially linear temperature profile between the heat exchangers, with $T_{\text{hot}} = 1.3$, in a tube closed at both ends ($f = \infty$). The initial excitation of the resonator was a standing wave of small amplitude at the resonator fundamental frequency in cold fluid. The results shown correspond to the early part of the process, while wave amplification is taking place, for $0 \leq t \leq 410$. Figures 2(a) and 2(b) show respectively, the evolution of acoustic pressure $Mp^{(1)}(0)$ and velocity $u(0^-)$ (on the left side of the heat exchangers). The results show the thermoacoustic instability resulting in an approximately exponential amplitude increases. Indeed when acoustic pressure is plotted on a logarithmic scale, Fig. 3(a), the envelope of the signal appears to be linear. However, in Fig. 3(b), the positive and negative parts of the acoustic pressure and velocity signals are noticeably asymmetric, as predicted from nonlinear theoretical models and observed in experiments.[11,14,28] Predictably, the dominant frequency is very close to 0.5, corresponding to the resonance in a tube at a uniformly cold temperature, closed at both ends, with no thermoacoustic power generation and no load. For the relatively modest temperature ratio of 1.3, the Lees/Rott dispersion relation,[1,29] which accounts for a temperature discontinuity at the location of the heat-exchangers section, yields a frequency that only differs by 0.053% from the resonant frequency in a tube entirely filled with cold fluid, which was used as the initial excitation. The effect of the thermoacoustic load resulting in a nonzero growth rate, which also shifts frequencies, is small too, as readily verified in a linear model accounting for a source of volume at the location of the temperature jump. The fundamental is the most energetic mode, which is consistent since the initial excitation starts by feeding energy in the fundamental exclusively. However, closer analysis of the signal shows that the first harmonic, oscillating twice as fast, is also unstable, as reported in both theoretical studies and experiments.[4,6,28]

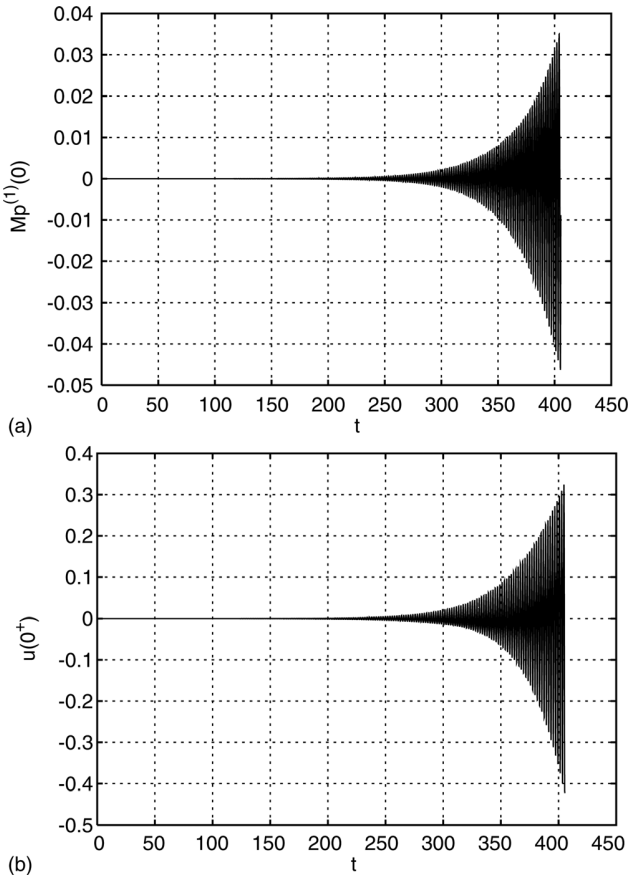

FIG. 2. Acoustic pressure $Mp^{(1)}(0)$ (a) and left velocity $u(0^-)$ (b) history, $f = \infty$, $T_{\text{hot}} = 1.3$, with linear initial temperature distribution and initial standing wave.

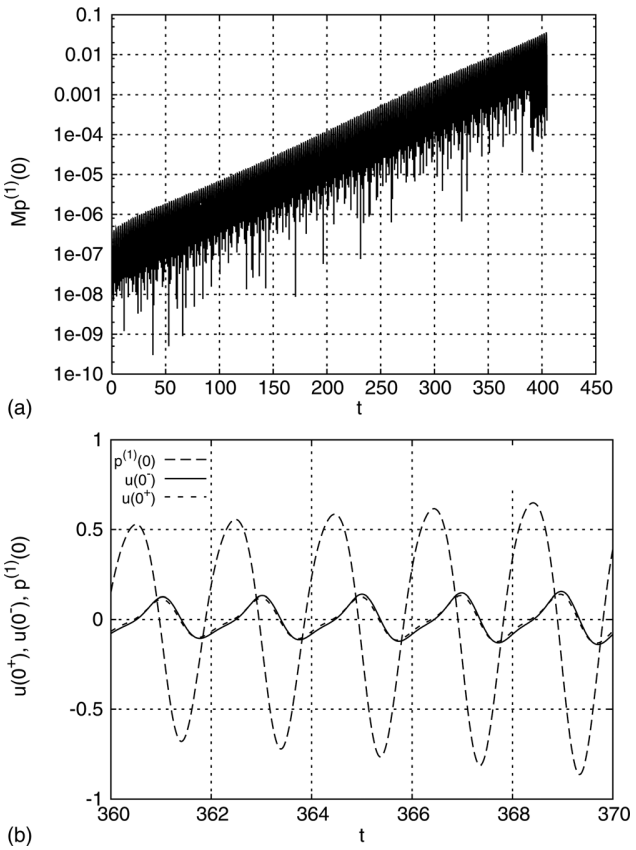

FIG. 3. Acoustic pressure $Mp^{(1)}(0)$ history, in semi-log scale (a) and detail (b) of acoustic pressure $p^{(1)}(0)$, left velocity $u(0^-)$, right velocity $u(0^+)$ history, $f = \infty$, $T_{\text{hot}} = 1.3$, with linear initial temperature distribution and standing wave as initial condition.

The difference between the left and the right velocity amplitudes is shown in Fig. 3, which presents a close-up view of acoustic pressure and axial velocities at the end of the computation. The phase shift between pressure and left velocity is close to 90°. Since the acoustic energy flux is proportional to the integral of the product pressure times velocity, which on the left, becomes zero in the stationary regime, a phase shift of 90° corresponds to a standing wave. Here,

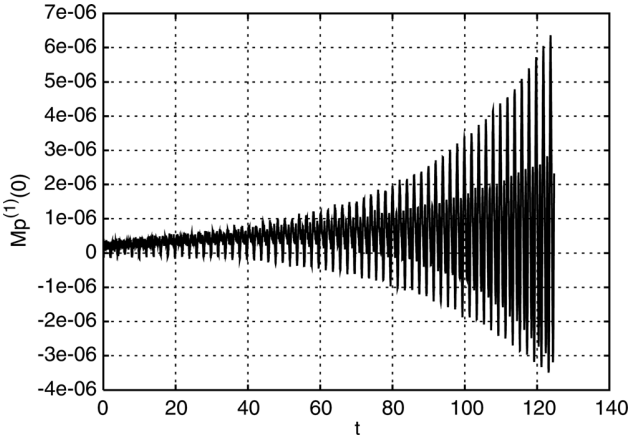

FIG. 4. Acoustic pressure $Mp^{(1)}(0)$ history, $f = \infty$, $T_{\text{hot}} = 1.3$, with linear initial temperature distribution and random noise as initial perturbation.

however, the amplitude is still increasing, which requires a nonzero energy flux, smaller on the left than on the right since the left side represents only about 9% of the resonator length.

In Fig. 3(b), corresponding to the end of the run in Fig. 2, the drive ratio at the heat-exchanger section location [defined as $\max|Mp^{(1)}(0)|$] is 3.5% and dimensionless velocities are approximately 0.15. Pursuing the simulation with such high velocities requires the time step to be significantly reduced. With no load (closed end, infinite f), saturation will only occur on a time scale of $1/M$. Indeed, the irreversibility due to damping in the heat-exchanger section is smaller than the acoustic energy fluxes by order M, while the resonator model is isentropic.

Figure 4 shows the growth of pressure for the same configuration and parameters ($T_{\text{hot}} = 1.3$, $f = \infty$, and linear initial temperature distribution), except for the initial excitation, which is a random noise. Since, in this case, there is no significant energy initially deposited in any mode in particular, the effect of the strong growth rate of the first harmonic becomes clear. Both the fundamental and the first harmonic appear to be unstable.

When increasing the hot temperature to $T_{\text{hot}} = 2$ in Fig. 5, starting from a standing wave, the first harmonic (second

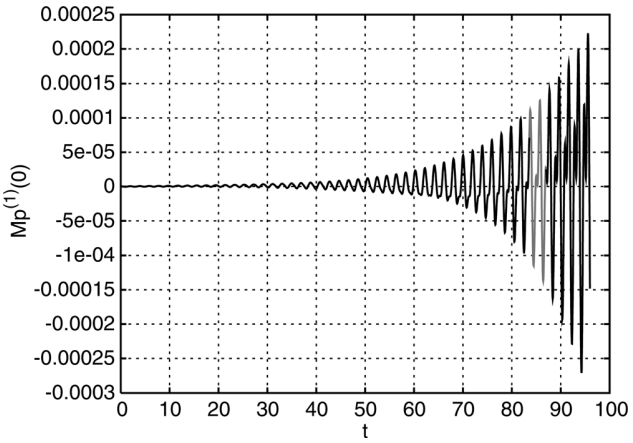

FIG. 5. Acoustic pressure $Mp^{(1)}(0)$ history, $f = \infty$, $T_{\text{hot}} = 2$, with linear initial temperature distribution and standing wave as initial perturbation.

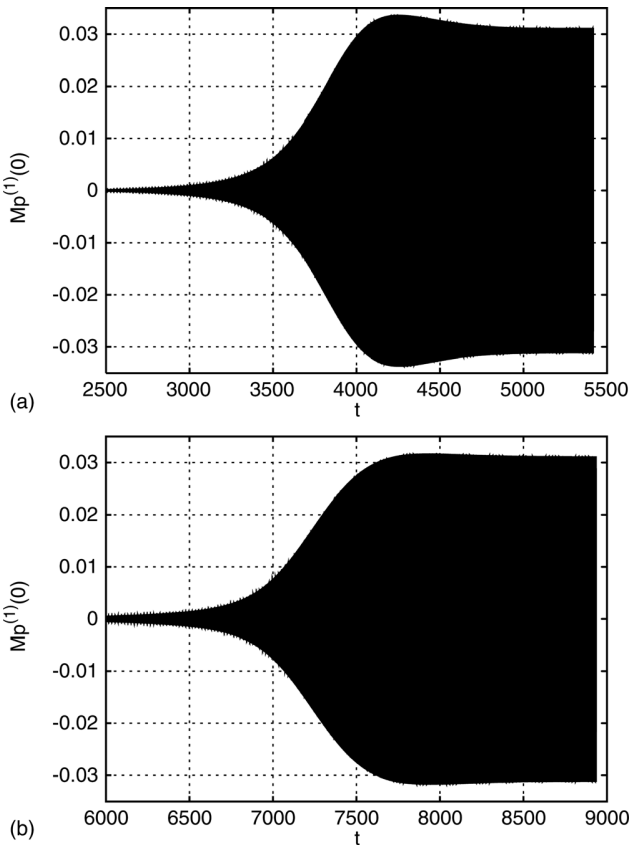

FIG. 6. Acoustic pressure $Mp^{(1)}(0)$ history, $t > 2500$, $f = 90$, $T_{\text{hot}} = 1.2$, with linear initial temperature distribution (a) or steady-state heat conduction initial temperature (b) and initial random noise.

mode) is clearly unstable and can be seen already very early on. Similar observations are made when starting with noise.

B. Periodic regime

In order to show the evolution of the wave toward a stationary regime, a purely resistive load was introduced at the right end. For f ranging between 80 and infinity, increasing

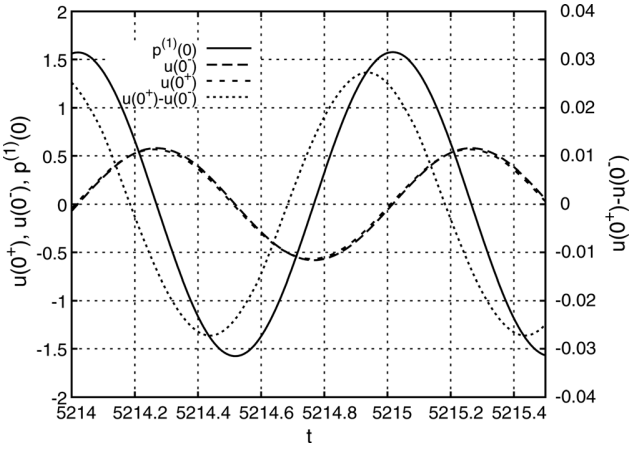

FIG. 7. Time history (detail) of acoustic pressure $p^{(1)}(0)$, left velocity $u(0^-)$, right velocity $u(0^+)$, difference $u(0^+) - u(0^-)$ (scale on right vertical axis), $t = \tilde{t}/(2\tilde{t}_{\text{ref}})$, $f = 90$, $T_{\text{hot}} = 1.2$ with linear initial temperature distribution and initial random noise.

the impedance f leads to an increase in the growth rate, and saturation comes sooner. Results below were obtained for $f = 90$, which leads to saturation with a reasonable pressure amplitude level and in a reasonable time. Two separate calculations were done for $f = 90$, both for a temperature ratio of 1.2. The first one started from an initially linear temperature distribution between heat exchangers, with results shown in Figs. 6(a) and 7. In the second simulation, temperature initial conditions considered a steady-state heat conduction field. Results are shown in Fig. 6(b). In the former case, saturation occurs after $t \simeq 4500$ (which corresponds to about 35 s in real time). Figure 7 shows acoustic pressure, axial velocities, and the difference between axial velocities for a narrow time window at the end of the simulation. The phase shift between acoustic pressure and left velocity is very close to 90° and the period is approximately 0.998, which is again very close to the first harmonic, and even more so if taking the presence of a temperature jump into account. Indeed, its period is 0.9986 in a tube closed at both ends (i.e., with no load) according to the Lees/Rott dispersion relation.[1,29] At the stationary regime, acoustics on the left side is a monochromatic standing wave since there is no longer any energy transfer. On the right side, however, the power developed by the heat-exchanger section acting as a source of volume is carried to the load by the acoustics, which consequently do no longer behave as a pure standing wave (Fig. 7). The final drive ratio $(\max|Mp^{(1)}(0)|)$ is about 3.2% and the velocity amplitudes are 0.59. The signal in Fig. 7 is now much more symmetric than for infinite f. An overshoot is clearly noticeable in the pressure amplitudes, before the stationary oscillatory regime is reached. The same observation has been reported in previous theoretical, numerical,[14,23] and experimental studies. This overshoot may be due to interaction between the evolution of the stack temperature and the thermoacoustic wave amplification, which are taking place simultaneously, each of which is characterized by its own time scale. The initially linear temperature gradient evolves mostly by conduction in the solid plates and in the fluid, toward a stationary solution which, for heavy stack plates, will be nearly steady. The time scale characterizing conduction in the stack is of the order of 1–2 h, i.e., approximately 3.5×10^6 dimensionless time units (based on the stack length and the thermal diffusivity of the stack plates $\tau \simeq \tilde{L}^2_{\text{stack}}/\alpha_s$). Meanwhile, the thermoacoustic engine provides for an increase in amplitude and delivers power to the load, until reaching an equilibrium. Here equilibrium, hence a nearly periodic regime, appears to be reached while the stack temperature is still adjusting due to its high thermal mass. In contrast, in the case of steady-state heat conduction field, the initial temperature profile has already been adjusted for conduction (but not for the effect of oscillating flow), and it is much closer to its final profile.

In the case of steady-state heat conduction, as a result of relatively poor conduction between heat exchangers and stack, the actual temperature gradient in the stack is much lower already when the device starts, the engine is clearly weaker, and wave amplification is slower, as observed by comparing times in Fig. 6(b) with those in Fig. 6(a). Figure 8 shows the initial temperature field, zooming between heater and stack plate, due to conduction but no motion, which is

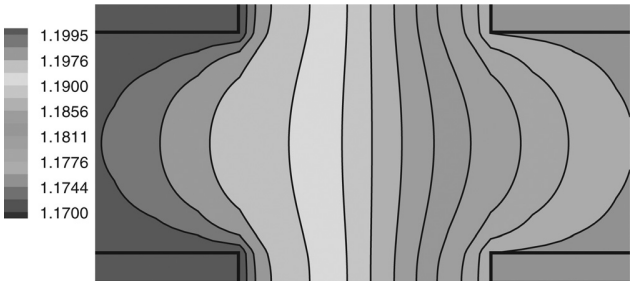

FIG. 8. Temperature field detail between the hot heat exchanger and the stack plates due to conduction (no motion), $T_{\text{hot}} = 1.2$, same view as Fig. 1 (bottom).

clearly two-dimensional. The initial temperature gradient in the stack plates is significantly smaller than the linear profile used as initial conditions in the previous case and much closer to the final profile, as shown in Fig. 9. This is due primarily to the gap between the heat exchangers and the stack ends. The gas layer in this gap is much less conductive than the solid plates and, therefore, it absorbs much of the temperature difference, resulting in a smaller gradient in the stack. The same drive ratio is reached eventually but, as Fig. 6(b) shows, there is almost no overshoot.

The unavoidable presence of a fluid layer between heat exchangers and plates has a definite impact on the growth rate. Thermal edge effects and gaps between the stack ends and the heat exchangers were further analyzed through linear and nonlinear studies in order to derive improved heat exchange laws and to optimize the systems.[30–34] The current model will allow for optimization of its width and exploration of the optimum values of other design parameters, such as stack and heat-exchanger location.

VI. CONCLUSION

A globally consistent low Mach number model of the thermoacoustic engine has been developed, based upon the assumption that the stack and heat-exchangers length is

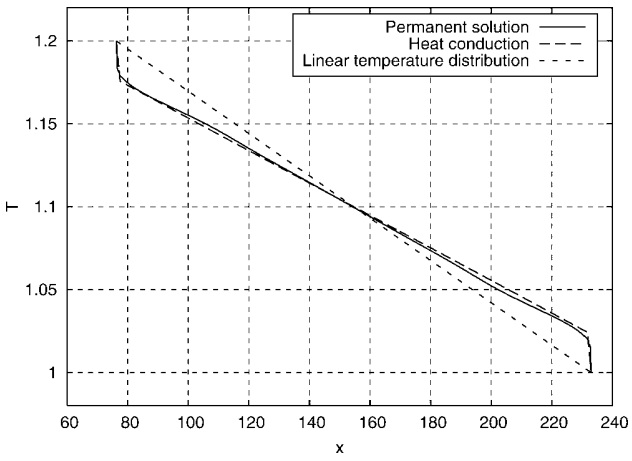

FIG. 9. Temperature distribution along the stack symmetry plane and in the gas from left to right heat exchanger, showing both initial conditions, linear distribution and heat conduction solution, and the mean stationary periodic solution for $f = 90$, $T_{\text{hot}} = 1.2$, and initial random noise.

comparable with the fluid particle displacement, resulting in a heat-exchanger section that is transparent to acoustic pressure but acts as a source of volume.

Transient processes whereby amplitude grows and eventually reaches a steady value are predicted, including frequencies and power fluxes. The key components of the thermoacoustic device are included. Yet by virtue of not needing a numerical solution in the resonator, and because the flow in the stack and heat exchangers is reduced to a low Mach number flow, implementation is orders of magnitude faster than compressible models of the entire device. Indeed, the current model entails solving numerically for only a small fraction of the overall volume, and the time step is not restricted by an acoustic Courant–Friedrichs–Lewy condition. The current approach is a good example whereby the singular perturbation technique can be used successfully, allowing the computational effort to be concentrated where it truly matters. Even so, large computations are still required, since the direct simulation of a transient period flow in the heat-exchanger section is still required.

The model will allow for exploring and understanding crucial trade-offs on stack position, stack wall thickness and thermal mass, heat-exchanger size and location, and load impedance including the trade-off between optimizing for device performance and optimizing for its ability to start, which may lead to conflicting requirements.

The resonator and the load models that were used are admittedly much simplified. However, the current approach can readily be extended to more realistic resonators as long as they can be described by linear acoustics, and to more complex load models, including multidimensional resonators with losses, complex losses, and loops, or in which the long acoustic resonator is replaced by a free piston, hence allowing for arbitrarily large pressure amplitudes, and a much higher power density. In particular, losses due to heat and momentum diffusion can readily be included, since these are linear in nature. Wave steepening cannot be dealt with; however, until shocks appear, wave steepening remains a fully reversible phenomenon, which as such does not directly contribute to losses.

ACKNOWLEDGMENTS

Support of the Natural Sciences and Engineering Research Council of Canada is gratefully acknowledged (L.B.). Computations were performed on the NEC-SX8 of the IDRIS-CNRS computing center, under Project No. i2009020599. The authors thank Professor Maurice-Xavier François for his interest and numerous fruitful exchanges on this work and for initiating the collaboration that made this study possible. Finally, support of the Algerian and French governments through a doctoral fellowship 2007–2008, "Programme Boursier Enseignants du Ministère Algérien de l'Enseignement Supérieur et de la Recherche Scientifique" is gratefully acknowledged (O.H.).

[1]N. Rott, "Damped and thermally driven acoustic oscillations in wide and narrow tubes," Z. Angew. Math. Phys. **20**, 230–243 (1969).
[2]G. W. Swift, "Thermoacoustic engines," J. Acoust. Soc. Am. **84**, 1145–1180 (1988).
[3]W. P. Arnott, H. E. Bass, and R. Raspet, "General formulation of thermoacoustics for stacks having arbitrarily shaped pore cross-sections," J. Acoust. Soc. Am. **90**, 3228–3237 (1991).
[4]A. A. Atchley, H. E. Bass, T. J. Hofler, and H. T. Lin, "Study of a thermoacoustic prime mover below onset of self-oscillation," J. Acoust. Soc. Am. **91**, 734–743 (1992).
[5]A. A. Atchley, "Standing wave analysis of a thermoacoustic prime mover below the onset of self-oscillation," J. Acoust. Soc. Am. **92**, 2907–2914 (1992).
[6]A. A. Atchley and F. M. Kuo, "Stability curves for a thermoacoustic prime mover," J. Acoust. Soc. Am. **95**, 1401–1404 (1994).
[7]W. P. Arnott, J. R. Belcher, R. Raspet, and H. E. Bass, "Stability analysis of a helium-filled thermoacoustic engine," J. Acoust. Soc. Am. **96**, 370–375 (1994).
[8]B. Ward, J. Clark, and G. W. Swift, *Design Environment for Low-Amplitude Thermoacoustic Energy Conversion (DeltaEC) User's Guide* (version 6.2) (Los Alamos National Laboratory, 2008), http://www.lanl.gov/thermoacoustics/UsersGuide.pdf.
[9]R. Raspet, J. Brewster, and H. E. Bass, "A new approximation method for thermoacoustic calculations," J. Acoust. Soc. Am. **103**, 2395–2402 (1998).
[10]A. T. A. M. de Waele, "Basic treatment of onset conditions and transient effects in thermoacoustic Stirling engines," J. Sound Vib. **325**, 974–988 (2009).
[11]S. Karpov and A. Prosperetti, "Nonlinear saturation of the thermoacoustic instability," J. Acoust. Soc. Am. **107**, 3130–3147 (2000).
[12]S. Karpov and A. Prosperetti, "A nonlinear model of thermoacoustic devices," J. Acoust. Soc. Am. **112**, 1431–1444 (2002).
[13]N. Cao, J. R. Olson, G. W. Swift, and S. Chen, "Energy flux density in a thermoacoustic couple," J. Acoust. Soc. Am. **99**, 3456–3464 (1996).
[14]M. F. Hamilton, Y. A. Ilinski, and E. Zabolotskaya, "Nonlinear two-dimensional model for thermoacoustic engines," J. Acoust. Soc. Am. **111**, 2076–2086 (2002).
[15]L. Bauwens, C. R. L. Bauwens, and I. Wierzba, "Oscillating flames: Multiple-scale analysis," Proc. R. Soc. London, Ser. A **465**, 2089–2110 (2009).
[16]S. Paolucci, "On the filtering of sound from the Navier-Stokes equations," Report No. SAND82-8257, Sandia National Laboratories (1982).
[17]L. Bauwens, "Near-isothermal regenerator: A perturbation analysis," AIAA J. Thermophys. Heat Transfer **9**, 749–756 (1995).
[18]L. Bauwens, "Oscillating flow of a heat-conducting fluid in a narrow tube," J. Fluid Mech. **324**, 135–161 (1996).
[19]A. Worlikar and O. Knio, "Numerical study of oscillatory flow and heat transfer in a loaded thermoacoustic stack," Numer. Heat Transfer, Part A **35**, 49–65 (1999).
[20]P. Duthil, C. Weisman, E. Bretagne, and M.-X. François, "Experimental and numerical investigation of heat transfer and flow within a thermoacoustic cell," Int. J. Transp. Phenom. **6**, 265–272 (2004).
[21]D. Marx and P. Blanc-Benon, "Computation of the temperature distortion in the stack of a standing-wave thermoacoustic refrigerator," J. Acoust. Soc. Am. **118**, 2993–2999 (2005).
[22]J. A. Lycklama à Nijeholt, M. E. H. Tijani, and S. Spoelstra, "Simulation of a traveling-wave thermoacoustic engine using computational fluid dynamics," J. Acoust. Soc. Am. **118**, 2265–2270 (2005).
[23]G. Y. Yu, E. C. Luo, W. Dai, and J. Y. Hu, "Study of nonlinear processes of a large experimental thermoacoustic-Stirling heat engine by using computational fluid dynamics," J. Appl. Phys. **102**, 074901–074907 (2007).
[24]D. Marx and P. Blanc-Benon, "Numerical simulation of stack-heat exchangers coupling in a thermoacoustic refrigerator," AIAA J. **42**, 1338–1347 (2004).
[25]P. Le Quéré, C. Weisman, H. Paillère, J. Vierendeels, E. Dick, R. Becker, M. Braack, and J. Locke, "Modelling of natural convection flows with large temperature differences: A benchmark problem for low Mach number solvers. Part 1. Reference Solutions," M2AN, Math. Modell. Numer. Anal. **39**, 609–616 (2005).
[26]Y. Saad and M. Schultz, "GMRES: A generalized minimal residual algorithm for solving nonsymmetric linear systems," SIAM (Soc. Ind. Appl. Math.) J. Sci. Stat. Comput. **7**, 856–869 (1986).
[27]W. Briggs, *A Multigrid Tutorial*, 2nd ed. (SIAM Publications, Philadelphia, 1987).
[28]P. Debesse, D. Baltean-Carlès, and F. Lusseyran, "Experimental analysis of nonlinear phenomena in a thermoacoustic system, nonlinear acoustics fundamentals and applications," in *Proceedings of the 18th International Symposium on Nonlinear Acoustics (ISNA)*, Stockholm, Sweden (July 7–10, 2008), Vol. 1022, pp. 355–358.

[29]C. H. Lees. "The free periods of a composite elastic column or composite stretched wire," Proc. Phys. Soc. **41**, 204–213 (1929). Cited in H. Guénoche, "Flame propagation in tubes and in closed vessels," in *Non-steady Flame Propagation*, edited by G. H. Markstein (Pergamon Press, New York, 1964), pp. 107–181.
[30]G. Mozurkewich, "Time-average temperature distribution in a thermoacoustic stack," J. Acoust. Soc. Am. **103**, 380–388 (1998).
[31]V. Gusev, "Relaxation-time approximation for analytical evaluation of temperature field in thermoacoustic stack," J. Sound Vib. **235**, 711–726 (2000).
[32]H. Ishikawa and D. J. Mee, "Numerical investigations of flow and energy fields near a thermoacoustic couple," J. Acoust. Soc. Am. **111**, 831–839 (2002).
[33]A. Berson and P. Blanc-Benon, "Nonperiodicity of the flow within the gap of a thermoacoustic couple at high amplitudes," J. Acoust. Soc. Am. **122**, 122–127 (2007).
[34]L. Zoontjens, C. Q. Howard, A. C. Zander, and B. S. Cazzolato, "Numerical study of flow and energy fields in thermoacoustic couples of non-zero thickness," Int. J. Therm. Sci. **48**, 733–746 (2008).

.

L. Ma, **C. Weisman**, D. Baltean-Carlès, I. Delbende, L. Bauwens, Effect of a resistive load on the starting performance of a standing wave thermoacoustic engine : A numerical study, J. Acoust. Soc. Am. 138 (2), 847–857, 2015.

Effect of a resistive load on the starting performance of a standing wave thermoacoustic engine: A numerical study

Lin Ma, Catherine Weisman,[a] Diana Baltean-Carlès, and Ivan Delbende
Université Pierre et Marie Curie UPMC Sorbonne Universités, UFR 919 - Laboratoire d'Informatique pour la Mécanique et les Sciences de l'Ingénieur, 91405 Orsay Cedex, France

Luc Bauwens
Department of Mechanical and Manufacturing Engineering, University of Calgary, Calgary, Alberta T2N 1N4, Canada

(Received 4 August 2014; revised 23 April 2015; accepted 8 July 2015; published online 17 August 2015)

The influence of a resistive load on the starting performance of a standing-wave thermoacoustic engine is investigated numerically. The model used is based upon a low Mach number assumption; it couples the two-dimensional nonlinear flow and heat exchange within the thermoacoustic active cell with one-dimensional linear acoustics in the loaded resonator. For a given engine geometry, prescribed temperatures at the heat exchangers, prescribed mean pressure, and prescribed load, results from a simulation in the time domain include the evolution of the acoustic pressure in the active cell. That signal is then analyzed, extracting growth rate and frequency of the dominant modes. For a given load, the temperature difference between the two sides is then varied; the most unstable mode is identified and so is the corresponding critical temperature ratio between heater and cooler. Next, varying the load, a stability diagram is obtained, potentially with a predictive value. Results are compared with those derived from Rott's linear theory as well as with experimental results found in the literature. © *2015 Acoustical Society of America*. [http://dx.doi.org/10.1121/1.4927092]

[JDM] Pages: 847–857

I. INTRODUCTION

A thermoacoustic engine is a device absorbing heat at the hot heat exchanger and releasing heat at the cold heat exchanger while producing acoustic work as an output. Engines are meant to carry a load, which in the case of an acoustic device might include a thermoacoustic refrigerator,[1] a pulse tube refrigerator,[2] a (possibly linear) electric generator,[3] or a piezoelectric transducer.[4] The strong coupling that will exist between the engine and the load influences both starting performance and steady (periodic) operation.

Thermoacoustic devices have been studied extensively for more than 30 years. Most of the work in the literature is based upon the linear theory developed by Rott[5] and later extended by Swift *et al.*[1,6] The theory can handle different geometries for the various parts of the system, such as stack, heat exchangers, and ducts. Numerical implementation is based upon a lumped element approximation.[7] The linear theory will then yield the acoustic field and, as a result, the performance of a given system when in the periodic regime.[1] Linear theory can also predict the onset conditions (critical starting temperature gradient) as a function of the mean pressure by performing a stability analysis for a fixed geometry and working fluid. Results from linear theory are in good agreement with experiments[8–10] for the onset of a standing wave thermoacoustic engine inside a resonator closed at both ends. Recently, a completely analytical boundary layer theory extending linear theory was developed by Sugimoto,[11,12] reducing the problem to a one-dimensional model. That theory was then used in an analytical stability analysis for systems with a stack under given temperature gradient inside straight or looped resonators, for given acoustic frequency, without resorting to lumped elements. Linear theory has important limitations: the stability analysis is performed in the frequency domain for each mode, the transient regime is not described, and nonlinear and multidimensional effects are not considered or are only partially taken into account.

Transient regimes were addressed by de Waele[13] who developed a one-dimensional time-dependent model of a thermoacoustic Stirling engine taking into account the dynamics of individual components, again using a lumped-element approximation. de Waele studied engine start phase and transient effects while acoustics is still considered linear. A mixed empirical and theoretical one-dimensional model was developed by Guedra and co-workers[14,15] based upon a transmission matrix formulation, also assuming linear acoustics. The transmission matrix was obtained experimentally from impedance measurements. Using that model, they studied the onset of oscillations for both a basic standing wave engine and a traveling wave-engine. None of these studies included the influence of a load on onset conditions.

In contrast, the influence of the load has been accounted for in studies of thermoacoustic devices in the periodic regime. The performance of a loaded thermoacoustic engine was investigated by Olson *et al.*,[16] and also others,[17,18] using linear theory[1] and the lumped elements approximation. More recently, Hatori *et al.*[19] developed an experimental method based on measuring the acoustic impedance of the engine and of the load separately, and predicted the operating point

[a]Electronic mail: catherine.weisman@limsi.fr

of the combination engine plus load. Coming to nonlinear models, some numerical simulations of the full compressible Navier–Stokes equations in loaded thermoacoustic devices with complicated geometry have been performed.[20,21] These simulations were performed using commercial codes and gave a good description of thermoacoustic engines in the transient and periodic regimes. However, each test case required extremely large and time consuming simulations; therefore, these are not appropriate for a parametric study of a variable load coupled with an engine.

The aim of the current work is to study the influence of a variable load on the marginal stability conditions of a standing-wave thermoacoustic engine. The model used implements a hybrid low Mach number approximation. It is based on coupling the two-dimensional nonlinear flow and heat exchange in the thermoacoustic active cell with one-dimensional linear acoustics in the loaded resonator. For a detailed description, see Ref. 22. In the load model used in the present study, instantaneous acoustic pressure and velocity are assumed to be in phase at the loaded end, and the load is thus reduced to a real scalar value measuring the ratio of velocity over acoustic pressure. For a given engine geometry and a given temperature ratio between heater and cooler, numerical simulations of the active cell show that depending on the load value, the engine will or will not start. From the numerical results, for any given configuration, a critical temperature ratio is thus determined, corresponding to the onset of thermoacoustic oscillations, together with the frequency of the corresponding, most unstable mode. The analysis is performed using a time-dependent nonlinear model that takes into account two-dimensional effects as well as multi-frequency content. Finally, the influence of the load on the starting phase of the engine is discussed and the results are compared, both with results derived from the linear theory and with Atchley's experiments,[8] bringing new insight into the engine-load coupling.

II. PHYSICAL MODEL

A. Low Mach number approximation

The geometry consists of a long tube with length $\tilde{L}_{res}$, within which an active cell is placed at a distance $\tilde{L}_L$ from the left end. The active cell consists of a stack of horizontal solid plates with length $\tilde{L}_{stack}$, placed between two heat exchangers also consisting of solid horizontal plates that have the same periodicity as the stack (see Fig. 1). The geometry can then be reduced to a domain consisting of two half-plates plus the gap between them, plus a region that extends away from the solid plates.

First, a dimensionless coordinate system $\hat{x}$ is introduced, that resolves the acoustic aspect of the device, which is thus scaled by the resonator length $\tilde{L}_{res}$. The inert resonator end located at $\hat{x} = -\hat{l}_L = -\tilde{L}_L/\tilde{L}_{res}$ is a closed end. The second resonator end consists of a load placed at a fixed location $\hat{x} = \hat{l}_R = 1 - \hat{l}_L$, described in more detail below. The active cell is positioned at $\hat{x} = 0$. It has negligible size when scaled by $\tilde{L}_{res}$, as discussed below [see Fig. 2(a)].

Next, a different dimensionless coordinate system (x, y) is introduced, that characterizes the active cell geometry,

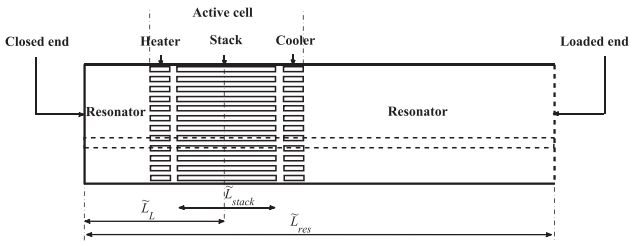

FIG. 1. Simplified geometry of a thermoacoustic engine.

where lengths are scaled by the stack length $\tilde{L}_{stack}$, in both x and y. The corresponding dimensionless geometrical parameters include the vertical gap or flow passage between two stack plates h, the stack porosity h/H, where H is the domain height, equal to the vertical gap plus the thickness of one stack plate, the vertical gap between two heat exchanger plates h_x, the horizontal gap between heat-exchangers and stack L_{xs}, and the heat-exchanger lengths L_{hx} and L_{cx} [see Fig. 2(b)].

The low Mach number model is described in detail in previous work.[22] The model assumes that the particle displacement spans a length on the order of $\tilde{L}_{stack}$, hence typical velocities on the order of $\tilde{U}_{ref} = \tilde{L}_{stack}/\tilde{\tau}$, where $\tilde{\tau}$ is on the order of the fundamental acoustic period of the empty resonator, $\tilde{\tau} = \tilde{L}_{res}/\tilde{c}$, and $\tilde{c}$ is the speed of sound. A reference Mach number $M = \tilde{U}_{ref}/\tilde{c}$ can then be introduced which also equals $M = \tilde{L}_{stack}/\tilde{L}_{res}$. In the following, the Mach number is assumed to be small or equivalently the stack is then taken to be much shorter than the resonator. The active cell size is then negligible in the $\hat{x}$ coordinate system.

Flow in the resonator is then described by linear acoustics. The solutions are expressed as a pair of planar traveling waves that move respectively left and right at the speed of sound. The two Riemann invariants $\mathcal{L}(\hat{x}, t)$ and $\mathcal{R}(\hat{x}, t)$ are used, defined by

$$\mathcal{L} = \gamma u - \sqrt{T}p', \quad \mathcal{R} = \gamma u + \sqrt{T}p' \tag{1}$$

with γ the ratio of specific heats, $u(\hat{x}, t)$ the dimensionless gas velocity, T the dimensionless temperature (using the cold temperature as a reference) which is assumed to be constant in each resonator part ($T = T_h$ on the left side of the

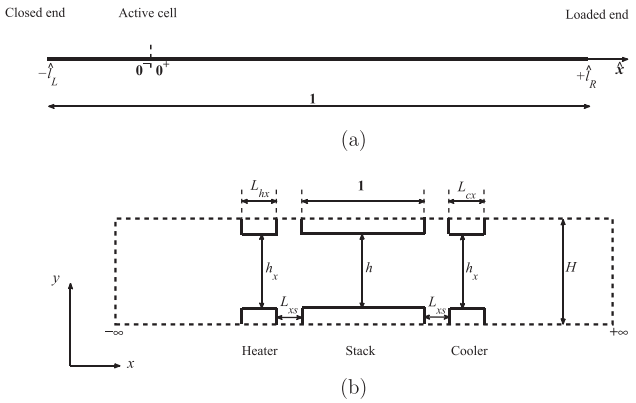

FIG. 2. Geometry of resonator (a) and of active cell geometry (b) in dimensionless coordinates.

active cell, and $T = T_c = 1$ on the right side), and $p'(\hat{x}, t)$ the dimensionless order M (acoustic) pressure (using the mean gas pressure as a reference). At each tube end, the boundary condition results in a relationship that determines the outgoing wave as a function of the incoming wave, as explained in Ref. 22. The order M pressure and acoustic velocity on both sides of the active cell ($\hat{x} = 0^{\pm}$) are expressed using these same quantities at previous times accounting for propagation on each side and reflections at the respective ends. The specific treatment of the loaded end will be described in detail in Sec. II B.

Flow in the active cell is described by two-dimensional Navier–Stokes equations, with order M^2 pressure gradients superimposed to a pressure spatially uniform up to order M, and varying density and temperature. The solid stack plate problem is described by the heat conduction equation. In the stack and heat exchanger plates, physical properties such as density, thermal conductivity, and heat capacity are taken to be constant. Thermal conductivity and heat capacity of the gas are also constant, with values corresponding to cold temperature, chosen as the reference temperature. Reference density of the gas is that corresponding to the reference (cold) temperature and the mean gas pressure.

At the solid-gas boundaries, continuity of temperature and heat flux are imposed, as well as a no slip condition. In the heat exchangers, uniform, constant temperatures are imposed with dimensionless values $T_c = 1$ in the cooler plates, $T_h > 1$ in the heater plates. Given the periodicity, open active cell boundaries are effectively adiabatic.

Boundary conditions at the open ends of the active cell are provided by appropriate matching of the inner (active cell) and outer (resonator) solutions. The latter are expressed using the Riemann invariants $\mathcal{L}$ and $\mathcal{R}$ defined by Eq. (1), traveling respectively left and right in the resonator, at the speed of sound. At each extremity of the active cell, the outgoing invariant is determined as a function of the incoming one, taking the corresponding resonator boundary conditions into account. These consist respectively of a zero velocity at the closed end, and the load, described in Sec. II B, at the loaded end.[22] Finally, a global energy balance over the active cell relates velocities at the two cell extremities to heat transfer.

From the standpoint of resonator acoustics, the active cell is transparent to pressure but provides a source of volume. From the standpoint of the active cell, matching with the resonator occurs at infinity so that, in principle, the active cell has infinite length on both sides. However the numerical domain has to be finite. Its length is chosen equal to 5 times the stack length, which ensures proper matching, as confirmed by validation. The dimensionless parameters characterizing the problem are then the reference Mach number M, the relative position of the active cell in the resonator $\hat{l}_L$, parameters describing the geometry of the active cell (H, h_s, h_x, L_{xs}, L_{hx}, L_{cx}), a Péclet number $P_e = \tilde{U}_{ref}\tilde{H}/\tilde{\alpha}_{ref}$, where $\tilde{\alpha}_{ref}$ is the reference thermal diffusivity, a Reynolds number $R_e = \tilde{\rho}_{ref}\tilde{U}_{ref}\tilde{H}/\tilde{\mu}_{ref}$, $\tilde{\rho}_{ref}$ and $\tilde{\mu}_{ref}$ being the reference density and viscosity, and the Péclet number $P_{es} = P_e\,\tilde{\alpha}_{ref}/\tilde{\alpha}_s$ in solid walls, where $\tilde{\alpha}_s$ is the thermal diffusivity of the solid material.

B. Load model

The present study considers a purely resistive load, so that instantaneous acoustic pressure $p'(\hat{l}_R, t)$ and velocity $u(\hat{l}_R, t)$ at the loaded end are assumed to be in phase. The load is thus characterized by a scalar value equal to the ratio of dimensionless acoustic pressure to velocity, i.e., $f = p'(\hat{l}_R, t)/u(\hat{l}_R, t)$, with f a positive real. Such a load behaves as a pure resistance in the electrical analogy. Actual loads may include inertial and capacitance effects; these will depend not only on mechanical design, but also on the driven devices. A detailed study of these issues is beyond the scope of the present work.

The limit value $f \to 0$ corresponds to an open end, with $p'(\hat{l}_R, t) = 0$, while the limit value $f \to \infty$ corresponds to a closed end, with $u(\hat{l}_R, t) = 0$.

The boundary condition at the load location $\hat{x} = \hat{l}_R$ is carried along the returning (left-moving) characteristic, resulting in the corresponding boundary condition at the right end of the active cell, at $\hat{x} = 0^+$. Specifically, the boundary condition at $\hat{x} = 0^+$ relates the current local value of the left-moving Riemann invariant and the value of the right-moving Riemann invariant at the same location but at a previous time that differs by the round trip time between the active cell and the load at the speed of sound $\sqrt{T_c}$,

$$\mathcal{L}(0^+, t) = Z\mathcal{R}(0^+, t - 2\hat{l}_R/\sqrt{T_c}), \tag{2}$$

in which a real coefficient Z was introduced, defined as

$$Z = \frac{\gamma - f}{\gamma + f}. \tag{3}$$

While f goes from zero for an open end to infinity for a closed end, Z has the finite span from -1 for a closed end to $+1$ for an open end. Furthermore, the expression emphasizes the particular value $f = \gamma$, for which Z vanishes, corresponding to a left-moving Riemann variable with zero value, regardless of the right-moving variable, hence to a nonreflecting load. If $Z = 0$, the solution no longer depends upon the length of the right side of the resonator; such a load may be difficult to implement, and of little practical value, as results below will confirm; however, that case still has some interest as it separates different regimes. In the framework of the harmonic approximation, it is possible to relate f or Z to the reflection coefficient at the loaded end hence to the standing wave ratio.[23] In that context the absolute value of Z is equal to the modulus of the reflection coefficient. The limit values $Z = \pm 1$ correspond to a pure standing wave in the resonator, while the limit case $Z = 0$ corresponds to a pure traveling wave moving from the active cell towards the load. Between those limit cases, the wave is a combination of two waves traveling in opposite directions with unequal amplitudes, i.e., neither standing or purely traveling. In the current study, however, the effect of the load parameter on starting performance will be investigated in the time domain with no *a priori* on the nature of the wave developing in the engine. Critical temperature ratio between heater and cooler and starting frequencies will be analyzed by varying the value of

f in the range 0 to $+\infty$. Results will be more conveniently shown as functions of the coefficient Z in the range $[-1, 1]$.

III. NUMERICAL SIMULATION

A. Algorithm

The problem in the active cell is solved numerically using a finite volume code.[22] Diffusion is dealt with implicitly while advection is explicit. The scheme is second-order accurate in space and in time. A fractional time step projection method adapted for variable density is used to enforce continuity. The ADI algorithm is used to solve the Helmholtz equation for time advance of temperature and velocities. A multigrid algorithm determines the pressure correction. Solutions of the coupled equations providing velocity boundary conditions and acoustic pressure at the active cell location from resonator acoustics and energy balance are appropriately integrated in the solution sequence.[22]

B. Procedure

Simulations account for a specific engine geometry, characterized by the reference Mach number M, the relative distance of the active cell to the left end $\hat{l}_L$, and the dimensions of the active cell H, h, h_x, L_x, and L_{xs}. Most of the current results were obtained for L_{xs} equal to h. Reference Péclet number P_e, solid Péclet number P_{es}, and Reynolds number R_e are maintained constant. The evolution in time of the velocity and temperature fields is computed for given heater and cooler temperatures and load. The required initial conditions consider fluid at rest and temperature profiles, obtained numerically, corresponding to steady conduction in the walls and in fluid at rest. Initial conditions also need to be specified for resonator acoustics, and these need to be nonzero since the steady solution to the global problem consists of fluid at rest, together with a stationary conduction solution. To that effect, and in order not to favor specific modes, an initial random noise is imposed in the resonators. Small $\mathcal{O}(10^{-4})$ random values are thus assigned to the Riemann invariants at the active cell entrance and exit for a time window prior to zero, of length equal to the round trip time between active cell and the respective resonator end.

Starting from initial conditions specified above, the velocity $u(x, y, t)$, dynamic pressure $p(x, y, t)$, temperature $T(x, y, t)$, and density $\rho(x, y, t)$ fields are calculated inside the active cell at each time step. Coupling at the active cell entrance and exit provides the velocity at the entrance $u(0^-, t)$ and exit $u(0^+, t)$ of the active cell, as well as the value of the acoustic pressure at the active cell location $p'(0, t)$ at each time step. The velocity values at the entrance and exit of the active cell serve as boundary conditions for velocity inside the active cell. The order M acoustic pressure $p'(0, t)$, which is included in the active cell model only through boundary conditions, is an outcome of the simulation. That quantity is analyzed here to characterize the device's regime: motion damping or amplification.

C. Post-processing

Acoustic modes are characterized by amplitude and complex frequency, i.e., frequency and growth rate. If the temperature ratio between heater and cooler is small, growth rates are all negative, i.e., the amplitudes of all modes decrease in time and motion stops. A critical temperature ratio is obtained when one of the modes exhibits positive growth: instability occurs and the device starts. In order to find the critical temperature ratio $T_{crit} = \tilde{T}_{hcrit}/\tilde{T}_c$ for a given load, repeated simulations are performed for increasing values of the hot temperature, until a first growth rate becomes positive.

The pressure signal $p'(0, t)$ is analyzed to extract the growth rate and frequency of the dominant modes, by fitting the signal to an approximation of the form

$$p'(0,t) = \sum_{i=1}^{n} A_i e^{\sigma_i t} \cos(\omega_i t) + B_i e^{\sigma_i t} \sin(\omega_i t), \tag{4}$$

where n is the desired number of modes, with typical value 4. The fitting uses a window that includes m consecutive data points, collected after several reference periods have elapsed so that a dominant exponential mode has emerged from the initial phase affected by initial conditions. In Eq. (4), σ_i is the growth rate of mode i, ω_i is its angular frequency, and A_i, B_i are amplitudes.

Fitting the $(A_i, B_i, \sigma_i, \omega_i)$ coefficients is performed using an iterative two stage procedure. Starting with an initial guess (σ_i, ω_i), the (A_i, B_i) coefficients are determined by least mean square error minimization, using the m data points. Then the (σ_i, ω_i) coefficients are obtained using a simplex algorithm. Iterations continue until the fit satisfies a given criterion, with the quadratic error below some adequate lower bound. The whole procedure is iterated until an error below 10^{-4} on (σ_i, ω_i) is reached.

IV. RESULTS

A. Conditions

Numerical simulations were carried out on an existing prototype of thermoacoustic engine,[22] with a "short" thermoacoustic active cell inserted in a long resonator closed at both ends. The engine is modeled as the simplified device introduced in Fig. 2, assuming acoustics is lossless in the resonators and concentrating all dissipation at the loaded end.

The working fluid is helium. The dimensions (resonator length, stack length, distance between the left end and the active cell, plate spacing) and the conditions of the experiments, such as mean pressure and cold temperature, are kept constant. The relevant dimensionless parameters are summarized in Table I, and the relevant fluid properties are summarized in Table II.

Numerical simulations were carried out using a regular two-dimensional mesh for the active cell, with either 2048×32 or 4096×64 grid points. The simulation domain is long enough to ensure that the flow velocity near the entrance and exit is parallel to the resonators. The time step is adjusted in order to satisfy the numerical stability

TABLE I. Dimensionless parameters characterizing the reference experimental device (Ref. 22).

M	P_e	P_{es}	R_e	$\hat{l}_L$	H	h/H	h_x/H	L_{hx}	L_{cx}	L_{xs}
0.02	1100	4900	1600	0.09	0.007	0.73	0.73	0.05	0.05	0.005

condition, with about 200 (coarse grid) to 2000 (fine grid) time steps per reference acoustic period. Typically only 60 min of CPU time are necessary for each numerical run (about 100 periods), such as the one shown in Fig. 3.

For given load value and given heater temperature, the time history of acoustic pressure in the active cell was recorded from the computation. An example of the time signal is shown in Fig. 3(a). The first oscillations are rather erratic [details are not shown in Fig. 3(a)] and they depend upon initial conditions. The signal eventually becomes smoother and amplitudes appear to correspond to a superimposition of exponentially varying modes. The signal appears to remain multi-frequency. This is confirmed in Fig. 3(b) which shows the corresponding spectrogram. In the figure, the angular frequency is scaled by a reference angular frequency ω_{ref} equal to the fundamental angular frequency of the empty resonator closed at both ends, filled with gas at a mean pressure $\tilde{P}_m$ and a temperature equal to the cold temperature $\tilde{T}_c$. At any given time, the power spectrum exhibits successive peaks corresponding to the resonant frequencies of the engine for the specific load value. As time evolves, most modes are damped while some are amplified. A more accurate determination of the frequencies and growth rates of the dominant modes is presented in Sec. IV B.

B. Results at a given active cell location

First, the effect of the load on the critical temperature ratio is studied, for a single active cell location.

Analyzing the pressure signal using the approach described in Sec. III C, the growth rate and frequency of the four dominant modes are calculated, for a range of increasing values of the temperature of the heater T_h, for a given load f, until unstable modes appear. The most unstable mode is identified as the first mode for which the growth rate σ goes from negative to positive, as T_h is increased. Plotting σ as a function of the dimensionless temperature T_h helps one to identify the precise value of the critical temperature ratio, as Fig. 4 shows. In the vicinity of the critical value, σ varies nearly linearly with T_h, and a precise determination of the critical temperature ratio is obtained by interpolation. For example in Fig. 4, the critical temperature ratio is found to be $T_{crit} = 1.845$.

TABLE II. Fluid properties in reference experiment (Ref. 22).

Helium gas					
$\tilde{P}_m$ MPa	$\tilde{T}_c$ K	$\tilde{\rho}$ kg m^{-3}	$\tilde{\mu}$ Pa s	$\tilde{c}_p$ J kg^{-1} K^{-1}	$\tilde{k}$ W m^{-1} K^{-1}
1.0	293	1.6	2×10^{-5}	5193	0.15

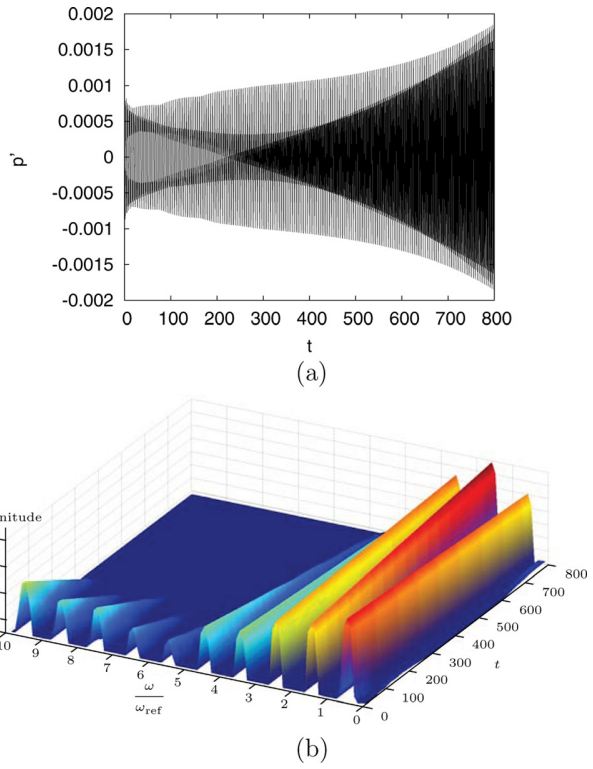

FIG. 3. (Color online) (a) Typical time signal of acoustic pressure $p'(0,t)$ and (b) associated spectrogram (the magnitude is the square root of the power density spectrum). $Z = 0.988$. $T_h = 1.08$.

Next, varying the load and reproducing the same procedure for each load value results in a stability diagram (Fig. 5) in the (Z, T_h) plane showing stable and unstable zones. The zones are separated by a stability curve connecting all the critical temperature ratios causing the engine to start. The region above the stability curve corresponds to instability. Figure 5 shows a stability domain roughly delimited by a symmetrical triangle peaking at $Z = 0$, when a semi-log scale is used.

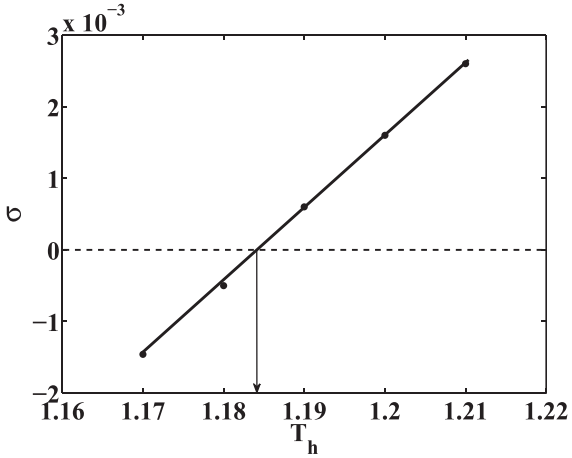

FIG. 4. Growth rate of most unstable mode as a function of the hot exchanger temperature, $Z = -0.963$.

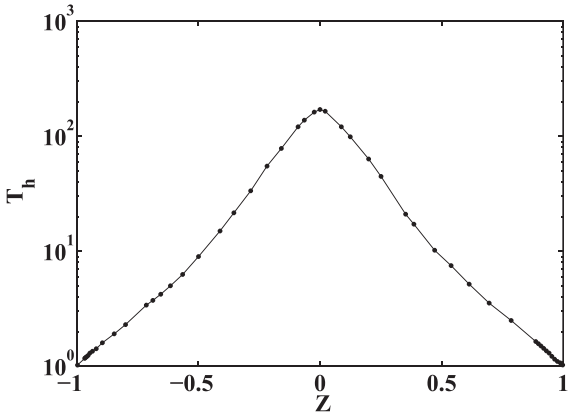

FIG. 5. Stability diagram in the (Z, T_h) plane, showing the stability curve (–•–). The region above the curve corresponds to instability.

Figure 6 shows the angular frequency ω of the first mode to become unstable as a function of Z. As $|Z|$ decreases, the frequency of the most unstable mode is observed to increase. Although the general shape of the curve is approximately symmetrical as it is in Fig. 5 for the critical temperature, the values of ω do not display any symmetry. Indeed, critical modes near $Z = -1$ are of the closed-end type (multiples of $\lambda/2$) whereas critical modes near $Z = 1$ are of the open-end type (odd multiples of $\lambda/4$). This results in distinct sets of onset frequencies, as is further discussed and analyzed in Secs. IV C and V when commenting on Figs. 7, 8, and 11.

For Z close to zero, Fig. 5 shows a very large critical temperature ratio, too large to be realistic. Likewise, frequencies become so high that resolution, both of the wavelength in space and of the period in time, becomes quite poor. Furthermore, these curves were obtained assuming constant viscosity and thermal conductivity conditions, which is unrealistic at high temperature. These results are thus somewhat dubious and, therefore, Fig. 5 merely gives a qualitative picture for Z close to zero. While such numerical critical temperature ratios may be of limited value, the conclusion is valid that in the vicinity of $Z = 0$ the device will not start for any realistic temperature ratio (T_h less than about 10), all modes remaining stable.

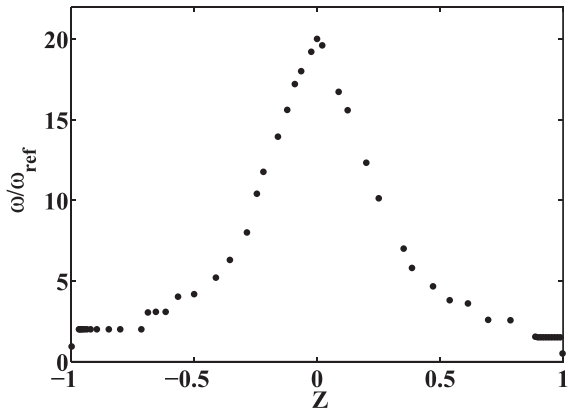

FIG. 6. Angular frequency of the most unstable mode scaled by ω_{ref}, as a function of Z.

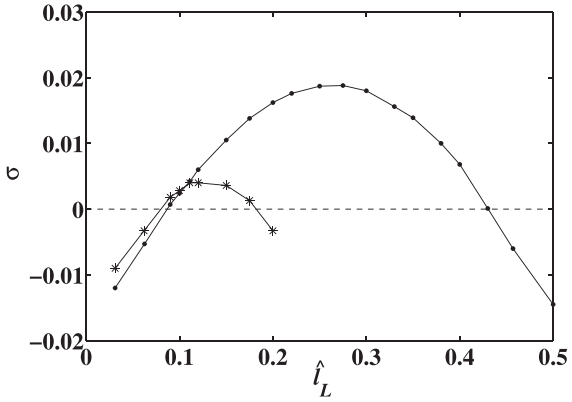

FIG. 7. Growth rates as a function of the active cell location for $0 < \hat{l}_L < 0.5$, $Z = -0.963$, $T_h = 1.2$. (–•–) fundamental mode (the $\lambda/2$ mode), (–∗–) first harmonic mode (the λ mode).

C. Results varying the active cell location or configuration

The stability diagrams shown in Figs. 5 and 6 can be used, for a given configuration, to predict the critical temperature ratio and the dominant frequency as a function of the load.

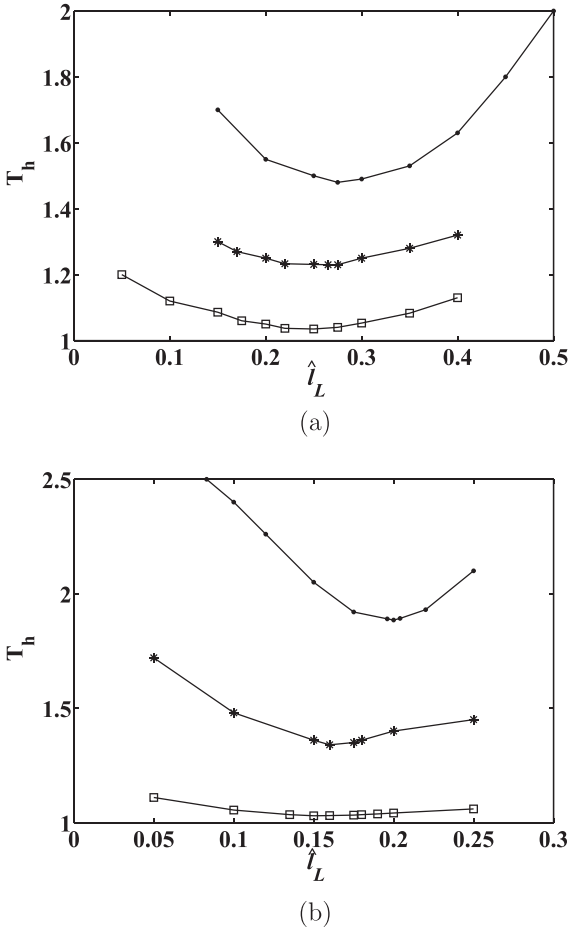

FIG. 8. Stability diagram showing the critical temperature ratio as a function of the active cell location for (a) (–□–) $Z = -0.99$, (–∗–) $Z = -0.92$, (–•–) $Z = -0.85$, the critical mode is the fundamental mode ($\lambda/2$), and (b) (–•–) $Z = 0.79$, (–∗–) $Z = 0.90$, (–□–) $Z = 0.99$, the critical mode is the first harmonic ($3\lambda/4$).

These diagrams are modified if the location of the active cell measured by $\hat{l}_L$ is varied. The stability curve becomes a stability surface, which can be used to predict the critical temperature ratio for a given setup. For given load and heater temperature values, the position of the active cell has to be within a certain region for the engine to start. For an active cell outside this region, all modes are dampened and the engine will not start.

Figure 7 shows the growth rate of the fundamental mode and of the first harmonic as a function of the active cell location for $Z = -0.963$ and $T_h = 1.2$. It is found that if the active cell is positioned at $0.083 < \hat{l}_L < 0.12$, the first harmonic is the most unstable mode. In contrast, if it is placed at $0.12 < \hat{l}_L < 0.43$, the fundamental mode is dominant. For that parameter setting, the overall optimal position for starting performance is $\hat{l}_L = 0.27$, for which the growth rate is maximum. Another way to address the issue is to determine the active cell location for which the critical temperature ratio is minimum. Figure 8 shows the value of the critical temperature ratio for varying active cell locations and for selected load values. Figure 8(a) shows results for negative values of Z near $Z = -1$, in which case both ends are closed. For each value of Z, there is one stack position that minimizes the critical temperature ratio. The optimal position is approximately 0.25 for $Z = -0.99$. Since the fundamental mode (the $\lambda/2$ mode) is the critical one in that region, this corresponds to a stack located at $\lambda/8 \simeq \hat{L}_{res}/4$ as expected ($\hat{L}_{res} = 1$). As Z departs from $Z = -1$, the wavelength increases so that the optimal position shifts towards the center of the resonator.

Figure 8(b) corresponds to positive values of Z, near $Z = 1$, for which the cold end is open. The optimal position is approximately 0.16 for $Z = 0.99$. Now the first harmonic (the $3\lambda/4$ mode) is the critical mode in that range of stack locations. This corresponds to a stack located at $\lambda/8 \simeq \hat{L}_{res}/6 \approx 0.17$. For decreasing values of Z, below $Z = 1$, the wavelength increases so that the optimal position again shifts towards the resonator center. Note that here the active cell is located at $\hat{l}_L \leq 0.25$. If the stack were placed further away, the fundamental mode would become the critical one and the optimal position would shift towards 0.5.

The effect of varying the distance between the heat exchangers and the stack L_{xs} was also studied. In all previous cases the horizontal spacing L_{xs} was equal to the vertical stack plate spacing h. Figure 9 shows the stability diagram for two other situations: for heat-exchangers and stack in direct contact ($L_{xs} = 0$) and doubling the horizontal spacing ($L_{xs} = 2h$). While placing the heat-exchangers and stack incontact together results in significant reduction of the critical temperature ratio for all values of the load (potentially leading to a significant increase in longitudinal conduction losses), the effect of doubling the spacing is insignificant. The nature of the critical modes will be discussed in Sec. V (see comments of Fig. 11).

V. COMPARISON WITH THE LINEAR THEORY

In this section the critical temperature ratio associated to a given acoustic mode is estimated following Rott's linear theory,[5,24] which is outlined here using dimensional values

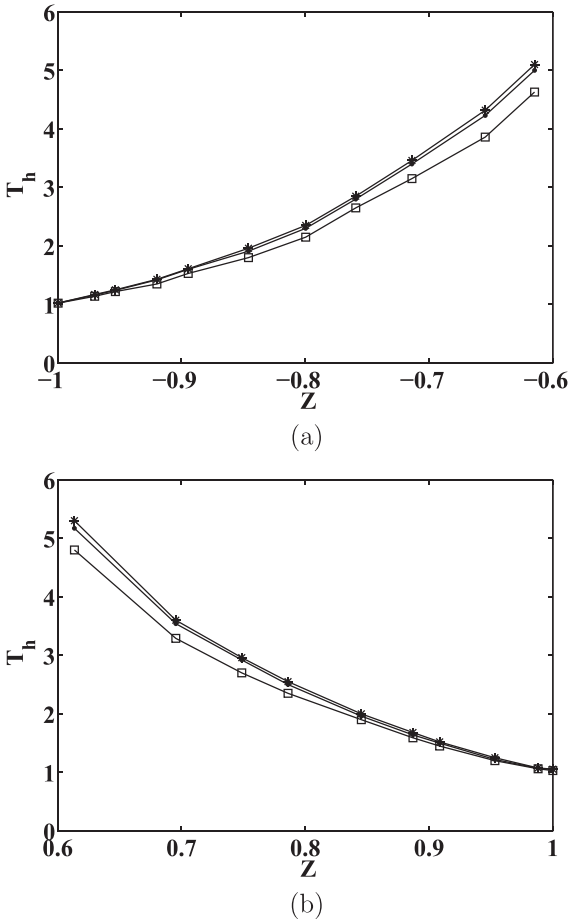

FIG. 9. Stability diagram in the (Z, T_h) plane, showing the stability curve (critical temperature ratios) for three distances between heat-exchangers and stack, (–□–) $L_{xs} = 0$, (–•–) $L_{xs} = h$, (–∗–) $L_{xs} = 2h$. (a) $-1 < Z < -0.6$, (b) $0.6 < Z < 1$.

for the various parameters. Linear results were obtained for a slightly different configuration, with the same total resonator length, stack length, and position of the stack center within the resonator as above. However, the detailed heat exchanger geometry used above was replaced by imposing a linear wall temperature profile in the stack, constant mean temperatures $\tilde{T}_h$ on the left side of the stack, and constant mean cold temperature $\tilde{T}_c$ on the right side.

The flow in the resonator tubes left and right of the stack was taken as one-dimensional isentropic linear acoustics with different speeds of sound corresponding to the respective temperatures $\tilde{T}_h$ and $\tilde{T}_c$. The boundary conditions on the left and right ends were the same as previously, with a load modeled as a real impedance $\tilde{R}$ relating acoustic velocity and acoustic pressure. The acoustic pressure and velocity amplitudes $[\tilde{p}'_h(\tilde{x}), \tilde{u}_h(\tilde{x})]$ on the left resonator part and $[\tilde{p}'_c(\tilde{x}), \tilde{u}_c(\tilde{x})]$ on the right resonator part are functions of position which can be expressed simply in terms of two unknowns, namely, the complex maximum amplitudes $\tilde{U}_h$ and $\tilde{U}_c$.

The stack region is described as a two-dimensional channel of height $2\tilde{y}_0$ equal to the vertical distance between stack plates, extending from $\tilde{x} = 0$ to $\tilde{x} = \tilde{L}_{stack}$. Following Rott's approach, solutions of the viscous flow equations are sought for as harmonic functions in time with angular frequency $\tilde{\omega}$,

using a boundary layer approximation and integrating vertically over the channel height. Also, the stack is assumed to be acoustically compact, so that the acoustic pressure amplitude $\tilde{p}'$ is homogeneous through the stack. Since temperature varies linearly through the stack, $d\tilde{T}/d\tilde{x}$ is a constant.

The resulting dimensional equation for the acoustic velocity in Fourier space is[25]

$$\frac{d\tilde{u}_1}{d\tilde{x}} - \frac{\tilde{f}_\kappa - \tilde{f}_\nu}{(1-\tilde{f}_\nu)(1-P_r)}\frac{1}{\tilde{T}}\frac{d\tilde{T}}{d\tilde{x}}\tilde{u}_1 = -\frac{i\tilde{\omega}}{\gamma \tilde{P}_m}\left[1+(\gamma-1)\tilde{f}_\kappa\right]\tilde{p}', \tag{5}$$

where $\tilde{P}_m$ is the gas mean pressure, Rott's factors are defined as

$$\tilde{f}_\nu = \frac{\tanh\left[(1+i)\tilde{y}_0/\sqrt{2\tilde{\mu}/(\tilde{\rho}\tilde{\omega})}\right]}{(1+i)\tilde{y}_0/\sqrt{2\tilde{\mu}/(\tilde{\rho}\tilde{\omega})}},$$
$$\tilde{f}_\kappa = \frac{\tanh\left[(1+i)\tilde{y}_0/\sqrt{2\tilde{k}/(\tilde{\rho}\tilde{c}_p\tilde{\omega})}\right]}{(1+i)\tilde{y}_0/\sqrt{2\tilde{k}/(\tilde{\rho}\tilde{c}_p\tilde{\omega})}} \tag{6}$$

with constant gas properties $\tilde{\mu}$, $\tilde{c}_p$, $\tilde{k}$ (therefore the Prandtl number P_r is constant also), and density $\tilde{\rho}$ depending on position through variation of temperature. The $\tilde{f}_\nu$ and $\tilde{f}_\kappa$ factors are functions of $\tilde{x}$. Equation (5) is a first order linear inhomogeneous equation, so the solution is expressed as

$$\tilde{u}_1(\tilde{x}) = \exp\left[\int_0^{\tilde{x}} \frac{\tilde{f}_\kappa(\tilde{x}_1)-\tilde{f}_\nu(\tilde{x}_1)}{(1-\tilde{f}_\nu(\tilde{x}_1))(1-P_r)}\frac{1}{\tilde{T}(\tilde{x}_1)}\frac{d\tilde{T}}{d\tilde{x}_1}d\tilde{x}_1\right]$$
$$\times\left\{C_1 - \int_0^{\tilde{x}}\frac{i\tilde{\omega}}{\gamma\tilde{P}_m}\left[1+(\gamma-1)\tilde{f}_\kappa(\tilde{x}_1)\right]\tilde{p}'\exp\left[-\int_0^{\tilde{x}_1}\frac{\tilde{f}_\kappa(\tilde{x}_2)-\tilde{f}_\nu(\tilde{x}_2)}{[1-\tilde{f}_\nu(\tilde{x}_2)](1-P_r)}\frac{1}{\tilde{T}(\tilde{x}_2)}\frac{d\tilde{T}}{d\tilde{x}_2}d\tilde{x}_2\right]d\tilde{x}_1\right\}, \tag{7}$$

in which C_1 is an integration constant.

That expression can be rewritten using the relationship between position and temperature as

$$\tilde{u}_1(\tilde{x}) = \exp\left[-\int_{\tilde{T}(\tilde{x})}^{\tilde{T}_h}\frac{\tilde{f}_\kappa(\theta)-\tilde{f}_\nu(\theta)}{[1-\tilde{f}_\nu(\theta)](1-P_r)}\frac{1}{\theta}d\theta\right]$$
$$\times\left\{C_1+\int_{\tilde{T}(\tilde{x})}^{\tilde{T}_h}\frac{i\tilde{\omega}}{\gamma\tilde{P}_m}\left[1+(\gamma-1)\tilde{f}_\kappa(\theta)\right]\tilde{p}'\right.$$
$$\left.\times\exp\left[\int_\theta^{\tilde{T}_h}\frac{\tilde{f}_\kappa(\theta^*)-\tilde{f}_\nu(\theta^*)}{[1-\tilde{f}_\nu(\theta^*)](1-P_r)}\frac{1}{\theta^*}d\theta^*\right]\frac{\tilde{L}_{stack}}{\tilde{T}_c-\tilde{T}_h}d\theta\right\}. \tag{8}$$

Boundary conditions are provided by matching with resonator acoustics. While the resonator acoustics yield velocities uniform transversally, the boundary layer model incorporated in the linear theory used in the stack results in a specific nonuniform velocity profile. Matching the mean velocities values is justified based upon a multiple length approach similar to that used above. Indeed the transition region is small compared with acoustic lengths, so that mass and pressure corrections due to the transition zone occur at higher order. For known boundary conditions at the outer resonator ends, acoustics yield a relationship between acoustic pressure in the stack, $\tilde{p}'$, and the uniform acoustic velocities, $\tilde{U}_h$ and $\tilde{U}_c$, respectively, on the left and right side. Continuity conditions require mean velocities and acoustic pressure to match at both stack ends.

Requiring the resulting globally homogeneous problem to have non-trivial solutions results in a dispersion relation that cannot be solved in closed form for the complex frequency ω. A numerical solution was thus implemented using a shooting method, integrating over the stack length, and iterating until the relationship between pressure and velocity at the end match the acoustic boundary condition. The method requires an initial guess for the complex frequency, conveniently provided by the numerical results of Sec. IV B.

Figures 10 and 11 show a comparison between numerical results and results obtained using the linear theory. Only the range $|Z| > 0.6$ is shown, which contains all cases of practical interest.

In Fig. 10, the critical temperature ratio is shown as a function of Z. There is very good agreement between the two approaches, with the ratio obtained through the linear theory slightly above the numerical values, which may be ascribed to a shorter length for lossless acoustics in the linear approach. As $Z \to -1$, the critical temperature ratio becomes very close to 1. For instance, for $Z = -0.997$, the critical temperature ratio is found to be $T_{crit} = 1.024$ numerically while linear theory gives $T_{crit} = 1.14$. Similarly, for an almost open-end resonator, $Z = 0.998$, numerical simulations yield a value $T_{crit} = 1.025$ vs $T_{crit} = 1.13$ from linear theory.

In Fig. 11, the onset frequency normalized by ω_{ref} is shown as a function of Z for both approaches, again showing excellent agreement. Also plotted (continuous lines) are the resonant frequencies of a lossless resonator with a temperature discontinuity positioned at $\hat{x} = 0$, for hot temperature T_h set to the critical value $T_{crit}(Z)$ determined by the simulation, for a closed right end in Fig. 11(a) or an open right end in Fig. 11(b). The small frequency increase as T_h increases is barely noticeable on the continuous (nearly horizontal) lines. The load itself has a small effect since the points from both

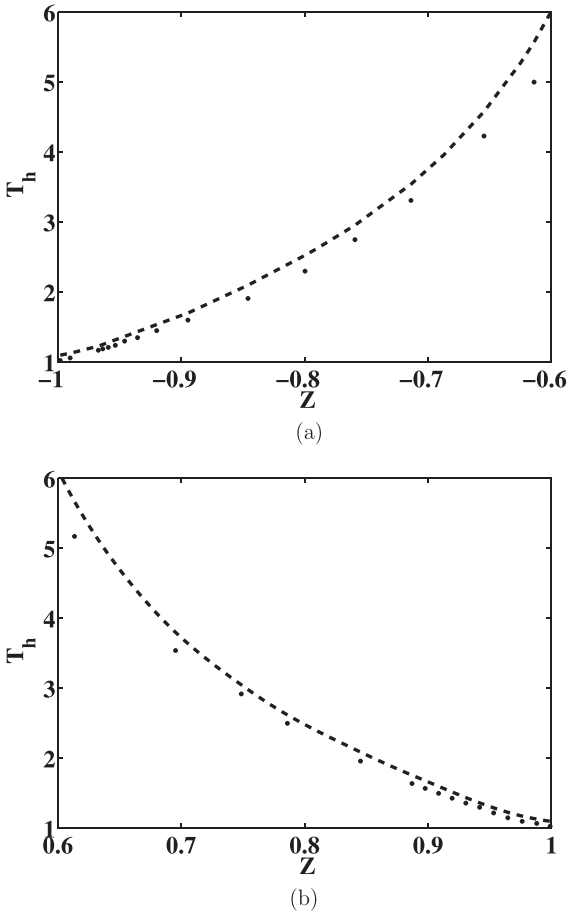

FIG. 10. Stability diagrams in the (Z, T_h) plane showing critical temperature ratios, (•) numerical simulation, (– – –) linear theory. (a) $-1 < Z < -0.6$; (b) $0.6 < Z < 1$.

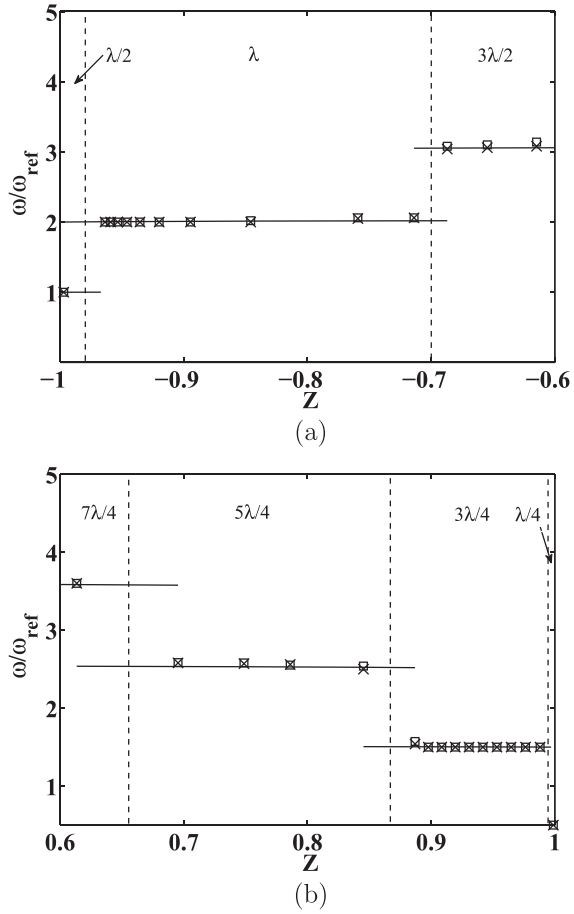

FIG. 11. Frequency of the most unstable modes vs Z. (□) Linear theory, (×) simulations, (a) $-1 < Z < -0.6$; (—) resonant frequencies of a closed-closed lossless resonator with temperature discontinuity at $\hat{x} = 0$ and $T_h = T_{crit}(Z)$ determined by numerical simulations, (– – –) approximate vertical separation between modes (multiples of $\lambda/2$). (b) $0.6 < Z < 1$, (—) resonant frequencies of an open-closed lossless resonator with temperature discontinuity at $\hat{x} = 0$ and $T_h = T_{crit}(Z)$, (– – –) approximate vertical separation between modes (odd multiples of $\lambda/4$).

numerical results and linear theory, and the points on the horizontal lines, which only take into consideration the changes in temperature due to Z, but not the values of Z itself only differ slightly. However, the most visible effect of the load is the switch in the first mode to become unstable (and thus of the onset frequency), represented by vertical lines in Fig. 11. In Fig. 11(a), each vertical range corresponds to a multiple of $\lambda/2$, and in Fig. 11(b), each vertical range corresponds to an odd multiple of $\lambda/4$. As $|Z|$ diminishes, progressively higher frequency modes are the first to become unstable. For the current configuration, $|Z|$ has to be extremely close to 1 for a fundamental mode to be the first to become unstable. The results, both numerical and from linear theory, show that as $|Z|$ decreases, the wavelengths of each mode increase. Thus the position within the resonator maximizing power shifts away from the closed end for each mode. Hence, the optimal position of the active cell for destabilizing any mode ($\lambda_n/8$, $n = 1, 2, 3, ...$) shifts to the right, as was already shown in Fig. 8. Mode n will remain the most unstable until $\lambda_n/8$ of the nth mode shifts too far away from the active cell location and $\lambda_{n+1}/8$ of the next mode becomes more favorably located, resulting in step increases in the frequency of the most unstable mode as shown in Fig. 11.

VI. COMPARISON WITH EXPERIMENTAL RESULTS

In this section, numerical results from the current model are compared with the experimental results of Atchley *et al.*[8] The experimental setup consists of a thermoacoustic cell that is about 6.5 cm long, with a 3.5 cm long stack inserted inside a 1 m long resonator closed at both ends, at about one tenth of its length, 0.87 m from the right end.[26] The inner radius of the resonator is 1.91 cm. Here its cross-sectional area is denoted by A. The only "load" on the engine is dissipation in the gas contained in the resonator (helium under pressure, initially at ambient temperature). The experiments[8] show that at low mean pressure, the most unstable mode is the first harmonic, while at higher pressure, the fundamental mode becomes the most unstable. There is also a region where both modes are unstable.

For comparison, simulations were performed for several mean pressure values. One of the model assumptions is that acoustics is lossless in the resonators so that all dissipation is due to the load, while the experimental results[8] were obtained with no load but with losses. For comparison, the load value in the present model was identified such that the

critical temperature ratio obtained by simulation matches the experiment. For $\tilde{P}_m = 0.44$ MPa, it is found that a dimensionless load value of $f = 45$ in the present model yields a critical heater temperature that coincides with the value obtained experimentally, $\tilde{T}_h = 660$ K. This value corresponds to a dimensional resistive load value $\tilde{R} = fM\tilde{P}_m/(A\tilde{U}_{ref}) = 17.1$ MPa s m^{-3}. The mode that becomes unstable is the fundamental mode, which is also consistent with the experiments. As the heater temperature is increased in the simulation while keeping the load value constant, the first harmonic also becomes unstable when $\tilde{T}_h =$ 821 K, which is again in agreement with the value $\tilde{T}_h \simeq 800$ K found in the experiment.

For $\tilde{P}_m = 0.15$ MPa, a load value $f = 16$ is necessary to reproduce the measured critical heater temperature $\tilde{T}_h = 718$ K, corresponding to dimensional value $\tilde{R} = 2.1$ MPa s m^{-3}. For that mean pressure value, the mode that first becomes unstable is the first harmonic, again in the experiments as well as in the present simulations. The load value that matches the experimental stability diagram of Atchley *et al.*,[8] shown in Fig. 12, is found to depend only on the mean pressure. In the electro-acoustic analogy, the cold resonator in the experimental configuration is a simple right-ended duct filled with helium prone to viscous and thermal dissipation. In the present model, the lossless resonator is connected to a purely resistive load, which is found to mainly play the role of thermal resistance. Indeed the thermal resistance in the experiment may be estimated based on the classical expression,[1] $R_\kappa = 2\gamma\tilde{P}_m/[\omega(\gamma-1)S\delta_\kappa]$, where S is the surface area of the resonator side and δ_κ the thermal boundary-layer thickness. If $\tilde{P}_m = 0.44$ MPa (respectively, 0.15 MPa), $\tilde{T}_{cold} = 293$ K, the thermal resistance is found to be on the order of 40 MPa s m^{-3} (respectively, 5 MPa s m^{-3}). For $\tilde{P}_m = 0.15$ MPa, the angular frequency corresponds to the first harmonic, since this is the mode that destabilizes first. These values are found to be in qualitative agreement with the abovementioned values $\tilde{R}$ obtained numerically, thus lossless acoustics with a loaded end can adequately model a dissipative resonator. Moreover, the value of the load strongly influences the ability of the thermoacoustic engine to start on its own.

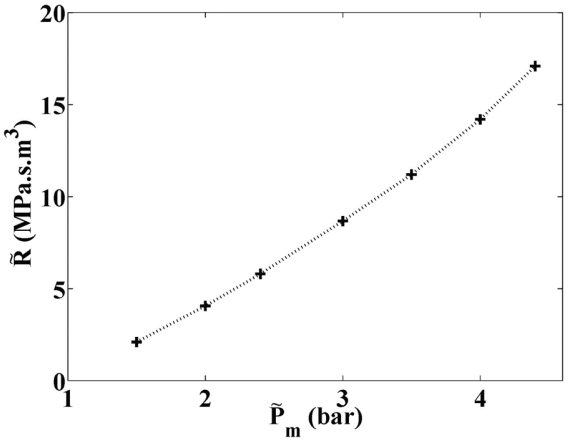

FIG. 12. Dimensional load $\tilde{R}$ yielding the critical temperatures of Atchley *et al.* (Ref. 8) vs mean pressure $\tilde{P}_m$.

VII. CONCLUSION

The dynamics of a thermoacoustic engine was investigated numerically for varying mean pressure and temperature ratio between heater and cooler. The model is based upon a low Mach number assumption, leading to a combination between a numerical solution of the flow and heat transfer in the active cell and an analytical solution of linear acoustics in the resonator. Numerical simulations were carried out on existing thermoacoustic engine configurations,[22,26] showing how a resistive load influences the onset of thermoacoustic oscillations.

The resistive load was varied to encompass a full range of situations from a resonator with a closed end to an open end, hence values range from infinity to zero. To that effect, for a large number of load values, the critical temperature ratio was determined, as well as the angular frequency of the most unstable mode. Results show that for a wide range of intermediate load values, the critical temperature ratio is so high that, in practice, the engine will not start on its own.

The active cell consisted of a stack of parallel plates placed between heat exchangers also made of plates aligned with the stack plates. For this simple configuration, comparison was possible between the numerical results and a theoretical analysis based on Rott's linear theory. Good agreement was found for both the critical temperature ratio and the dominant oscillation frequency. The hybrid numerical model will be most useful whenever a realistic active cell with complex geometry must be dealt with, for example, for misaligned plates or even fully three-dimensional configurations.

The current model of a lossless resonator associated with a resistance placed at the resonator end can be extended to describe real loads to which the thermoacoustic engine is coupled. The approach used also allows one to account for dissipation in a simple experimental resonator with a closed end,[8] provided the resistive load value is adequately chosen. In that case, the load is mainly associated with the thermal resistance of the resonator.

ACKNOWLEDGMENTS

This work was financed by a Ph.D. grant from Université Pierre et Marie Curie. Support of the Natural Sciences and Engineering Research Council of Canada is gratefully acknowledged (L.B.).

[1]G. W. Swift, "Thermoacoustic engines," J. Acoust. Soc. Am. **84**, 1145–1180 (1988).
[2]R. Radebaugh, "A review of pulse tube refrigeration," Adv. Cryog. Eng. **35B**, 1191–1205 (1990).
[3]A. Migliori and G. W. Swift, "Liquid sodium thermoacoustic engine," Appl. Phys. Lett. **53**, 355–357 (1988).
[4]C. Jensen and R. Raspet, "Thermoacoustic power conversion using piezoelectric transducer," J. Acoust. Soc. Am. **128**(1), 98–103 (2010).
[5]N. Rott, "Damped and thermally driven acoustic oscillations in wide and narrow tubes," Z. Angew. Math. Phys. **20**, 230–243 (1969).
[6]W. P. Arnott, H. E. Bass, and R. Raspet, "General formulation of thermoacoustics for stacks having arbitrarily shaped pore cross section," J. Acoust. Soc. Am. **90**, 3228–3237 (1991).
[7]B. Ward, J. Clark, and G. W. Swift, "Design environment for low-amplitude thermoacoustic energy conversion (DeltaEC) user's guide (version 6.2)," Los Alamos National Laboratory (2008).

[8]A. A. Atchley and F. M. Kuo, "Stability curves for a thermoacoustic prime mover," J. Acoust. Soc. Am. **95**, 1401–1404 (1994).
[9]W. P. Arnott, J. R. Belcher, R. Raspet, and H. E. Bass, "Stability analysis of a helium-filled thermoacoustic engine," J. Acoust. Soc. Am. **96**, 370–375 (1994).
[10]T. Yazaki, A. Iwata, T. Maekawa, and T. Tominaga, "Travelling wave thermoacoustic engine in a looped tubeT," Phys. Rev. Lett. **81**, 3128–3131 (1998).
[11]N. Sugimoto, "Thermoacoustic-wave equations for gas in a channel and a tube subject to temperature gradient," J. Fluid Mech. **658**, 89–116 (2010).
[12]H. Hyodo and N. Sugimoto, "Stability analysis for the onset of thermoacoustic oscillations in a gas-filled looped tube," J. Fluid Mech. **741**, 585–618 (2014).
[13]A. T. A. M. de Waele, "Basic treatement of onset conditions and transient effects in thermoacoustic Stirling engines," J. Sound Vib. **325**, 974–988 (2009).
[14]M. Guedra, G. Penelet, P. Lotton, and J.-P. Dalmont, "Theoretical prediction of the onset of thermoacoustic instability from the experimental transfer matrix of a thermoacoustic core," J. Acoust. Soc. Am. **130**, 145–152 (2011).
[15]M. Guedra, G. Penelet, and P. Lotton, "Experimental and theoretical study of the dynamics of self-sustained oscillations in a standing wave thermoacoustic engine," J. Appl. Phys. **115**, 024504 (2014).
[16]J. R. Olson and G. W. Swift, "A loaded thermoacoustic engine," J. Acoust. Soc. Am. **98**, 2690–2693 (1995).
[17]R. Bao, G. B. Chen, K. Tang, Z. Z. Jia, and W. H. Cao, "Effect of RC load on performance of thermoacoustic engine," Cryogenics **46**, 666–671 (2006).
[18]P. Duthil, D. Baltean Carlès, A. Bétrancourt, M.-X. François, Z. B. Yu, and J. P. Thermeau, "Experiments and valve modeling in thermoacoustic device," Adv. Cryog. Eng. **51**(B), 1095–1102 (2006).
[19]H. Hatori, T. Biwa, and T. Yazaki, "How to build a loaded thermoacoustic engine," J. Appl. Phys. **111**, 074905 (2012).
[20]G. Y. Yu, E. C. Luo, W. Dai, and J. Y. Hu, "Study of nonlinear processes of a large experimental thermoacoustic-Stirling heat engine by using computational fluid dynamics," J. Appl. Phys. **102**, 074901 (2007).
[21]J. A. Lycklama à Nijeholt, M. E. H. Tijani, and S. Spoelstra, "Simulation of a traveling-wave thermoacoustic engine using computational fluid dynamics," J. Acoust. Soc. Am. **118**, 2265–2270 (2005).
[22]O. Hireche, C. Weisman, D. Baltean-Carlès, P. Le Quéré, and L. Bauwens, "Low Mach number analysis of idealized thermoacoustic engines with numerical solution," J. Acoust. Soc. Am. **128**(6), 3438–3448 (2010).
[23]R. Raspet, J. Bruster, and H. E. Bass, "New approximation method for thermoacoustic calculations," J. Acoust. Soc. Am. **103**(5), 2395–2402 (1998).
[24]N. Rott, "Thermoacoustics," Adv. Appl. Mech. **20**, 135–243 (1980).
[25]G. W. Swift, *A Unifying Perspective for Some Engines and Refrigerators* (Acoustical Society of America, Melville, NY, 2002), p. 90, Eq. 4.70.
[26]A. A. Atchley, H. E. Bass, T. J. Hofler, and H. T. Lin, "Study of a thermoacoustic prime mover below onset of self-oscillation," J. Acoust. Soc. Am. **91**, 734–743 (1992).

.

I. Reyt, V. Daru, H. Bailliet, S. Moreau, J.-C. Valière, D. Baltean-Carlès, C. Weisman, “Fast acoustic streaming in standing waves : Generation of an additional outer streaming cell”, J. Acoust. Soc. Am. 134 (3), 1791-1801, 2013.

Fast acoustic streaming in standing waves: Generation of an additional outer streaming cell

Ida Reyt
LIMSI-CNRS UPR 3251, Bât. 508 rue John Von Neumann, Campus Univ. Paris Sud, 91403 Orsay, France

Virginie Daru[a)]
Arts et Métiers ParisTech Lab. DynFluid, 151 bd de l'hôpital, 75013 Paris, France

Hélène Bailliet, Solène Moreau,[b)] and Jean-Christophe Valière
Institut Pprime, CNRS - Université de Poitiers–ENSMA, Département Fluides–Thermique–Combustion, ENSIP, 6 rue Marcel Doré Bât. B17–BP 633, 86022 Poitiers Cedex, France

Diana Baltean-Carlès[a)] and Catherine Weisman[a),c)]
UPMC Paris06 UFR 919, 4 Place Jussieu, 75252 Paris Cedex 05, France

(Received 18 April 2013; revised 11 July 2013; accepted 22 July 2013)

Rayleigh streaming in a cylindrical acoustic standing waveguide is studied both experimentally and numerically for nonlinear Reynolds numbers from 1 to 30 [$\mathrm{Re}_{NL} = (U_0/c_0)^2(R/\delta_\nu)^2$, with U_0 the acoustic velocity amplitude at the velocity antinode, c_0 the speed of sound, R the tube radius, and δ_ν the acoustic boundary layer thickness]. Streaming velocity is measured by means of laser Doppler velocimetry in a cylindrical resonator filled with air at atmospheric pressure at high intensity sound levels. The compressible Navier-Stokes equations are solved numerically with high resolution finite difference schemes. The resonator is excited by shaking it along the axis at imposed frequency. Results of measurements and of numerical calculation are compared with results given in the literature and with each other. As expected, the axial streaming velocity measured and calculated agrees reasonably well with the slow streaming theory for small Re_{NL} but deviates significantly from such predictions for fast streaming ($\mathrm{Re}_{NL} > 1$). Both experimental and numerical results show that when Re_{NL} is increased, the center of the outer streaming cells are pushed toward the acoustic velocity nodes until counter-rotating additional vortices are generated near the acoustic velocity antinodes. © *2013 Acoustical Society of America*. [http://dx.doi.org/10.1121/1.4817888]

PACS number(s): 43.25.Nm, 43.25.Gf [TB] Pages: 1791–1801

I. INTRODUCTION

Rayleigh streaming refers to the second order mean velocity that is generated by effects related with the interaction of a solid surface and an acoustic wave in a fluid. In thermoacoustic devices, acoustic streaming results in convected heat flow that can reduce the efficiency of the devices. Because the power density of a thermoacoustic device is roughly proportional to the square of the acoustic pressure amplitude, the study of high acoustic amplitude phenomena is important to the field of thermoacoustics. A better understanding and characterization of the corresponding so-called "fast" Rayleigh streaming is therefore useful to assess its impact on the efficiency of thermoacoustic devices.

The reference solution derived by Rayleigh[1] concerns streaming generated by a standing wave between two infinite, widely separated plates. Together with further studies by Nyborg[2] and Westervelt,[3] this work yielded the so-called Rayleigh-Nyborg-Westervelt (RNW) streaming theory. For a better application to thermoacoustics, this theoretical description has evolved in order to refine thermal effect description and to remove the restrictions to wide channels and to slow streaming. Concerning the first two points, during the last decades, thermoacoustic applications have motivated several theoretical works to take into account thermal effects[4,5] and/or to remove the restriction to large channels.[6,7] However, all these theoretical developments were restricted to slow streaming where fluid inertia is neglected. The dimensionless number characterizing the inertial effects with respect to viscous effects is the nonlinear Reynolds number Re_{NL} defined by Menguy and Gilbert.[8] For slow streaming the nonlinear Reynolds number is such that $\mathrm{Re}_{NL} \ll 1$. The influence of fluid inertia was studied only by Menguy and Gilbert and for Re_{NL} up to only about two; using a perturbation method with asymptotic expansions followed by time-averaging, they developed boundary layer streaming equations, matched with nonlinear streaming equations in the main acoustic field, thus demonstrating a noticeable distortion of the streaming velocity field.

Previous simulations of acoustic streaming in the linear regime were conducted by solving the flow dynamics between two plates inside a thermoacoustic refrigerator.[9] More recently, Aktas and Farouk[10] performed numerical simulations in the linear and nonlinear streaming regimes, solving the full compressible Navier-Stokes equations in the plane case with a flux corrected transport scheme. The

[a)]Also at: LIMSI-CNRS UPR 3251, 91403 Orsay, France.
[b)]Current address: Laboratoire Roberval CNRS 6253, Université de Technologie de Compiègne BP 20529, 60205 Compiègne Cedex, France.
[c)]Author to whom correspondence should be addressed. Electronic mail: weisman@limsi.fr

acoustic excitation was provided by a moving wall. Their results show a distortion of the streaming field and the existence of multiple streaming cells for small values of Re_{NL}, even for values less than one. In their analysis, the authors correlate the existence of the nonlinear streaming regime with the values of the aspect ratio of the waveguide and with a different streaming Reynolds number [$\mathrm{Re}_s = U_0^2/(\nu\omega)$, ω being the angular frequency]. When their results are analyzed as a function of Re_{NL}, the tendencies depicted are in contradiction with experiments.[11,12] One of the goals of the present paper is to present direct numerical simulations of the Navier-Stokes equations in the cylindrical case using a recently developed high resolution numerical scheme[13] tested successfully in several cases (including acoustics and streaming[14,15]). In the present simulations, the acoustic wave is excited by shaking the entire resonator and there are no restrictions on the value of the Re_{NL}.

With respect to experimental studies, thanks to improving techniques in fluid dynamics, measurements of the streaming in a standing wave guide have been performed recently.[11,16–19] Experimental works by Sharpe, Greated, and collaborators[16] and by Thompson and Atchley[19] first allowed quantitative study of streaming velocity in the core region on the basis of particle image velocimetry (PIV) or laser Doppler velocimetry (LDV) measurements. Moreau *et al.*[11] first performed LDV measurements of streaming in both the core and the near wall region to characterize inner streaming vortices. Their measurements were performed for Re_{NL} up to 140 but they mainly focused on inner streaming cells evolution. In their experimental study, Thompson and Atchley[19] considered streaming for Re_{NL} up to 20 and found that the streaming fields is distorted for high nonlinear Reynolds number in correlation with the increasing temperature gradient along a streaming cell. Nabavi *et al.*[12] analyzed streaming in a square channel on the basis of PIV measurements; they found that for Re_{NL} up to 25, streaming cells are regular and correspond to "classical" streaming flow, whereas when Re_{NL} exceeds 25, streaming deforms to irregular and complex shaped patterns. Another goal of the present work is to present results of measurements of the streaming velocity field generated by an acoustic standing wave in a cylindrical resonator by means of LDV from low to high acoustic amplitudes (up to Re_{NL} greater than 25).

In the present study, numerical and experimental results are successfully compared with available theoretical expectations in the linear regime. For this purpose, a slow streaming analytical model that has been developed previously[6] for the calculation of Rayleigh streaming in a cylindrical waveguide is used. Then the analysis of the nonlinear regime is conducted for the first time with a coupled numerical/experimental approach on a cylindrical geometry, and the results are confronted. Both simulations and experiments show that streaming at high Re_{NL} is associated with additional outer streaming cells appearing at a critical value of this number of about $\mathrm{Re}_{NL} = 30$.

Section II presents the different methods for the calculation of streaming that are used or referred to in this paper (direct numerical method, work by Bailliet *et al.*,[6] and work by Menguy and Gilbert[8]). The dimensionless numbers used to describe the problem of Rayleigh streaming in a standing wave guide are presented as it is necessary to consider the respective values of these numbers in order to validate the comparison between numerical and experimental results. In Sec. III, experimental setup and procedure are presented. Section IV presents the numerical method used to calculate streaming velocity. Finally in Sec. V, these numerical and experimental results are compared with each other and with the available literature.

II. FUNDAMENTAL EQUATIONS AND NONDIMENSIONAL ANALYSIS

All the methods used to calculate the streaming flow in this paper are based on the fundamental equations that describe an acoustic wave propagation in the laminar regime along the z axis, in a cylindrical tube of radius R filled with air at atmospheric pressure. The ratio of the wavelength to the transverse dimension is supposed to be large so that the wave is plane. Air is considered as a Newtonian compressible fluid and there is no mean flow apart from acoustic streaming. Gravity is neglected. Neglecting the bulk viscosity in comparison with the shear viscosity, these fundamental equations (Navier-Stokes equations) that describe the fluid motion are written as

$$\begin{cases} \dfrac{\partial \rho}{\partial t} + \nabla \cdot (\rho \mathbf{u}) = 0 \\ \dfrac{\partial (\rho \mathbf{u})}{\partial t} + \nabla \cdot (\rho \mathbf{u} \otimes \mathbf{u}) + \nabla p = \nabla \cdot (\bar{\bar{\tau}}) \\ \dfrac{\partial (\rho E)}{\partial t} + \nabla \cdot (\rho E \mathbf{u} + p\mathbf{u}) = \nabla \cdot (k \nabla T) + \nabla \cdot (\bar{\bar{\tau}}\mathbf{u}), \end{cases} \tag{1}$$

where ρ is the density, p is the pressure, $\mathbf{u}$ is the flow velocity vector, $E = e + (1/2)\mathbf{u} \cdot \mathbf{u}$ is the total energy, with $e = p/(\gamma - 1)\rho$ the internal energy, γ the specific heat ratio, $\bar{\bar{\tau}} = -(2/3)\mu(\nabla \cdot \mathbf{u})\bar{\bar{I}} + 2\mu\bar{\bar{D}}$ the viscous stress tensor, with $\bar{\bar{I}}$ the identity tensor, $\bar{\bar{D}} = (1/2)(\nabla \mathbf{u} + \nabla \mathbf{u}^T)$ the strain rate tensor, μ the dynamic viscosity, k the thermal conductivity. The gas is considered as a perfect gas obeying the state law $p = r_g \rho T$, where T is the temperature and r_g is the constant of the perfect gas (air in the present case).

A. Nondimensional analysis

In the previous equations, there are 6 unknown physical variables, ρ, $\mathbf{u}$ (three components), p and T [the internal energy e can be replaced by $(c_p/\gamma)T$, c_p being the specific heat capacity at constant pressure] and six equations. The problem is written in a dimensionless form, using standard fluid mechanics scalings

$$\hat{\nabla} = \frac{\nabla}{L_0}, \quad \hat{t} = \frac{t}{t_0}, \quad \hat{\mathbf{u}} = \frac{\mathbf{u}}{U_0}, \quad \hat{p} = \frac{p}{p_0}, \quad \hat{\rho} = \frac{\rho}{\rho_0},$$
$$\hat{T} = \frac{T}{T_0}, \quad \hat{\mu} = \frac{\mu}{\mu_0}, \quad \hat{k} = \frac{k}{k_0}, \tag{2}$$

where L_0, t_0, U_0 are reference scales for length, time and velocity (based on the acoustic propagation), and p_0, ρ_0, T_0, μ_0,

k_0 are scales for pressure, density, temperature, dynamic viscosity and conductivity (based on fluid properties at rest). In the context of acoustics, the adiabatic speed of sound is defined as $c_0 = \sqrt{(\partial p/\partial \rho)_{s,0}}$, also written as $c_0 = \sqrt{\gamma(p_0/\rho_0)}$ using the first-order Taylor expansion of pressure. The characteristic acoustic time and length scales are given by $t_0 = 1/\omega$, $L_0 = c_0/\omega$, where ω is the fundamental acoustic angular frequency. U_0 is a reference value of the acoustic velocity, for example the maximum amplitude of the fundamental component of the wave. With these reference scales, three independent dimensionless numbers are defined by rewriting the set of Eq. (1): the acoustic Mach number $M = U_0/c_0$, the acoustic Reynolds number $\mathrm{Re} = \rho_0 c_0^2/\mu_0\omega$, and the Prandtl number $\mathrm{Pr} = \mu_0 c_p/k_0$.

Equation (1) in dimensionless form is indeed

$$\begin{cases} \dfrac{\partial \hat{\rho}}{\partial \hat{t}} + M\hat{\nabla}\cdot(\hat{\rho}\hat{\mathbf{u}}) = 0 \\ \dfrac{\partial(\hat{\rho}\hat{\mathbf{u}})}{\partial \hat{t}} + M\hat{\nabla}\cdot(\hat{\rho}\hat{\mathbf{u}}\otimes\hat{\mathbf{u}}) + \dfrac{1}{\gamma M}\hat{\nabla}\hat{p} = \dfrac{1}{\mathrm{Re}}\hat{\nabla}\cdot(\hat{\bar{\tau}}) \\ \dfrac{1}{\gamma}\dfrac{\partial(\hat{\rho}\hat{T})}{\partial \hat{t}} + M^2(\gamma-1)\dfrac{\partial\left(\hat{\rho}\dfrac{1}{2}|\hat{\mathbf{u}}|^2\right)}{\partial \hat{t}} + \dfrac{M}{\gamma}\hat{\nabla}\cdot(\hat{\rho}\hat{T}\hat{\mathbf{u}}) + M^3(\gamma-1)\hat{\nabla}\cdot\left(\hat{\rho}\hat{\mathbf{u}}\dfrac{1}{2}|\hat{\mathbf{u}}|^2\right) + \dfrac{\gamma-1}{\gamma}M\hat{\nabla}\cdot(\hat{\rho}\hat{\mathbf{u}}) \\ \quad = \dfrac{1}{\mathrm{RePr}}\hat{\nabla}\cdot(\hat{k}\hat{\nabla}\hat{T}) + \dfrac{1}{\mathrm{Re}}M^2(\gamma-1)\hat{\nabla}\cdot(\hat{\bar{\tau}}\hat{\mathbf{u}}). \end{cases} \tag{3}$$

The working fluid being air, the Prandtl number is fixed, of order 1. This leaves out two nondimensional numbers to monitor wave propagation in the tube (M and Re). In order to characterize the streaming flow associated with a standing wave, the ∇ operator should be separated into an axial and a radial part, that is, a separate reference length scale for the radial direction has to be introduced, inducing that a supplementary nondimensional number is needed. Menguy and Gilbert[8] showed that this additional required number is the Shear number, defined as $\mathrm{Sh} = \delta_\nu/R$, $\delta_\nu = \sqrt{2\nu/\omega}$ being the acoustic boundary layer thickness in the near wall region (with $\nu = \mu/\rho_0$ the kinematic viscosity).

Here, the acoustic wave amplitude ranges from linear ($M \ll 1$) to weakly nonlinear. The Reynolds number compares inertial effects and viscous effects over the wavelength and is large with respect to 1 for the present range of audible frequencies. Then, the third dimensionless number compares the boundary layer thickness to the tube radius. The hypothesis $\mathrm{Sh} \ll 1$ corresponds to large tubes, which is the case in all the studies we deal with in this paper. Finally when working with air, the same flow behavior is expected for studies where $M \ll 1$, $\mathrm{Re} \gg 1$ and $\mathrm{Sh} \ll 1$. This asymptotic similarity will be considered as valid for the numerical and experimental flows under study in the following. In order to be able to compare our experimental and numerical results to a reference, in the following section, two available models for streaming flow are briefly presented: a linear model developed by Bailliet *et al.*[6] (used for quantitative comparison with direct numerical simulations and experiments in the slow streaming regime) and a nonlinear model developed by Menguy and Gilbert[8] (used for the description of the evolution of the streaming flow for moderate streaming regime). The latter shows that when dealing with streaming flow, an additional dimensionless number has to be considered, as discussed in the following.

B. Slow streaming

In the literature, there are several analytical models for slow streaming.[2,3,7] In this paper, the model developed by Bailliet *et al.*[6] is used. This model is based on the fundamental equations presented above. Additional assumptions allow us to obtain an expression of the second order time averaged axial velocity as function of the first order acoustic quantities. The streaming is supposed to be slow so that the effect of inertia on the streaming motion is neglected by comparison with viscous effects. The solid is supposed to have an infinite heat capacity. Under these assumptions, the method of successive approximation is applied, the first order quantities having a $e^{-i\omega t}$ dependence. Through time averaging a combination of the continuity equation and of the axial component of the Navier-Stokes equations written to the second order, the following equation is obtained:

$$\frac{1}{R^2}\mu_0\nabla_\eta^2\langle u_2\rangle = \partial_z p_2 + \partial_z(\rho_0\langle u_{1z}^2\rangle) + \frac{1}{R}\nabla_\eta(\rho_0\langle u_{1z}u_{1\eta}\rangle) - \frac{1}{R^2}\nabla_\eta(\langle\mu_1\nabla_\eta u_{1z}\rangle), \tag{4}$$

where $\langle - \rangle$ denotes the time average and $\eta = r/R$, with r the radial coordinate. An expression for the second order pressure gradient $\partial_z p_2$ is obtained by writing that, in a closed resonator, there is no net mass flow across the section, i.e., the second order time average mass flow rate across the cross section must be zero. Successive integration of the expression obtained yields the second order pressure gradient as a function of the first order acoustic quantities. In turn,

successive integration of Eq. (4) yields the axial streaming velocity [see formula (16) from Bailliet *et al.*[6]]. In the case of widely spaced parallel plates, this velocity is equal to the one obtained by the RNW theory, but the calculation is valid also for narrow guides (that is in the near wall region of any guide) and it takes into account the dependence of viscosity on temperature. This calculation is also valid in the presence of a temperature gradient (not set in the present study). This analytical study will be used as a reference for our experimental and numerical results. However, high acoustic amplitudes will be considered here and therefore the slow streaming assumption is expected to be restrictive, and the effect of streaming inertia should be analyzed.

C. Effect of inertia on streaming

The only available theoretical study that is not restricted to slow streaming is the one by Menguy and Gilbert.[8] By writing the fundamental equations up to the third order in the main acoustic field followed by time averaging over the acoustic period, Menguy and Gilbert derived the governing equations for the streaming field in the boundary layer and in the main central part of the tube. Under the above presented assumptions ($M \ll 1$, $\mathrm{Re} \gg 1$, $\mathrm{Sh} \ll 1$), an asymptotic analysis can be performed, allowing to derive the fluid behavior at the first and second order. A time averaging over the acoustic period yields equations for streaming flow both inside and outside the acoustic viscous/thermal boundary layer. Under the previous hypotheses on M, Re, and Sh numbers, streaming equations inside the boundary layer are always linear. Outside the boundary layer, streaming equations can be linear or nonlinear depending on the ratio between inertia and viscous terms. Menguy and Gilbert[8] showed that in the central part of the tube, the equation that governs the streaming velocity $\hat{u}_s$ has a unique nonlinear term

$$\frac{\mathrm{Sh}^2}{M^2}\frac{1}{\hat{r}}\frac{\partial}{\partial \hat{r}}\left(\hat{r}\frac{\partial \hat{u}_s}{\partial \hat{r}}\right).$$

This clearly shows that the outer streaming nonlinearity depends only upon one dimensionless number

$$\mathrm{Re}_{NL} = \frac{M^2}{\mathrm{Sh}^2}$$

called the nonlinear Reynolds number, which compares inertia and viscosity. For $\mathrm{Re}_{NL} = O(1)$ the classical streaming models are no longer valid and the nonlinear effects of inertia must be taken into account. The latter cause distortion of the streaming velocity field in the tube and Menguy and Gilbert[8] discuss the distortion of the toroidal vortex patterns. When $\mathrm{Re}_{NL} \ll 1$, inertia terms are negligible with respect to viscous terms and the streaming equation reduces to the linear model of streaming (see Sec. II B).

Finally, four dimensionless numbers are to be considered when dealing with Rayleigh streaming. At fixed Pr, for asymptotic similarity when $M \ll 1$, $\mathrm{Sh} \ll 1$ and $\mathrm{Re} \gg 1$, the nonlinear Reynolds number is expected to be the driving parameter for acoustic streaming. The behavior of the streaming flow will then be analyzed and discussed upon the values of the nonlinear Reynolds number.

III. EXPERIMENTAL APPARATUS AND PROCEDURE

The setup used to observe the phenomenon of acoustic streaming is shown in Fig. 1 and consists in a cylindrical tube connected at each end to a loudspeaker via connecting tubes designed to avoid separation effect related to the singularities in change of section. The cylindrical part of the waveguide has inner radius $R = 19.5$ mm and the waveguide is filled with atmospheric air. The total length of the wave guide is $L_{\mathrm{exp}} = 2.13$ m and the system is tuned on two distinct frequencies corresponding to two different resonant modes: the first mode corresponding to $L_{\mathrm{exp}} = \lambda/2$ and the third mode corresponding to $L_{\mathrm{exp}} = 3\lambda/2$, λ being the wavelength of the fundamental mode.

In the following, results will be presented for acoustic streaming across one or two cells and whatever the working frequency, the position along the guide axis will be given by the axial coordinate z, with $z = \pm\lambda/4$ corresponding to two adjacent streaming cells.

The acoustic wave is generated by two loudspeakers driven by a wave generator whose frequency and amplitude are controlled. Wood smoke is used as seeding particles in order to perform LDV measurements. The single component LDV system is a Dantec Dynamic model 2580, the probe is mounted on a three-axis positioning system. The argon krypton laser has an optical wavelength of 514.5 μm and a power of 25 W. The parameters of LDV system are adjusted for sound measurements[20] and the axial streaming velocity is measured following the work of Valière *et al.*[21] along the centerline of the guide. The LDV measurements yield the Eulerian particle velocity. In agreement with Moreau *et al.*,[11] measurements were performed more than 26 min after the acoustic field is switched on and are stable after this time. Also, following this latter reference, in order to reach convergence in the measured streaming velocity, we choose to acquire either 70 000 points or to stop acquisition after 10s. This gives a good compromise between a sufficient number of measured tracer particles per point for a precise

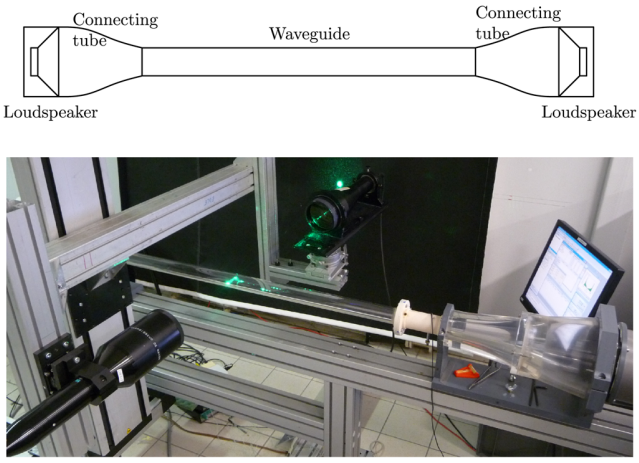

FIG. 1. (Color online) Photo and diagram of the experimental apparatus.

streaming velocity measurement and a small measuring time resulting from a correct seeding.

In order to get as close as possible to the isothermal boundary conditions used in the numerical calculation and because it was found in the literature that temperature gradients along the guide walls greatly influence Rayleigh streaming,[19] the resonator wall is forced to correspond to an isothermal boundary condition with the help of fans used to insure that the wall temperature is equal to the room temperature. The temperature is measured along one streaming cell using seven thermocouples with a resolution of about 0.05 °C. These thermocouples are placed at the outer wall of the resonator and are insulated from the external environment by a polystyrene covering. Using fans to force heat transfer from the guide to the environment yields a residual temperature difference of 0.3 °C between the acoustic velocity node and antinode at $\mathrm{Re}_{NL} = 31.8$. This temperature difference would be equal to 3.1 °C if no fans were used.

IV. NUMERICAL APPROACH

A. Numerical method

In order to initiate an acoustic standing wave in the cylindrical tube of length L, it is shaken in the longitudinal direction z, so that an harmonic velocity law is imposed, $\vec{V}(t) = (0, V(t))^T$, with $V(t) = z_p\omega\cos(\omega t)$, z_p being the amplitude of the tube displacement. The flow can be modeled by the compressible Navier-Stokes Eq. (1), expressed in the moving frame attached to the tube, so that a forcing source term h^s is added to the system of Eq. (1). The model can be written in vector form

$$\frac{\partial w}{\partial t} + \frac{1}{r}\frac{\partial}{\partial r}[r(f - f^v)] + \frac{\partial}{\partial z}(g - g^v) = h + h^s, \tag{5}$$

where w is the vector of conservative variables $(\rho, \rho u, \rho v, \rho E)^T$, f and g are the inviscid fluxes $f = (\rho u, \rho u^2 + p, \rho uv, \rho Eu + pu)^T$ and $g = (\rho v, \rho uv, \rho v^2 + p, \rho Ev + pv)^T$, f^v, and g^v being the viscous fluxes $f^v = [0, \tau_{rr}, \tau_{rz}, \quad k(\partial T/\partial r) + u\tau_{rr} + v\tau_{rz}]^{\mathrm{T}}$, $\quad g^v = [0, \tau_{rz}, \tau_{zz}, k(\partial T/\partial z) + u\tau_{rz} + v\tau_{zz}]^T$. The source terms read $h = [0, -(\tau_{\theta\theta}/r) + (p/r), 0, 0]$, $h^s = [0, 0, -\rho(dV/dt), -\rho u(dV/dt)]^T$.

The model is numerically solved by using high order finite difference schemes, developed by Daru and Tenaud.[13] An upwind scheme, third order accurate in time and space, is used for convective terms, and a centered scheme, second order, is used for diffusion terms. Traveling shock waves are present in the flow for high acoustic levels, which generate numerical oscillations. However they are of weak intensity and produce very small oscillations that do not spoil the solution. Thus it was not necessary to add a costly shock capturing procedure.

The numerical procedure is briefly described thereafter. Denoting by $w^n_{i,j}$ the numerical solution at time $t = n\delta t$ and grid point $(r, z) = (i\delta r, j\delta z)$, with δt and δr, δz the time and space discretization steps respectively, the following Strang splitting procedure is used to obtain a second order accuracy every two time steps:

$$w^{n+2}_{i,j} = L_{\delta r}L_{\delta z}L_{\delta z}L_{\delta r}w^n_{ij}, \tag{6}$$

where $L_{\delta r}$ (resp. $L_{\delta z}$) is a discrete approximation of $L_r(w) = w + \delta t[-(1/r)(rf)_r + (1/r)(rf^v)_r + h + h^s]$ [resp. $L_z(w) = w + \delta t\ (-g_z + g^v_z)$]. The 1D operators being similar in both directions, only the r operator is described. The scheme is implemented as a correction to the second order MacCormack scheme. It consists of three steps, as follows:

$$\begin{aligned}
w^*_{i,j} &= w^n_{i,j} - \frac{\delta t}{r_{i,j}\delta r}[r_{i+(1/2),j}(f_{i+1,j} - f^v_{i+(1/2),j}) - r_{i-(1/2),j}(f_{i,j} - f^v_{i-(1/2),j})]^n + \delta t(h + h^s)^n_{i,j}\\
w^{**}_{i,j} &= w^*_{i,j} - \frac{\delta t}{r_{i,j}\delta r}[r_{i+(1/2),j}(f_{i,j} - f^v_{i+(1/2),j}) - r_{i-(1/2),j}(f_{i-1,j} - f^v_{i-(1/2),j})]^*\\
w^{n+1}_{i,j} &= \frac{1}{2}(w^n_{i,j} + w^{**}_{i,j}) + \frac{1}{r_{i,j}}(r_{i+(1/2),j}C^r_{i+(1/2),j} - r_{i-(1/2),j}C^r_{i-(1/2),j}).
\end{aligned} \tag{7}$$

In (7), the subscripts $(i \pm 1/2, j)$ denote a value at the interface between cells (i, j) and $(i \pm 1, j)$. The viscous fluxes are discretized at each interface using centered second order finite differences. The corrective terms $C^r_{i\pm(1/2),j}$ provide the third order accuracy and upwinding for the inviscid terms. Details on the model can be found in Daru *et al.*[14,15,22]

The physical boundary conditions employed in the moving frame are: no slip on the wall, symmetry at the ends of the tube, and isothermal walls.

The acoustic streaming is generated by the interaction of the imposed plane standing wave and the tube wall. Resonant conditions are imposed, for which $L = \lambda/2$, λ being the wavelength calculated for a dissipative gas. The boundary layer δ_ν is of small thickness and must be correctly resolved by the discretization mesh. After several trials, it was found that a value of five points per boundary layer thickness is sufficient for reasonable accuracy of the simulations. All results presented below are thus obtained using a Cartesian mesh of rectangular cells of constant size δr and δz, composed of 500 points in the axial direction z, and of $5 \times R/\delta_\nu$ points in the radial direction.

The flow being assumed to be axisymmetric (at least in the range of parameters treated), only the region $0 \le r \le R$ and $0 \le z \le L$ was considered. Also, the scheme being fully

explicit, the time step δt is fixed such as to satisfy the stability condition of the scheme. In all cases considered here, the time step limitation is acoustic, it reads $\delta t \leq \frac{1}{2}\delta r/c_0$. Taking $\delta t = \frac{1}{2}\delta r/c_0$ and $\delta r = \delta_\nu/5$, this results in a number of time steps N_T per period of oscillation proportional to $\sqrt{L}$, $N_T = 1/(f\delta t) = 10\sqrt{(2\pi c_0)/\nu}\sqrt{L}$.

Because the LDV measurements yield the Eulerian particle velocity, the numerical results are based on the Eulerian time-average of fluid velocity. The numerical streaming velocity is obtained by calculating a simple mean value of the particle velocity over the discretized acoustic period, thus a time average made with respect to the fixed measuring position, for each mesh point.

B. Simulation parameters

A cylindrical tube is considered, initially filled with air at standard thermodynamic conditions, $p_0 = 101\,325$ Pa, $\rho_0 = 1.2$ kgm^{-3}, $T_0 = 294.15$ K. The thermo-physical properties of air are $\mu_0 = 1.795 \times 10^{-5}$ kgm^{-1} s^{-1} and $k_0 = 0.025$ Wm^{-1} K^{-1}. Viscosity is expressed as a power law of temperature, $\mu(T) = \mu_0(T/T_0)^{0.77}$. Also for air, $\gamma = 1.4$ and $r_g = 287.06$ Jkg^{-1} K^{-1}. The Prandtl number Pr is equal to 0.726. This results in an initial speed of sound $c_0 = 343.82$ ms^{-1}.

In the experimental case presented in Sec. III, the half-wavelength is about 0.7 m long, which would yield a limiting time step corresponding to $N_T \approx 25\,000\sqrt{L}$, that is 21 000 iterations per period. Since transients of several hundreds of periods may be needed in order to reach stabilized streaming flow, several millions of iterations are necessary for each simulation. Considering these numerical constraints, a high-frequency wave is chosen for numerical calculations, with $f = 20\,000$ Hz. Taking into account the viscous dissipation, this corresponds to a shorter wave guide with $L = 8.396$ mm. The resulting boundary layer thickness is $\delta_\nu = 1.54 \times 10^{-5}$ m. For computational ease, the Shear number was fixed in the numerical simulations to be $1/40$.

The time step $\delta t = 8 \times 10^{-9}$s is chosen in order to satisfy the numerical stability condition, corresponding to 6250 time iterations per period. The acoustic velocity produced in the wave guide depends on the imposed amplitude of the horizontal displacement z_p. It varies approximately linearly with z_p, for a given ratio R/δ_ν. Therefore it is possible via the only choice of z_p to approximately set the value of the desired nonlinear Reynolds number Re_{NL}, so that to approximately fit the ones obtained in experimental configurations.

V. RESULTS AND DISCUSSION

As seen in Secs. III and IV, several differences exist between experimental and simulated configurations. As discussed in Sec. II these differences should not be associated with different behaviors of acoustic streaming if the nonlinear Reynolds number Re_{NL} is the same, and if the other relevant dimensionless numbers Sh, Re, and M are of the same order of magnitude. The acoustic amplitude of the fundamental mode at the velocity antinode $z = 0$ is chosen as the velocity reference U_0.

Table I summarizes then the values of these dimensionless parameters for both the experimental and numerical configurations together with the ones for several studies of the literature[8,10,12,19] that are used for comparison with the present study.

As shown by Table I and as stated in the previous Sec. IV, all numerical calculations were performed for a given frequency in air at atmospheric pressure, corresponding to one acoustic Reynolds number Re. Because the experimental setup could be tuned at two different resonant modes, two different Re numbers could be achieved. Whatever the frequency condition is in numerical and experimental configurations, the acoustic Reynolds number is always much larger than one. Therefore, we can expect similarity to hold between the different configurations studied here in terms of Re.

When working on the $\lambda/2$ experimental mode, the Sh number is $1.2 \cdot 10^{-2}$ (the corresponding experimental configurations are labeled E_1 and E_2), whereas when working on the $3\lambda/2$ experimental mode, the Sh number is $7.2 \cdot 10^{-3}$

TABLE I. Nondimensional numbers used for the present study together with those of several studies in the literature.

Reference	Name	Re_{NL}	M	Sh	Re
Experiments (present study)	E_1	0.47	$8.2 \cdot 10^{-3}$	$1.2 \cdot 10^{-2}$	$1.4 \cdot 10^{7}$
	E_2	4.8	$2.6 \cdot 10^{-2}$		
	E_3	7.7	$2 \cdot 10^{-2}$	$7.2 \cdot 10^{-3}$	$5.2 \cdot 10^{6}$
	E_4	14.6	$2.7 \cdot 10^{-2}$		
	E_5	31.8	$4 \cdot 10^{-2}$		
Numerical (present study)	N_1	0.25	$1.2 \cdot 10^{-2}$	$2.5 \cdot 10^{-2}$	$6.3 \cdot 10^{4}$
	N_2	4.91	$5.5 \cdot 10^{-2}$		
	N_3	7.93	$7.0 \cdot 10^{-2}$		
	N_4	15.2	$9.7 \cdot 10^{-2}$		
	N_5	38.6	$15 \cdot 10^{-2}$		
Menguy and Gilbert[8]		$[0.5 - 2]$	$\ll 1$	$\ll 1$	$\gg 1$
Thompson *et al.*[19]		$[2.1 - 22]$	$[8 - 25] \cdot 10^{-3}$	$5.3 \cdot 10^{-3}$	$4.1 \cdot 10^{6}$
Nabavi *et al.*[12]		$[6.6 - 78]$	$[7.7 - 34] \cdot 10^{-3}$	$[3 - 4] \cdot 10^{-3}$	$[1 - 1.9] \cdot 10^{6}$
Aktas and Farouk[10]		$[0.035 - 16.4]$	$[3.7 - 79] \cdot 10^{-3}$	$[2 - 10] \cdot 10^{-2}$	$6.6 \cdot 10^{4}$

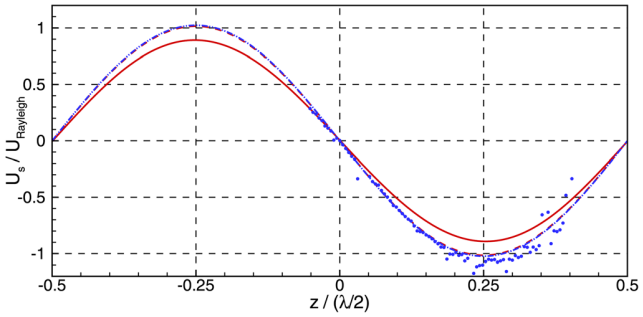

FIG. 2. (Color online) Variation of the axial streaming velocity component along the central axis of the guide normalized by $U_{\text{Rayleigh}} = (-3/8)(U_0^2/c_0)$. (−) N_1 numerical simulation at $\text{Re}_{NL} = 0.25$; (- -) analytical results using the conditions of the simulation; (•) E_1, experimental measurements $\text{Re}_{NL} = 0.47$; (- · -) analytical results using the conditions of the experiment.

(labeled E_3 to E_5). In the numerical simulations the Sh number is $2.5 \cdot 10^{-2}$. As will be shown in the following section, such differences in Sh numbers do not yield any significant difference in the acoustic streaming regime.

Finally, by changing the acoustic amplitude, the M and Re_{NL} numbers are modified. Since the Re_{NL} number is the relevant parameter to study nonlinear acoustic streaming, numerical and experimental configurations were chosen such that the Re_{NL} numbers are as close as possible for comparisons. The corresponding acoustic Mach number ranges from $8.2 \cdot 10^{-3}$ to $4 \cdot 10^{-2}$ for experiments and from $1.2 \cdot 10^{-2}$ to $1.5 \cdot 10^{-1}$ for numerical simulations, and therefore attention should be paid to the possible effects of such different dynamic ranges.

In the following Secs. V A–V C, results for experiments and numerical simulations are presented for different ranges of Re_{NL}, then in Sec. V D the effect of other dimensionless numbers are considered and discussed.

A. Streaming velocity at low nonlinear Reynolds number

The results presented in this section refer to situations where the nonlinear Reynolds number Re_{NL} is smaller than one. The experimental case selected for this comparison at low nonlinear Reynolds number corresponds to $\text{Re}_{NL} = 0.47$ (E_1), and the numerical simulation case corresponds to $\text{Re}_{NL} = 0.25$ (N_1).

Figure 2 displays results from measurements and from numerical simulations for the axial streaming velocity component u_s along the scaled central axis $z/(\lambda/2)$ together with two different results from the analytical analysis presented in Sec. II corresponding to the numerical and experimental cases respectively. In all figures, the velocities are normalized by $U_{\text{Rayleigh}} = (3/8)(U_0^2/c_0)$ that corresponds to the amplitude of the streaming velocity in Rayleigh's theory. The nonlinear effects being negligible for these values of Re_{NL}, the axial streaming velocity should follow Rayleigh's law for linear streaming, which is $u_{\text{Rayleigh}} = (-3/8)(U_0^2/c_0)$ $\sin(4\pi z/\lambda)$ in the present coordinate system. Figure 2 shows that it is indeed the case for all results presented in the figure, except for a slight difference between numerical and both analytical and experimental results. The source of this difference is unclear. The acoustic wave is created in a different manner in the three studies (analytical, numerical, and experimental). This can create discrepancies between the results. Moreover, it is important to recall that the numerical simulations are long and the streaming flow is of the second order. These are difficult conditions, especially for small values of the nonlinear Reynolds number. Therefore this difference in streaming velocity between numerical and analytical results is very satisfying.

The streamlines of the streaming flow are plotted in Fig. 3. Two outer streaming cells and two inner cells can be observed, corresponding to the classical Rayleigh streaming pattern. The streaming vortices are present either sides of the central axis and spaced at interval of $\lambda/4$. For outer streaming, the flow along the central axis is directed toward the acoustic velocity antinodes and returns in the vicinity of the wall to complete a closed loop. In the near wall region, the inner streaming vortices have directions of rotation opposite to those of the outer cells. In the cylindrical resonator, those vortices form toroidal flows around the central axis.

Figure 4 shows the variation of the axial streaming velocity component along the radial axis on a cross-section positioned at $z = -\lambda/8$, for the same cases as in Fig. 2. There is good agreement between all results in the core flow, away from the walls. Small discrepancies between numerical and experimental results can be observed near the walls, when $0.8R < r < R$ that can be attributed to the difference between the Shear numbers in the experimental and numerical configurations. To cope with this effect of different Shear numbers, the evolution of the streaming radial dependency $u_s(r)$ will no further be discussed, but only the evolution of the axial dependency $u_s(z)$ along the axis with Re_{NL}.

Also, given the similarity between the two analytical curves along the center line, it is chosen in the following to plot only the analytical result corresponding to the experimental configuration.

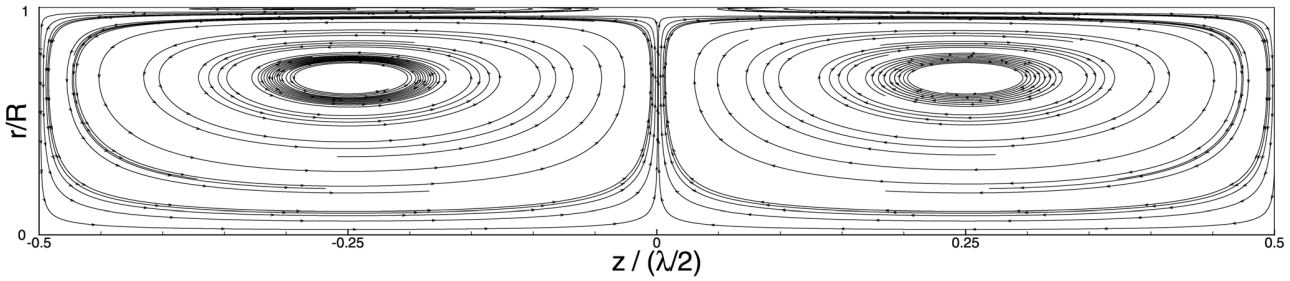

FIG. 3. Streamlines of the streaming flow, from numerical simulation at $\text{Re}_{NL} = 0.25$.

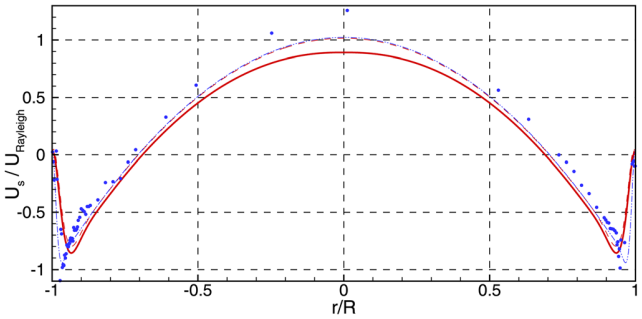

FIG. 4. (Color online) Variation of the normalized axial streaming velocity component along the radial axis, at $z = -\lambda/8$. (−) N_1, numerical simulation at $\mathrm{Re}_{NL} = 0.11$; (- -) analytical results using the conditions of the simulation; (•) E_1, experimental measurements at $\mathrm{Re}_{NL} = 0.47$; (-··-) analytical results using the conditions of the experiment.

B. Streaming velocity at moderate nonlinear Reynolds number

Figures 5–7 display results of measurements and calculations for the centerline streaming velocity along the axis for increasing values of Re_{NL}, up to $\mathrm{Re}_{NL} \approx 15$. They show that as Re_{NL} increases, the streaming velocity departs from the linear theoretical expectation, especially at streaming antinodes [i.e., $z/(\lambda/2) = \pm 0.25$ in the considered figures] where it gets significantly lower than Rayleigh expectation. As shown in Fig. 6, the streaming structure keeps its symmetry with respect to the $z = 0$ position, both in numerical simulations and in experimental measurements. It was checked that this symmetry is kept even for higher amplitude, and therefore, in the rest of the figures, measurements are presented along one cell only [from about $z = 0$ to $z/(\lambda/2) = 0.5$].

The figures clearly show a continuous decrease of the maximum value of the streaming velocity as Re_{NL} increases both in the experimental results and the numerical simulations even so the decrease is not as pronounced in the numerical simulations as in experiments (see Fig. 7). Potential sources of this discrepancy will be discussed in Sec. V D.

C. Streaming velocity at high nonlinear Reynolds number

As the Reynolds number is further increased, as shown in Fig. 8, the difference between measured and calculated

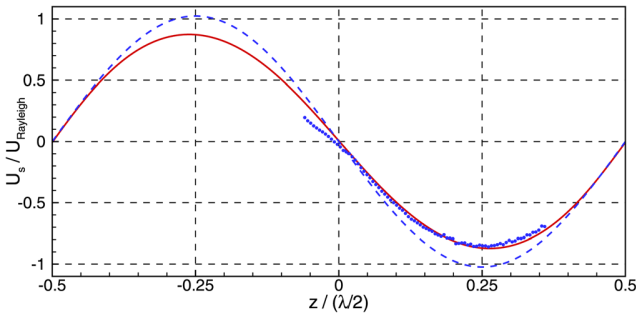

FIG. 5. (Color online) Variation of the normalized axial streaming velocity component along the central axis of the guide. (- -) Analytical results using the conditions of the experiment; (•) E_2, experimental measurements at $\mathrm{Re}_{NL} = 4.8$; (−) N_2, numerical simulation $\mathrm{Re}_{NL} = 4.91$.

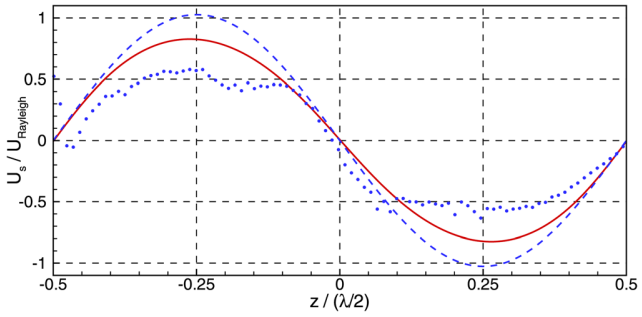

FIG. 6. (Color online) Variation of the normalized axial streaming velocity component along the central axis of the guide. (- -) Analytical results using the conditions of the experiment; (•) E_3, experimental measurements at $\mathrm{Re}_{NL} = 7.7$; (−) N_3, numerical simulation at $\mathrm{Re}_{NL} = 7.93$.

streaming on one hand, and linear theory on the other hand is even more pronounced.

In Fig. 8, experimental results are very different from the linear theory along the axis except near the streaming velocity nodes [$z = 0$ and $z/(\lambda/2) = 0.5$ positions]. In the $z = 0$ region, the curve for the measured streaming velocity along the central axis has successive changes of slope. The maximum measured streaming velocity keeps on decreasing when Re_{NL} is increased until it crosses the zero-velocity axis for $\mathrm{Re}_{NL} > 30$, corresponding to the apparition of a new streaming cell.

The numerical simulation shows an overall similar behavior, although the new cells appearing around the central axis are smaller in the z extent. Near the ends of the guide small additional cells appear in the numerical simulations. The streamlines obtained numerically are shown on Fig. 9 enabling the visualization of the new streaming cells. Even if the experimental and numerical results do not superimpose perfectly, it is remarkable that the same qualitative and overall quantitative behaviors are observed for close values of the Re_{NL} number. Figure 10 shows the numerical results for the modification of the streaming field as Re_{NL} increases, clearly exhibiting the emergence of new streaming cells for Re_{NL} greater than 30.

D. Discussion

As seen in the previous sections, numerical, experimental and analytical results all agree for small values of Re_{NL}.

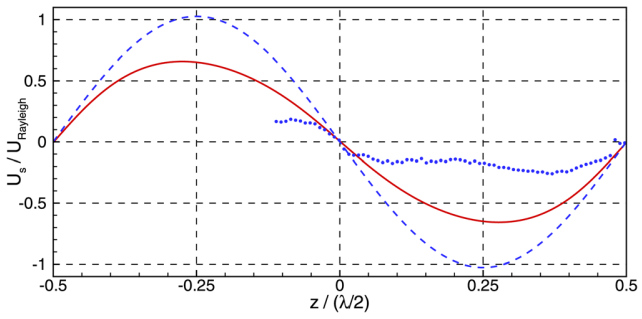

FIG. 7. (Color online) Variation of the normalized axial streaming velocity component along the central axis of the guide. (- -) Analytical results using the conditions of the experiment; (•) E_4, experimental measurements at $\mathrm{Re}_{NL} = 14.6$; (−) N_4, numerical simulation at $\mathrm{Re}_{NL} = 15.2$.

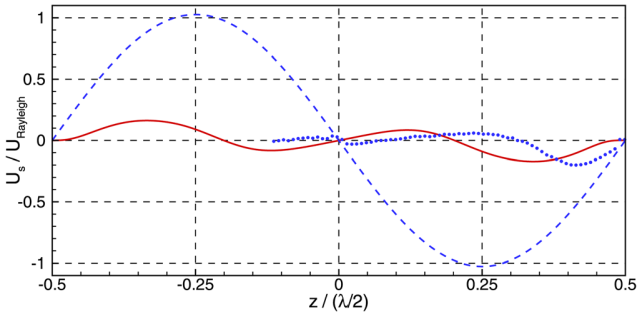

FIG. 8. (Color online) Variation of the normalized axial streaming velocity component along the central axis of the guide. (- -) Analytical results using the conditions of the experiment; (•) E_5, experimental measurements at $Re_{NL} = 31.8$; (−) N_5, numerical simulation at $Re_{NL} = 38.6$.

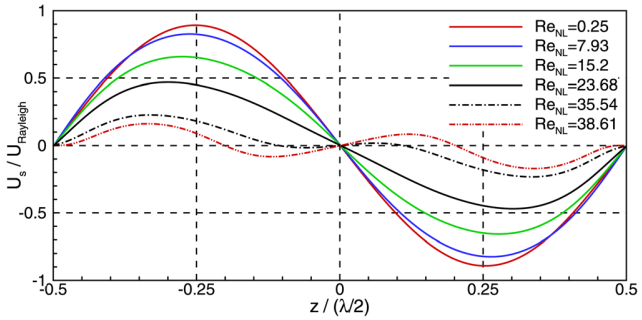

FIG. 10. (Color online) Numerical simulations: variation of the normalized axial streaming velocity component along the central axis of the guide for several values of Re_{NL}.

As Re_{NL} increases, the tendencies are similar for numerical simulations and experiments: the levels of dimensionless streaming decrease and new streaming cells appear at a critical value $Re_{NL} \approx 30$. In order to identify a physical source for this evolution of streaming with Re_{NL}, several hypotheses are discussed in the following sections on the basis of the present literature review.

1. Thermal effects

Following Thompson *et al.*,[19] the influence of thermal effects can be questioned. They performed measurements in a standing wave guide for nonlinear Reynolds numbers up to 22, the three other dimensionless numbers (M, Re, and Sh) respecting the above mentioned asymptotic conditions of our study, see Table I. They explored the evolution of the streaming for three different thermal conditions: isothermal, uncontrolled and insulated and for different nonlinear Reynolds numbers. They observed that when the magnitude of the temperature gradient was increased by changing the thermal condition for a given high nonlinear Reynolds number, the magnitude of the streaming decreased and the shape of the streaming cell became increasingly distorted. They found that the thermoacoustically induced axial temperature gradient strongly influences the axial component of the acoustic streaming velocity and concluded that the deviation from the theories of Rott (characterizing slow streaming with an axial temperature gradient) is due to the influence of thermal effect more than fluid inertia.

In our numerical simulations, isothermal boundary conditions are imposed and thermal effects are accounted for. Nevertheless, the axial streaming velocity profile is deformed with increasing Re_{NL}. The same tendency is observed in the experimental results presented in Figs. 5–8, even if the thermal condition maintained for our set up is only *quasi*-isothermal (as a 0.3 °C temperature difference between acoustic velocity node and acoustic velocity antinode is measured). For $Re_{NL} = 31.8$ the streaming flow already presents additional vortices compared to Rayleigh expectation, as shown by the change of sign of the axial streaming velocity in Fig. 8.

Therefore, if we agree that thermal effects are very important in understanding acoustic streaming (the difference between experimental and numerical thermal conditions could be at the origin of the difference in results) it appears from our study that the presence of a temperature gradient is not the cause of the divergence from slow streaming expectation at high Re_{NL} observed both numerically and experimentally.

2. Irregular streaming

Another possible cause of streaming distortion at high amplitudes exposed in the numerical and experimental literature is the change of regime from "regular" (or classical) to "irregular" streaming. In the literature the term "regular" is used when streaming flow exhibits the well-known patterns (toroidal outer and inner cells), while the term "irregular" is used to characterize any streaming flow that deviates from these patterns.

Aktas and Farouk[10] studied acoustic streaming in a 2D rectangular channel numerically. They found that there is a limit in the value of the enclosure height to wavelength ratio above which the streaming flow structures are always irregular and complex. Since their working frequency is constant, it is equivalent to consider a limit value of the inverse of the Shear number. Based on their numerical results, they

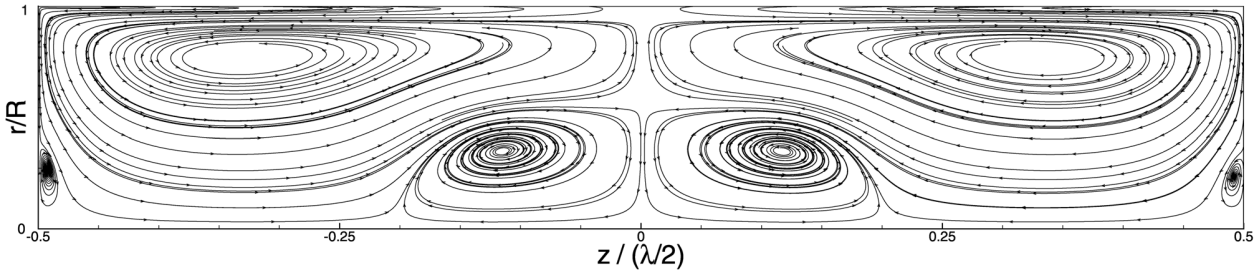

FIG. 9. Streamlines of the streaming flow, from numerical simulation at $Re_{NL} = 38.6$.

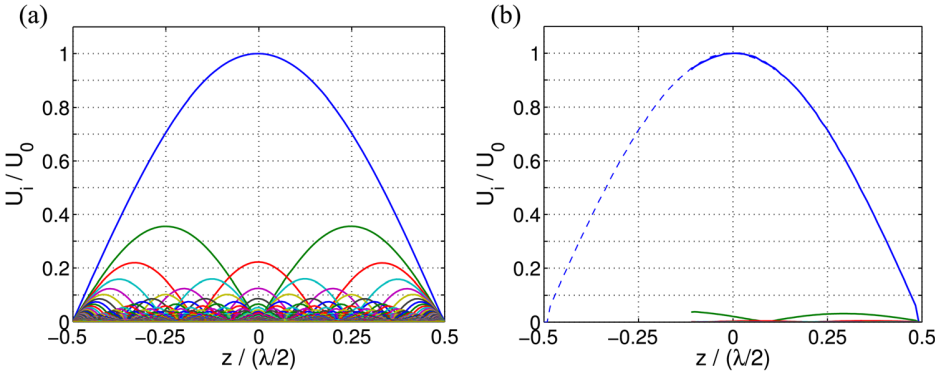

FIG. 11. (Color online) Distribution of the harmonics along the guide. (a) Numerical simulation N_5; (b) experimental study E_5.

estimate this limit value of $1/\mathrm{Sh}$ between 30 and 40. In the present paper, results for values greater or equal to 40 are shown, and we do observe regular streaming for low values of Re_{NL} (cases E_1 and N_1). The results presented by Aktas and Farouk[10] do not exhibit any clear correlation between the regularity of the streaming and the value of Re_{NL}. For example, for two nonlinear Reynolds numbers corresponding to slow streaming cases $\mathrm{Re}_{NL} = 0.10$ (called C-3 in their paper) and $\mathrm{Re}_{NL} = 0.08$ (D-2), they observe two different streaming structures, respectively classical and irregular. The case with irregular streaming structure has a value of $1/\mathrm{Sh}$ of 40. This last case is almost similar to our simulation N_1 where $\mathrm{Re}_{NL} = 0.25$, shown in Fig. 3. In this figure, the streaming velocity field is clearly regular. Although our results are obtained for axisymmetrical configurations, whereas those of Aktas and Farouk[10] concern a rectangular enclosure, previous work[14] showed similar behavior in planar geometry compared to the present observations in the axisymmetrical case. This is indeed coherent with the asymptotic approach.

In the experimental literature, Nabavi *et al.*[12] mentioned irregular Rayleigh streaming for nonlinear Reynolds number above 20. Their experiments were performed in the case of isothermal boundary conditions. They found that for nonlinear Reynolds number above 25, the classical streaming deforms to an irregular and complex flow structure. The deformation they observe is similar to what we observe for some of their irregular cases, however the pattern of the irregular streaming is not always consistent among the experiments and with the value of Re_{NL}. In the above presented results, the streaming flow remains stable, consistent and show a continuous evolution from low to high amplitudes. Measurements have been repeated several times, they were always performed for steady flow and the results obtained are very reproducible.

Finally, we choose not to use the terms "regular" or "irregular" to describe the streaming flow regimes observed both numerically and experimentally. Instead, we would rather describe them as "regular" streaming flow regimes with either two ($\mathrm{Re}_{NL} < 30$) or three ($\mathrm{Re}_{NL} > 30$) toroidal structures, with a smooth transition as Re_{NL} increases.

3. Nonlinear propagation

Our analysis has been done under the assumption of low Mach number. But as the nonlinear Reynolds number increases, so does the Mach number, creating situations where nonlinear acoustic propagation should be of importance, thus the generation of higher harmonics has to be considered. This brings up the question of higher harmonics influence on the streaming in competition with inertial effects associated with high values of nonlinear Reynolds number.

Figure 11 shows the harmonic distribution of the acoustic field, obtained by projecting the total velocity signals on a sine basis, in both numerical [Fig. 11(a)] and experimental [Fig. 11(b)] results for $\mathrm{Re}_{NL} \approx 30$. It shows that the nonlinear propagation induces the existence of shockwaves in the simulations whereas the magnitude of higher harmonics never reaches more than 4% of the magnitude of the fundamental in the experiments, due to the difference in geometrical configurations between experimental and numerical studies. Now for a first approach a superposition principle is applied in order to identify the acoustic streaming due to multiple frequency components. But this crude assumption cannot cope with nonlinear effects. So, as stated in Sec. II C, because the boundary layer can be considered as a region where the streaming is linear, we choose to superimpose the streaming fields resulting from higher harmonics in the vicinity of this region. We choose the particular radial position corresponding to the limit between inner and outer streaming cell, which is at $(R - r) \approx 3\delta_\nu$, at which the streaming is expected to be close to linear streaming. Figure 12 shows the streaming velocity obtained from the numerical simulation at $\mathrm{Re}_{NL} = 38.6$ (N_5), the analytical calculation resulting from the fundamental component of the numerical signal,

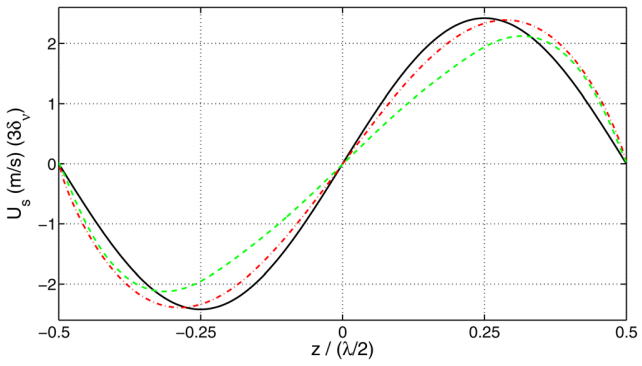

FIG. 12. (Color online) Streaming velocity profile along the axis of the guide at $(R - r) \approx 3\delta_\nu$, for $\mathrm{Re}_{NL} = 38.6$. (—) Analytical solution; (- · -) Streaming velocity from analytical superposition of frequency components of the numerically calculated acoustic velocity; (- -) Numerical simulation.

and the analytical calculation resulting from the linear superposition of all the harmonic components of the numerical signal. First, the distortion of the streaming close to the boundary layer (Fig. 12) is found to be much weaker than in the core of the resonator (Figs. 8 and 10). The effect of the harmonics superposition at $(R-r) \approx 3\delta_\nu$ results in a shift of the streaming velocity maxima toward the acoustic velocity nodes associated with a small change in the velocity magnitude. The same type of distortion can be observed on the numerical profile (Fig. 12), but with a stronger change in the velocity magnitude (the maximum value and the slope of the curve at $z = 0$ are much smaller). Moreover, as the distortion in acoustic streaming is qualitatively the same in both experimental and numerical study along the centerline of the guide, we conclude that while the harmonic content of experimental and numerical signals are very different, the influence of higher harmonics is not the main cause of the divergence of the streaming field from Rayleigh's expectation.

Finally we are left with only one hypothesis to explain this divergence: the inertial effects cannot be neglected anymore when the streaming is fast.

VI. CONCLUSION

In this paper a coupled experimental and numerical study of Rayleigh streaming from low to high acoustic amplitudes was conducted. As expected, slow streaming (both numerically and experimentally obtained) agrees with analytical slow streaming expectations for small Re_{NL}. The divergence from these analytical results that occurs when the Re_{NL} is increased is very similar for numerical and experimental results. As Re_{NL} increases, the cell centers are pushed towards the acoustic velocity nodes and the maximum axial streaming velocity decreases with respect to the analytical Rayleigh reference amplitude. It was also shown that for Re_{NL} larger than about 30, additional outer cells are formed through a smooth transition between coherent streaming flow patterns. This is why the streaming flow regimes can be called "regular" throughout the transition between two ($\mathrm{Re}_{NL} < 30$) and three ($\mathrm{Re}_{NL} > 30$) toroidal structures. After having considered all potential sources for the observed divergence from slow streaming flow, we have concluded that inertial effects on acoustic streaming are the main source. Logically the Re_{NL} is the driving parameter for the acoustic streaming in the regime considered here.

ACKNOWLEDGMENTS

All the experiments were conducted at the Pprime Institute. The authors wish to acknowledge the technical support of Pascal Biais, Laurent Philippon, and Philippe Szeger. The authors wish to thank the GDR 3058 Thermoacoustique (thermoacoustics research group) to have given them the impetus for this collaboration.

[1]L. Rayleigh, "On the circulation of air observed in Kundt's tubes, and on some allied acoustical problems," Philos. Trans. R. Soc. London **175**, 1–21 (1884).
[2]W. L. Nyborg, *Acoustic Streaming* (Academic, New York, 1965), Vol. 2B(11).
[3]P. J. Westervelt, "The theory of steady rotational flow generated by a sound field," J. Acoust. Soc. Am. **25**, 60–67 (1953).
[4]J. Olson and G. Swift, "Acoustic streaming in pulse tube refrigerators: tapered pulse tubes," Cryogenics **37**, 769–776 (1997).
[5]M. F. Hamilton, Y. A. Ilinskii, and E. A. Zabolotskaya, "Thermal effects on acoustic streaming in standing waves," J. Acoust. Soc. Am. **114**, 3092–3101 (2003).
[6]H. Bailliet, V. Gusev, R. Raspet, and R. A. Hiller, "Acoustic streaming in closed thermoacoustic devices," J. Acoust. Soc. Am. **110**, 1808–1821 (2001).
[7]M. F. Hamilton, Y. A. Ilinskii, and E. A. Zabolotskaya, "Acoustic streaming generated by standing waves in two–dimensional channels of arbitrary width," J. Acoust. Soc. Am. **113**, 153–160 (2003).
[8]L. Menguy and J. Gilbert, "Nonlinear effect of the inertia of the fluid on acoustic streaming in cylindrical guides," J. Acoust. Soc. Am. **105**, 958 (1999).
[9]D. Marx and P. Blanc-Benon, "Computation of the mean velocity field above a stack plate in a thermoacoustic refrigerator," C. R. Méc. **332**, 867–874 (2004).
[10]M. K. Aktas and B. Farouk, "Numerical simulation of acoustic streaming generated by finite-amplitude resonant oscillations in an enclosure," J. Acoust. Soc. Am. **116**, 2822–2831 (2004).
[11]S. Moreau, H. Bailliet, and J.-C. Valière, "Measurements of inner and outer streaming vortices in a standing waveguide using laser Doppler velocimetry," J. Acoust. Soc. Am. **123**, 640–647 (2008).
[12]M. Nabavi, K. Siddiqui, and J. Dargahi, "Analysis of regular and irregular acoustic streaming patterns in a rectangular enclosure," Wave Motion **46**, 312–322 (2009).
[13]V. Daru and C. Tenaud, "High order one-step monotonicity-preserving schemes for unsteady compressible flow calculations," J. Comput. Phys. **193**, 563–594 (2004).
[14]V. Daru, D. Baltean-Carlès, C. Weisman, P. Debesse, and G. Gandikota, "Two-dimensional numerical simulations of nonlinear acoustic streaming in standing waves," Wave Motion **50**, 955–963 (2013).
[15]V. Daru and X. Gloerfelt, "Aeroacoustic computations using a high order shock-capturing scheme," AIAA J. **45**, 2474–2486 (2007).
[16]J. Sharpe, C. Greated, C. Gray, and D. M. Campbell, "The measurements of acoustic streaming using particle image velocimetry," Acustica **68**, 168–172 (1989).
[17]M. Campbell, J. Cosgrove, C. Greated, S. Jack, and D. Rockliff, "Review of LDA and PIV applied to the measurement of sound and acoustic streaming," Opt. Laser Technol. **32**, 629–639 (2000).
[18]M. Thompson and A. Atchley, "Simultaneous measurement of acoustic and streaming velocities in a standing wave using laser Doppler anemometry," J. Acoust. Soc. Am. **117**, 1828–1838 (2005).
[19]M. Thompson, A. Atchley, and M. Maccarone, "Influences of a temperature gradient and fluid inertia on acoustic streaming in a standing wave," J. Acoust. Soc. Am. **117**, 1839–1849 (2005).
[20]S. Moreau, H. Bailliet, J.-C. Valière, R. Boucheron, and G. Poignand, "Development of laser techniques for acoustic boundary layer measurements. Part II: Comparison of LDV and PIV measurements to analytical calculation," Acta Acust. Acust. **95**, 805–813 (2009).
[21]J.-C. Valière, S. Moreau, and H. Bailliet, "Development of laser techniques for acoustic boundary layer measurements. Part I: LDV signal processing for high acoustic displacements," Acta Acust. Acust. **95**, 585–594 (2009).
[22]V. Daru and C. Tenaud, "Evaluation of TVD high resolution schemes for unsteady viscous shocked flows," Comput. Fluids **30**, 89–113 (2001).

.

V. Daru, C. Weisman, D. Baltean-Carlès, I. Reyt, H. Bailliet, « Inertial effects on acoustic Rayleigh streaming flow : Transient and established regimes », Wave Motion 74, 1-17, 2017.

Wave Motion 74 (2017) 1–17

Contents lists available at ScienceDirect

Wave Motion

journal homepage: www.elsevier.com/locate/wavemoti

Inertial effects on acoustic Rayleigh streaming flow: Transient and established regimes

Virginie Daru [a,b], Catherine Weisman [b,c], Diana Baltean-Carlès [b,c,*], Ida Reyt [a,d], Hélène Bailliet [d]

[a] Arts et Métiers ParisTech, Lab. DynFluid, 151 Bd. de l'Hôpital, 75013 Paris, France
[b] LIMSI, CNRS, Université Paris-Saclay, Bât. 508, Rue John Von Neumann, Campus Universitaire, F-91405 Orsay Cedex, France
[c] Sorbonne Universités, UPMC Univ Paris 06, UFR d'Ingénierie, 4 Place Jussieu, 75252 Paris Cedex 05, France
[d] Institut Pprime, CNRS - Université de Poitiers - ENSMA, ENSIP, 6 rue Marcel Doré, Bât. B17 - BP 633, 86022 Poitiers Cedex, France

HIGHLIGHTS

- Nonlinear inertial effects produce patterns different from DNS and experiments.
- Time evolutions of streaming cells near the wall and in the core are analyzed.
- The full streaming equations are solved numerically to obtain the established flow.
- Nonlinear inertial effects produce patterns different from DNS and experiments.
- Nonlinear inertial effects cannot explain the mutation of streaming at high levels.

ARTICLE INFO

Article history:
Received 27 October 2016
Received in revised form 21 April 2017
Accepted 5 June 2017
Available online 19 June 2017

Keywords:
Rayleigh streaming
Standing wave
Inertial effects
Nonlinear streaming
Transient evolution

ABSTRACT

The effect of inertia on Rayleigh streaming generated inside a cylindrical resonator where a mono-frequency standing wave is imposed, is investigated numerically and experimentally. To this effect, time evolutions of streaming cells in the near wall region and in the resonator core are analyzed. An analogy with the lid-driven cavity in a cylindrical geometry is presented in order to analyze the physical meanings of the characteristic times.

Inertial effects on the established streaming flow pattern are then investigated numerically using a code solving the time averaged Navier–Stokes compressible equations, where a mono-frequency acoustic flow field is used to compute the source terms.

It is shown that inertia of streaming cannot be considered as the leading phenomenon to explain the mutation of streaming at high acoustic levels.

1. Introduction

Acoustic streaming is often pointed out as being responsible for misunderstood thermal losses in thermoacoustic machines [1]. Among the different streaming flows found in such devices, Rayleigh streaming consists of a mean flow, of second order, which is produced by the interaction between the acoustic wave and a solid wall [2]. The pioneering work of Rayleigh was continued with the studies, among others, of Schlichting [3], Nyborg [4], Westervelt [5], Rudenko and Soluyan [6], yielding the steady streaming theory. Later, thermal effects were taken into account by Rott [7], the compressibility of the fluid by Qi [8] and more recently semi-analytical models adapted for thermoacoustic applications

* Corresponding author.
E-mail address: baltean@limsi.fr (D. Baltean-Carlès).

http://dx.doi.org/10.1016/j.wavemoti.2017.06.001
0165-2125/

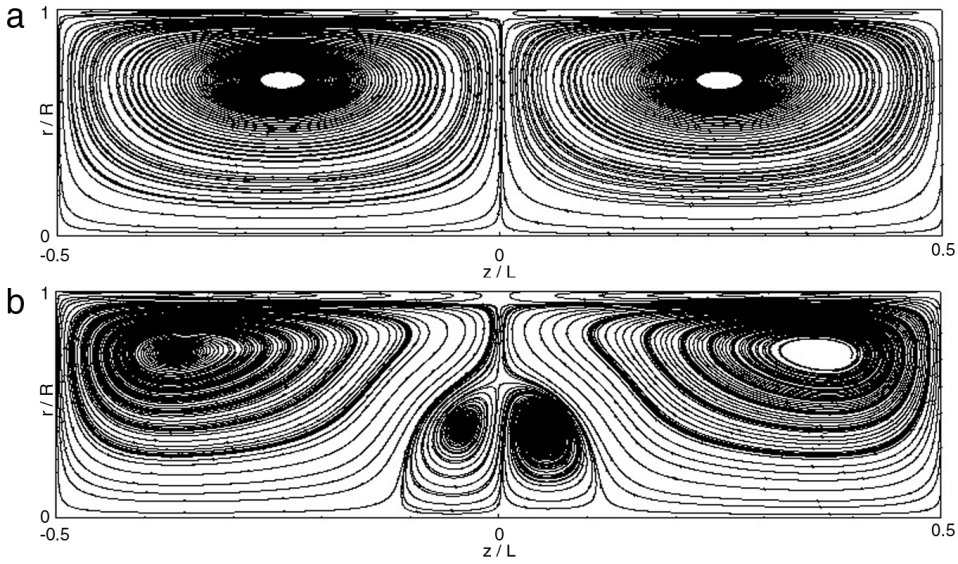

Fig. 1. Streamlines of streaming velocity fields without (a) and with (b) the extra contra-rotating cell (results of numerical simulations N_1 and N_2).

were developed (see for example [9,10]). These theoretical models, used to describe the streaming flow in the slow regime, are based on the method of successive approximations in powers of the Mach number, performed up to the second order and followed by time averaging over the acoustic period, yielding linear equations for streaming flow.

For high intensity acoustic waves, the streaming flow is referred to as nonlinear streaming or fast streaming. In this case, the effect of fluid inertia was first considered by [11–14] in unbounded or semi-infinite spaces, and more recently by Menguy and Gilbert [15] in resonators and thus for Rayleigh streaming. In the weakly nonlinear study proposed by [15], the method of successive approximations is performed up to the third order and separate solutions are obtained for the near-wall region (inner streaming) and in the resonator core (outer streaming). The global solution is obtained by applying matching conditions to the streaming velocity components. The inner streaming approximate equations were shown to remain linear in the weakly nonlinear case, while the outer streaming flow is affected by inertia [15].

Numerical simulations for acoustic Rayleigh streaming can be found in the literature starting in the 1990's. Two approaches are used: one is based on solving the full Navier–Stokes equations for low and high intensity waves and extract the mean flow from the instantaneous flow [16–18], and recently [19–22] and the other approach is based on solving streaming equations for the mean flow in the linear case [23,24] or in the nonlinear case [25]. Numerical simulations as well as experimental studies (for example [26,27]) in large resonators have shown the two regimes of streaming flows associated with standing waves: slow streaming similar to Rayleigh type streaming or fast streaming where the mean flow is strongly modified when the intensity of the acoustic wave is increased. The dimensionless number commonly used to differentiate between slow and fast streaming is the nonlinear Reynolds number Re_{NL} [15], defined by $Re_{NL} = (M \times R/\delta_\nu)^2$, where M is the acoustic Mach number, $M = U_{\max}/c_0$, with $U_{\max}$ the acoustic velocity amplitude at the velocity antinode and c_0 the speed of sound, R the guide radius and $\delta_\nu = \sqrt{2\nu/\omega}$ the acoustic boundary layer thickness, ω being the pulsation and ν the kinematic viscosity of the gas. Fig. 1(a) shows the streaming flow pattern (i.e. the streamlines for the steady mean velocity field, with the average performed over an acoustic period) in a half-plane containing the axis of a cylindrical waveguide of axial extension $\lambda/2$ in the slow streaming regime (result from the numerical simulation N_1 further described in this paper). This pattern is symmetrical with respect to the guide center and is composed of four streaming cells: two inner toroidal cells close to the tube wall and two outer toroidal cells in the core. The established streaming flow behavior for high acoustic amplitudes (i.e. in the nonlinear regime of streaming) was previously analyzed numerically [19] (with a DNS code) and experimentally [28]: additional streaming cells were observed inside the resonator [29]. Fig. 1(b) shows the distorted streaming pattern (result from the numerical simulation N_2 further described in this paper) in the fast streaming regime, when two new streaming cells are observed in the center of the guide, near the acoustic velocity antinode ($z/L = 0$) [19,28,29]. Several sources could potentially be responsible for this mutation of streaming pattern: thermal effects were considered [26], as well as nonlinear propagation [29] and it was concluded that inertial effects on acoustic streaming could be the main source [29]. In the literature there is no study available that allows to conclude about the role of inertia in the behavior of streaming when the latter is "fast". The current study aims at investigating the hypothesis that inertia is responsible for the mutation of streaming flow at high levels by using both experimental and numerical results.

In Section 2, numerical methods and experimental setup are presented. Section 3 describes the establishment of slow and fast streaming using numerical and experimental observations. Time evolutions of inner and outer streaming cells are discussed. In order to analyze the associated physics, Section 4 shows the streaming flow equations and a scale analysis used to point out the leading parameters. The characteristic time scales are estimated according to the configuration parameters and compared with numerical and experimental results.

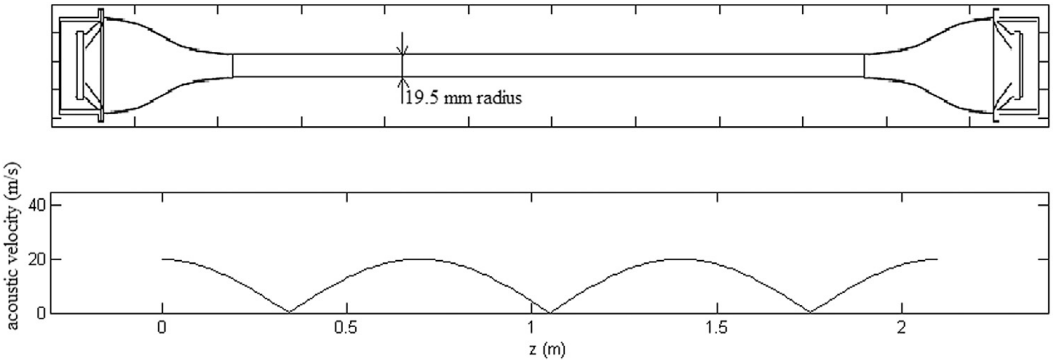

Fig. 2. Sketch of experimental setup and wave pattern for the working frequency.

In order to further isolate the driving effect of inner streaming on outer streaming, the problem of a flow inside a cylindrical tube with prescribed axial velocity on the walls is solved and analyzed in Section 5. Then the role of inertia on the established nonlinear streaming flow patterns is examined (Section 6) by solving the time-averaged isentropic Navier–Stokes compressible equations (AMS), where a mono-frequency acoustic flow field is used to compute the different terms that are sources of streaming flow. The effect of increasing the amplitude of the acoustic flow field on the streaming flow is analyzed. The results are compared with the predictions of the asymptotic model developed in [15] for the weakly nonlinear regime.

2. Methods and set-up

In this section, the experimental setup and the numerical configurations and methods used to investigate the effect of inertia during the establishment of the streaming flow and on the steady state flow are presented briefly (see [29] for more detail). The experimental and numerical configurations are very different in physical dimensions and in frequency but it was checked in [29] that they are asymptotically similar for acoustic and streaming flow. It was shown indeed that the same flow behavior is to be expected if $M \ll 1$, $Re_{ac} \gg 1$ and $Sh \ll 1$ (where $Re_{ac} = \frac{1}{2}\left(\frac{\lambda}{\pi\delta_v}\right)^2$, $Sh = \frac{\delta_v}{R}$, λ being the acoustic wavelength). Both experimental and numerical configurations match these conditions (see Table 1 in [29]).

2.1. Experimental set-up

The set-up used to study acoustic streaming consists of a cylindrical glass tube of radius $R_{exp} = 19.5$ mm filled with air at atmospheric pressure and at ambient temperature (Fig. 2). In order to reach high acoustic levels, the acoustic sound wave is generated by two loudspeakers (one at each end of the guide), tuned at the same frequency, that are driven in opposite phase. Those loudspeakers are connected to the main part of the guide via connecting tubes designed to avoid separation effects related to the singularities in change of section. The total length of the wave guide is $L_{exp} = 2.13$ m and the system is tuned at a frequency $f_{exp} = 240$ Hz so that to excite the third mode of the system. This choice of working frequency allows to perform measurements on a streaming cell away from singularities. The set-up geometry prevents the wave distortion even at high levels.

A wave generator provides the loudspeakers input signal, whose frequency and amplitude are controlled, as well as a trigger reference signal, used to synchronize the laser Doppler measurement system. Velocity measurements are started when the acoustic field is switched on in order to measure the transient evolution of the streaming velocity field. Those measurements are performed at different locations within the streaming cells. The laser system used and the processing of the laser signal are described in [28].

2.2. Numerical methods

For the numerical calculation, we consider a cylindrical tube of length L and radius R, initially filled with air, considered as an ideal gas. An acoustic standing wave is initiated by shaking the tube in the axial direction (z) with given amplitude and frequency, so that a harmonic velocity law is imposed, $\mathbf{V}(t) = V(t)\vec{e}_z$, with $V(t) = z_p\omega\cos(\omega t)$, ω being the angular frequency and z_p the amplitude of the tube displacement.

The flow verifies the compressible Navier–Stokes equations expressed in the moving frame attached to the tube, with an additional forcing source term depending on $\mathbf{V}$:

$$\begin{cases} \dfrac{\partial \rho}{\partial t} + \nabla\cdot(\rho\mathbf{v}) = 0 \\ \dfrac{\partial \rho\mathbf{v}}{\partial t} + \nabla\cdot(\rho\mathbf{v}\otimes\mathbf{v}) + \nabla p = \nabla\cdot(\bar{\bar{\tau}}) - \rho\dfrac{d\mathbf{V}}{dt} \end{cases} \tag{1}$$

Table 1
Parameters of different presented cases (N: numerical, E: experimental).

Name	f (Hz)	R/δ_v	R/L	$U_{\max}$ (m/s)($z=0$)	M	Re_{NL}
N_1	20 000	50	0.09	0.5	1.45×10^{-3}	0.005
N_2	20 000	50	0.09	61.83	0.18	80.84
E_2	240	138	0.027	23	0.067	85.22

where p is the pressure, ρ is the density, $\mathbf{v} = u\vec{e}_z + v\vec{e}_r$ is the flow velocity, $\bar{\bar{\tau}} = -\frac{2}{3}\mu(\nabla\cdot\mathbf{v})\bar{\bar{I}} + 2\mu\bar{\bar{D}}$ the viscous stress tensor of a Newtonian fluid, $\bar{\bar{D}}$ the strain tensor, μ the dynamic viscosity which is supposed to be constant. In this formulation we have neglected the bulk viscosity since $\frac{M^2}{Sh^2 Re_{ac}^2} \ll 1$ [30].

We consider an isentropic state law for the ideal gas, given by

$$p - p_0 = c_0^2(\rho - \rho_0), \tag{2}$$

where p_0, ρ_0 and c_0 are respectively the constant initial pressure, density and sound velocity. Therefore the energy equation is decoupled from the other equations and we only solve the mass and momentum equations (Eqs. (1) and (2)), excluding thermal effects in our study.

No slip conditions are used on the solid boundary $r = R$, i.e. $\mathbf{v}(r = R, z) = 0$. On the axis $r = 0$, symmetry conditions are used, i.e. $\mathbf{v}(r = 0, z) = u(z)\vec{e}_z$ with $\frac{\partial u}{\partial r}(r = 0, z) = 0$. On the vertical boundaries $z = 0, L$, symmetry conditions are also used, i.e. $\mathbf{v}(r, z = 0, L) = v(r)\vec{e}_r$ with $\frac{\partial v}{\partial z}(r, z = 0, L) = 0$.

Due to the geometry, shock waves are generated in the simulations but it was checked that they are of small intensity and do not affect drastically the streaming flow [19,29]. The presence of harmonics will also be addressed in Section 6 of the present article.

The unsteady equations (Eq. (1)) are solved numerically using third order finite difference schemes [19,29]. The mean (streaming) flow is obtained from calculating a simple mean value for each physical quantity (velocity, pressure, density) over an acoustic period.

For simulations, the reference air pressure is $p_0 = 101\,325$ Pa and the density is $\rho_0 = 1.2$ kg/m^3. The reference speed of sound is $c_0 = 343.82$ m/s. The air viscosity is $\mu = 1.795 \times 10^{-5}$ kg m^{-1} s^{-1}. Resonant conditions are imposed, for which $L = \lambda/2$. Numerical values are $f_{num} = 20\,000$ Hz, so that $\lambda/2 = 8.396$ mm and the acoustic period is $T_{num} = 50 \times 10^{-6}$ s. All results presented below are obtained using a regular mesh of rectangular cells composed of 500 points in the axial direction, and of $5 \times R/\delta_v$ points in the radial direction. The time step δt is fixed equal to 8×10^{-9} s.

3. Establishment of acoustic streaming

In order to study the establishment of the streaming flow generated by a sinusoidal standing wave independently from the transient of its acoustic source, the numerical code described in Section 2.2 is used in the following modified manner: for time stepping during the transient of acoustics, at the end of each acoustic period, the instantaneous fields are reinitialized by subtracting the mean flow over that period. Hence, the streaming flow is calculated here only once the acoustics is established, in order to dissociate the transient of streaming from the establishment of acoustics. Of course this cannot be done in experiments so we chose to discuss only experimental results for which the establishment of streaming has its own time scale, which is not the case of experimental results at low levels.

The different case parameters are summarized in Table 1. Subscript 1 is used to denote slow streaming and subscript 2 is used to denote fast streaming.

3.1. Slow streaming

Figs. 3 and 4 address the case of slow streaming flow (for N_1). The established streaming flow pattern is very regular and corresponds to the representation in Fig. 1(a). Fig. 3 shows the time evolution of the streaming pattern: contours of axial streaming velocity are displayed (with color code) and streamlines are superimposed on the right half plane section. On Fig. 3(b) are also displayed two specific locations that will be used for further investigations: $I(r = R - 3\delta_v, z = L/4)$ representing the place of maximum inner streaming velocity and $O_c(r = 0, z = -L/4)$ representing the center of the plane section and the place of maximum outer streaming velocity in the slow regime. Note that the aspect ratio (height/length) of the displayed figures is equal to 0.25 which is much larger than the actual aspect ratio (height/length = 0.09) so that both inner and outer streaming are visible. One can observe that the establishment of the streaming flow occurs in several stages: The inner streaming cell is established first (Fig. 3(a)) and then does not evolve very much. The magnitude of the outer streaming velocity increases on a longer time scale (Fig. 3(b), (c) and (d)). This is in agreement with the results of previous numerical simulations [25].

The time evolution of the streaming velocity at some specific points can also be displayed. Fig. 4(a) shows the time evolution of the axial streaming velocity at I (see Fig. 3(b)). Fig. 4(b) shows the time evolution of the axial streaming velocity

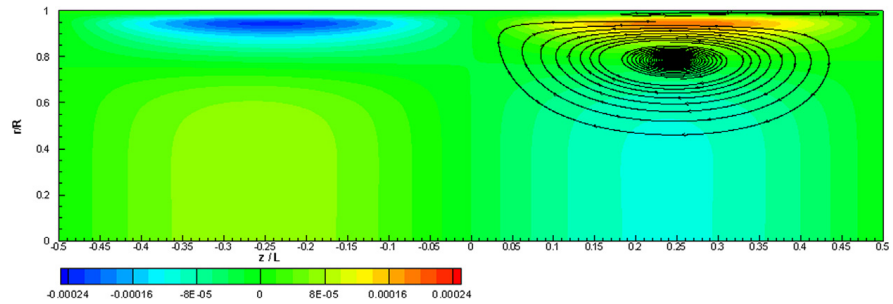

(a) $t = 5.75 \times 10^{-3}$ s.

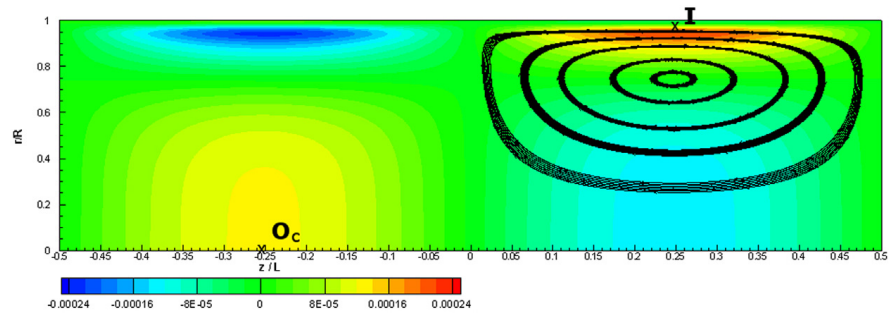

(b) $t = 6.25 \times 10^{-3}$ s.

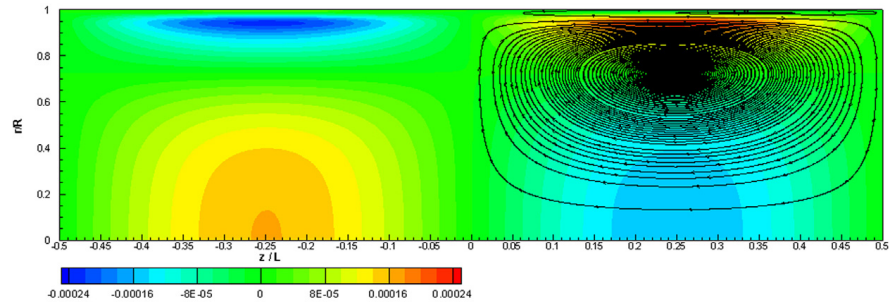

(c) $t = 6.75 \times 10^{-3}$ s.

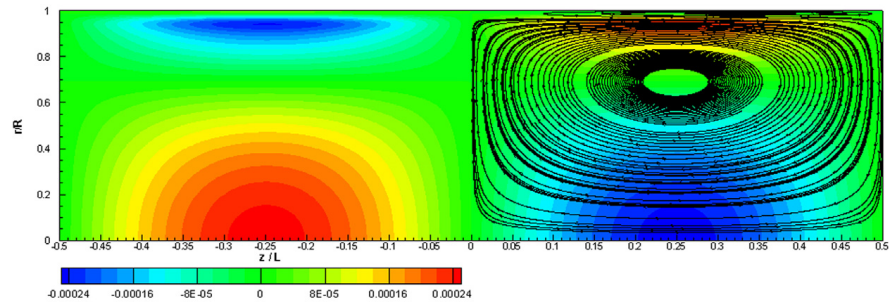

(d) $t = 1 \times 10^{-2}$ s.

Fig. 3. Contours of the axial streaming velocity (with color codes in m/s) at different times during the transient evolution of N_1. Streamlines are superimposed on the right half plane section (real aspect ratio height/length=0.09). (For interpretation of the references to color in this figure legend, the reader is referred to the web version of this article.)

at the center of the plane section O_c (see Fig. 3(b)). In agreement with Fig. 3 the inner streaming (Fig. 4(a)) is established much faster than outer streaming (Fig. 4(b)). As expected from Rayleigh calculations [2], the steady state values at O_I and O_c are roughly equal.

In the experiments, the establishment of acoustics at low amplitudes is very long (see Fig. 13 of [28]). In this case, the evolution of streaming is intrinsically linked to that of acoustics and the associated establishment time scales, determined by fitting an $\exp(-t/\tau)$ law to experimental data, are very close ($\tau_{ac} = 190$ s and $\tau_{st} = 233$ s). As will be shown in the next section, acoustics' transient is much shorter for high amplitudes (τ_{ac} is of the order of tenths of seconds) so that the establishment of streaming can be observed for different locations in the wave guide.

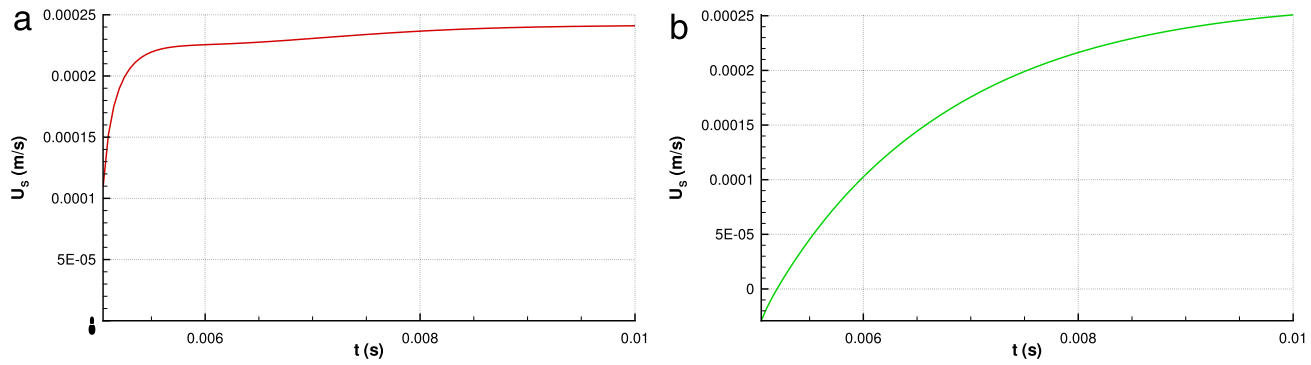

Fig. 4. Time evolution N_1. Axial streaming velocity at (a) I and (b) O_c.

3.2. Fast streaming

Figs. 5–7 address cases of fast streaming flow (for N_2 and E_2 respectively). The established streaming flow pattern is strongly distorted with respect to the slow streaming case, and two extra contra-rotating streaming cells are present near the acoustic velocity antinode (see Fig. 5(d)), in agreement with Fig. 1(b).

Fig. 5 shows the time evolution of the streaming patterns: contours of axial velocity are displayed on the left, and streamlines are displayed on the right. On Fig. 5(d) are also displayed two specific locations that will be used for further investigations: O_e representing the place on the axis corresponding to the maximum velocity inside the extra contra-rotating cell and $O_{c\text{-}exp}$ representing the location on the axis, close to the position $z = L/4$, where measurements were performed to characterize the transient of the main outer streaming cell (both locations are on the right half side of the resonator). Here also the aspect ratio of the displayed figures is increased so that both inner and outer streaming are visible. One can observe that the establishment of the streaming flow occurs in several stages:

The inner streaming cell is established first, typically after 3×10^{-3} s (see Fig. 5(a)) and then does not evolve very much. It is not as symmetrical as in the case of slow streaming (Fig. 3(a)), the cell centers being shifted towards the resonator closed ends (acoustic velocity node).

The magnitude of the outer streaming velocity increases on a longer time scale, and the main outer cell centers progressively shift towards the resonator closed ends (Fig. 5(b), (c) and (d)). Conversely to the slow streaming case, the maximum velocity of the outer streaming cell is smaller than that of inner streaming, as can be seen on the color code.

The emergence of the extra contra-rotating cell happens last (Fig. 5(d)).

On Fig. 6 are presented numerical time evolutions of the streaming velocity at I, O_c (defined in the previous section, Fig. 3(b)) and at the place on the axis corresponding to the maximum velocity inside the extra contra-rotating cells O_e (refer to Fig. 5(d)). First, this figure show that the time evolution of the inner streaming velocity at I (Fig. 6(a)) is similar to the case of slow streaming (similar time scale).

Conversely in the core, the velocity increase for the location O_c (Fig. 6(b)) depicts clearly an inflection point so that two characteristic time scales can be distinguished. Finally for the location O_e (Fig. 6(c)) the velocity is first positive before becoming negative meaning that the contra-rotating cell appears after a certain time. A third time scale emerges from this time evolution. Note that the appearance of the extra cell does not modify the time evolution of streaming outside the extra cell (see Fig. 6(a) and (b)).

On Fig. 7 are presented experimental time evolutions for inner streaming at location I (Fig. 7(a)), for outer streaming on the axis $r = 0$ at location $O_{c\text{-}exp}$ (Fig. 7(b)) and at the extra contra-rotating cell center O_e (Fig. 7(c)) for the fast streaming case E2. Similar behavior to numerical results for equivalent positions can be observed on the experimental measurements and several distinct time scales are visible. The inner streaming is established first. Time evolution of outer streaming at $O_{c\text{-}exp}$ shows a distinct time scale. The magnitude of the contra-rotating cell maximum velocity is very small but the establishment of the extra streaming cell at O_e is on a distinguished time scale from the last two.

In the experiment E_2 the established value in the inner cell ($U_s \simeq 0.5$ m/s at I) is much greater than the established value in the core of the guide ($U_s \simeq 0.01$ m/s at $O_{c\text{-}exp}$), as can be seen on Fig. 7. Similar observations were made on the simulation results in Fig. 5(b). Therefore, both experiments and numerical simulations show that nonlinear phenomena have very small influence on the streaming velocity in the boundary layer.

In summary, for slow streaming flow, only one time scale is necessary to describe the dynamics of streaming in the core of the waveguide. On the contrary for fast streaming flow, three different time scales were observed numerically and two experimentally in the core of the waveguide. At this stage the results seem to indicate that inner streaming flow is hardly modified by nonlinear effects (inertia included) at high levels. On the contrary the outer streaming is very strongly modified. This is in agreement with Menguy and Gilbert findings [15] which stated that inertia affects outer streaming but not inner streaming. However, it is necessary first to clearly identify the effect of inertia on the establishment of streaming. At this stage one cannot indeed assess whether inertial effects are truly responsible for the emergence of the new streaming cell.

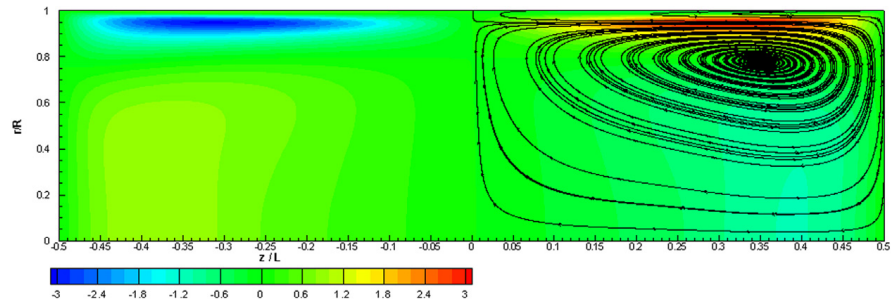

(a) $t = 2.75 \times 10^{-3}$ s.

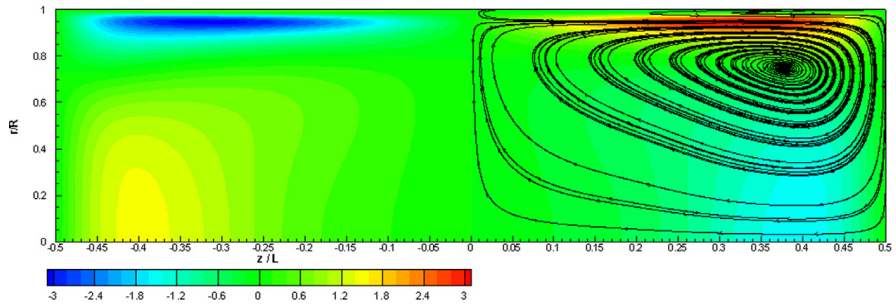

(b) $t = 3.25 \times 10^{-3}$ s.

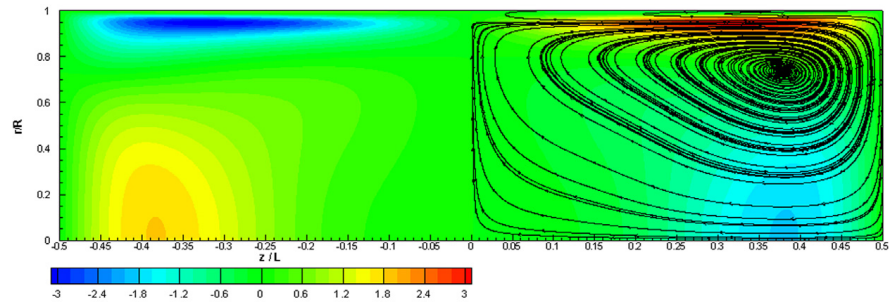

(c) $t = 3.75 \times 10^{-3}$ s.

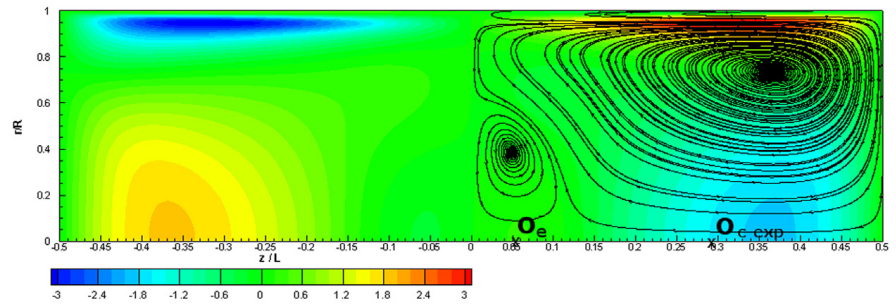

(d) $t = 1 \times 10^{-2}$ s.

Fig. 5. Contours of the axial streaming velocity (with color code) at different times during the transient evolution of N_2. Streamlines are superimposed on the right half plane section (real aspect ratio height/length = 0.09). (For interpretation of the references to color in this figure legend, the reader is referred to the web version of this article.)

In the next section, the equations governing the streaming flow are presented along with a scale analysis in order to exhibit governing dimensionless numbers and time scales for the establishment of inner and outer streaming flows. The expected time scales for the configuration under study are then calculated and compared with fits to the curves shown in the present section.

4. Scale analysis of slow and fast streaming flow

In order to analyze the dynamics of the streaming flow and particularly the competition between diffusion at the origin of streaming and convection associated to nonlinear inertial effects, a scale analysis based on the full equations governing

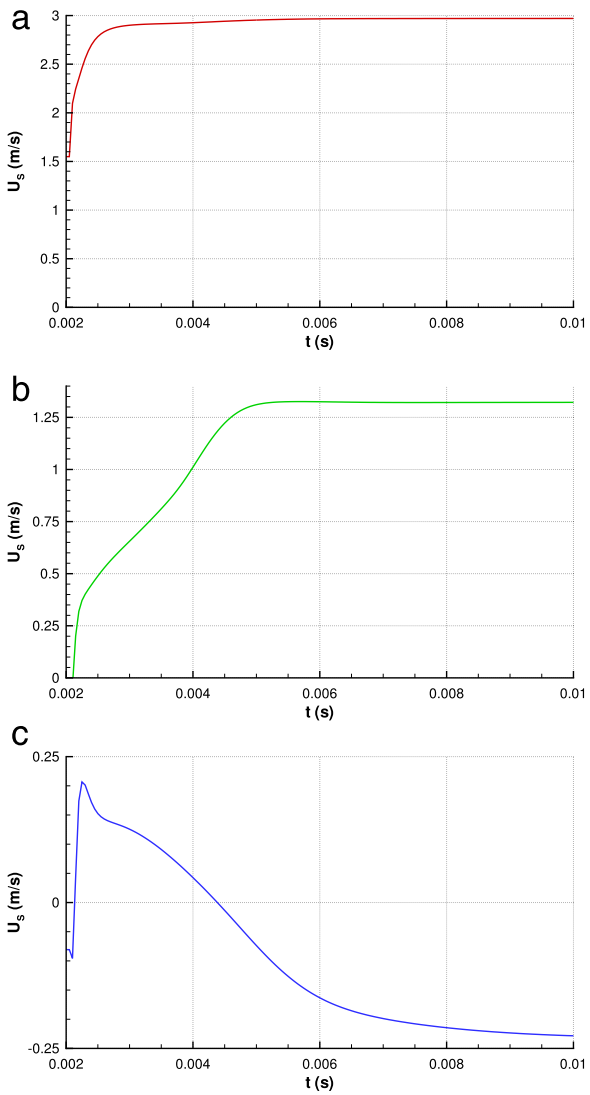

Fig. 6. Time evolution N_2. Axial streaming velocity at (a) I (b) O_c and (c) O_e.

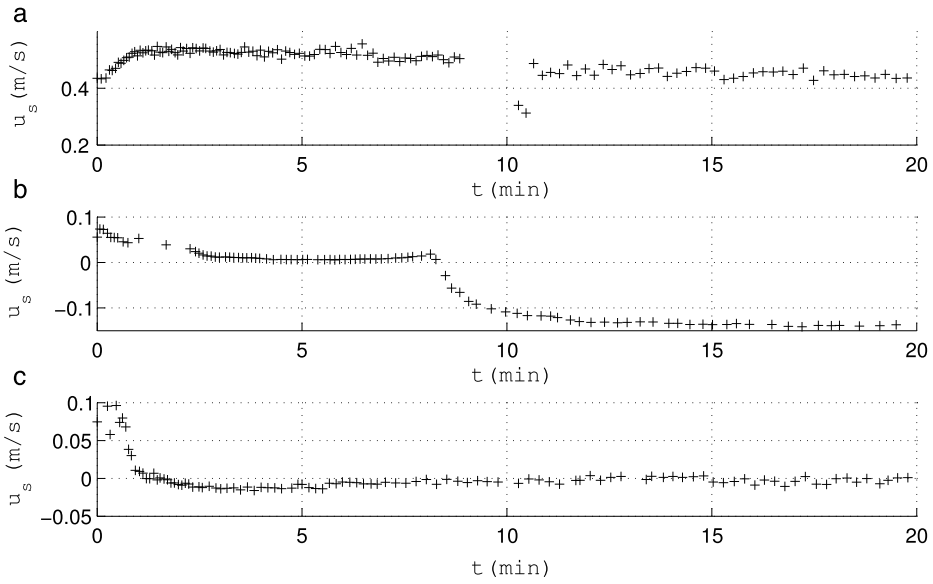

Fig. 7. Time evolution in the fast streaming case E_2. Axial streaming velocity at (a) I (b) O_{c-exp} and (c) O_e.

the streaming flow is conducted below. Our approach is similar to that developed by Boufermel et al. [24] for computing the average mass transport velocity $\frac{\overline{\rho \mathbf{v}}}{\overline{\rho}}$ in the slow streaming regime, as well as to that developed by Moudjed et al. [31] in the somehow different configuration of bulk streaming.

Focus is on outer streaming, whose transient and established regimes was shown to be drastically modified in the fast nonlinear regime.

4.1. Equations governing the streaming flow

Particle velocity $\mathbf{v}$, fluid density ρ and pressure p are decomposed into a fluctuating, periodic component, and a steady component (corresponding to the time average of the variable over the period, i.e. corresponding to the streaming flow)

$$(\mathbf{v}, \rho, p) = (\mathbf{v}' + \bar{\mathbf{v}}, \rho' + \bar{\rho}, p' + \bar{p}), \tag{3}$$

the fluctuating component being denoted by a $'$ superscript and the average operator by an overline. The time average of the fluctuating component is zero. Conversely to usual models of slow streaming, in the present approach no assumption is done on the magnitude of the fluctuation with respect to the steady component. The equations are therefore correct whether the streaming flow is slow or fast.

With this decomposition, the double and triple averaged products between any three variables f, g, h become:

$$\begin{cases} \overline{fg} &= \bar{f}\bar{g} + \overline{f'g'} \\ \overline{fgh} &= \bar{f}\bar{g}\bar{h} + \overline{f'g'}\bar{h} + \overline{f'h'}\bar{g} + \overline{g'h'}\bar{f} + \overline{f'g'h'}. \end{cases} \tag{4}$$

The equations governing the streaming flow are obtained by averaging over the acoustic period the full compressible (isentropic) instantaneous Navier–Stokes equations (1) and the isentropic state law (2). Using the double and triple averaged products detailed in Eq. (4) then results in the following time averaged equation system:

$$\begin{cases} \dfrac{\partial \overline{\rho}}{\partial t} + \nabla \cdot (\overline{\rho}\, \bar{\mathbf{v}}) &= -\nabla \cdot (\overline{\rho' \mathbf{v}'}) \\ \dfrac{\partial \overline{\rho}\, \bar{\mathbf{v}}}{\partial t} + \nabla \cdot (\overline{\rho}\, \bar{\mathbf{v}} \otimes \bar{\mathbf{v}}) + \nabla \bar{p} &= \nabla \cdot (\bar{\bar{\tau}}) + \bar{F}, \end{cases} \tag{5}$$

and $\bar{p} - p_0 = c_0^2(\overline{\rho} - \rho_0)$, where $\bar{\bar{\tau}}$ is the averaged viscous tensor and $\bar{F}$ is the excitation force given by:

$$\bar{F} = -\nabla \cdot (\overline{\rho' \mathbf{v}'} \otimes \bar{\mathbf{v}} + \bar{\mathbf{v}} \otimes \overline{\rho' \mathbf{v}'} + \overline{\rho} \overline{\mathbf{v}' \otimes \mathbf{v}'} + \overline{\rho' \mathbf{v}' \otimes \mathbf{v}'}). \tag{6}$$

Note that $\bar{F}$ is the sum of the source terms, representing the nonlinear contribution of the imposed acoustic field.

4.2. Scale analysis

The equation system (5) is written in dimensionless form, using standard fluid mechanics scalings, detailed in the following. As stated previously, focus is on the resonator core. In a cylindrical wave guide, streaming cells are toroidal of axial dimension $\lambda/4$ and radial dimension R in the core of the resonator. Therefore the axial variable z is scaled with $\lambda/4$ and the radial variable r with R.

Mean velocity is scaled with a reference value of the axial streaming velocity U_s. Density is scaled with ρ_0. Pressure variations are scaled with (δp), not specified at this stage of the scale analysis. The aim of the study is to determine the role of inertia on streaming in the fast regime. Therefore, time is scaled with the characteristic convection time scale in the axial direction $t_c = \lambda/(4U_s)$.

Scalings can then be summarized as follows:

$$r^* = \frac{r}{R}, \qquad z^* = \frac{z}{\lambda/4}, \qquad \mathbf{v}^* = \frac{\bar{\mathbf{v}}}{U_s}, \qquad t^* = \frac{t}{t_c}, \qquad \rho^* = \frac{\overline{\rho}}{\rho_0}, \qquad p^* = \frac{\bar{p} - p_0}{(\delta p)}. \tag{7}$$

Also, the fluctuation variables required to assemble the source terms are scaled with the acoustic amplitudes as follows:

$$\mathbf{v}'^* = \frac{\mathbf{v}'}{U_{\max}}, \qquad \rho'^* = \frac{\rho'}{\rho_{\max}}, \tag{8}$$

$\rho_{\max}$ being the amplitude of density fluctuations at acoustic antinode position in the standing wave. Whenever two different spatial derivatives are involved, the coefficient multiplying each dimensionless term is chosen with respect to the dominant spatial derivative under plane wave assumption: $R \ll \lambda$. In particular, scaling the viscous stress tensor yields a $\frac{\mu U_s}{R^2}$ factor, and scaling the divergence operator $\nabla \cdot (\mathbf{v}^*)$ yields a $\frac{U_s}{\lambda/4}$ coefficient. The following dimensionless equations are deduced from (5):

$$\begin{cases} \dfrac{\rho_0}{t_c}\dfrac{\partial \rho^*}{\partial t^*} + \dfrac{\rho_0 U_s}{\lambda/4} \nabla \cdot (\rho^* \mathbf{v}^*) = -\dfrac{\rho_{\max} U_{\max}}{\lambda/4} \nabla \cdot (\overline{\rho'^* \mathbf{v}'^*}) \\ \dfrac{\rho_0 U_s}{t_c}\dfrac{\partial \rho^* \mathbf{v}^*}{\partial t_c^*} + \dfrac{\rho_0 U_s^2}{\lambda/4} \nabla \cdot (\rho^* \mathbf{v}^* \otimes \mathbf{v}^*) + \dfrac{(\delta p)}{\lambda/4} \nabla p^* = \dfrac{\mu U_s}{R^2} \nabla \cdot (\bar{\bar{\tau}}^*) + \bar{F}, \end{cases} \tag{9}$$

with

$$\overline{F} = -\frac{\rho_{\max} U_{\max} U_s}{\lambda/4} \nabla \cdot (\overline{\rho'^* \mathbf{v}'^*} \otimes \mathbf{v}^* + \mathbf{v}^* \otimes \overline{\rho'^* \mathbf{v}'^*} + \frac{\rho_0 U_{\max}}{\rho_{\max} U_s} \overline{\rho}^* \overline{\mathbf{v}'^* \otimes \mathbf{v}'^*} + \frac{U_{\max}}{U_s} \overline{\rho'^* \mathbf{v}'^* \otimes \mathbf{v}'^*}). \tag{10}$$

Then, multiplying the mass equation with $\lambda/(4\rho_0 U_s)$ and the momentum equation with $\lambda/(4\rho_0 U_s^2)$ and using $t_c = \lambda/(4U_s)$ one can obtain:

$$\begin{cases} \dfrac{\partial \rho^*}{\partial t^*} + \nabla \cdot (\rho^* \mathbf{v}^*) = -\dfrac{\rho_{\max}}{\rho_0} \dfrac{U_{\max}}{U_s} \nabla \cdot (\overline{\rho'^* \mathbf{v}'^*}) \\ \dfrac{\partial \rho^* \mathbf{v}^*}{\partial t^*} + \nabla \cdot (\rho^* \mathbf{v}^* \otimes \mathbf{v}^*) + \dfrac{(\delta p)}{\rho_0 U_s^2} \nabla p^* = \dfrac{1}{Re} \nabla \cdot (\bar{\bar{\tau}}^*) + \overline{F}^*, \end{cases} \tag{11}$$

where the dimensionless excitation force, gathering all the source terms is expressed as:

$$\begin{aligned} \overline{F}^* = & -\frac{\rho_{\max}}{\rho_0} \frac{U_{\max}}{U_s} \nabla \cdot (\overline{\rho'^* \mathbf{v}'^*} \otimes \mathbf{v}^* + \mathbf{v}^* \otimes \overline{\rho'^* \mathbf{v}'^*}) \\ & - \frac{U_{\max}^2}{U_s^2} \nabla \cdot (\rho^* \overline{\mathbf{v}'^* \otimes \mathbf{v}'^*}) - \frac{\rho_{\max}}{\rho_0} \frac{U_{\max}^2}{U_s^2} \nabla \cdot (\overline{\rho'^* \mathbf{v}'^* \otimes \mathbf{v}'^*}). \end{aligned} \tag{12}$$

The system equations (Eq. (11)) is the dimensionless form of the general governing streaming equations (Eq. (5)). The Reynolds number $Re = \frac{4U_s}{\lambda} \frac{R^2}{\nu}$ that appears in the momentum equation is the Reynolds number characterizing the mean flow in a thin tube, defined as the ratio between the diffusion time scale in the radial direction $t_d = R^2/\nu$ and the convection time scale in the axial direction $t_c = \lambda/(4U_s)$, $Re = t_d/t_c$. Note that t_d is equivalent (with a different length reference value) to the characteristic time for streaming development defined by Amari et al. in [32] and used to obtain the transient linear streaming equations. Under the assumptions that acoustic perturbations are small (i.e. of order $M = \frac{U_{\max}}{c_0} \ll 1$) and the streaming field is of order M^2 ($U_s = MU_{\max}$), this Reynolds number can be rewritten as $Re = \frac{4}{\pi} \frac{M^2}{Sh^2} = \frac{4}{\pi} Re_{NL}$, Re_{NL} being the commonly introduced nonlinear Reynolds number.

Under these assumptions, the Reynolds number Re and the nonlinear Reynolds number Re_{NL} are thus of the same order of magnitude. However, since the Reynolds number Re is defined directly with the value of the maximum streaming velocity, it describes more accurately the influence of inertia in the nonlinear regime in the core of the wave guide than Re_{NL}. Indeed, previous numerical and experimental studies [29] have shown that in the nonlinear regime, the maximum value of the axial streaming velocity on the tube axis is much smaller than slow streaming expectations $3U_{\max}^2/(8c)$. Therefore the nonlinear Reynolds number Re_{NL} overestimates the influence of inertia on the streaming flow. For example, in the numerical case N_2, the Reynolds number based on the maximum value of U_s on the axis is $Re = 17.1$ while the corresponding nonlinear Reynolds number is $Re_{NL} = 80.84$. Nonetheless Re cannot be estimated before the simulations/experiments whereas Re_{NL} can be calculated from the acoustics and thus remains useful.

Another Reynolds number used in the literature to distinguish linear from nonlinear regime was the streaming Reynolds number used by Stuart et al. [11] defined as $Re_s = \frac{U_s \lambda}{2\pi\nu}$. It can be expressed as $Re_s = Re \frac{\lambda^2}{R^2}$ and also has the drawback to overestimate the nonlinear inertial effects on Rayleigh streaming.

In the case $Re \ll 1$ (which also means that convection time is much greater than diffusion time) and under the assumption of small perturbations ($M = \frac{U_{\max}}{c_0} = \frac{U_s}{U_{\max}} \ll 1$), the inertial term and the time depending term can both be neglected with respect to the viscous term. The magnitude of source terms is then estimated :

$$\frac{\rho_{ac}}{\rho_0} \frac{U_{ac}}{U_s} \nabla \cdot (\overline{\rho'^* \mathbf{v}'^*} \otimes \mathbf{v}^* + \mathbf{v}^* \otimes \overline{\rho'^* \mathbf{v}'^*}) = O\left(M \cdot \frac{1}{M}\right) = O(1), \tag{13}$$

$$\frac{U_{\max}^2}{U_s^2} \nabla \cdot (\rho^* \overline{\mathbf{v}'^* \otimes \mathbf{v}'^*}) = O\left(\frac{1}{M^2}\right), \tag{14}$$

$$\frac{\rho_{\max}}{\rho_0} \frac{U_{\max}^2}{U_s^2} \nabla \cdot (\overline{\rho'^* \mathbf{v}'^* \otimes \mathbf{v}'^*}) = O\left(M \cdot \frac{1}{M^2}\right) = O\left(\frac{1}{M}\right). \tag{15}$$

$\overline{F}^*$ is then of order $\frac{1}{M^2}$. The pressure gradient must have the same order of magnitude as $\overline{F}^*$ which yields also the pressure variations scale $(\delta p) = \rho_0 U_{\max}^2 = p_0 M^2$. The magnitude of the source term in the mass equation is estimated as previously: $\frac{\rho_{\max}}{\rho_0} \frac{U_{\max}}{U_s} \nabla \cdot (\overline{\rho'^* \mathbf{v}'^*}) = O(1)$. Finally, the steady linear equations for the streaming flow (dimensional form) are then deduced from the first order approximation of the momentum equation and (5) gives:

$$\begin{cases} \nabla \cdot (\overline{\rho} \overline{\mathbf{v}}) = -\nabla \cdot (\overline{\rho' \mathbf{v}'}) \\ \nabla \overline{p} = \nabla \cdot (\bar{\bar{\tau}}) - \overline{\mathbf{F}}, \end{cases} \tag{16}$$

where $\bar{F} \approx \nabla \cdot (\overline{\rho \mathbf{v}' \otimes \mathbf{v}'})$.

As the Re number is increased i.e. $Re \gtrsim 1$, inertial and time depending terms cannot be neglected anymore and the complete unsteady form of streaming equations (5) with all the source terms should be used. In this case the diffusion time scale becomes larger than the convection time scale, thus the overall process is faster and the steady state is reached earlier.

Table 2
Reynolds numbers of different presented cases (N: numerical, E: experimental).

Name	U_s (at I) (m/s)	U_s (at O_c) (m/s)	Re_{NL}	$Re(I)$	$Re(O_c)$
N_1	2.42×10^{-4}	2.63×10^{-4}	0.005	2.24×10^{-3}	2.43×10^{-3}
N_2	3.18	1.84	80.84	29.44	17
E_2	0.5	0.01	85.22	35.26	0.7

4.3. Reynolds numbers and time scale values for slow and fast outer streaming

Table 2 displays the values of the axial streaming velocity at points I or O_c, and of the corresponding Reynolds number of previously described cases N_1, N_2 and E_2.

The previous analysis can also be used to estimate quantitatively the expected time scales of the streaming time evolutions for outer streaming, in the slow and fast streaming regime, that was described qualitatively in Section 3.

In the slow streaming case, diffusion of momentum in the radial direction is expected to be dominant. The convection time variations take place over a very long scale and they are very small, therefore only time variations over a diffusion time scale are significant. The associated characteristic time scale for the establishment of outer streaming is $t_d = R^2/\nu$, which, using the parameter values in Table 2 for N_1, amounts to $t_d = 0.026$ s. Taking into account the fact that the streaming velocity at O_c in Fig. 4(b) is not established in 0.01 s, this is a coherent result.

Based on known analytical solutions of the unsteady pure diffusion equation, if diffusion were dominant the time evolution curves should be in the form $u(t) = u_\infty(1 - e^{-t/\tau})$, where the time constant τ is the time needed for the value u to reach 63% of the established value u_∞ and the time constant needed to achieve 99.999% of the established value is equal to 10τ. The time evolution curve at O_c in Fig. 4(b) is actually very well fitted with such a diffusion curve, and the quantitative fit gives $\tau \simeq 0.0015$ s and therefore $10\tau = 0.015$ s, which is the same order of magnitude as t_d.

In the fast streaming case N_2, in the core, transverse diffusion is expected to compete with convection in the axial direction. The value of the theoretical diffusion time scale t_d is still the same, since it does not depend on the excitation level ($t_d = 0.026$ s). The first velocity increase in the time evolution curve at O_c (Fig. 6(b)) can be fitted by assuming dominant diffusion and the obtained characteristic time scale is the same as in the slow streaming case. Therefore transverse diffusion is dominant at first in the establishment of the outer streaming, just like in the slow streaming case. Assuming next that the second velocity increase in the time evolution curve at O_c (Fig. 6(b)) is related to convection, the theoretical time scale associated with convection along the length $\lambda/4$ with velocity U_s at the location I is $t_c = \lambda/(4U_s) = 1.6 \times 10^{-3}$ s based on the parameters in Table 2. This increase is 20 times faster than that of the diffusion process. A linear fit of the second velocity increase at O_c on Fig. 6(b) gives $t_{cfit} \approx 10^{-3}$ s, which is of the same order as t_c. This shows that the second velocity increase is indeed related to convection in the axial direction. Note that convective transport is much faster than diffusive transport and that the steady state is reached earlier than in the slow streaming case N_1, in agreement with the analysis given at the end of Section 4.2.

In the experimental case $E2$, Fig. 7 shows the evolution of streaming at the three different locations I, $O_{c\text{-}exp}$ and O_e. Two separate slopes in the time evolution of streaming at $O_{c\text{-}exp}$ are also observed, but these are not due to the competition between diffusion and convection as was the case for numerical results. Actually our experimental set up does not allow to observe this competition: the theoretical value of the radial diffusion time scale is $t_d = 24$ s and the convection time scale in the axial direction calculated for E_2 based on the maximum value of U_s at I location (read in Fig. 7(a)) is $t_{cE2} = 0.71$ s. It can be observed that acoustics requires about 3 min to be established. The transient of acoustics is therefore too long to allow to separately identify the establishment of streaming. Moreover one measurement point actually corresponds to an integration of results of particle velocity measurements over several seconds: indeed in order to obtain converged results of the particle velocity estimate, several thousands of seeding particles need to have crossed the measuring volume [27,33]. The associated measuring time depends on the data rate associated with the seeding density; in our set up this process can take as long as 10 s. Therefore it is impossible to distinguish time scales as short as t_d or t_c. The evolution of streaming shown in Fig. 7 can be supposed to result from heat transfer effects. Indeed measurements give an estimate of the mean velocity, that is equal to streaming velocity only if no heat convection occurs. In the case of E_2 experiments, a 4 K temperature difference in the guide wall temperature was measured across a distance of $\lambda/4$. The temperature establishment was found to last for 20 min, probably due to the time needed to reach thermal equilibrium between thermoacoustic, conduction and convection heat fluxes. It can thus be assumed that the measured time evolution of mean velocity is not the only result of acoustic streaming. In the following, only the numerical results will be considered.

In the next section, the driving effect of inner streaming on the outer streaming will be analyzed. Indeed, an analogy with the lid-driven cavity in a cylindrical geometry is presented in order to identify the physical meanings of the characteristic times.

5. Lid-driven cavity analogy

Based on the observation that inner streaming drives outer streaming with competing diffusion and convection, and in order to mimic the establishment of outer streaming, we introduce an equivalent fluid-mechanics problem. We therefore consider the establishment of flow in a lid-driven cavity, but with a cylindrical geometry, and assume that the “lid” is the tube envelope where the inner streaming velocity is imposed.

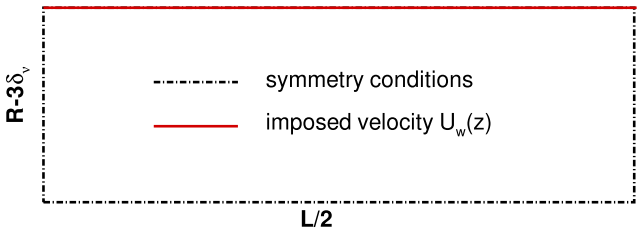

Fig. 8. Schematics of the lid-driven cylindrical flow problem: geometry and boundary conditions.

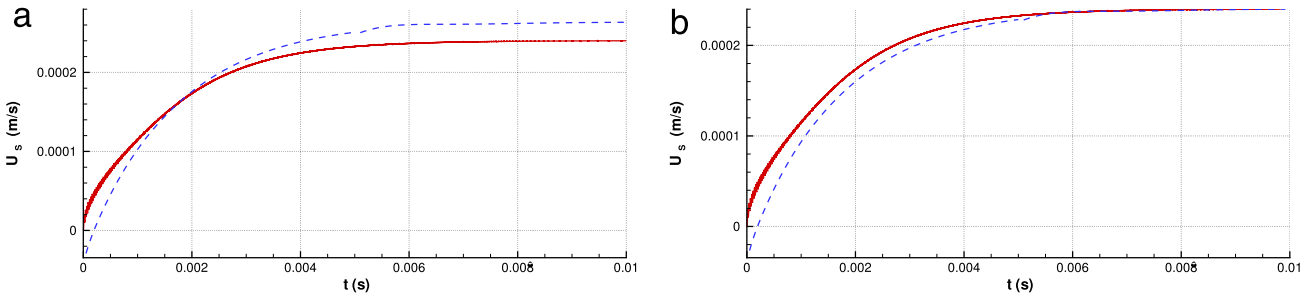

Fig. 9. (a) Time evolution (—) of U ($z = L/4, r = 0$) in lid-driven cavity for U_w from N_1, and (— —) of U_s at O_c from Fig. 4. (b) Same with both curves normalized to reach the same steady-state value. (For interpretation of the references to color in this figure legend, the reader is referred to the web version of this article.)

5.1. Description of the problem

The problem being axisymmetric, the geometry is defined by $z \in [0, L/2]$ and $r \in [0, R - 3\delta_\nu]$. The viscous flow is governed by the following equations, which are the same as in Eq. (1) without the acoustic source terms:

$$\begin{cases} \dfrac{\partial \rho}{\partial t} + \nabla \cdot (\rho \mathbf{v}) = 0 \\ \dfrac{\partial \rho \mathbf{v}}{\partial t} + \nabla \cdot (\rho \mathbf{v} \otimes \mathbf{v}) + \nabla p = \nabla \cdot (\bar{\bar{\tau}}) \end{cases} \tag{17}$$

This system is completed with the isentropic state law Eq. (2). Symmetry conditions are imposed at the vertical walls $z = 0, L/2$ and on the horizontal axis $r = 0$. The boundary condition at the wall $r = R - 3\delta_\nu$ (the "lid") is that the velocity is only axial. Its value $U_w(z)$ is equal to the streaming axial velocity profile $U_s(z)$ along the tube at $r = R - 3\delta_\nu$ given by direct numerical calculations described in the previous sections (see Fig. 8). There is initially no flow in the cavity. The numerical procedure is the same as that described in Section 2.2. The simulations show that the flow is almost incompressible (density variations are less than 0.006%).

5.2. Results

A first simulation (low level) is run with U_w corresponding to the established U_s at $r = R - 3\delta_\nu$ for N_1 case (slow streaming). Fig. 9(a) shows (in red) the time evolution of the axial velocity U at $r = 0$ and $z = L/4$ (center of the mimicked streaming cell). The time evolution of the streaming velocity at O_c (same location) in Fig. 4 is reproduced in blue dots. Fig. 9(b) shows both curves normalized so that they reach the same steady state value. Both curves are very similar with similar time scales, which confirms that transverse diffusion of momentum is the dominant physical phenomenon for the establishment of the slow streaming pattern.

A simulation at higher level is run with U_w corresponding to the established U_s at $r = R - 3\delta_\nu$ for N_2 case (fast streaming). Fig. 10(a) shows (solid red line) the time evolution in the lid-driven cavity of the axial velocity U at $r = 0$ and $z = L/4$. The time evolution of the streaming velocity at O_c (same location) given by Fig. 6(b) is reproduced in blue dots. Both curves are very similar in shape, although the maximum value obtained for the streaming curve is about half of that in the lid-driven cavity. Fig. 10(b) shows the same curves normalized to reach the same steady-state. Both curves are almost superimposed, which shows that the time scales are the same and that the change of slope in the curve is indeed related to the inertial effect, when convection becomes strong enough to compete efficiently with diffusion and to modify the time evolution. However, as stated above the established streaming velocity is much smaller than that obtained in the lid-driven cavity. This suggests that the inertial effects of the lid-driven cavity model are not sufficient to correctly model the change in the streaming flow field.

Fig. 11 shows several snapshots of contours of the axial velocity in the lid-driven cavity during the transient evolution. Streamlines are superimposed on the right half plane section (the simulations are performed on a length $L/2$ and the solution

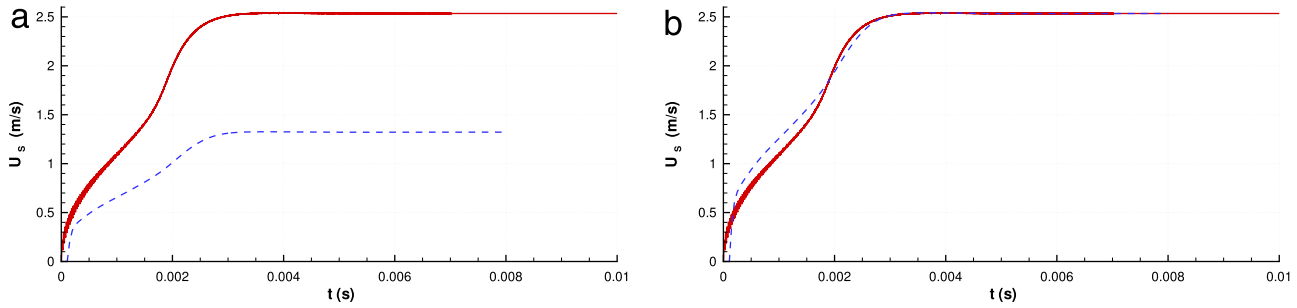

Fig. 10. (a) Time evolution (—) of U ($z = L/4$, $r = 0$) in lid-driven cavity for U_w from N_2, and (— —) of U_s at O_c from Fig. 6. (b) Same with both curves normalized to reach the same steady-state value. (For interpretation of the references to color in this figure legend, the reader is referred to the web version of this article.)

in the right half plane section is constructed by symmetry). Comparison with Fig. 5 shows that the time evolution of patterns are very similar which confirms that the transient evolution of the streaming patterns comes from competing diffusion and convection in a manner analogous to the lid-driven cavity. However, an important difference exists: there is no extra streaming cell in the lid-driven cavity.

Fig. 12 shows axial profiles of U on the axis $r = 0$ for corresponding times of Fig. 11. The axial profile imposed at the wall $r = R - 3\delta_\nu$ is also shown. At early times the axial profile of U is similar to the profile of U_w, which confirms that momentum diffusion in the radial direction is dominant. The distortion observed in the last profile is due to convection in the axial direction.

A similar simulation can be conducted using the experimental configuration of E_2. Fig. 13 shows the time evolution of the axial velocity U at $r = 0$ and $z = L/4$ in the lid-driven cavity (the experimental inner streaming axial profile is imposed at the lid). The associated time scales are of the same order as t_d and t_c calculated in Section 4.3, and the transient behavior of the flow is analogous to that observed in Fig. 10. As mentioned earlier, this evolution cannot be highlighted experimentally.

This analysis shows that although diffusion and convection do compete in the establishment of the streaming flow in a similar manner as in the lid-driven cavity problem, this is not enough to explain the emergence of the new streaming cell. Therefore, at this stage, we can conclude that the lid-cavity model is not complete enough to describe the mutation of streaming at high levels.

In the next section, the complete streaming equations (5) are solved numerically, with a mono-frequency acoustic source used to compute the different source terms. The effect of increasing the amplitude of the acoustic flow field is analyzed.

6. Averaged model simulation for the streaming flow

The high-level mono-frequency acoustic field source used in this section is obtained in two steps. Firstly a DNS simulation at very low-level amplitude is run until a steady streaming flow is obtained. The resulting acoustic field, calculated by subtracting the streaming flow from the total velocity field ($\mathbf{v}' = \mathbf{v} - \overline{\mathbf{v}}$, $\rho' = \rho - \overline{\rho}$), contains insignificant level of harmonics. Then this acoustic field ($\mathbf{v}'$, ρ') is multiplied by a coefficient α chosen to obtain high values of the nonlinear Reynolds number Re_{NL}. This acoustic field is used to compute the source terms so that the following averaged Navier–Stokes equations are solved for the unknown streaming field ($\mathbf{v}_S$, ρ_S, p_S):

$$\begin{cases} \dfrac{\partial \rho_S}{\partial t} + \nabla \cdot (\rho_S\, \mathbf{v}_S) & = -\alpha^2 \nabla \cdot (\overline{\rho' \mathbf{v}'}) \\ \dfrac{\partial \rho_S\, \mathbf{v}_S}{\partial t} + \nabla \cdot (\rho_S\, \mathbf{v}_S \otimes \mathbf{v}_S) + \nabla p_S & = \nabla \cdot (\bar{\bar{\tau}}_S) + \bar{F}_1, \end{cases} \tag{18}$$

with $\bar{F}_1$ defined by

$$\bar{F}_1 = -\nabla \cdot (\alpha^2 \overline{\rho' \mathbf{v}'} \otimes \mathbf{v}_S + \alpha^2 \mathbf{v}_S \otimes \overline{\rho' \mathbf{v}'} + \alpha^2 \rho_S \overline{\mathbf{v}' \otimes \mathbf{v}'} + \alpha^3 \overline{\rho' \mathbf{v}' \otimes \mathbf{v}'}) \tag{19}$$

and $p_S - p_0 = c_0^2(\rho_S - \rho_0)$. The boundary conditions are no slip on the outside wall parallel to the horizontal symmetry axis, and symmetry conditions on the vertical boundaries and horizontal axis.

These equations, very similar to Eqs. (5), are solved with the same numerical method as presented in Section 2.2.

This AMS approach can be used to study the influence of inertial effects on the streaming flow for a monofrequency high amplitude acoustic forcing field. This is equivalent to the strategy followed in [15]. In this way we are able to exclude the influence on the streaming flow of higher harmonics in the acoustic signal. This numerical approach is used here to investigate nonlinear Reynolds numbers Re_{NL} ranging from 0.002 up to 94 (corresponding to Re ranging from 0.0025 to 30.81).

Fig. 14 displays the axial streaming velocity component U_s obtained with the AMS simulation scaled by the Rayleigh streaming maximum velocity $3 \times U_{\max}^2/(8c_0)$ along the scaled central axis z/L for $R/\delta_\nu = 40$ and $0.002 \leq Re_{NL} \leq 94$. For

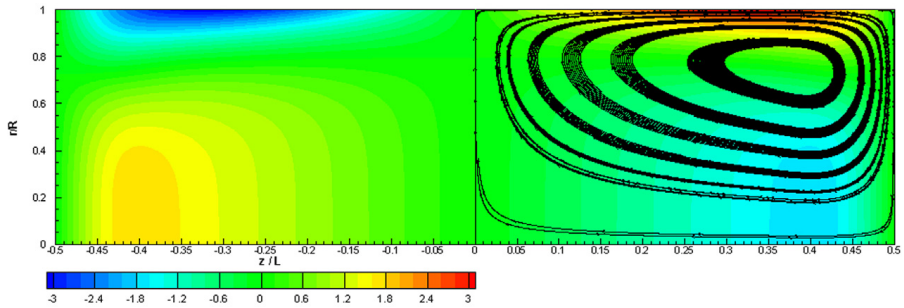

(a) $t = 7.5 \times 10^{-4}$ s.

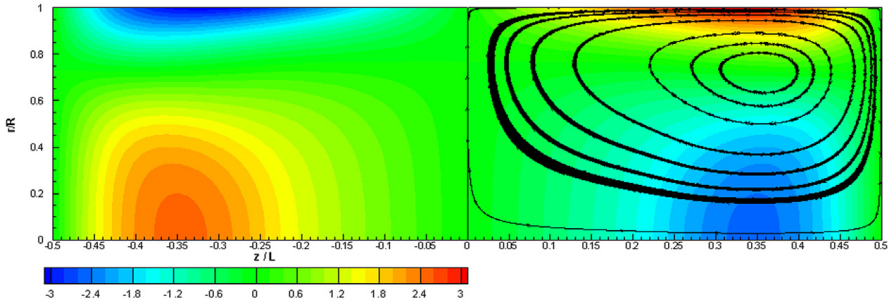

(b) $t = 1.25 \times 10^{-3}$ s.

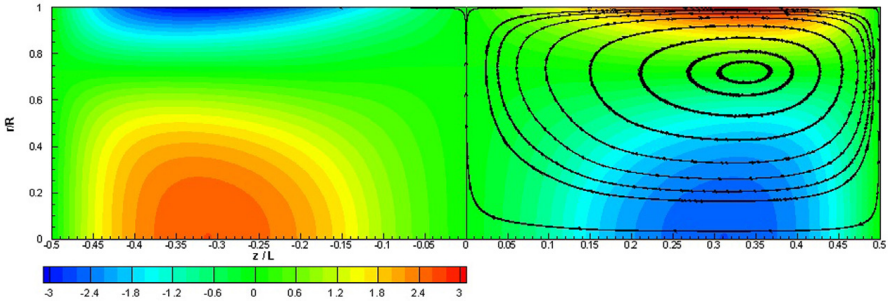

(c) $t = 1.75 \times 10^{-3}$ s.

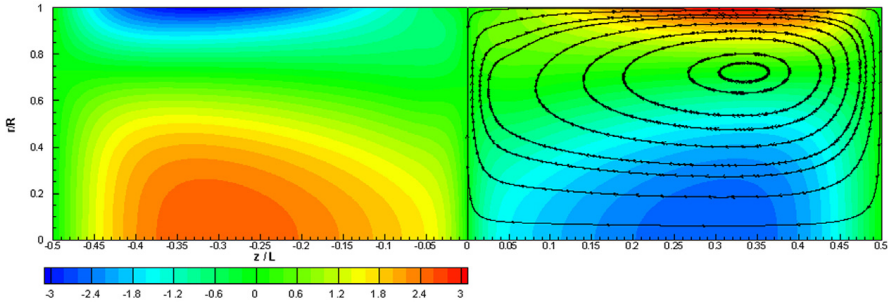

(d) $t = 1 \times 10^{-2}$ s.

Fig. 11. Contours of the axial velocity (with color code) at different times during the transient evolution in the lid-driven cavity for U_w from N_2. Streamlines are superimposed on the right half plane section. (For interpretation of the references to color in this figure legend, the reader is referred to the web version of this article.)

increasing Re_{NL} numbers, the sine function associated to slow streaming becomes steeper next to the resonator center, at the acoustic velocity antinode location, and not next to the resonator ends (acoustic velocity nodes locations). This behavior is in agreement with the predictions of the nonlinear model developed by Menguy and Gilbert [15] at moderate nonlinear Reynolds numbers $Re_{NL} = O(1)$. The direction of distortion is opposite to that observed in the full DNS simulations and experiments [28,29].

In Fig. 15, the dimensionless streaming velocity is plotted along the axis for DNS, AMS and Lid-driven cavity (LDC) simulations, for slow-streaming (N_1) and fast-streaming (N_2). For slow-streaming, all three simulations give analogous

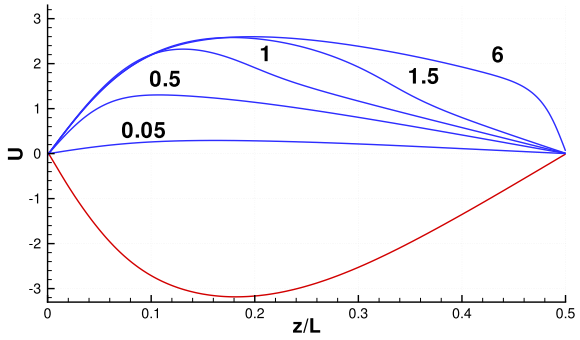

Fig. 12. Axial profiles of U at $r = 0$ (in blue) for corresponding times expressed in 10^{-3} s and at $r = R - 3\delta_v$ (in red) in the lid-driven cavity for U_w from N_2. (For interpretation of the references to color in this figure legend, the reader is referred to the web version of this article.)

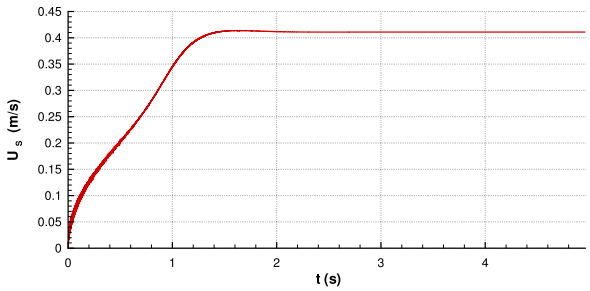

Fig. 13. Time evolution of $U(z = L/4, r = 0)$ in lid-driven cavity for U_w from E_2.

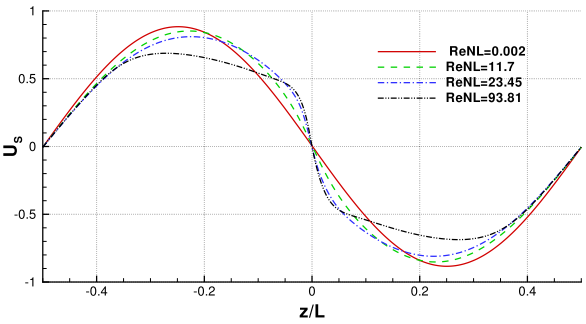

Fig. 14. AMS results for streaming velocity scaled by $3 \times U_{\max}^2/(8c_0)$ along the axis, $R/\delta_v = 40$.

profiles even though the LDC streaming velocity is slightly smaller. This is because the lid-cavity model does not include the acoustic source terms.

For fast-streaming, the AMS result shows the same behavior as the lid-driven cavity. Once again the LDC streaming velocity is slightly smaller, because that model does not include the acoustic source terms. For the AMS simulations, the associated axial velocity contours and streamlines are displayed in Fig. 16. They are similar to those obtained for the lid driven cavity flow, in the steady state (see Fig. 11(d)). On the contrary, the DNS streaming velocity on the axis is globally much smaller, and shows the presence of new streaming cells.

Both the lid-driven cavity and the AMS approaches show that when the intensity of a monofrequency wave is increased, the streaming flow becomes nonlinear because of inertial effects, but the distortion of the Rayleigh streaming profile is different than in DNS simulations or experiments.

This shows that in order to explain the mutation of the streaming flow at high levels, other effects must be analyzed. The only effects that have not been considered yet are the consequences of nonlinear interaction between the streaming flow and acoustics, i.e. the modification of the acoustic flow by the streaming flow. This is currently under study.

7. Conclusion

In this paper the effect of inertia on Rayleigh streaming was investigated numerically and experimentally.

Time evolution of streaming patterns were analyzed. Based on an analysis of the equations driving the streaming flow, two time scales were identified: the diffusion and the convection time scales. The ratio of these time scales is a Reynolds

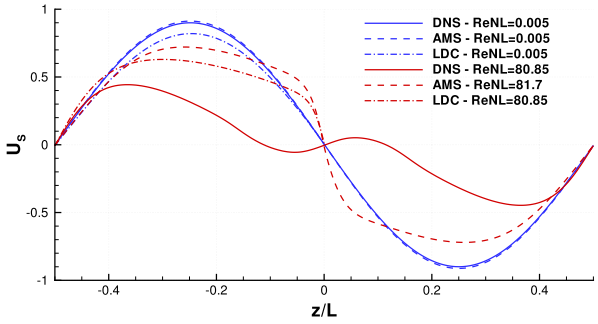

Fig. 15. Dimensionless streaming velocity along the axis. Comparison of DNS (solid lines), AMS (dashed lines) and Lid-Driven Cavity, LDC (dashed–dotted lines) results, $R/\delta_\nu = 50$, for slow-streaming (in blue) and fast-streaming (in red). (For interpretation of the references to color in this figure legend, the reader is referred to the web version of this article.)

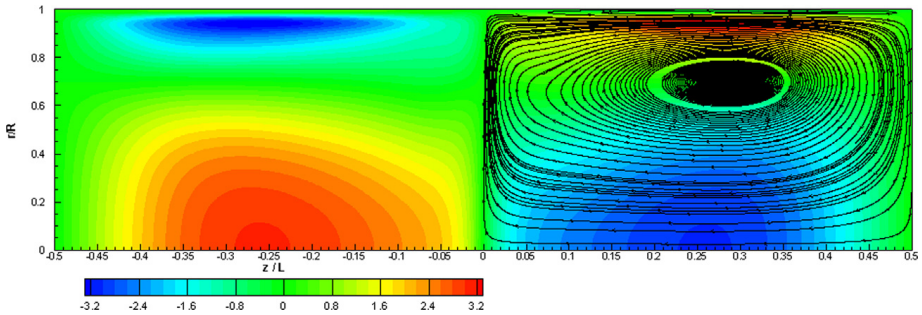

Fig. 16. AMS results, $R/\delta_\nu = 50$. Isolines of the axial streaming velocity colored by its value and the streamlines of the streaming flow. (For interpretation of the references to color in this figure legend, the reader is referred to the web version of this article.)

number $Re = \frac{4U_s}{\lambda}\frac{R^2}{\nu}$ that characterizes the streaming flow and separates the linear from the nonlinear regime. This number is proportional to the nonlinear Reynolds number Re_{NL} only when the streaming flow is of order $M^2 c_0$.

The time evolution of outer streaming was mimicked by analyzing a lid-driven flow. It was confirmed that in a first stage, the outer fast streaming cells are created due to momentum diffusion in the radial direction and that in a second stage, the streaming cells are distorted due to convection in the axial direction. But no extra cell is created in the lid-driven cavity.

Nonlinear inertial effects on the established streaming flow were further investigated using a numerical approach that solves the full streaming flow equations with an imposed monofrequency acoustic wave source computed from the DNS. These simulations as well as the lid-driven cavity simulations show similar results: The streaming patterns in the core of the waveguide are different than those observed in DNS simulations and experiments.

Therefore inertial effects cannot be considered as the leading phenomenon to explain the mutation of streaming at high acoustic levels. Nonlinear interactions between the streaming flow and acoustics have to be considered, which will be the scope of further studies.

Acknowledgment

The authors wish to thank J. Gilbert for many fruitful discussions on this work.

References

[1] G.W. Swift, D.L. Gardner, S. Backhaus, Acoustic recovery of lost power in pulse tube refrigerators, J. Acoust. Soc. Am. 105 (1999) 711–724.
[2] L. Rayleigh, On the circulation of air observed in Kundt's tubes, and on some allied acoustical problems, Philos. Trans. R. Soc. 175 (1884) 1–21.
[3] H. Schlichting, Berechnung ebener periodischer Grenzschicht- strommungen [calculation of plane periodic boundary layer streaming], Phys. Zcit. 33 (1932) 327–335.
[4] W.L. Nyborg, Acoustic streaming, in: W.P. Mason (Ed.), Physical Acoustics, Vol. 2B, Academic Press, New York, 1965, pp. 265–331.
[5] P.J. Westervelt, The theory of steady rotational flow generated by sound fields, J. Acoust. Soc. Am. 25 (1953) 60–67.
[6] O.V. Rudenko, S.I. Soluyan, Theoretical Fundations of Non- Linear Acoustics, English Translation, Plenum, New York, 1977, p. 187-211.
[7] N. Rott, The influence of heat conduction on acoustic streaming, Z. Angew. Math. Phys. 25 (1974) 417–421.
[8] Q. Qi, The effect of compressibility on acoustic streaming near a rigid boundary for a plane traveling wave, J. Acoust. Soc. Am. 94 (1993) 1090–1098.
[9] H. Bailliet, V. Gusev, R. Raspet, R.A. Hiller, Acoustic streaming in closed thermoacoustic devices, J. Acoust. Soc. Am. 110 (2001) 1808–1821.
[10] M.F. Hamilton, Y.A. Ilinskii, E.A. Zabolotskaya, J. Acoust. Soc. Am. 114 (6) (2003) 3092–3101.
[11] J.T. Stuart, Double boundary layer in oscillatory viscous flow, J. Fluid Mech. 24 (1966) 673–987.
[12] J. Lighthill, Acoustic streaming, J. Sound Vib. 61 (1978) 391–418.
[13] V.E. Gusev, O.V. Rudenko, Nonsteady quasi-one-dimensional acoustic streaming in unbounded volumes with hydrodynamic nonlinearity, Sov. Phys. - Acoust. 25 (1979) 493–497.

[14] N. Riley, Streaming from a cylinder due to an acoustic source, J. Fluid Mech. 180 (1987) 319–326.
[15] L. Menguy, J. Gilbert, Non-linear acoustic streaming accompanying a plane stationary wave in a guide, Acta Acust. 86 (2000) 249–259.
[16] A. Gopinath, A.F. Mills, Convective heat transfer due to acoustic streaming across the ends of a Kundt tube, J. Heat Transfer 116 (1994) 47–53.
[17] M. Kawahashi, M. Arakawa, Nonlinear phenomena induced by finite-amplitude oscillation of air column in closed duct, JSME Int. J. 39 (1996) 280–286.
[18] M.K. Aktas, B. Farouk, Numerical simulation of acoustic streaming generated by finite-amplitude resonant oscillations in an enclosure, J. Acoust. Soc. Am. 116 (5) (2004) 2822–2831.
[19] V. Daru, D. Baltean-Carlès, C. Weisman, P. Debesse, G. Gandikota, Two-dimensional numerical simulations of nonlinear acoustic streaming in standing waves, Wave Motion 50 (2013) 955–963.
[20] A.A. Gubaidullin, A.V. Yakovenko, Effects of heat exchange and nonlinearity on acoustic streaming in a vibrating cylindrical cavity, J. Acoust. Soc. Am. 137 (2015) 3281–3287.
[21] A.A. Gubaidullin, A.V. Pyatkova, Acoustic streaming with allowance for heat transfer, Acoust. Phys. 62 (3) (2016) 300–305.
[22] C. Scalo, S.K. Lele, L. Hesselink, Linear and nonlinear modelling of a theoretical travelling-wave thermoacoustic heat engine, J. Fluid Mech. 766 (2015) 368–404.
[23] M. Cervenka, M. Bednarik, Variety of acoustic streaming in 2D resonant channels, Wave Motion 66 (2016) 21–30.
[24] A. Boufermel, N. Joly, P. Lotton, M. Amari, V. Gusev, Velocity of mass transport to model acoustic streaming: Numerical application to annular resonators, Acta Acust. United Acust. 97 (2) (2011) 219–227.
[25] S. Boluriaan, P.J. Morris, Numerical simulation of acoustic streaming in high amplitude standing wave, in: AAIA Paper 2003–3152 (9th AIAA/CEAS Aeroacoustics Conference and Exhibit, 12–14 May 2003, Hilton Head, South Carolina).
[26] M. Thompson, A. Atchley, M. Maccarone, Influences of a temperature gradient and fluid inertia on acoustic streaming in a standing wave, J. Acoust. Soc. Am. 117 (2005) 1839–1849.
[27] S. Moreau, H. Bailliet, J.-C. Valière, Measurements of inner and outer streaming vortices in a standing waveguide using laser doppler velocimetry, J. Acoust. Soc. Am. 123 (2008) 640–664.
[28] I. Reyt, H. Bailliet, J.C. Valière, Experimental investigation of acoustic streaming in a cylindrical wave guide up to high streaming Reynolds numbers, J. Acoust. Soc. Am. 135 (2014) 27–37.
[29] I. Reyt, V. Daru, H. Bailliet, S. Moreau, J.C. Valière, D. Baltean-Carlès, C. Weisman, Fast acoustic streaming in standing waves: Generation of an additional outer streaming cell, J. Acoust. Soc. Am. 134 (3) (2013) 1791–1801.
[30] C. Olivier, G. Penelet, G. Poignand, J. Gilbert, P. Lotton, Weakly nonlinear propagation in thermoacoustic engines: A numerical study of higher harmonics generation up to the appearance of shock waves, Acta Acust. United Acust. 101 (5) (2015) 941–949.
[31] B. Moudjed, V. Botton, D. Henry, H. Ben Hadid, J.-P. Garandet, Scaling and dimensional analysis of acoustic streaming jets, Phys. Fluids 26 (2014) 093602.
[32] M. Amari, V. Gusev, N. Joly, Temporal dynamics of the sound wind in acoustitron, Acta Acust. United Acust. 89 (2003) 1008–1024.
[33] J.-C. Valière, S. Moreau, H. Bailliet, Development of laser techniques for acoustic boundary layer measurements. Part I: LDV signal processing for high acoustic displacements, Acta Acust. United Acust. 95 (2009) 585–594.

Notes et Documents LIMSI N^{O} : 2020 - 2
Septembre 2020

Auteur (Author) : Catherine WEISMAN

Titre : Modélisation et simulation d'écoulements et transferts convectifs. Applications en thermoacoustique. Mémoire d'Habilitation à Diriger des Recherches.

Title: Modeling and simulation of convective flow and heat transfer, thermoacoustic applications.

Nombre de pages (Number of pages) : 187

Résumé : *Ce mémoire synthétise 29 années d'enseignement et de recherche. Les travaux de recherche portant sur la modélisation et la simulation numérique d'écoulements et transferts de chaleur sont présentés en quatre chapitres : les deux premiers chapitres portent sur la convection naturelle en cavité différentiellement chauffée, partiellement remplie d'un milieu poreux d'une part, et à grands écarts de température d'autre part (convection hors Boussinesq, hypothèse faible Mach). Les applications du modèle faible Mach à l'étude des machines thermoacoustiques (pompe à chaleur et moteur) sont détaillées dans le troisième chapitre. Le dernier chapitre rassemble les études autour du streaming acoustique en guide d'ondes à faible et fort niveau acoustique.*
Mots clés : convection naturelle, milieu poreux, thermoacoustique, faible Mach, streaming acoustique

Abstract : *This document synthesizes 29 years of teaching and research. Four chapters are used to present research work on modeling and numerical simulation of flow and heat transfer : analyses of natural convection flows in a differentially heated fluid cavity are detailed in the first two chapters, with the cavity partially filled with porous media (chap. 1) and when large temperature differences are considered (non-Boussinesq flow, low Mach number approximation, chap. 2). Applications of a low Mach number model to the study of thermoaoustic heat pumps or engines are presented in chapter 3. The last chapter gathers analyses of acoustic streaming developing in a wave guide at low and high acoustic amplitude.*
Key words: Natural convection, porous media, thermoacoustics, low Mach number, acoustic streaming